Genetic Algorithm Optimisation Methods Applied to the Indoor Optical Wireless Communications Channel

By

Matthew David Higgins

A thesis submitted in partial fulfilment of the requirements for the degree of Doctor of Philosophy

School of Engineering

THE UNIVERSITY OF WARWICK

June 2009

For the love of my life, Liang

Table of Contents

List of Figures

List of Tables

List of Abbreviations

ADR - Angular Diversity Receivers

BER - Bit Error Rate

BPSK - Binary Phase Shift Keying

CMOS - Complementary Metal-Oxide-Semiconductor

CON - Concertina

CPC - Compound Parabolic Concentrator

DTIRC - Dielectric Totally Internally Reflecting Concentrator

DPPM - Differential Pulse Position Modulation

FOV - Field of View

GA - Genetic Algorithm

IM/DD - Intensity Modulation Direct Detection

IrDA - Infrared Data Association

IR - Infrared

ISI - Inter Symbol Interference

LED - Light Emitting Diode

LOS - Line of Sight

LSMS - Line Strip Multispot

LTI - Linear Time Invariant

MRC - Maximal Ratio Combining

MSD - Multispot Diffusion

NOB/E - Non Optimised Bandwidth when Empty

NOB/M - Non Optimised Bandwidth with Movement

NOrms/E - Non Optimised RMS Delay Spread when Empty

NOrms/M - Non Optimised RMS Delay Spread with Movement

OA - Optical Antenna

OB/E - Optimised Bandwidth when Empty

OB/M - Optimised Bandwidth with Movement

OFDM - Orthogonal Frequency Division Multiplexing

Orms/E - Optimised RMS Delay Spread when Empty

Orms/M - Optimised RMS Delay Spread with Movement

OOK - On Off Keying

OW - Optical Wireless

PPM - Two Pulse Position Modulation

QoS - Quality of Service

RCLED - Resonant Cavity Light Emitting Diode

RF - Radio Frequency

RMS - Root Mean Square

SNR - Signal to Noise Environment

SUS - Stochastic Uniform Sampling

UWB - Ultra Wide Band

VCSEL - Vertical Cavity Surface Emitting Laser

WA - Wrap Around

List of Algorithms

Acknowledgements

I would like to thank all those that have helped me to complete this work. First and foremost, sincere gratitude goes to my supervisors, Prof. Roger J. Green and Dr. Mark S. Leeson, for their uncompromising support, guidance, constructive suggestions, and valuable time along the way. It has been a privilege to work with them, and I will always be grateful for the opportunities they have allowed me to take. I also wish to thank Prof. Nigel G. Stocks for his help in obtaining me funding during my time at Warwick, and the time he spent listening to my problems during several years of postgraduate staff student liaison committee meetings.

Special thanks also goes to my parents Lynn and David, and my sister Amy, for their support during this work. They have always done their best for me, and provided everything I needed. I also wish to thank my mother- and father-in-law for having faith in me. Last but not least, I wish to thank my wife, Liang. She was always there for me and she kept me smiling during the tough times, especially towards the end. She provided all the motivation and reasons I needed to complete this work and push myself as hard as I did. She made the whole PhD experience a worthwhile effort.

Declaration

This thesis is submitted in partial fulfilment for the degree of Doctor of Philosophy under the regulations set out by the Graduate School at the University of Warwick. This thesis is solely composed of research completed by Matthew David Higgins, except where stated, under the supervision of Prof. R. J. Green and Dr. M. S. Leeson between the dates of September 2005 and June 2009. No part of this work has been previously submitted to any institution for admission to a higher degree.

Matthew David Higgins

June 2009

Abstract

This thesis details an investigation into the application of genetic algorithms to indoor optical wireless communication systems. The principle aims are to show how it is possible for a genetic algorithm to control the received power distribution within multiple dynamic environments, such that a single receiver design can be employed lowering system costs. This kind of approach is not typical within the research currently being undertaken, where normally, the emphasis on system performance has always been linked with improvements to the receiver design.

Within this thesis, a custom built simulator has been developed with the ability to determine the channel characteristics at all locations with the system deployment environment, for multiple configurations including user movement and user alignment variability. Based on these results an investigation began into the structure of the genetic algorithm, testing 192 different ones in total. After evaluation of each one of the algorithms and their performance merits, 2 genetic algorithms remained and are proposed for use. These 2 algorithms were shown capable of reducing the receiver power deviation by up to 26%, and forming, whilst the user perturbs the channel, through movement and variable alignment, a consistent power distribution to within 12% of the optimised case.

The final part of the work, extends the use of the genetic algorithm to not only try to optimise the received power deviation, but also the received signal to noise ratio deviation. It was shown that the genetic algorithm is capable of reducing the deviation by around 12% in an empty

environment and maintain this optimised case to within 10% when the user perturbs the channel.

Publications Associated with this Research Work

The following journal and conference papers have been published as a result of the work contained within this thesis. They have not been referenced throughout, but form the general foundation for what is presented herein.

Journal Papers

M. D. Higgins, R. J. Green, and M. S. Leeson, "Receiver alignment dependence of a GA controlled optical wireless transmitter," *Journal of Optics A: Pure and Applied Optics*, vol. 11, no. 7, p. 075403, 2009.

M. D. Higgins, R. J. Green, and M. S. Leeson, "A genetic algorithm method for optical wireless channel control," *IEEE J. Lightwave Tech.*, vol. 27, no. 6, pp. 760–772, 2009.

R. J. Green, H. Joshi, M. D. Higgins, and M. S. Leeson, "Recent developments in indoor optical wireless systems," *IET Communications*, vol. 2, no. 1, pp. 3–10, 2008.

Conference Papers

R. Green, M. Higgins, H. Joshi, and M. Leeson, "Bandwidth extension for optical wireless receiver-amplifiers," in *10^{th} Anniversary International Conference on International Transparent Optical Networks, ICTON 2008.*, Athens, Greece, vol. 4, pp. 201–204, 22-26 June 2008.

M. S. Leeson, R. J. Green, and M. D. Higgins, "Photoparametric amplifier frequency converters," in *10^{th} Anniversary International Conference on International Transparent Optical Networks, ICTON 2008.*, Athens, Greece, vol. 4, pp. 197–200, 22-26 June 2008.

M. D. Higgins, R. J. Green, and M. S. Leeson, "Genetic algorithm channel control for indoor optical wireless communications," in *10^{th} Anniversary International Conference on International Transparent Optical Networks, ICTON 2008.*, Athens, Greece, vol. 4, pp. 189–192, 22-26 June 2008.

Chapter 1

Introduction

Indoor optical wireless (OW) communication systems using an infrared (IR) carrier is an interesting technology that combines the high bandwidth availability of communications in the optical domain, with the traits of mobility, found in the more traditional radio frequency (RF) wireless communications systems. Compared to an RF system, OW offers the advantageous opportunity for high speed medium to short range communications operating within a virtually unlimited and unregulated bandwidth spectrum using lower cost components. Furthermore OW systems are capable of secure deployment with immunity to adjacent communication cell interference due to the inability for the signal radiation to penetrate opaque barriers such as walls. Topologically speaking, the IR radiation can be reflected off the walls, as in a diffuse system, providing user movement flexibility at the expense of multipath distortion, but immune to multipath fading, or it can undergo a direct line of sight (LOS) path, resulting in higher data rates and lower power consumption [1].

The technology is not without it drawbacks compared to RF techniques, such as the requirement for a base station to be situated within every room, and the susceptibility of the signal to the intense ambient background light from the sun, incandescent and fluorescent lights. However, even with these implementation challenges, the pioneering work by Gfeller *et al.* in 1979 [2, 3],

whereby a fully diffuse system was formed transmitting at only $125\,\mathrm{kbit\,s^{-1}}$, was not short lived. By 1985, OW system performance ranged from low power LOS systems operating at $19.2\,\mathrm{kbit\,s^{-1}}$ to higher power ones operating at a $1\,\mathrm{Mbit\,s^{-1}}$ milestone [4, 5, 6, 7]. By 1990 the LOS systems had reached their next milestone of $50\,\mathrm{Mbit\,s^{-1}}$ [8, 9, 10], which by 1994 the same bit rate could be extended to mobile diffuse systems of up to $155\,\mathrm{Mbit\,s^{-1}}$ when operated in LOS mode [11, 12, 13].

Since then, the techniques and applied applications found within OW communications have become more advanced and more interesting. Conceptions such as multispot diffusion (MSD), angular diversity and rate adaptive modulation schemes, are relevant to the work here and so will be discussed shortly. Furthermore, the conventional RF community has now accepted that optical wireless is part of the electromagnetic communication spectrum, at least, in part, thanks to a Wireless World Research Forum White Paper [14] and the continual work of the commercial entity, the Infrared Data Association (IrDA) [15]. OW communications is, however, not alone in the market place, and although it can be considered as a complementary technology with conventional RF techniques, RF communications has also improved in recent years with competition from newer systems employing ZigBee, Bluetooth, WiFi and ultrawideband (UWB) to name but a few [16, 17, 18, 19], and as such work must still continue in advancing OW communications to the limit.

In this chapter an up to date review of OW communications will be presented. To begin with, the relevant fundamentals of channel theory will be covered providing an insight into the design challenges involved in deploying high performance systems. This is followed by a section on modulation theory, in which, the key performance metrics of modulation schemes will be evaluated with reference to recent developments. The chapter then goes onto providing a review of recent developments in OW transmitter and receiver design with specific focus on the various implementable OW system configurations. A review of the use of intelligent systems for

OW applications is then provided, which as will seen, the number of applications is very few in number, leading to a section on the aims and motivations of the work presented here. Finally a outline of the structure is presented outlining the order of work as it was completed.

1.1 Infrared Channel Overview

In virtually all short range, indoor applications intensity modulation direct detection (IM/DD), is the only practical transmission technique [20]. Here, an infrared emission capable device emits and instantaneous optical power $X(t)$, propagating through the channel and incident upon the receiver's optical detector. The received signal $Y(t)$, is then the integration of the detected optical power over the area of the detectors surface, multiplied by the photodetectors responsivity R [21]. Typically the photo detectors used in a receiver have large areas of the order $10^6 - 10^8$ square wavelengths, resulting in optically incoherent reception without multipath fading [22]. The channel can be modelled as baseband linear time invariant (LTI), with impulse response $h(t)$, that only changes significantly when the source, receiver or reflectors are moved by distances in the order of centimetres. For nearly all indoor applications the transmission is operated in the presence of intense infrared and visible background radiation, $N(t)$, that can be modelled as additive white Gaussian, independent of $X(t)$, and as such a simplified channel model for the IM/DD link is given by [23]

$$Y(t) = RX(t) * h(t) + N(t) \tag{1.1}$$

Where $*$ denotes the convolution operation. Through necessity, as $X(t)$ represents power, it cannot be negative, and average optical power, P_{av}, is proportional to the time integral of $X(t)$ [24]

$$P_{av} = \lim_{T\to\infty} \int_{-T}^{T} X(t)dt \qquad \text{for} \qquad X(t) \geq 0 \tag{1.2}$$

rather than the usual $|X(t)|^2$, which is appropriate when $X(t)$ represents amplitude. In the electrical domain, the signal to noise ratio (SNR) is proportional to $|X(t)|^2$, thus is a major

challenge to produce a high SNR at useful data rates, since the optical average transmission power needs to be higher compared to the electrical domain.

The reason achieving a high SNR is a challenge under these constraints is that the average transmitted power cannot exceed predefined eye safety limits set by IEC 60825 regulations [25]. Further to this the optical channel path loss is given by

$$H(0) = \int_{-\infty}^{\infty} h(t)dt \tag{1.3}$$

such that the received power is given by

$$P_{rec} = H(0)P_{av} \qquad \text{(W)} \tag{1.4}$$

Therefore, not only are the eye safety regulation limiting, but also, the specific impulse response between a given source and receiver, inherent factors in obtaining a suitable SNR at the receiver.

The actual impulse response itself is the final channel challenge for an OW system designer. The impulse response, $h(t)$ is unique to a given source and receiver configuration within the environment they are deployed within. This means the position and orientation of the source and transmitter, along with source properties such as radiation emission pattern, and receiver properties such as field of view (FOV) and active collection area, are factors of $h(t)$. Coupling these with the dimensions of the environment and any object enclosed, along with their respective reflectivity coefficients, an essentially infinite number of possible impulse responses exist. Furthermore the impulse response not only dictates the path loss but also the degree to which inter symbol interference (ISI) will affect the transmitted signal as it is reflected around the room [26, 27, 28].

1.2 Modulation Overview

The modulation procedure employed in IM/DD systems may be carried out in two stages. The first is an optional modulation of a carrier frequency by the data signal, and the second is the modulation of the emitted infrared light. Low frequency components close to DC should be avoided for data transmission, as the receiver is dominated by shot noise generated by ambient light. The quality of a modulation code is dictated by the reliability of transmission [29, 30], the bandwidth efficiency [31, 32] and the power efficiency that it offers under typical noise and multipath conditions in the optical wireless channel [33].

Considering firstly how reliable a modulation scheme is, a good technique should adapt the signal to the OW channel in such a way as to allow reception and consequent demodulation at the receiver end within the limit of the acceptable bit error rate (BER). Specifically a reliable modulation scheme will be able to deal with ISI and variations in the data signal DC content. Additionally, the modulation scheme should be resistant to modulation independent effects of the channel such as phase jitter from the signal power variation, pulse extension from reflected signal paths and pulse distortion from the near-field signal clipping. A second measure of a good modulation scheme is the bandwidth efficiency, defined as the ratio of achievable bit rate to bandwidth. The higher the bandwidth efficiency of a scheme, the higher the data rate will be in a given environment and for many indoor environments, where bandwidth the limiting factor, it is of great importance to utilise efficiently. Finally, power efficiency, defined as the ratio of energy per optical pulse to mean energy required per bit, is the last empirical test of a modulation scheme. Due to eye safety limits, power efficiency must be maximised, however typically one cannot be increased without lowering the other as the duty cycle of the modulated waveform is the ratio of bandwidth efficiency and power efficiency [34].

A detailed comparative analysis of several binary modulation schemes is provided in [35]. Here the relative performance characteristics of on off keying (OOK), two pulse position modulation

(2-PPM), and subcarrier binary phase-shift keying (BPSK) is presented. It is shown that the power efficiency of OOK and 2-PPM are the same, whereas, for BPSK, the power efficiency is 3 dB less due to BPSK consisting of half the transmit pulse energy. The bandwidth requirements of 2-PPM and BPSK are the same, being twice that is needed for OOK. Thus, at lower data rates, OOK emerges as the most suitable modulation scheme amongst binary modulation schemes. At higher data rates, $10\,\mathrm{Mbit\,s^{-1}}$, it suffers from a large power penalty resultant of multipath dispersion [36].

The earlier generation of OW systems described earlier, were predominantly based upon binary modulation, however in recent years several new schemes have been developed that may be of interest to the work presented here. Differential PPM (DPPM) is a simple modification of PPM that can achieve improved power and/or bandwidth efficiency, and is superior to PPM in optical multiple-access applications. A DPPM symbol is obtained from the corresponding PPM symbol by deleting all of the 'off' chips following the 'on' chip and furthermore, DPPM detection does not require symbol synchronisation, reducing receiver complexity, that was necessary in the case of utilising PPM. It was shown in [37, 38] that, for a given bandwidth, DPPM requires less power than PPM. For only slightly more bandwidth, 16-DPPM provides a 3 dB power gain over 4-PPM. For a 1.4 dB power penalty, 16-DPPM also produces the same bit rate as 16-PPM, but uses less than half the bandwidth. Alternatively, using a scheme based upon Trellis coding, whereby the modulation is designed to minimise the Euclidean distance between allowed signal sequences, the OW multipath dispersion penalties have been mitigated [22, 39].

Although the optical wireless channel can support high bit rate transmission, it is not possible to constantly maintain the SNR to support this because of the changes in the impulse response, the subsequently change the path loss between source and receiver, along with possible abrupt changes in ambient light conditions. It is however, possible and, more important, to reduce the data rate, achieving an acceptable BER and maintaining a high quality of service (QoS), than

loosing the data link entirely. There are several rate adaptive modulation schemes that have been developed recently, and that are of interest to this work. In [40] a scheme is shown based on the use of variable silence periods and OOK formats with memory. Here the variable silence periods are used to modify the statistics of the amplitude sequence related to the message sequence, providing an increase in the peak to average optical power ratio. The scheme provides a wide ranging data rate, but advantageously, results in reduced implementation complexity, compared with a scheme based upon repetition coding specified by the IrDA standard [41].

Another recently developed idea is the use of the frequency domain method of adaptively multiplexing orthogonal sub-carriers [42]. This technique is analogous to adaptive orthogonal frequency division multiplexing (OFDM) in the RF domain. Here the system dynamically adjusts the transmission rate to the OW channel conditions by assigning suitable modulation formates to individual sub-carriers, thus fully utilising the channel capacity. The rate adaptation if maintained even under a worst case scenario by using the lowest sub-carriers over a low rate link, thus maintaining a minimum QoS. The lowest rate carriers are chosen to be those suitable for transmission under extreme conditions, such as the low complexity modulation formats, OOK or PPM. The data rate is chosen on a carrier by carrier basis, and, therefore the system is able to adapt to a wide range of channel conditions.

1.3 Transmitter and Receiver Overview

As with any mobile communication system, the objective is to provide the user with a high degree of movement, coupled with a high data rate. In addition to modulation aspects, transmitter and receiver design are also important factors in system performance. The design techniques employed to realise them should take into account the configuration of the system.

A diffuse system requires a high power transmitter and a sensitive receiver, due to the high

path loss from the multiple reflections incurred between the source and the receiver, limiting the rate of modulation that can be achieved [43]. The low level of optical power often present at the receiver makes the utilisation of optical concentrators to maximise light collection beneficial [44, 45]. However, the high level of ambient light present results in shot noise over the entire FOV of the optical concentrator plus detector combination. This can be ameliorated by optical and electrical filtering [46]. The LOS channel offers higher speed due to lower path loss, but requires a high degree of alignment, which cannot be blocked, limiting user mobility. Photogenerated noise can also be reduced due to the narrower FOV employed in the optical front end of the receiver. A more modern approach described in recent literature, is the quasi-diffuse, or tracked system, employing a multibeam transmitter and an angular diversity receiver.

The purpose of the quasi diffuse transmitter is to create multiple narrow beams targeted in different directions. By using such beams, the system requires lower transmitter power, has a lower path loss and reduced multipath dispersion, in comparison with single wide-angle transmitters, but the user still has freedom of movement [47]. Figure 1.1 shows some of the possible multispot diffusion patterns that can be achieved using quasi diffuse transmitters, including a novel line strip multispot system (LSMS) [48].

Multispot diffusion can be achieved by implementing arrays of illuminating elements, coupled to conventional lenses or computer generated holograms [49, 50, 51]. It is also possible to target the narrow fields towards a reflective surface, such as the ceiling as in Figure 1.1, or provide many direct LOS links from a base station situated on the ceiling, projecting down onto the receiver [52].

Angular diversity receivers (ADRs) utilise an array of narrow FOV receiving elements that are pointed in different directions and/or have different spatial locations, combining to create a wide-angle receiver. Each element has its own amplifier circuitry, and the system may employ signal processing to determine which elements are receiving signals, allowing the rejection of

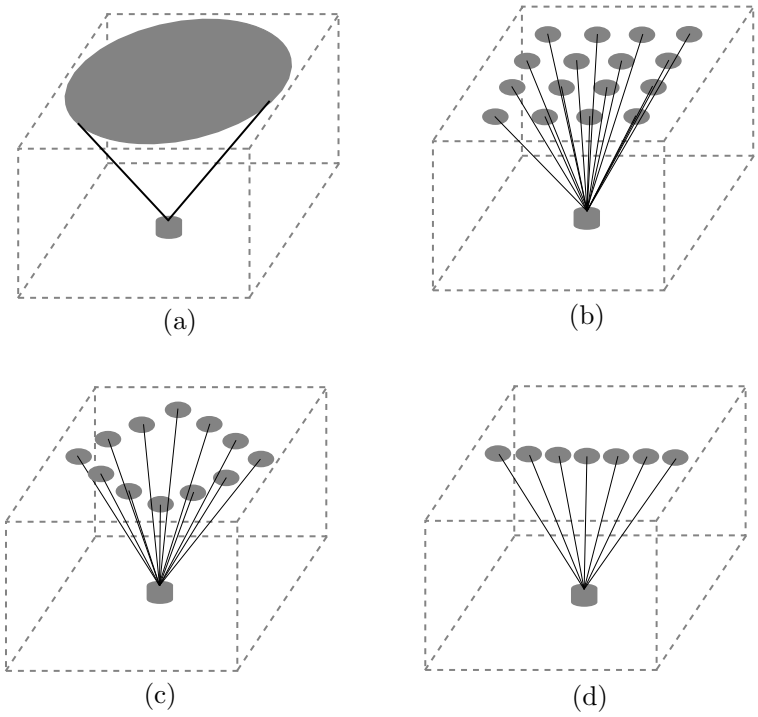

Figure 1.1: Types of multispot diffusion patterns. (a) Conventional diffuse transmitter. (b) Uniform multispot diffusion. (c) Diamond multispot diffusion. (d) LSMS diffusion.

some inputs, or power saving by deactivating those elements receiving only noise. Multipath dispersion effects can also be mitigated by rejecting elements that receive weak signals from reflections if a LOS link is present. Another advantage is that each element with a narrow FOV is smaller than a single element with a wide FOV, so the capacitance of each detector is smaller, thus increasing the bandwidth of the receiver. The disadvantage of using ADRs is the added complexity of the receiver, which has to incorporate multiple detectors, each with its own amplifier and an overall processor.

The ADR can be either imaging or non-imaging, as shown in Figure 1.2. The former employs only one imaging optical concentrator that forms an image of the received light onto the photode-

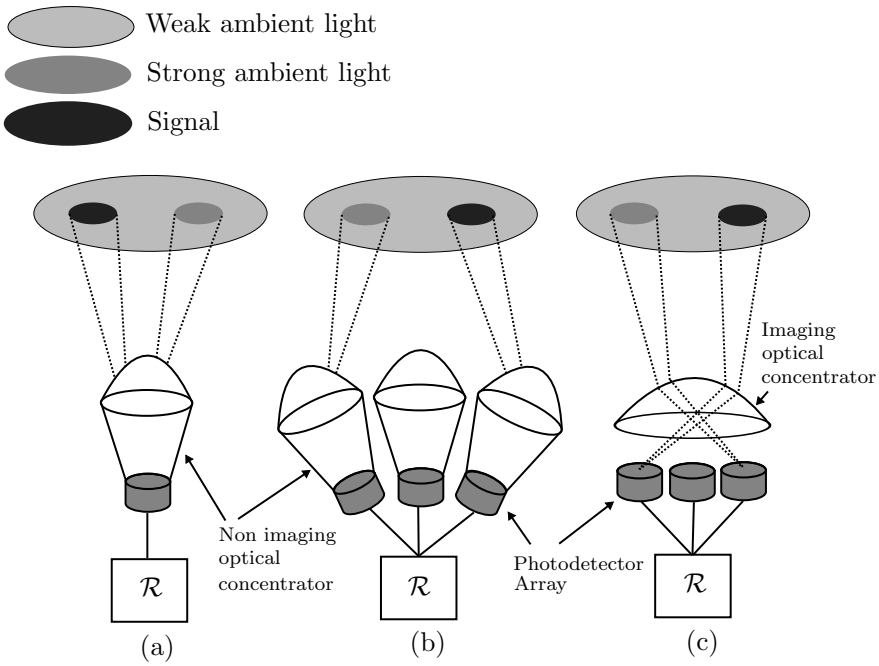

Figure 1.2: Angular diversity receiver examples. (a) Single element receiver. (b) Angular diversity receiver (non imaging). (c) Angular diversity receiver (imaging).

tector array, thus sending the light that arrives from different directions to different detectors. The latter couples each element to a non-imaging optical concentrator with a filter, and the receiver can then determine from where the light arrived via knowledge of the receiver orientation and the FOV attained by each element/concentrator.

A number of non-imaging concentrators have been proposed in the past, two of the most-popular being the hemispherical (truncated spherical) dielectric concentrator [53, 54, 55], and the rotationally symmetric compound parabolic concentrator (CPC) [56, 57]. Hemispherical concentrators achieve a high FOV and gain, provided the hemisphere radius is large compared to the detector [58], and an optical filter can be placed between the concentrator and the detector or on the surface of the hemisphere. While the filter placed on the surface of the hemisphere provides a 3 dB power advantage, it has to be traded off with the increased complexity of filter fabrication

[1]. CPCs on the other hand, can be designed for any FOV, and utilise thin film planar optical filters which are easier to fabricate and tune to a desired central wavelength in the bandpass region. Due to the fact the FOV can be controlled, a higher optical gain can be achieved along with rejecting more background illumination. Recently another alternative has been presented in the form of a three dimensional dielectric totally internally reflecting concentrator (DTIRC), or optical antenna (OA), which also uses a planar optical filter between the concentrator and the detector, but, unlike the CPC, it can have a variety of entrance aperture shapes, giving it a smaller size and the ability for higher optical gain compared to the traditional CPC [44].

Imaging ADRs offer two advantages. Firstly, the bulk size of the receiver is reduced, as only one imaging optical concentrator is needed for the whole device. Secondly, the photodiode array is flat and may be fabricated into a highly scalable integrated circuit, offering high pixel density [59].

As stated above, the ADRs requires signal processing to determine which pixels should be used. In [60], a system using multiple narrow beam transmitters and multiple narrow FOV receivers, transmitting at $70\,\mathrm{Mbit\,s^{-1}}$ over a range of 4.2 m using OOK with a BER of 10^{-9} compared the effectiveness of different signal combining schemes. Maximal Ratio Combining (MRC), which performs a weighted sum based on the signal amplitude to noise power spectral densities, and low pass filtering with a cut off point appropriate to the modulation speed, emerged as the most effective signal-combining scheme.

To quantify the effectiveness of using a quasi-diffuse system, Kahn *et al.* [59] compared an imaging ADR system transmitting at $30\,\mathrm{Mbit\,s^{-1}}$ using OOK modulation targeting a BER of 10^{-9}, with a conventional wide FOV single element receiver. It was found that, when considering LOS links from a wide angle transmitter, the use of a 7 pixel imaging receiver required 3.7 dB less power than a single element receiver with equivalent optical properties. Furthermore,

if the number of pixels was increased to over 1000, then a 13 dB transmitter power reduction was achieved. The work also compared MRC with simply selecting the pixel with the highest SNR, and demonstrated that MRC required slightly less power. Moreover, if the wide angle LOS transmitter was replaced by a multi-spot transmitter, creating a diffuse signal on the ceiling this particular configuration required up to 7 dB less transmitted power. Employing the multi-pixel ADR arrangement led to gains of up to 12 dB for greater than 1000 pixels.

In [61], the development of a combined directed, for high speed, and diffuse link, for connectivity, system was demonstrated. In this approach, the diffuse link was provided by a high power laser directed at a diffusely radiating surface, and the directed link was implemented with a vertical cavity surface emitting laser (VCSEL) diode array with focusing lens. The imaging ADR in this work, [61], utilised an array of avalanche photodiodes to take advantage of their higher sensitivity because ambient-related shot noise has less effect on diversity receivers. A microcontroller in the ADR allowed all the pixels to be active if no LOS link was present, or selectively activate individual pixels when a LOS transmission was found. To obtain error-free data transmission between the transmitter and receiver at 1.8 m, 400 mW of power was required by the diffuse laser transmitter, whilst only 0.35 mW was required by the LOS directed laser diode transmitter. The final system capability demonstrated was 155 Mbit s^{-1} over a range of 2 m, using a 233 MHz phase shift key subcarrier.

The first fully integrated diversity system was presented in [62] using custom electronics, over commercially available components, to obtain improved performance. The transmitter consisted of an array of resonant cavity light emitting diodes (LED's) flip-chip bonded to complementary metal-oxide-semiconductor (CMOS) driver circuitry and integrated with the transmitter optics. A wavelength of 980 nm was employed because current devices at other wavelengths are not advanced enough for the level of integration intended. This however, restricted transmitter power for eye safety reasons. The imaging ADR consisted of an array of p-i-n photodiodes flip-chip

bonded to custom CMOS circuitry. The use of integrated circuitry offers good scalability, and employing CMOS permits custom fabrication of low-cost, highly-functional devices [52]. The aim of the project was to reach $155\,\mathrm{Mbit\,s^{-1}}$ over $2-3$m, and, to date [63], the system has reached $100\,\mathrm{Mbit\,s^{-1}}$.

Finally, a novel form of imaging receiver was presented in [64]. This consisted of a single photodetector, placed on a miniaturised positioning mechanism that allowed it to move under the focal plane of the imaging lens. Advantage was taken of the slow variation in the signal position occurring in mobile systems, which permitted searching for the best SNR via a simple search algorithm in real time. The system has similar benefits to the others described, in that ambient light is rejected and power can be saved at the transmitter by reducing path loss through LOS transmission. One drawback shown in the paper was that when the signal link was completely blocked, the system had to search again for a connection. The project, albeit in the simulation stage, was aimed at portable equipment applications as the receiver complexity was low, yet still it was able to maintain the advantages of diversity receivers over those using a single wide-angle receiver. The initial published simulation results predicted a 50% power saving at the transmitter by using the single channel imaging receiver, compared to a similar angle diversity receiver, whilst also increasing the available channel bandwidth.

1.4 Intelligent Systems Overview

Although the use of intelligent techniques have found numerous applications within telecommunications, from fibre systems [65, 66, 67] to free space optics [68], to the countless number already employed in RF applications such as antenna design and receiver array control [69, 70, 71, 72], there has been very little application off the techniques to optical wireless communications.

Very recently, work was published [73] based upon the use of optimising, through simulated

annealing [74], the multispot diffusion pattern generated by holographic diffusers. In this work the simulated annealing method was employed to find the design of the holographic diffuser required to produce either a low power deviation, lower multipath dispersion, or a combination of both. By changing the holographic diffuser design, they quote improvements of up to an 85%, in reduction of the standard deviation of the received power throughout the room, when coupled with a receiver with a 30° FOV. The work also covers the application in a second environment with lesser improvements. The work was later extended [75] to include the use of a genetic algorithm (GA), and a modified GA that incorporates elements of the simulated annealing process. However upon comparison of their results, they concluded the GA was not satisfactory as an optimiser, and very few results were published. Furthermore, they concluded that the GAs ability to optimise the effects of multipath dispersion was also limited, concluding this is a physical factor that needs to be mitigated with more advanced receiver techniques.

In [76] a complex system was demonstrated that makes great improvements in overcoming the channel induced multipath distortion resulting from the multiple reflections around the diffuse environment. By sending the received signal through a feature extraction algorithm based upon wavelet analysis, an artificial neural network pattern recognition post processor is employed to rebuild the original signal. The results were successful in that, for the system to run at a BER of 10^{-5}, required 2 dB, 8 dB and 17 dB, less SNR than systems with maximum likelihood detection, filtered or unfiltered receivers respectively. The results shown, although conducted within a fully diffuse environment, only accounted for one source receiver configuration.

In [77, 78], a fuzzy logic based handover decision algorithm was developed for use in systems where OW and RF networks coexist. In these types of networks, handover from one system to another is a problem due to different interruption schemes and traffic modes. The strength of the fuzzy logic approach to uncertainties and conflicting decision metrics, gives the handover algorithm an improved QoS though lower packet transfer delay. One of the most important

aspects to this work is that the authors highlighted the dynamics of the mobile channel. Each handover decision is different, and previous structured algorithms are only effective under certain conditions, making their approach very beneficial.

1.5 Aims and Motivations

Indoor optical wireless is, inherently, a cellular system [79, 80]. Each room, or section of a room, will have within it a base station linked to the backbone network [81]. It can also be assumed that every environment that a base station resides within , will be different. The advantages of OW such as high speed communications may be beneficial to scenarios in the workplace, but each workplace will have a different topology of furniture and seating arrangements. The low cost appeal of OW will allow systems to be deployed in residential environments, where, for example in living rooms and bedrooms, the type of furnishing and flooring is also unique. The immunity to RF interference may appeal to heavy industrial users, where there is no furniture but sparsely open plan factories or warehouses with reflective surfaces, such as concrete and steel for example, that are not normally found elsewhere. From a channel perspective, it is therefore reasonable to assume that no two environments are identical.

This argument can be carried through to the channel noise sources. The typical lighting found in office environments, although possibly similar from office to office, is certainly different to the ones found in residences. Some offices have many windows, whilst some do not, making sunlight different in each location. Industrial applications may be purely illuminated with artificial light. These channel variability challenges are enough on their own if one considers the environment to be static. Realistically, this cannot be assumed, as OW systems are about connecting users in a flexible way. Even if the users moved slowly, or assumptions were made about their typical behaviours, the channel can still change with simple actions like rearranging the furniture or substituting carpet for wooden flooring.

Furthermore, it needs to be assumed that there are multiple end users within each unique environment. Each of these users has upon them a battery powered portable device such a mobile phone or laptop. Historically, with work from standards bodies such as the IrDA, each of the devices is most likely very similar, or conform to some minimum technical specification of operational requirement. Furthermore, from a marketing point of view, the standards agencies or the parties with financial interest in the devices, try and make them as cheap as possible, and attempt to put them in as many devices as possible.

This leads to somewhat challenging system design requirements, of how to make a single, mass producible and cheap receiver design operate in an infinite number of channel scenarios, whilst still being able to market the device as user friendly. The system element not mentioned so far, is that of the transmitter. The transmitter stands alone as something that can be flexibly designed. The transmitter should be cost effective, or good value of money, but it does not have to be disposably cheap as with the receiver. The transmitter should be power efficient, but not necessarily low power, as it is connected to the backbone network, so potentially near a power plug. Finally the transmitter should be unobtrusive, but does not have to be small. The transmitter, is therefore one possible avenue of research that could lead to a solution to this system design challenge.

In the case of all the aforementioned receiver techniques proposed, each one has their respective merits in mitigating certain channel factors such as bandwidth or received power limitations. However, given the cellular nature of OW, one has to weigh the added complexity, cost and physical size of each receiver within the cell against the benefits they entail. There is an argument with economies of scale, such that the larger the uptake, the lower the cost of each unit. The argument, however can also be debated the other way, if one considers that the cost and complexity overhead of the entire system will be influenced more, by the number of users or

receivers present in a cell, than by the single base station.

The aim of this work, is to prove, in principle, the conceptual idea, that a genetic algorithm approach, can be used to optimise several OW channel characteristics. It is intended to show that the channel can be itself, designed, accounting for environmental and user movement induced channel variability. Much of the motivation for this work comes from a personal experience in receiver design, whereby it was never known how much power or bandwidth to expect from the channel, for each application at hand, such that, the choice of appropriate receiver design or topology to implement and develop, was always a difficult decision. The work will in general, focus purely on the algorithm and the effects of its use on the channel. A small amount of receiver analysis is performed, but only to the extent of physical parameters that affect the channel response such as FOV. It is not the intent of this work to develop a bespoke system with the highest bit rate, SNR or focus exclusively on some other system performance characteristic, but rather, assume as wide a range of variables as possible, proving the method has a high degree of flexibility.

To the best of the author's knowledge, GAs have not been applied in this way, with this focus, on indoor optical wireless communication systems, and it will be shown that their use will bring benefits to the research area. It should also be stated that the method and results presented here are not mutually exclusive, baring the one exception of computer generated holograms, with other research ideas currently being undertaken elsewhere, and this work is not shown to be a solution, but be part of the solution. It is hoped that the benefits of this work, are taken further by others, particularly the receiver designers who may be able to match an algorithm of their own, with their complementary receiver designs, potentially fulfilling the system design requirements. Furthermore, like any new idea, there are trade-offs, and they will be fully detailed. Emphasis will also be placed on critical self analysis of the results and on the validity and conditions for which they hold true.

1.6 Outline of the Thesis

The work in this thesis is outlined in the following chapters. Each chapter has its own objects and conclusions that will be highlighted at their respective beginning and ends. Chapter 2 provides a detailed channel model for an indoor optical wireless communication channel. This chapter is vital for the analysis within the rest of the thesis, providing all fundamental equations and explanation of the channel's performance characteristics. Within the chapter, a purpose built channel simulator is designed, that forms the platform for all results, which to prove their validity, is characterised in terms of accuracy and computational effort. The simulation platform also includes a purpose built object intersection algorithm, required for simulating user movement. Within this chapter, the first provisional analysis is conducted within the channel, illustrating, in a quantive fashion, the problems the system designer is facing.

Chapter 3, contains the theory required in understanding how the received power at a given location within the environment can be modified. It details how, by knowing the impulse response between a source and receiver, the GA is able to control it. Some simplifications to the model are then presented with a strong justification. This is followed by a theoretical introduction to the GA, covering all aspects needed for the work, before beginning the GA development. Once the GA framework has been established, provisional results are shown before a thorough analysis of the effectiveness of the GA with different receiver characteristics. At this point a generalised receiver is formed, for evaluation of the algorithms effectiveness in handling user movement in multiple environments.

Chapter 4, begins with the next stage of user induced channel perturbation analysis, in quantifying the effect of dynamic receiver orientation. The GA is then subjected to the perturbation, and shown to be effective in mitigating, to some extent, the effects of the user, not only ran-

domly aligning the receiver, but also moving in a further two environments. This chapter further contains results of the GA effectiveness at reducing received power deviation around a further two environments when there are multiple users moving. These tests were the toughest given the GA, and possibly the scenarios that show the highest level of realism to the scenarios.

Chapter 5, moves on from attempts to reduce the deviation in received power, to reducing the deviation in the received signal to noise ratio. The received noise power is different in each location of the room, similar to the signal power, and as such the SNR is not uniform. It also affects the BER of a system. The work in this chapter is very slightly different as reducing the deviation in peak received power, when coupled with the change in received noise power, the change to SNR is not predictable. The GA is modified here with a new fitness function that accounts for SNR. In this chapter a detailed noise model is also presented that allows the SNR to be transposed to BER, which unfortunately as will be shown is not as suitable for the GA to optimise as required.

Chapter 6, then concludes the work, with a note to further work that may be suitable for investigation given the results that are presented here. At the end of the chapters are several appendices, listing detailed tables of results of computational time and error results, a complete list of every GA algorithmic permutation tested, with results in the algorithm test room, and a complete appendix detailing more of the specifics regarding user movement positional attributes.

Chapter 2

The Optical Wireless Channel

2.1 Introduction

For a system designer a detailed knowledge of the channel is vital for the effective development and optimisation of the major components within the system such as transmitter, receiver and the modulation scheme. In this chapter a channel model is proposed with a detailed discussion and justification to the choice of simulation method, reflection model, accuracy or error levels and the model constraints and assumptions presumed. The design of the simulator is essential for the work presented within the thesis, and, as such, the research emphasis is placed upon development of this flexible platform. It is necessary to be able to determine the channel's impulse response for a wide range of scenarios, including those with user movement, and so a custom ray object intersection algorithm is also proposed. Research emphasis will also need to be placed upon computational efficiency, and the mathematical and algorithmic optimisations that need to be accounted for are discussed because, without them, the future work could not be completed. Furthermore, there is one more capability that is required from the simulator that will be discussed further in chapter 3, in that the model must allow for dynamically variable source radiation emission powers.

Due to the importance of determining the channel impulse response, a variety of methods have been previously proposed, each with a respective set of objectives, advantages and disadvantages [82]. Closed form approximations [3], which provides the possibility to simply investigate basic configurations and conduct simple analysis on factors such as material reflectivity and the source intensity profile, are too complex when considering multiple reflections. Experimental characterisation [83, 84, 85], is an expensive and lengthy task that has to be done on a channel by channel basis [86].

A general simulation method, first proposed by Barry [87], using some techniques borrowed from the ray tracing community [88], provided the ability, with relative ease of implementation, to determine the impulse response for a system where the signal underwent any number of reflections for any configuration of source and receiver inside an arbitrary empty rectangular room. However, due to the algorithm being recursive, the computational time is exponential, and the memory requirements were impractical beyond three reflections. A solution to overcoming the memory requirements, with a slight improvement in computation time, was proposed by López-Hernández in [89], using a method of dividing the simulation into time, as opposed to reflections. A further refinement came from Carruthers [90, 91] when the algorithm was applied iteratively allowing for the computational time to be proportional to the square of the number reflections required. The method also allowed the possibility of simulating scenarios with multiple transmitters and receivers without considerable time penalties.

An alternative simulation approach, based on a statistical model, was proposed by Pérez-Jiménez [92]. In this method the root mean square (RMS) delay spread, and mean excess delay are estimated, based purely upon the known geometric factors of the system configuration such as transmitter and receiver positions and orientation. The values are then compared against an initial impulse response $h(t)$ and either a Rayleigh or Gamma function, adjusting the $h(t)$ until it fits the distribution. The method is described as being faster than the work of Barry. How-

ever, no computational times were provided and the requirement for an initial impulse response makes this approach hard to justify for use. Moreover the authors presented shortly afterwards a new method based upon a mixed deterministic Monte Carlo ray tracing algorithm [93, 94, 95]. By sending out rays from the source in a pseudo random nature and literally tracing the rays through the reflections, the room does not need to be partitioned into elements, as was the case with the Barry method, thus the level of accuracy is determined not by the spacial segmentation, but by the choice in the number of rays. The authors still base their impulse response calculations on the original Barry formulations, but the use of rays allows the unnecessary calculations from rays that would never be incident upon the receiver to be omitted. The method presented is potentially beneficial in terms of computational time, albeit through the choice of reduction in the number of rays, and would be convenient to implement on vectorised graphics processors. However, as the rays are generated statistically, each run of the simulation provided different results, and it has been shown that simulation of the same system configuration 100 times provides a relative error of between 5% and 20% between each run [96].

Finally there is one other statistically based simulation technique that was presented in [97, 98], called "random walk". Here a ray is generated with a pseudo random direction and traced around the environment, determining on its path, if and when, it hits a surface. If it hits a surface it is reflected with a new path in a pseudo random direction. This process is continued until, eventually it reaches the receiver. The method has shown merit for the problems involving integrating sphere diffusers that are inherently small (5-100cm) and spherical reflective environments. However, for larger, non spherical environments, such as the work presented here, the channel model simulation technique is not readily applicable.

After discussing the system model in section 2.2, the modified impulse response calculations, although largely based upon the work by Barry, will be presented in section 2.3. Section 2.4 provides the details of the object intersection algorithm implemented with an analyis of the

precision errors found in simulation. Section 2.5 provides justification for the model assumptions implemented with an error analysis. Section 2.6 provides results that verify the simulator against known results and an analysis of the effects on the number of reflections, number of diffusion spots and the FOV of the receivers with regards to received power levels, bandwidth and RMS delay spread.

2.2 System Model

The system deployment environment is considered to be an arbitrary indoor rectangular room of width, X_e, depth, Y_e, and height, Z_e, such as an office, lecture theatre or living room. The boundaries of the environment, defined to be the floor, ceiling and walls, enclose a transmitter capable of firstly forming a diffusion spot geometry upon the ceiling, and secondly, that each spot intensity can be dynamically and independently controlled.

The three most common techniques for producing the diffusion spots are to use either a holographic diffuser [99, 100, 101], multiple light sources [102, 103, 104], such as white LEDs [105, 106, 107], or a 2-D VCSEL or resonant cavity LED (RCLED) [108, 52], array.

Holographic diffusers employ computer-generated holograms, designed to diffuse the emitted radiation from a single Laser source. The intensity and/or distribution of the spot geometry, such as uniform, diamond or line-strip [109], can be easily defined, and the resultant projected spots will be reflected according to the material properties of the ceiling. However, to the best of the author's knowledge, holographic diffusers are unable to control the power of each individual projected spot dynamically and, as such, will not be considered any further as a viable transmitter option.

Multiple optical sources allow for any spot pattern geometry to be installed on the ceiling of the

room, and whilst it is possible to control the distribution of emitted radiation from each source through the use of lenses or other diffuser techniques [98, 110], traditionally the optical source is an LED, which emits radiation with a generalised Lambertian radiation intensity pattern [21]. Dynamic control of an individual spot is also possible, as each source can be considered independent. The installation of multiple optical sources may seem 'bespoke', but the use of white LED which not only act as transmission sources, but also serve to illuminate the environment, have beneficial properties such as lower power consumption, heat dissipation and cost [111].

Using the 2-D VCSEL/RCLED array of emitting devices, flip-chip bonded to an array of CMOS driver circuitry, allows for a highly-integrated transmitter solution [62]. The driver circuitry is capable of controlling each element's emitted power, along with any other signal processing techniques currently realisable in CMOS. Furthermore, it is possible to integrate beam shaping and steering optics, that can control the position of each of the resultant projected spots on the ceiling [112], which will then be reflected, according to the reflection properties of the ceiling.

Independent of which technology is used in the transmitter, the radiation it emits, if incident upon the boundaries of the environment or the surfaces of objects, will be reflected with an intensity distribution that is predominately determined by the angle of the radiations incidence, and the roughness of the reflection surface. A suitable measure of the surfaces roughness is given by the Rayleigh criterion whereby a surface can be considered smooth if [113]

$$\zeta < \frac{\lambda}{8\cos\theta_i} \qquad \text{(m)} \tag{2.1}$$

Where ζ is the maximum height of the surface irregularities, λ is the wavelength of the incident radiation at an angle θ_i, referenced from the surface normal. Therefore for normally incident infrared radiation, with $\lambda \approx 800\,\text{nm}$, the surface will be rough if $\zeta > 0.1\,\mu\text{m}$.

Surfaces that are considered rough under the Rayleigh criteria in (2.1), reflect radiation with a intensity distribution function, $R(\theta_o)$, that can be correctly approximated by Lamberts gener-

alised cosine law [114]

$$R(\theta_o) = \rho \frac{n+1}{2\pi} P_i \cos^n(\theta_r) \qquad (\mathrm{W\,sr^{-1}}) \tag{2.2}$$

Where ρ is the reflectivity coefficient of the material, P_i is power of the incident wave, n is the Lambertian order and θ_o is the angle of observation. An ideal Lambertian diffuser, where the surface will look equally bright when observed from any angle [115], is found by setting $n = 1$. Figure 2.1(a), shows the resultant reflected intensity distribution for surfaces with a higher Lambertian order, $n = \{1, 4, 15, 15\}$, resulting in higher directionality.

For surfaces that (2.1) defines to be smooth, the intensity distribution of the reflected radiation, is to an extent, dependent upon the the angle of the incident radiation, such as an ideal mirror for example. However, as not all materials are ideal, the intensity distribution is more accurately described as the sum of two components [116]

$$R(\theta_o, \theta_i) = R_d(\theta_o) + R_s(\theta_o, \theta_i) \qquad (\mathrm{W\,sr^{-1}}) \tag{2.3}$$

Where R_d and R_s are the diffuse and specular components respectively, noting the diffuse component is not dependent upon the angle of incidence, θ_i. A suitable model for approximating these non ideal surfaces is provided by Phong [117, 118]

$$R(\theta_i, \theta_o) = \rho P_i \left[\frac{n+1}{2\pi} r_d \cos^n(\theta_o) + (1 - r_d) \frac{m+1}{2\pi} \cos^m(\theta_o - \theta_i) \right] \tag{2.4}$$

Where m is the directivity of the specular component, r_d is the proportion of incident signal that is reflected diffusely and assumes values between 0 and 1. Setting $r_d = 1$ indicates a pure diffuse reflector and reduces equation (2.4) to (2.2). An example of how the specular component changes the reflected intensity distribution can be seen in figure 2.1(b), where two different materials are shown with parameters approximated from [113, 118]. Material 1 has the parameters $\theta_i = 30°, m = 20, r_d = 0.6$ and $\rho = P_i = 1$, while material 2 has the parameters $\theta_i = -40°, m = 50, r_d = 0.95$ and $\rho = P_i = 1$.

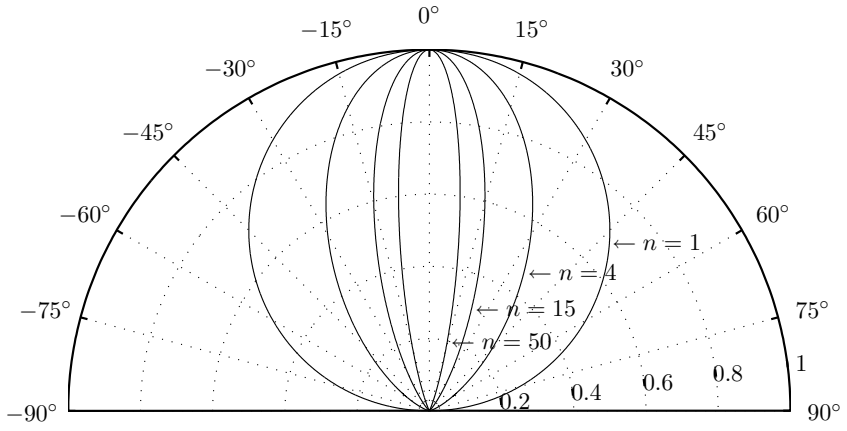

(a)

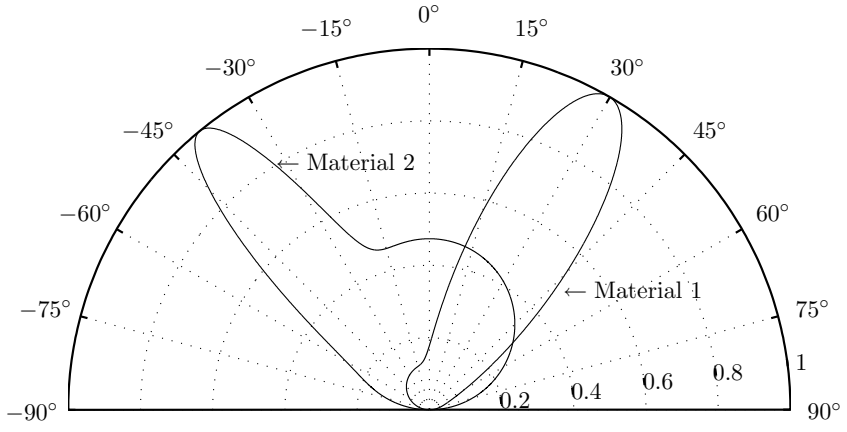

(b)

Figure 2.1: Lambertian and Phong reflection model comparison. (a) Lamberts generalised cosine law. (b) Phongs model.

Most materials found in a typical office or home environment, such as painted and unpainted cement or plaster, unpainted wood and ceramic floor tile exhibit a Lambertian intensity distribution, whereas Formica, varnished wood and glass exhibit a characteristic better described by Phong [113]. There is some debate in the literature over whether or not the use of Phong is beneficial in determining a more accurate impulse response [119]. In [113] and [118], channel models were presented for single reflection scenarios, comparing the results for using Lambertian and Phong models. The results concluded that the channel response was almost identical, except where the transmitter and receiver are in close proximity, where at these positions Phong's model increases the path loss by about 5 dB more than when Lambert's model is used. It was also noted that Phong's model would be computationally more expensive than Lambert's model beyond determination of one reflection.

From this point onwards it will be assumed that all the boundaries of the environment and the surfaces of the objects will reflect radiation according to Lambert's model. Therefore, as each diffusion spot on the ceiling, formed using either multiple optical sources or a 2-D VCSEL/RCLED array, will exhibit a Lambertian intensity distribution, each of the I diffusion spots on the ceiling independent sources $\mathcal{S}_i$. The only error induced with this assumption is a delay and propagation loss between the emitting element of an 2-D VCSEL/RCLED array and the diffusion spot position. In an arbitrary room, the number of possible transmitter and diffusing spot positions is essentially infinite, and so this assumption also serves to simplify the argument for the model whilst maintaining generality to the application. Each source $\mathcal{S}_i$ will have an associated position vector $\mathbf{r}_{\mathcal{S}_i}$, unit length orientation vector $\hat{\mathbf{n}}_{\mathcal{S}_i}$, power $P_{\mathcal{S}_i}$ and uniaxial symmetric, with respect to $\hat{\mathbf{n}}_{\mathcal{S}_i}$, Lambertian radiation intensity profile $R(\phi)$ given by

$$R(\phi) = \frac{n+1}{2\pi} P_{\mathcal{S}_i} \cos^n(\phi) \qquad \text{for } \phi \in [-\pi/2, \pi/2] \tag{2.5}$$

Where the mode number, n, can be set to $n = 1$ for an pure Lambertian diffuser, such as the ceiling, and set to $n > 1$ for a diffusion spot that represents an independent LED with higher directionality.

It is also assumed that a single receiver design will be deployed within the environment, allowing the possibility to model the existence of J receivers, $\mathcal{R}_j$. Knowing that receivers $\mathcal{R}_j$ and $\mathcal{R}_{j+1}$ are of the same design, it is possible to readily interchange between describing a system with J receivers at multiple locations and a system with one receiver at J locations. Each receiver will have a position vector, $\mathbf{r}_{\mathcal{R}_j}$, orientation vector $\hat{\mathbf{n}}_{\mathcal{R}_j}$, active optical collection area $A_{\mathcal{R}_j}$ and a field of view $FOV_{\mathcal{R}_j}$ defined as the maximum uniaxial symmetric incident angle of radiation with respect to $\hat{\mathbf{n}}_{\mathcal{R}_j}$, that will generate a current in the photodiode.

Furthermore, as all the surfaces exhibit the same generalised Lambertian intensity distribution pattern, independent of the angle of incidence, following the technique described in [87], all surfaces are partitioned into L elements $\mathcal{E}_l$ with a position vector $\mathbf{r}_{\mathcal{E}_l}$, unit length orientation vector $\hat{\mathbf{n}}_{\mathcal{E}_l}$, and size $A_{\mathcal{E}_l} = 1/\Delta A^2(\mathrm{m})$, where ΔA is the desired number of elements per metre. A given element will sequentially behave, firstly as a receiver $\mathcal{E}_l^{\mathcal{R}}$ with a hemispherical FOV, for which the received power $P_{\mathcal{E}_l}$ can be determined, and secondly as a source $\mathcal{E}_l^{\mathcal{S}}$, with a radiation intensity profile $R(\phi)$ is given by (2.5) setting $n = 1$ and $P_{\mathcal{S}_i} = \rho_{\mathcal{E}_l} P_{\mathcal{E}_l}$, where $\rho_{\mathcal{E}_l}$ is the reflectivity of the element.

Whilst the emitted radiation from the transmitter propagates within the air of the environment the atmospheric manifestations of absorption, Mie scattering and scintillation [120] are not considered as the range of indoor channel is small, making the effects negligible [121].

2.3 Impulse Response Calculations

For the system model described in section 2.2, the infrared radiation incident upon a receiver $\mathcal{R}_j$ will be the result of the radiation emitted from a source $\mathcal{S}_i$ that has propagated directly through an unobstructed LOS path, and/or from radiation that has undergone a finite number

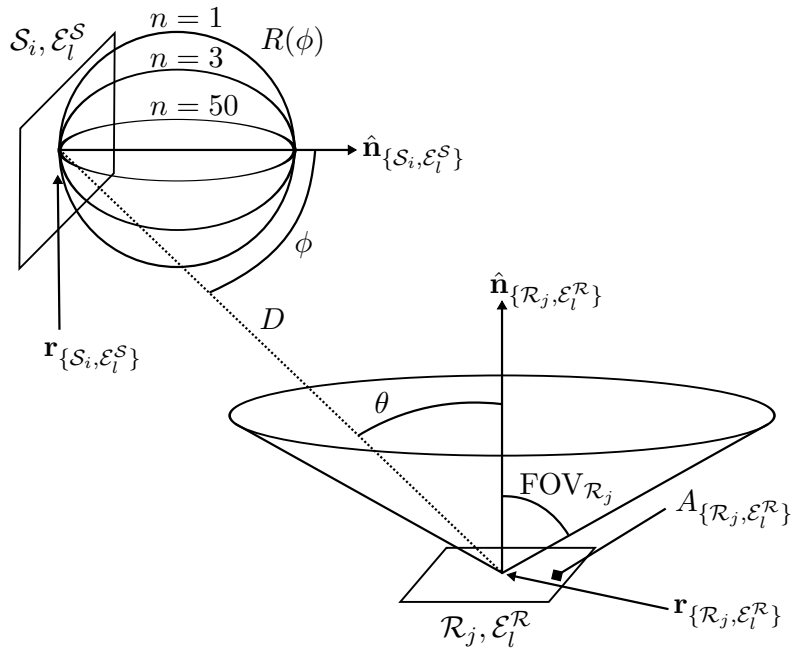

Figure 2.2: Source, receiver and reflector geometry [87].

or order, k, of reflections off the boundaries to the environment and the surfaces of the objects.

It is known [85] that for an intensity modulated direct detection scenario, where the movement of the sources, $\mathcal{S}_i$, receivers $\mathcal{R}_j$, and any mobile objects within the environment are slow compared to the bit rate of the system, no multipath fading occurs. It is also known [85] that the channel can be deemed LTI, for which, a fundamental property of any LTI system is that it can be completely characterised by it's impulse response $h(t)$ [122], and is given by [87, 90]

$$h(t;\mathcal{S}_i,\mathcal{R}_j) = \sum_{k=0}^{k} h^k(t;\mathcal{S}_i,\mathcal{R}_j) \tag{2.6}$$

Where $h^k(t;\mathcal{S}_i,\mathcal{R}_j)$ is the impulse response of the system for radiation undergoing k reflections between $\mathcal{S}_i$ and $\mathcal{R}_j$. Throughout this work, the number of bounces may be referred to using the the terminology of order and component. The definition of a component, for example the 2^{nd} component, is when radiation that undergoes exactly 2 reflections is being quantified, whilst

order, for example the 2nd order, is the summation of all components up to and including the order value.

The impulse response is found by allowing the source, $\mathcal{S}_i$, to emit a Dirac impulse at $t = 0$, that is setting $P_{\mathcal{S}_i} = 1\,\mathrm{W}$, then the LOS ($k = 0$) impulse response is given by the resultant scaled and delayed δ-function

$$h^0(t; \mathcal{S}_i, \mathcal{R}_j) \approx R(\phi_{ij}) \frac{\cos(\theta_{ij}) A_{\mathcal{R}j}}{D_{ij}} V(\frac{\theta_{ij}}{\mathrm{FOV}_{\mathcal{R}j}}) \delta(t - \frac{D_{ij}}{c}) \tag{2.7}$$

Where, referring to figure 2.2, $D_{ij} = ||\mathbf{r}_{\mathcal{S}_i} - \mathbf{r}_{\mathcal{R}_j}||$ is the distance between the source and receiver, c is the speed of light. ϕ_{ij} and θ_{ij} are the angles between $\hat{\mathbf{n}}_{\mathcal{S}_i}$ and $(\mathbf{r}_{\mathcal{R}_j} - \mathbf{r}_{\mathcal{S}_i})$ and between $\hat{\mathbf{n}}_{\mathcal{R}_j}$ and $(\mathbf{r}_{\mathcal{S}_i} - \mathbf{r}_{\mathcal{R}_j})$ respectively. $V(x)$ represents the the visibility function, where $V(x) = 1$ for $|x| \leq 1$, and $V(x) = 0$ otherwise.

For radiation undergoing a higher number of reflections, the higher order impulse response, $(k > 0)$, is given by

$$h^k(t; \mathcal{S}_i, \mathcal{R}_j) = \sum_{l=1}^{L} h^{(0)}(t; \mathcal{S}_i, \mathcal{E}_l^{\mathcal{R}}) * h^{(k-1)}(t; \mathcal{E}_l^{\mathcal{S}}, \mathcal{R}_j) \tag{2.8}$$

Where the $k-1$ impulse response, $h^{(k-1)}(t; \mathcal{E}_l^{\mathcal{S}}, \mathcal{R}_j)$, can be found iteratively from [91]

$$h^k(t; \mathcal{E}_l^{\mathcal{S}}, \mathcal{R}_j) = \sum_{l=1}^{L} h^{(0)}(t; \mathcal{E}_l^{\mathcal{S}}, \mathcal{E}_l^{\mathcal{R}}) * h^{(k-1)}(t; \mathcal{E}_l^{\mathcal{S}}, \mathcal{R}_j) \tag{2.9}$$

Where all the zero order, $k = 0$, impulse responses in (2.8) and (2.9) are found by careful substitution of the variables in (2.7) with their counterpart variables associated with $\mathcal{E}^{\mathcal{S}_l}$ and $\mathcal{E}_l^{\mathcal{R}}$.

It can also be seen that the iterative method is computationally favourable to scenarios with more sources than receivers, $(I > J)$, such that determining the impulse response involves solving $h^{(0)}(t; \mathcal{E}_l^{\mathcal{S}}, \mathcal{R}_j)$, iterating with (2.9) to $h^{(k-1)}(t; \mathcal{E}_l^{\mathcal{S}}, \mathcal{R}_j)$ followed by substitution into (2.8) for each source. The iteration routine is thus performed J times.

Alternatively for a scenario with $J > I$, through the knowledge that convolution is a linear operation, (2.8) can be rearranged to form [90]

$$h^k(t;\mathcal{S}_i,\mathcal{R}_j) = \sum_{l=1}^{L} h^{(k-1)}(t;\mathcal{S}_i,\mathcal{E}_l^{\mathcal{R}}) * h^0(t;\mathcal{E}_l^{\mathcal{S}},\mathcal{R}_j) \tag{2.10}$$

And the $k-1$ impulse response $h^{(k-1)}(t;\mathcal{S}_i,\mathcal{E}_l^{\mathcal{R}})$ can be found iteratively using [90]

$$h^k(t;\mathcal{S}_i,\mathcal{E}_l^{\mathcal{R}}) = \sum_{l=1}^{L} h^{(k-1)}(t;\mathcal{S}_i,\mathcal{E}_l^{\mathcal{R}}) * h^0(t;\mathcal{E}_l^{\mathcal{S}},\mathcal{E}_l^{\mathcal{R}}) \tag{2.11}$$

Where all the zero order, $k = 0$, responses in (2.10) and (2.11) are found by careful substitution of the variables in (2.7) with their counterpart variables associated with $\mathcal{E}^{\mathcal{S}_l}$ and $\mathcal{E}_l^{\mathcal{R}}$. It can now be seen that $h^k(t;\mathcal{S}_i,\mathcal{R}_j)$ is found by first using $h^{(0)}(t;\mathcal{S}_i,\mathcal{E}_l^{\mathcal{R}})$, iterating with (2.11) to $h^{(k-1)}(t;\mathcal{S}_i,\mathcal{E}_l^{\mathcal{R}})$ and then substituting into (2.10) for each receiver, thus the iteration is only performed I times.

The segmentation of the environment boundaries and surfaces of the objects into elements with area $A_{\mathcal{E}_l}$ as described in section 2.2 for use in the version of (2.7) associated with $\mathcal{E}_l^{\mathcal{R}}$ means that $h(t)$ will be subjected to spacial discretisation, that, in turn, leads to temporal discretisation. The normally piecewise continuous function of $h(t)$ will now be the finite sum of scaled and delayed δ-functions, that need to be smoothed by subdividing the time reference, t, into bins of width Δt and summing the power in each bin. $h(t)$ will therefore be more representative of a histogram, that approximates $h(t)$ as ΔA and Δt approach 0 [87]. In this work $\Delta t = 0.1\,\text{ns}$, and ΔA will be discussed in section 2.5.

The discretisation, however, also leads to another computational efficiency improvement. The histogram of $h^k(t)$ for $k > 0$ will consist of many time bins from $t = 0$ to $t =$ time end, but for the zero order responses $k = 0$, the response will only consist of a single scaled and shifted δ-function. This means that many of the convolution operations required in (2.11) and (2.9) do need be performed in the *true* way that iterates over the entire length of the histogram. Instead

it is known [123] that the convolution of two δ-functions is simply another δ-function with a magnitude equal to their product initiated at a shifted time point equal to the sum of their original time positions minus one. To take advantage of this, the program implementation will be founded upon three matrices, S, E, and R that will be used to store the zero order impulse response for $\mathcal{S}_I$ to $\mathcal{E}_L^{\mathcal{R}}$, $\mathcal{E}_L^{\mathcal{S}}$ to $\mathcal{E}_L^{\mathcal{R}}$, and $\mathcal{E}_L^{\mathcal{S}}$ to $\mathcal{R}_J$, respectively.

$$\mathsf{S} = \begin{bmatrix} h^{(0)}(t;\mathcal{S}_1,\mathcal{E}_1^{\mathcal{R}}) & \dots & h^{(0)}(t;\mathcal{S}_I,\mathcal{E}_1^{\mathcal{R}}) \\ \vdots & \ddots & \vdots \\ h^{(0)}(t;\mathcal{S}_1,\mathcal{E}_L^{\mathcal{R}}) & \dots & h^{(0)}(t;\mathcal{S}_I,\mathcal{E}_L^{\mathcal{R}}) \end{bmatrix} \tag{2.12}$$

$$\mathsf{E} = \begin{bmatrix} h^{(0)}(t;\mathcal{E}_1^{\mathcal{S}},\mathcal{E}_1^{\mathcal{R}}) & \dots & h^{(0)}(t;\mathcal{E}_1^{\mathcal{S}},\mathcal{E}_L^{\mathcal{R}}) \\ \vdots & \ddots & \vdots \\ h^{(0)}(t;\mathcal{E}_L^{\mathcal{S}},\mathcal{E}_1^{\mathcal{R}}) & \dots & h^{(0)}(t;\mathcal{E}_L^{\mathcal{S}},\mathcal{E}_L^{\mathcal{R}}) \end{bmatrix} \tag{2.13}$$

$$\mathsf{R} = \begin{bmatrix} h^{(0)}(t;\mathcal{E}_1^{\mathcal{S}},\mathcal{R}_1) & \dots & h^{(0)}(t;\mathcal{E}_L^{\mathcal{S}},\mathcal{R}_1) \\ \vdots & \ddots & \vdots \\ h^{(0)}(t;\mathcal{E}_1^{\mathcal{S}},\mathcal{R}_J) & \dots & h^{(0)}(t;\mathcal{E}_L^{\mathcal{S}},\mathcal{R}_J) \end{bmatrix} \tag{2.14}$$

These matrices, each element being determined using (2.7), allow for any path between $\mathcal{S}_i$ and $\mathcal{R}_j$ to be found by simply looping through the suitable elements in accordance with the equation pairs (2.8) and (2.9) or (2.10) and (2.11) before a final summation in (2.6) that provides the final result.

It can be seen that matrices S, E and R are to some extent storage arrays. However, they are storage arrays for the zero order impulse response only, not the entire impulse response train, such that each element contains only two values, the magnitude and its associated impulse time. This allows the memory requirements of the arrays to be kept to a minimum. In MATLAB, if the arrays fit within the computers physical memory as opposed to the swap space, the computational efficiency is higher, and it was found that recalculation, or iterating through the matrices S, E and R, is faster, than forming a larger storage array or database which accumulates the

results throughout the bounces.

Once the impulse response of the system is known, it is possible to determine the following quantities that can be used to define the performance characteristics [124];

- DC Gain: The DC gain of the system $H(0)$ for a power in power out system can be obtained from the summation of the impulse response following

$$H(0) = \int_{-\infty}^{\infty} h(t)dt \tag{2.15}$$

- Path Loss: Path loss is defined as the inverse value of the DC gain given in equation 2.15. That is, path loss can be represented by on a linear scale by:

$$\text{path loss} = \frac{1}{H(0)} \tag{2.16}$$

or as a logarithmic (dB) scale by:

$$\text{path loss} = -10\log_{10}(H(0)) \qquad \text{(dB)} \tag{2.17}$$

- Dynamic Range: The signal power received, given by the equation 2.15, could vary within the room, and it is important to know the maximum and minimum range of this power as to make sure the receiver is not saturated.

- Bandwidth: The bandwidth of the channel can be derived from the Fourier transform of the impulse response. The frequency at which the magnitude of $20\log_{10} H(\omega)$ decreases by 3 dB with respect to the zero frequency or DC channel.

- RMS delay spread: The multipath distortion can cause ISI, such that a useful parameter that quantifies the spread of $h(t)$ is

$$\sigma = \sqrt{\frac{\int_{-\infty}^{\infty}(t-\mu)^2 h^2(t)dt}{\int_{-\infty}^{\infty} h^2(t)dt}} \qquad \text{(ns)} \tag{2.18}$$

Where μ is defined as:

$$\mu = \frac{\int_{-\infty}^{\infty} t h^2(t)dt}{\int_{-\infty}^{\infty} h^2(t)dt} \tag{2.19}$$

2.4 The Intersection Algorithm

As described in section 2.2 the boundaries of the environment and the surfaces of the objects, are segmented into L elements that act as both a source $\mathcal{E}_l^{\mathcal{S}}$ and receiver $\mathcal{E}_l^{\mathcal{R}}$. The impulse response calculations of section 2.3, do not need to take into account if the element is from the ceiling, floor, walls or an object. They only need to know the elements respective properties of position, orientation, reflectivity and FOV. Furthermore, for an empty room, it is physically impossible for one element to block the emitted radiation from a source or element acting as a source travelling to a receiver, or element acting as a receiver. The inclusion of objects requires that the visibility function, V of (2.7) be modified to include blockage along with FOV.

The method used is based upon a combination of ray tracing techniques proposed by Kay and Kajiya [125] and by Glassner [126, 127], as their techniques are independent of the ray's properties such as power or time delay, returning only a logical 0 for ray-object intersection, or 1 for an unobstructed path. Moreover although for the work described here, only a rectangular box is required to represent objects, their solutions are compatible with many other ray tracing primitives such as planes, spheres or quadrics for example. It is also assumed that the normals to the object are in the same directions as the normals to the environments coordinate system such that the object could be placed perfectly in a corner of the room.

For simplicity of terminology and explanation, the implemented method described below is illustrated as the intersection of the radiation emitted from a source $\mathcal{S}_i$ incident upon a receiver $\mathcal{R}_j$ allowing for easy comparison with equation 2.7. With careful substitution of the variables the process is identical to radiation incident upon an element,$\mathcal{E}_l^{\mathcal{R}}$ or receiver,$\mathcal{R}_j$, from either a source, $\mathcal{S}_i$ or element acting as a source, $\mathcal{E}_l^{\mathcal{S}}$.

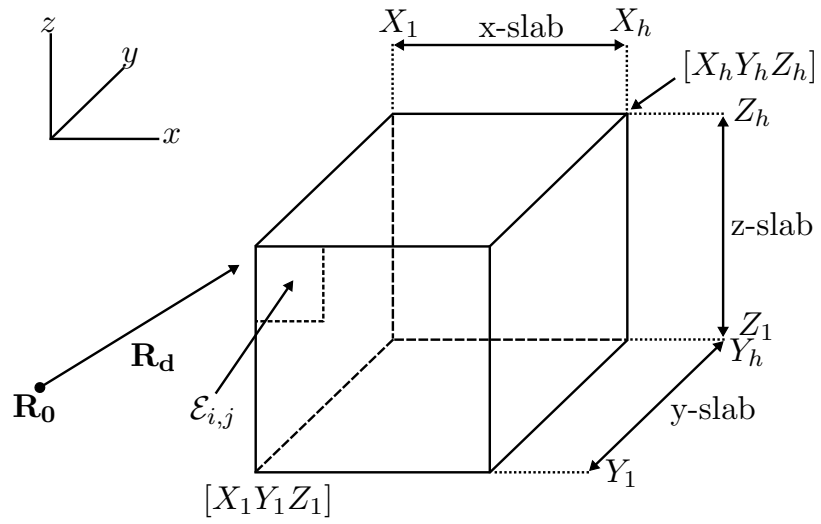

(a)

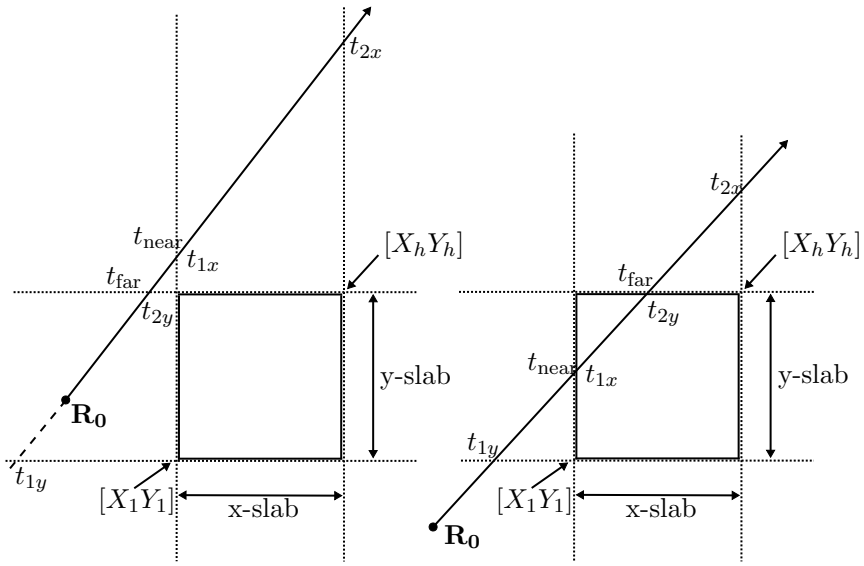

(b)

Figure 2.3: Diagrammatic intersection algorithm. (a) Representation of slabs and rays. (b) Graphical representation of algorithm 2.1.

Referring to figure 2.3(a) and defining the box to have a minimum and maximum extent given by

$$\text{Box's Mimimum Extent} \equiv \mathbf{B_1} = [X_1 Y_1 Z_1] \tag{2.20}$$

$$\text{Box's Maximum Extent} \equiv \mathbf{B_h} = [X_h Y_h Z_h] \tag{2.21}$$

A ray can be defined such that its origin is the position vector of the source

$$\mathbf{R}_{\text{origin}} \equiv \mathbf{R_0} = \mathbf{r}_{\mathcal{S}_i} = [X_0 Y_0 Z_0] \tag{2.22}$$

With a normalised direction vector given by

$$\mathbf{R}_{\text{direction}} \equiv \mathbf{R_d} = \frac{(\mathbf{r}_{\mathcal{R}_j} - \mathbf{r}_{\mathcal{S}_i})}{||\mathbf{r}_{\mathcal{R}_j} - \mathbf{r}_{\mathcal{S}_i}||} = [X_d Y_d Z_d] \tag{2.23}$$

Therefore a ray is explicitly defined by, and any point on the ray can be found using

$$\mathbf{R}(t) = \mathbf{R_0} + \mathbf{R_d} \times (t) \qquad \text{for } t > 0 \tag{2.24}$$

Allowing the ability to find the distance the ray travelled for the intersection, if it exists, whilst the point at which $t = 0$ is subject to various precision errors, and will be discussed in section 2.4.1.

Using $\mathbf{B_1}$ and $\mathbf{B_h}$ a set of 'slabs' is formed, where a slab is simply the space between two parallel planes, for which the intersection of a set of slabs defines a bounding volume as in figure 2.3(a) which shows three slabs forming a rectangular box. For each call of the visibility function in (2.7), the determination of a ray intersecting the box is found by keeping track of the near and far slab intersection distances on all axes using the pseudo code in algorithm 2.1 with reference to figure 2.3(b).

1: Set $t_{\text{near}} = -\infty$, $t_{\text{far}} = \infty$, $V = 0$

2: **for** Each set of planes x, y, z **do**

3: **if** The direction vector $X_d = 0$, the ray must be parallel to the plane **then**

4: **if** The origin of the ray lies outside of the slabs $X_0 < X_1 \mid X_0 > X_h$ **then**

5: **return** $V = 1$, the ray cannot intersect the object

6: **else**

7: Calculate the intersection distance to the planes

8: $t_1 = (X_1 - X_0)/X_d \qquad t_2 = (X_h - X_0)/X_d$

9: **if** $t_1 > t_2$ **then**

10: swap t_1 and t_2

11: **if** $t_2 < t_{\text{near}}$ **then**

12: set $t_{\text{far}} = t_2$

13: **if** $t_{\text{near}} > t_{\text{far}}$ **then**

14: **return** $V = 1$,the box is missed

15: **if** $t_{\text{far}} < 0$ **then**

16: **return** $V = 1$, the box is behind the ray

Algorithm 2.1: The ray object intersection algorithm. Adapted from [126].

The algorithm keeps track of the near and far intersection points, but it does not record them or use them to find the actual intersection distance. This is a problem when multiple objects are present, as the algorithm cannot tell if the intersection will occur after the ray has reached its destination. For example, consider the presence of one large object and a second smaller object situated behind it. A ray from a source could have a direction vector that intersects both objects, and where the ray should be incident upon the first larger object and shadowed on the second but the algorithm will incorrectly cause a shadow on the first at all points that would have hit the smaller object.

To solve this issue the algorithm uses t_{far} and (2.24) to form the position vector of intersection

$$\mathbf{R_I} = \mathbf{R_0} \times \mathbf{R_d} t_{\text{far}} \tag{2.25}$$

Then, if the $||\mathbf{R_I}|| < D_{ij}$, then the intersection happens before the ray reaches its unobstructed destination and $V = 0$ as given by the algorithm.

2.4.1 Precision Errors

Consider an arbitrary element acting as a source, $\mathcal{E}_l^{\mathcal{S}}$, on the surface of an object, as shown in figure 2.3(a), which will have an associate position vector $\mathbf{r}_{\mathcal{E}_l}$ that is also the origin of the ray $\mathbf{R_0}$ it is emitting, for which at least one of the components must meet the condition

$$(X_0 = X_1 \mid X_h) \mid (Y_0 = Y_1 \mid Y_h) \mid (Z_0 = Z_1 \mid Z_h) \tag{2.26}$$

Providing three possible ranges of position vector

$$\mathbf{R_0} = \begin{cases} [X_0, \quad Y_1 < Y_0 < Y_h, \quad Z_1 < Z_0 < Z_h] & \text{for} \quad X_0 = X_1 \mid X_h \\ [X_1 < X_0 < X_h, \quad Y_0, \quad Z_1 < Z_0 < Z_h] & \text{for} \quad Y_0 = Y_1 \mid Y_h \\ [X_1 < X_0 < X_h, \quad Y_1 < Y_0 < Y_h, \quad Z_0] & \text{for} \quad Z_0 = Z_1 \mid Z_h \end{cases} \tag{2.27}$$

Using these cases, in conjunction with algorithm 2.1, leads to several other provisionally incorrect results. Firstly, should the direction of the emitted ray from the arbitrary element, $\mathcal{E}_l^{\mathcal{S}}$, be parallel to any plane of the object, the **if** statement in line 4 will never be satisfied, thus never returning $V = 1$, which cannot be true in reality as a ray can pass parallel without being blocked.

If the direction of the ray is not parallel to any plane

$$(X_d \neq 0) \mid (Y_d \neq 0) \mid (Z_d \neq 0) \tag{2.28}$$

From line 8, t_1 and t_2 becomes

$$t_1 = \left([X_1, Y_1, Z_1] - [X_0, Y_0, Z_0]\right) / [X_d, Y_d, Z_d] \tag{2.29}$$

$$= \begin{cases} [0| - \text{ve}, -\text{ve}, -\text{ve}]/[X_d, Y_d, Z_d] & \text{for} \quad X_0 = X_1 | X_h \\ [-\text{ve}, 0| - \text{ve}, -\text{ve}]/[X_d, Y_d, Z_d] & \text{for} \quad Y_0 = Y_1 | Y_h \\ [-\text{ve}, -\text{ve}, 0| - \text{ve}]/[X_d, Y_d, Z_d] & \text{for} \quad Z_0 = Z_1 | Z_h \end{cases} \tag{2.30}$$

$$t_2 = \left([X_h, Y_h, Z_h] - [X_0, Y_0, Z_0]\right) / [X_d, Y_d, Z_d] \tag{2.31}$$

$$= \begin{cases} [+\text{ve}|0, +\text{ve}, +\text{ve}]/[X_d, Y_d, Z_d] & \text{for} \quad X_0 = X_1 | X_h \\ [+\text{ve}, +\text{ve}|0, +\text{ve}]/[X_d, Y_d, Z_d] & \text{for} \quad Y_0 = Y_1 | Y_h \\ [+\text{ve}, +\text{ve}, +\text{ve}|0]/[X_d, Y_d, Z_d] & \text{for} \quad Z_0 = Z_1 | Z_h \end{cases} \tag{2.32}$$

Now, from line 9, if, $t_1 > t_2$, the value of t_1 and t_2 needed to be interchanged, but from the surface conditions the command will never be instigated resulting in $t_1 \leq 0$ and $t_2 \geq 0$ for all conditions. This, therefore, means $t_{\text{near}} \not> t_{\text{far}}$ and $t_{\text{far}} \not< 0$, returning $V = 0$ incorrectly.

The final problem with the intersection algorithm is due the use of floating point arithmetic where calculation imprecision can creep in [128]. For example, taking the case when t is very close to, but not equal to zero in (2.24). It is possible that rounding errors within the floating point arithmetic creep into the algorithm in contrast to the use of the inequalities that are exact mathematical operators. This allows for a situation where a ray can be emitted from a source only for these compound errors to determine that the ray has instantaneously intersected the object. The solution to this problem coincidently agrees with the solution to the aforementioned problem. By passing a reduced object volume to the intersection algorithm, that is, moving the surface a small fraction in the negative direction to the surface's normal, the elements acting as sources, still in their original position, will not be blocked from transmission. Furthermore passing a reduced object volume allows the magnitude of the intersection distance to be slightly larger when compared to the magnitude of the distance between a source and a objects surface

element. After a few trial and error runs, each object surface would be moved negative to its normal by 1 mm.

2.5 Computational Effort and Error

From section 2.2, one of the factors that still needs to be determined is the value of the number of segments per meter, ΔA. This value is not only important for the accuracy of the program, but is predominantly responsible for the time a solution takes to compute. There is no correct way to conduct this kind of error analysis. The number of possible scenarios is essentially infinite if one considers every size of room, reflectivity characteristics, and the position of the objects, transmitters, and receivers for example. One possible way, however, is to simulate many receivers in a single environment, and then take the mean error over all receivers. By taking a very high resolution simulation, $\Delta A(\text{Max})$, that takes too long to be practical but is done only once, can allow determination of a benchmark set of impulse responses. The resolution can then be reduced to a point where the time is reduced to one that is practical with an acceptable error. The level of segmentation will also be varied, depending upon which order bounce is required, such that higher order impulse responses that require more effort anyway, are given less elements to compute.

The room simulated will have a width, $X_e = 5\,\text{m}$, depth, $Y_e = 5\,\text{m}$ and height, $X_e = 3\text{m}$. The reflectivity of the floor, $\rho = 0.3$ whilst the reflectivity of the walls and ceiling $\rho = 0.8$. The source was positioned centrally on the ceiling at $x = 2.5\,\text{m}, y = 2.5\,\text{m}, z = 3\,\text{m}$, orientated vertically downwards and considered to have a pure Lambertian optical intensity distribution. Each receiver was orientated vertically upwards, and had an area $\Delta A_{\mathcal{R}} = 1\,\text{cm}^2$ and a $\text{FOV}_{\mathcal{R}} = 85°$. The number of receivers were varied between 1 and 1024 with position vectors that are uniformly distributed over the width and depth of the room at a height $y = 1\,\text{m}$. All simulations were carried out on a machine using Matlab 2006a 32 bit under Windows XP with a Pentium 4HT

3 GHz CPU and 2 GB of RAM.

The error presented here is determined in two ways. The absolute error is given by

$$\text{mean error} = \frac{1}{N}\sum_{t=1}^{N} |h^{(k)}_{\Delta A}(t, \mathcal{S}, \mathcal{R}_{i,j}) - h^{(k)}_{\Delta A(\text{Max})}(t, \mathcal{S}, \mathcal{R}_{i,j})| \tag{2.33}$$

Where k is the order of the bounce. ΔA is the segmentation per metre. N is the number of samples in the impulse response. $\Delta A(\text{Max})$ is the maximum segmentation resolution possible using the computer, due to time and memory requirements. The mean percentage error (MPE) is given by

$$\text{MPE} = \frac{100}{N}\sum_{t=1}^{N} \frac{|h^{(k)}_{\Delta A}(t, \mathcal{S}, \mathcal{R}_{i,j}) - h^{(k)}_{\Delta A(\text{Max})}(t, \mathcal{S}, \mathcal{R}_{i,j})|}{h^{(k)}_{\Delta A(\text{Max})}(t, \mathcal{S}, \mathcal{R}_{i,j})} \tag{2.34}$$

Full tables of results for the error analysis can be seen in appendix A, but figure 2.4 provides the select information required.

By definition, there is no error caused by segmentation for the zero order calculations. The first order error was found by setting $\Delta A(\text{Max}) = 300$, where for 1024 receivers, the time was 7644 s $\approx$ 2 h. From the percentage error and and time taken results of figures 2.4(b) and 2.4(a), for the first order impulse response calculations presented hereafter, $\Delta A = 20$, will be used as the mean error is less than 0.5% over the room for a computational time of approximately 27 s for 1024 receivers.

For the second order bounce, the computer was not limited by time, but by memory as more impulse responses had to be stored, so setting $\Delta A(\text{Max}) = 10$, took 3762 s $\approx$ 1 h. Comparing figures 2.4(c) and 2.4(d), $\Delta A = 6$ allows an average error of less than 1% to be obtained with a simulation time at approximately 10 min.

For the third order bounce, to find the impulse response for the 1024 receivers using $\Delta A(\text{Max}) = 5$, required a simulation time of 83 738 s $\approx$ 24 h. This is, incidentally, the time taken by Barry

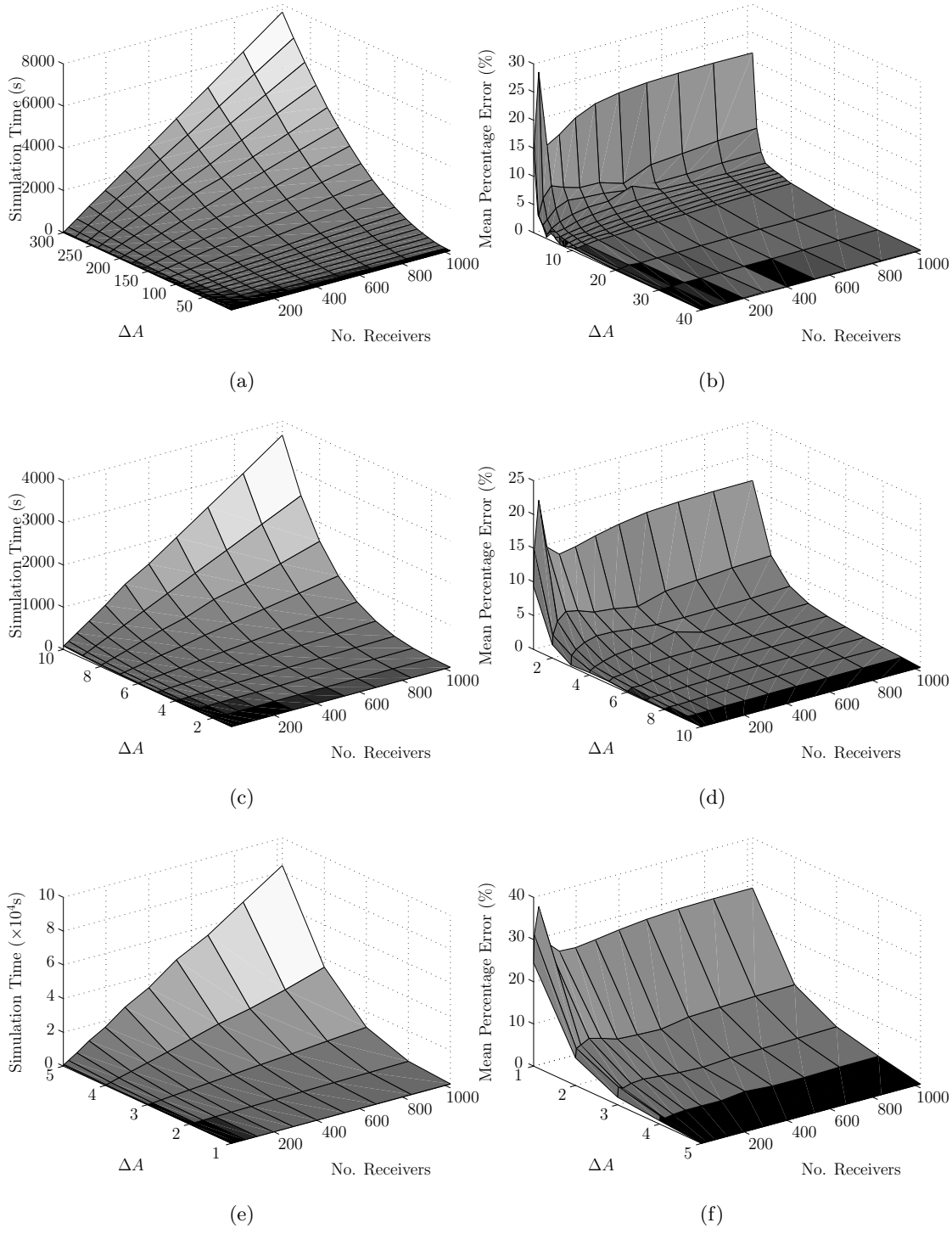

Figure 2.4: Computational time and error graphs. 1st order: (a) time, (b) percentage error. 2nd order: (c) time, (d) percentage error. 3rd order: (e) time, (f) percentage error.

[87] to compute just the third order impulse response between one transmitter and receiver. Comparing figures 2.4(e) and 2.4(f), the resolution for this work would be set to $\Delta A = 2$, allowing the result to be found within $\approx 30\,\text{min}$.

2.6 Testing the Simulator

2.6.1 A Comparison with 'Barry'

To test the functionality of the simulator, and to begin to provide the information about the channel that was the initial aim of the work, configuration A from Barry [87], was simulated as a means of verification. The room had a width $X_e = 5\,\text{m}$, depth, $Y_e = 5\,\text{m}$ and height, $X_e = 3\,\text{m}$. The reflectivity of the floor, $\rho = 0.3$, whilst the reflectivity of the walls and ceiling $\rho = 0.8$. The source was positioned centrally on the ceiling at $x = 2.5\,\text{m}, y = 2.5\,\text{m}, z = 3\,\text{m}$, orientated vertically downwards and considered to have a pure Lambertian optical intensity distribution, $(n = 1)$. The receiver is orientated vertically upwards, had an area $\Delta A_{\mathcal{R}} = 1\,\text{cm}^2$, and a $\text{FOV}_{\mathcal{R}} = 85^\circ$ and placed at a position of $x = 0.5\,\text{m}$,$y = 1\,\text{m}$ and $z = 0\,\text{m}$, i.e on the floor.

Figure 2.5(a) shows the individual component impulse responses, with figure 2.5(b), providing the third order (summation of each component) impulse response. Using equation (2.15),$H^{(0)}(t) = 1.23\,\mu\text{W}$, $H^{(1)}(t) = 0.505\,\mu\text{W}$, $H^{(2)}(t) = 0.430\,\mu\text{W}$ and $H^{(3)}(t) = 0.297\,\mu\text{W}$. All but $H^3(t)$ are identical to the published results for which Barry reported $H^{(3)}(t) = 0.269\,\mu\text{W}$, a difference of $28\,\text{nW}$, although, as $H^3(t)$ is the sum of each time bin, that difference is also the sum of errors over the 1024 time bins. The third order impulse response has $H(0) = 2.47\,\mu\text{W}$, compared to the results published of $H(0) = 2.4\,\mu\text{W}$ published by Barry. From the total power received, $h^{(0)}(t), h^{(1)}(t), h^{(2)}(t)$ and $h^{(3)}(t)$ contribute $50.6\%, 20.7\%, 17.7\%$ and 11% respectively.

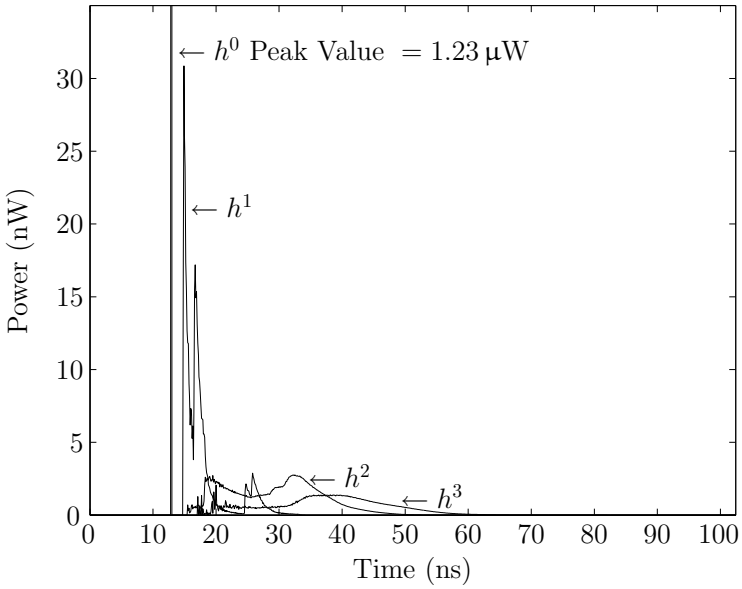

(a)

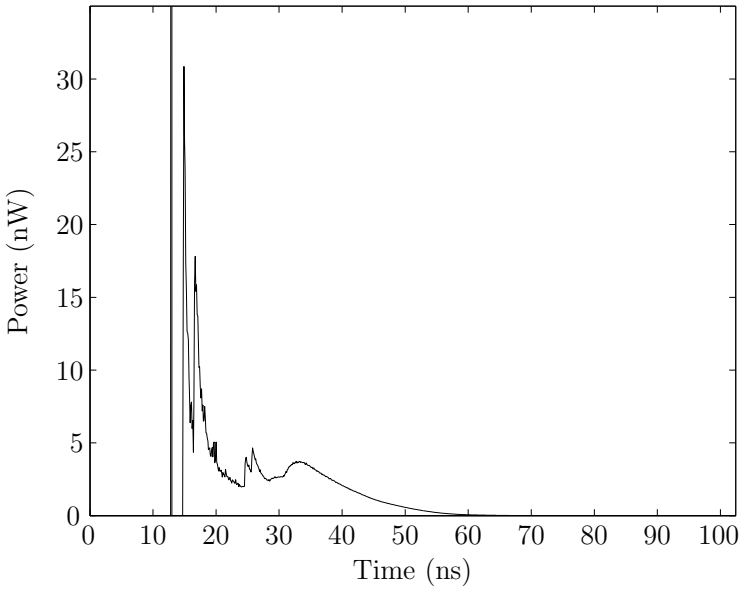

(b)

Figure 2.5: Reproduction of the results published by 'Barry' [87]. (a) Individual component impulse responses. (b) Third order impulse response.

2.6.2 Characteristics Over the Entire Room

Now that the program has been validated, and whilst Barry presented results for only one receiver location, it is important to look at how the impulse response changes throughout the room. Uniformly distributing 1024 receivers over the room at a height of 1 m as opposed to Barry where it was on the floor, but keeping everything else identical, figure 2.6 shows the individual components powers of $H^{(0)}(0), H^{(1)}(0), H^{(2)}(0)$ and $H^{(3)}(0)$ respectively. For the LOS link, $k = 0$ the total received power varies between 0.514 µW and 7.91 µW. Defining deviation from peak power to be the difference between maximum and minimum power divided by maximum power, these results indicate an approximate 94% power deviation from peak power. The first order component varies between 0.233 µW and 0.664 µW with the second order between 0.427 µW and 0.504 µW, whilst the third component varies between 0.209 µW and 0.406 µW.

As can be seen in figure 2.7, looking closely at the edges of the distribution, because the higher order components have a considerably smaller magnitude compared to the zero order link, the total received power does not change much with the addition of the higher orders, with the maximum power received in the room at the centre, directly under the transmitter or diffusion spot of 8.89 µW to a minimum in the corner of the room at 1.66 µW, equating to a difference of received power around the room of 7.23 µW, or 81% power deviation.

However, the reflected power does have a considerable effect on the bandwidth within the environment. Figure 2.8 shows the bandwidth change at the receiver locations as the number of reflections is increased. Beginning with the first order bandwidth, composing the LOS and first reflection, the minimum bandwidth at any location within the room is 78 MHz. The blank areas of the graphs imply that the bandwidth at these positions is beyond the resolution of the simulator using the sampling time of 0.1 ns (500 MHz). Inclusion of the second reflection reduces the minimum bandwidth to 19.5 MHz, whilst the third bounce reduces this further to only 14.6 MHz.

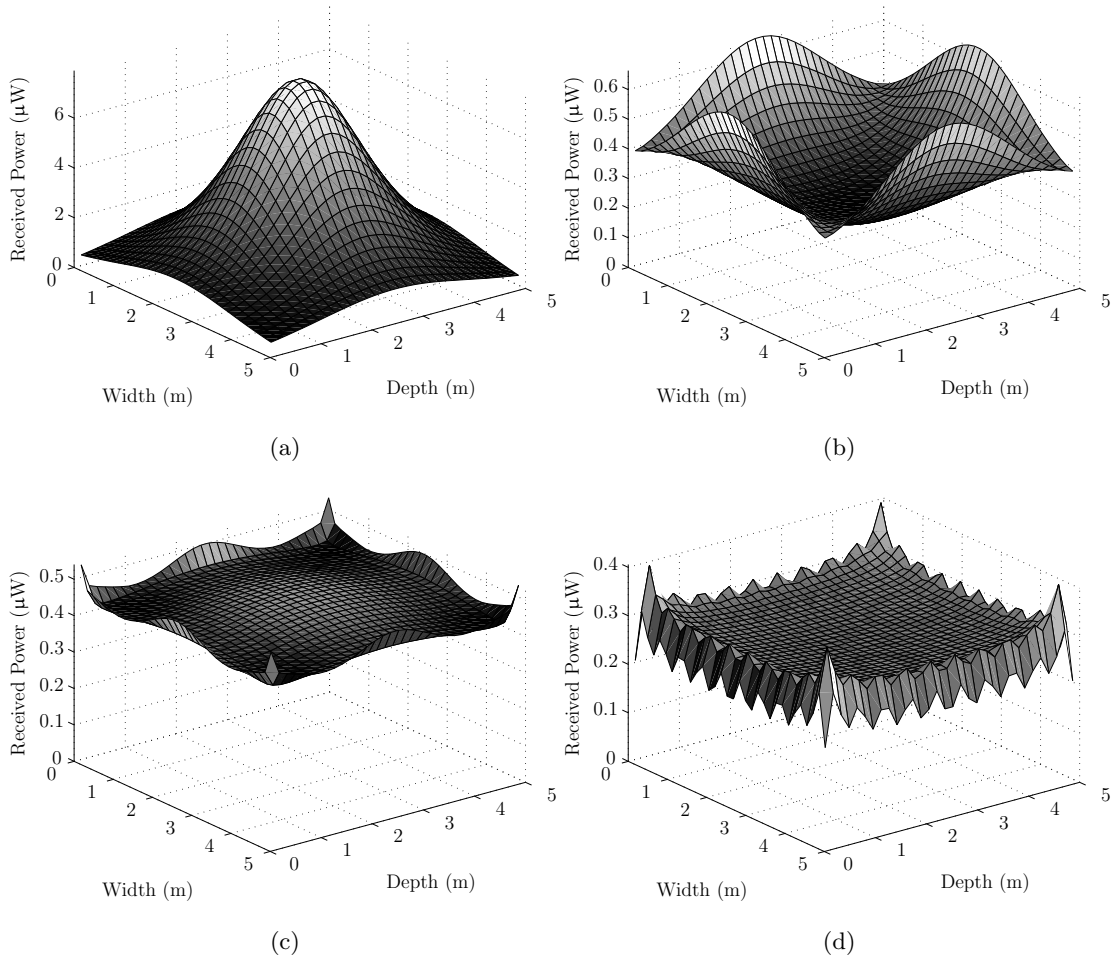

Figure 2.6: Component power impulse responses over the entire room. (a) Zero order component. (b) First order component. (c) Second order component. (d)Third order component.

Furthermore, the higher component reflections have a considerable effect on the RMS delay spread, as shown in figure 2.9, which for the first, second and third order components varies from between 0.052 ns and 0.262 ns, 0.127 ns and 0.689 ns and 0.172 ns and 1.23 ns, respectively. The worst case is when the RMS delay spread is higher.

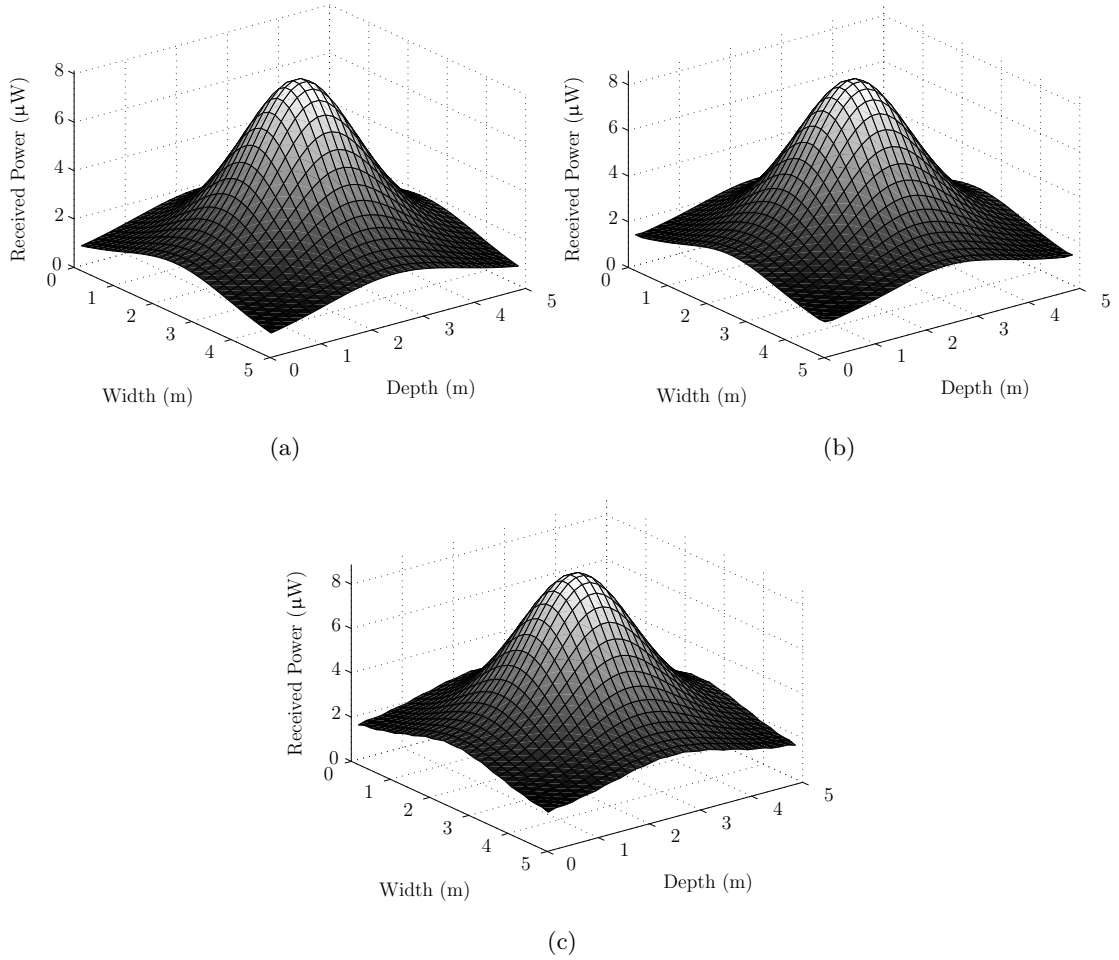

Figure 2.7: Impulse response order comparison. (a) First order. (b) Second order. (c) Third Order.

2.6.3 Multi Diffusion Spot Results

It is also possible to look at how the power, bandwidth and RMS delay spread are quantified when multi diffusion spots are formed on the ceiling. Taking the same room configuration as already established, and, with the 1024 receivers uniformly distributed over the room at a height of 1 m, the $\mathrm{FOV}_{\mathcal{R}_j}$ was varied in the set $\{10°, 15°, \ldots, 85°\}$, and the number of spots was changed within the set $\{9, 16, 25\}$. Although it is possible to provide a higher number of diffusion spots, the cost of the system would increase, thus it was decided not to increase the

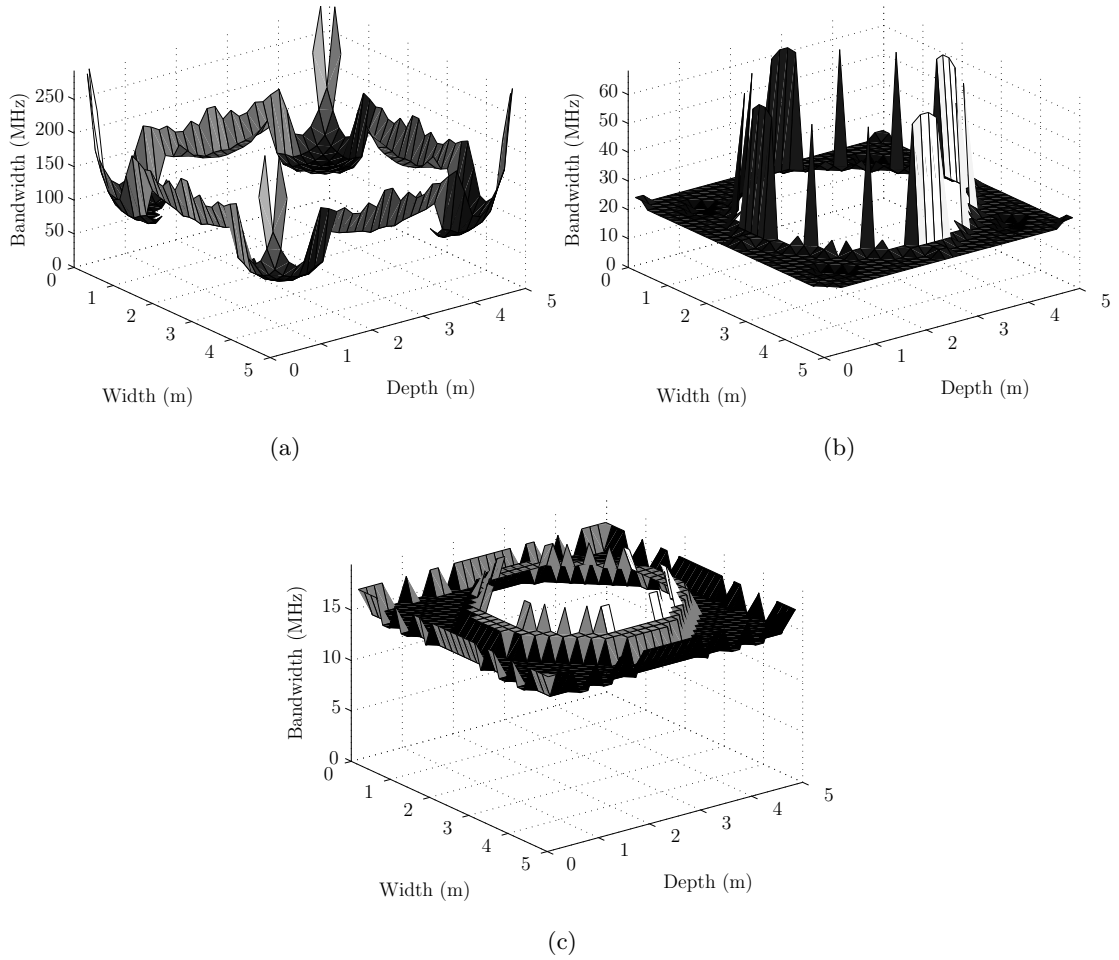

Figure 2.8: Bandwidth variation with order. (a) First order. (b) Second order. (c) Third order.

number. Furthermore, as a rough justification to the discussion in section 2.5, as those results were based upon one diffusion spot, for the simulation with 25 sources, the simulation time was approximately 18 h, highlighting the need for the earlier analysis into choosing a suitable set of ΔA.

Figures 2.10,2.11 and 2.12 provide some examples of the power distribution for situations involving narrow $\text{FOV}_{\mathcal{R}_j}$ receivers, possibly the kind of angles required for diversity detection. When there are 16 diffusion spots upon the ceiling and $\text{FOV}_{\mathcal{R}_j} = 15°$, figure 2.10(a) shows the power varying from between 0.762 µW and 9.02 µW, such that there was a deviation of 8.26 µW

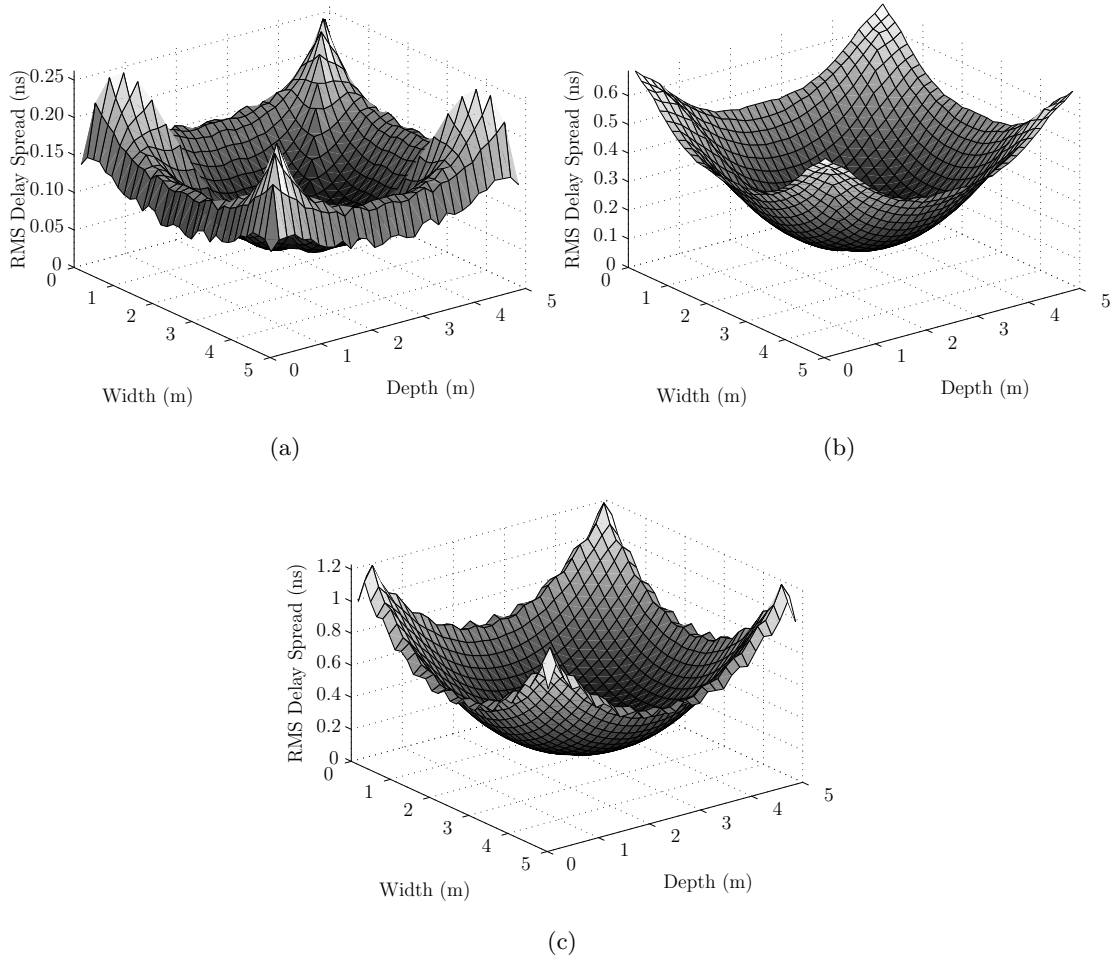

Figure 2.9: RMS delay spread variation with order. (a) First order. (b) Second order. (c) Third order.

or 91% power deviation. The corresponding bandwidth, figure 2.10(b), has minima at 12.2 MHz with a resulting RMS delay spread, figure 2.10(c), varying between 0.110 ns and a very high 10.1 ns.

If the user wishes a slightly more consistent power distribution, a slightly larger $\text{FOV}_{\mathcal{R}_j} = 25°$ under 25 spots, as shown in figure 2.11(a), will provide a power variation of between 11.8 µW and 29.4 µW, or a deviation of 17.6 µW, 60%. The corresponding bandwidth, figure 2.11(b), has minima at 14.6 MHz, and an RMS delay spread, figure 2.11(c) that has a much lower variation

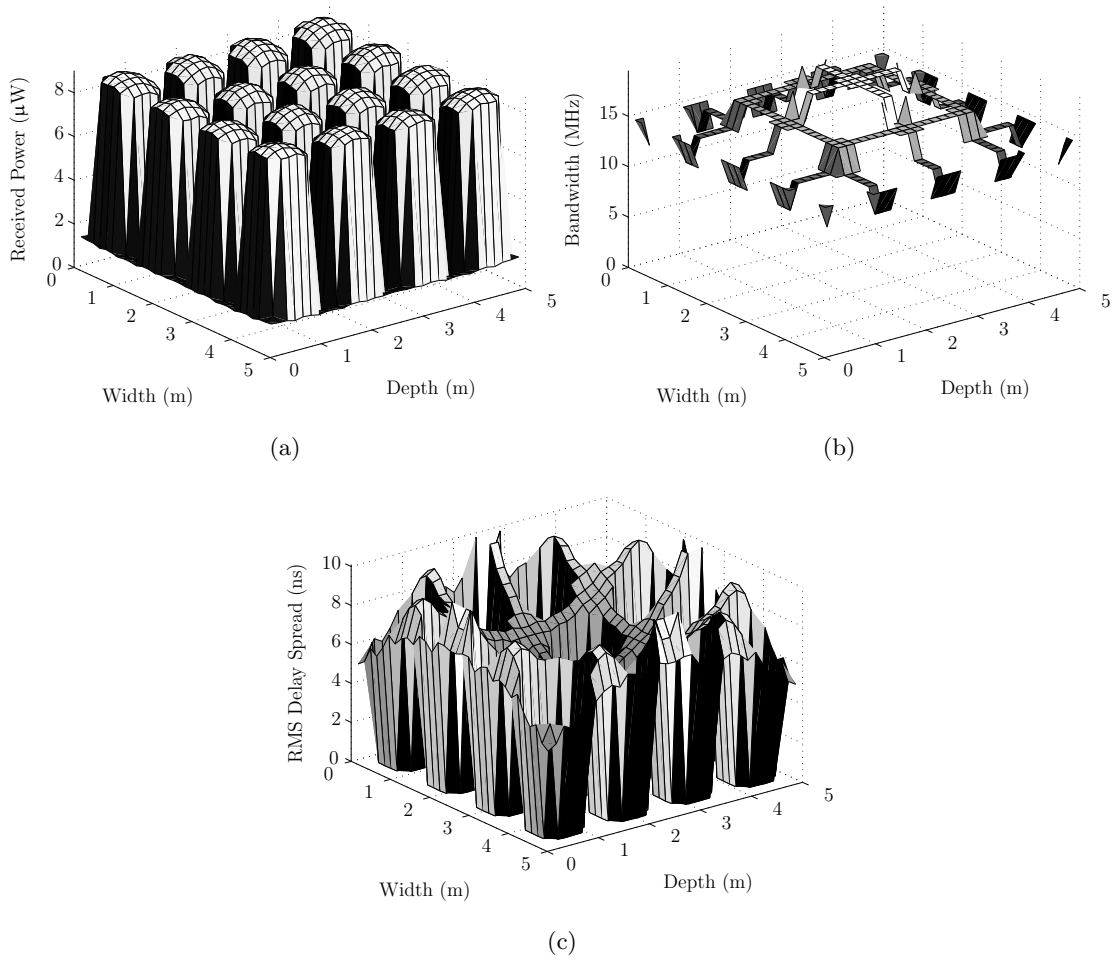

Figure 2.10: Multi spot diffusion example distributions for $I = 16$ and $\text{FOV}_{\mathcal{R}_j} = 15°$. (a) Power. (b) Bandwidth. (c) RMS delay spread.

of between 0.228 ns and 0.874 ns. Even further, the same number of spots could be used with a $\text{FOV}_{\mathcal{R}_j} = 35°$, whereby the power distribution, as shown in figure 2.12(a), varies between 14.7 μW and 43.9 μW, or a deviation of 29.2 μW, 66%. The corresponding bandwidth, figure 2.12(b), shows the scenario has a minimum of 14.6 MHz, whilst figure 2.12(c), shows the RMS delay spread varying between 0.397 ns and 1.10 ns.

These figures provide one of the most illustrative arguments for the use of diversity detection. On the one hand there is the possibility of the achieving, what is in effect, an infinite bandwidth

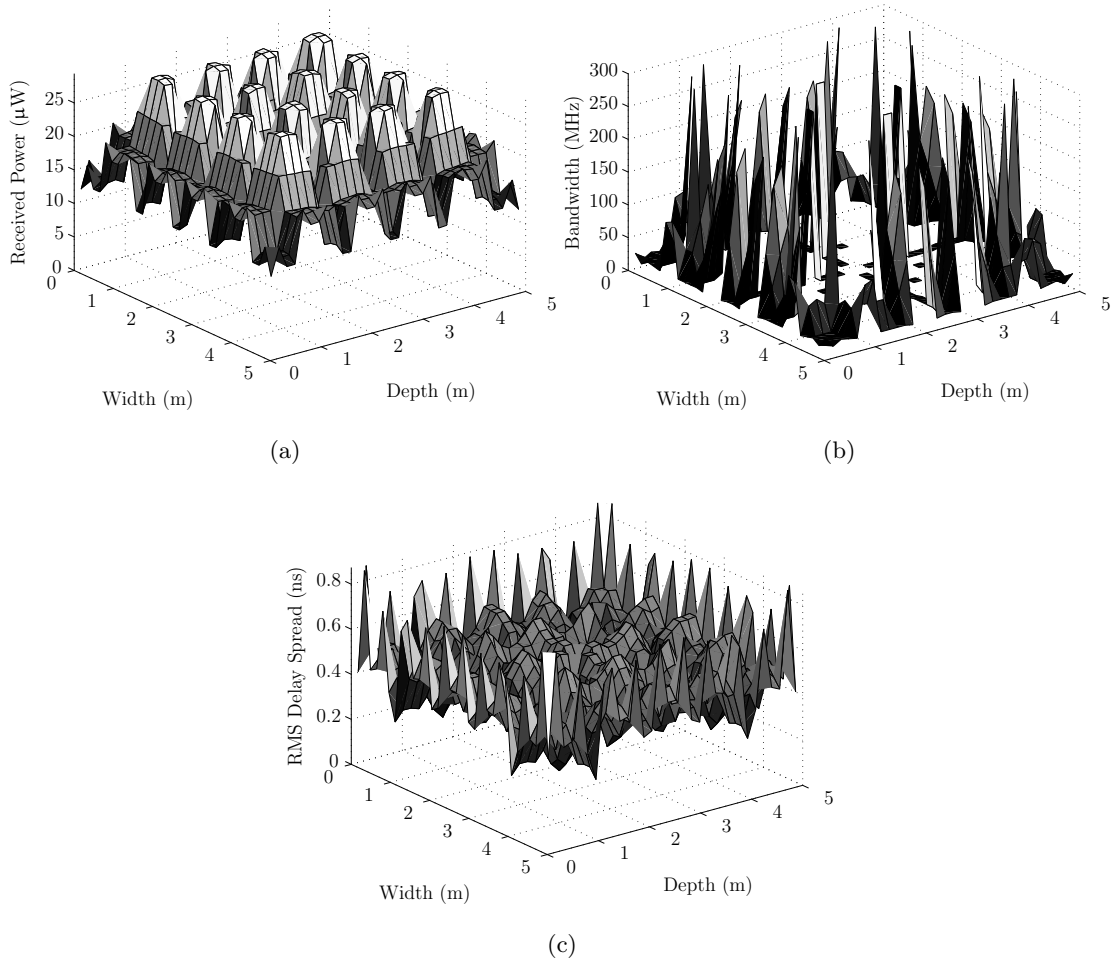

Figure 2.11: Multi spot diffusion example distributions for $I = 25$ and $\text{FOV}_{\mathcal{R}_j} = 25°$. (a) Power. (b) Bandwidth. (c) RMS delay spread.

due primarily to the high magnitude of the LOS link present at some locations. These figures also provide a good argument for not using them also, as it can be seen that there are locations where the bandwidth is limited and the RMS delay spread is comparatively high. The scale of the change in received power at different locations requires a receiver with a large dynamic range. Therefore, should there not be a LOS present, or the FOV is too small, or the number of spots be not quite right, then the performance will become degraded.

For the higher $\text{FOV}_{\mathcal{R}_j}$, figures 2.13(a), 2.14(a) and 2.15(a) show the deviation from peak

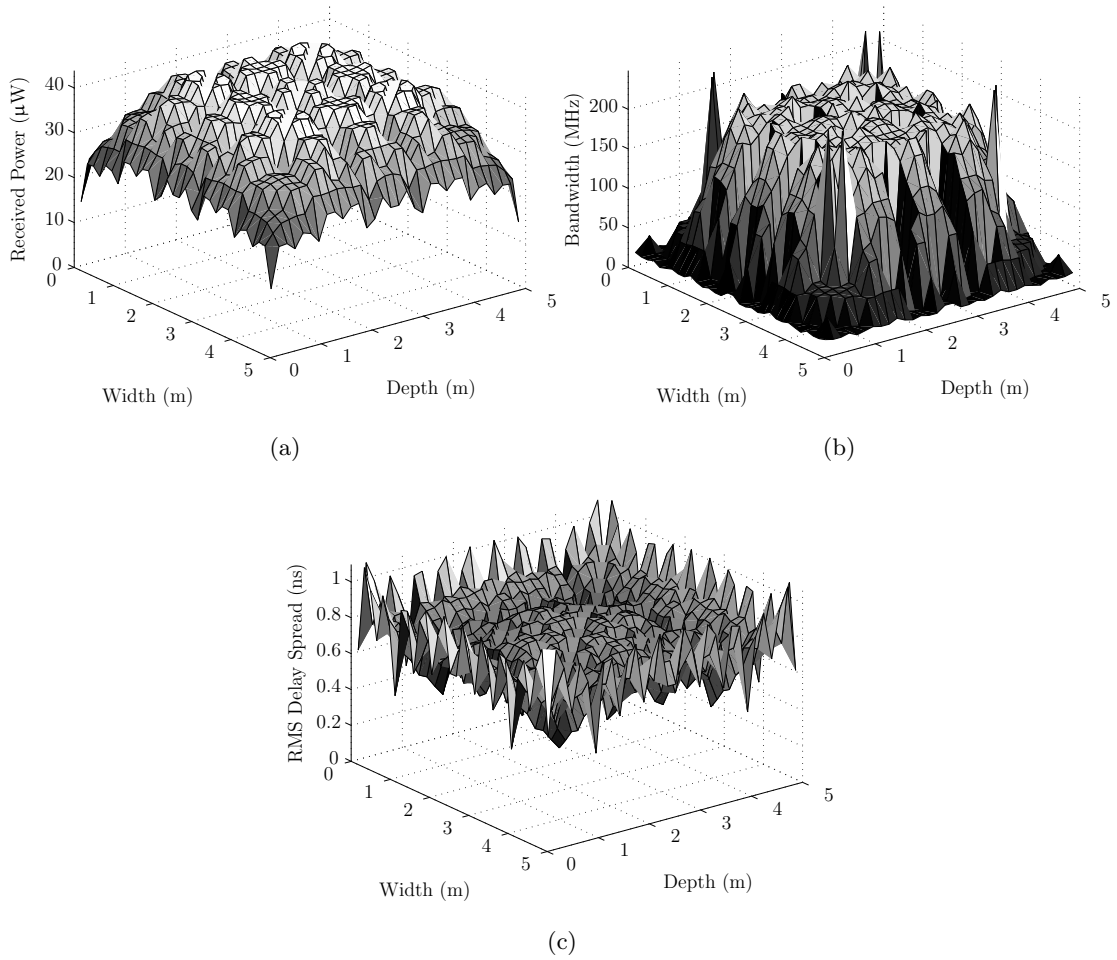

Figure 2.12: Multi spot diffusion example distributions for $I = 25$ and $\text{FOV}_{\mathcal{R}_j} = 35°$. (a) Power. (b) Bandwidth. (c) RMS delay spread.

power for $9, 16$ and 25 spots respectively. To achieve the lowest deviation from peak power a $\text{FOV}_{\mathcal{R}_j} > 50°$ is required. Conversely, one very important point to make about the results in figures 2.13(b), 2.14(b) and 2.15(b), which show the minimum bandwidth and maximum RMS delay spread within the environment, is that the bandwidth increases slightly with increasing $\text{FOV}_{\mathcal{R}_j}$, a concept that may seem contrary to traditional thought. However these worst case results are found near the walls of the room, as shown in figures, 2.10(b), 2.11(b) 2.12(b). Due to the parameters of the simulation at these positions, a receiver and ceiling diffusion spot are 8 cm and 50 cm from the wall respectively. This means that, at the lower FOVs, there is no direct

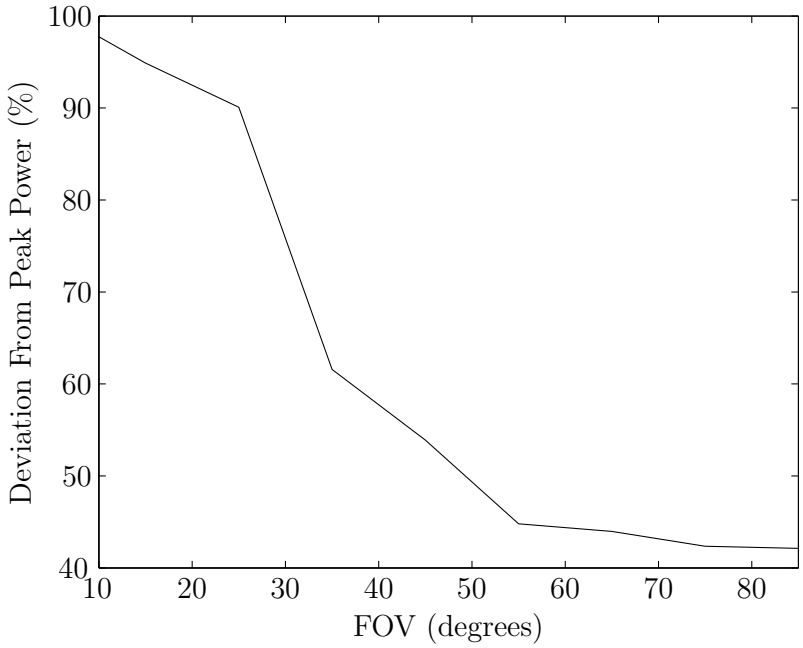

(a)

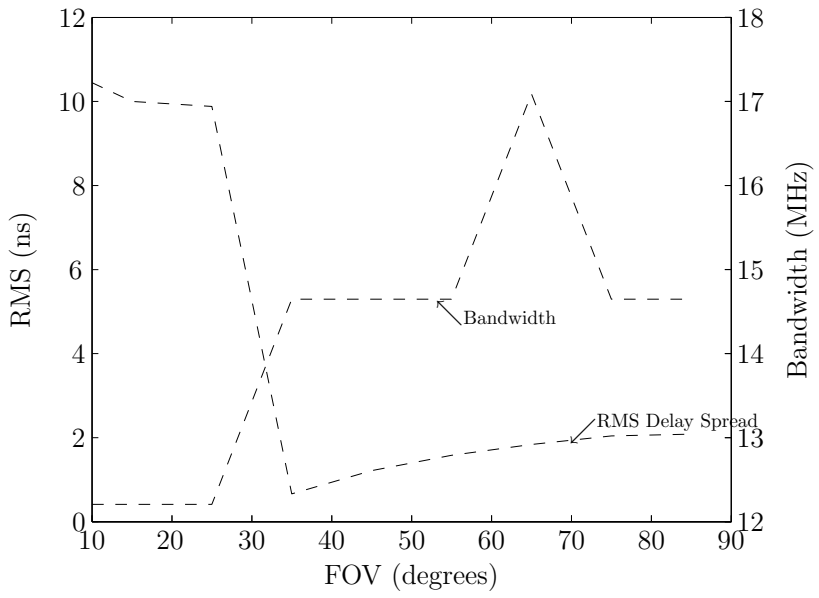

(b)

Figure 2.13: Varying the number of diffusion spots and the receiver FOV for $I = 9$. (a) Power deviation. (b) Bandwidth and RMS delay spread.

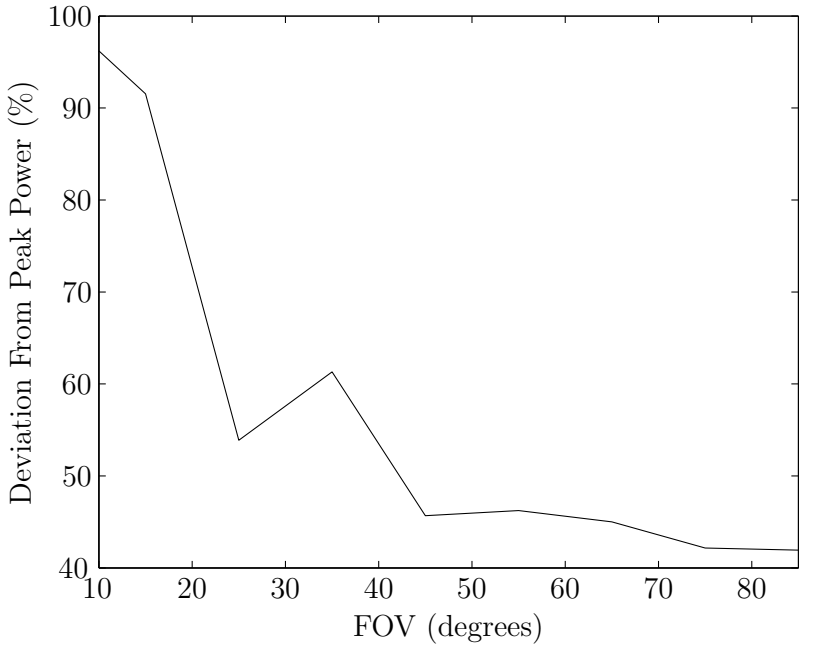

(a)

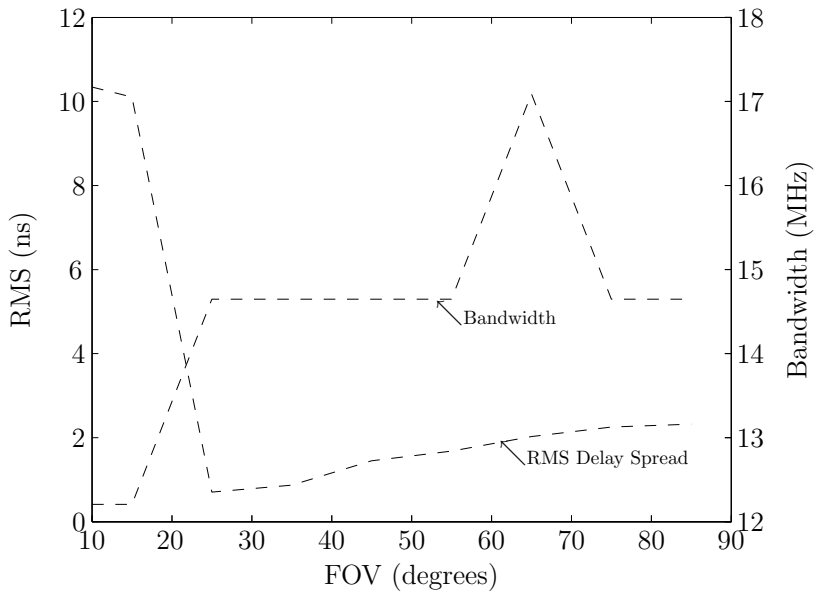

(b)

Figure 2.14: Varying the number of diffusion spots and the receiver FOV for $I = 16$. (a) Power deviation. (b) Bandwidth and RMS delay spread.

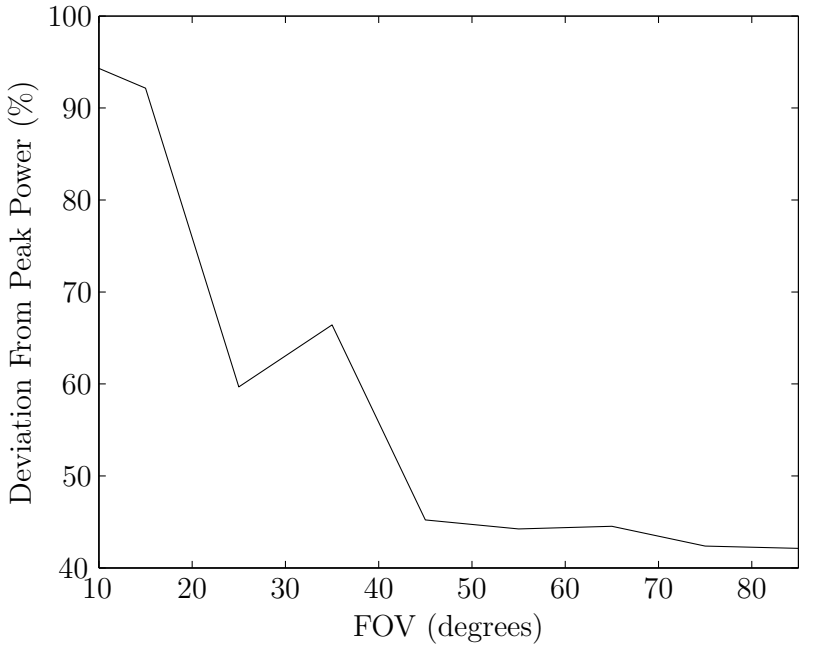

(a)

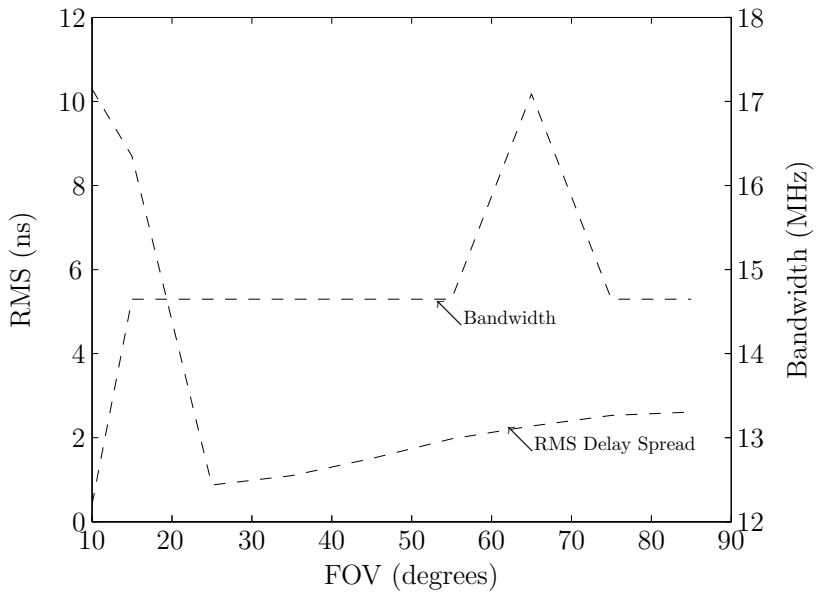

(b)

Figure 2.15: Varying the number of diffusion spots and the receiver FOV for $I = 25$. (a) Power deviation. (b) Bandwidth and RMS delay spread.

LOS link present, and, consequently, all incident radiation is a result of multiple reflections, lowering the bandwidth. As the FOV increases, more LOS links are formed, and the power from the LOS links is larger relative to the power from the reflections, increasing bandwidth. Finally, at very large FOVs, the worst case bandwidth reduces slightly as the magnitude of the power from the reflections increases relative to that from the LOS link.

2.7 Conclusion

In this chapter a purpose built simulator was developed including the provisions for objects and user movement, which is required in the next chapter. The simulator was validated against known results, both other simulation and measured results, showing good correspondence with what is expected. The choice of simulation method has been justified against other methods, along with critical analysis of the decision chosen to implement the simulator the way it was shown, and precision errors have been accounted for. Provisional results were shown, concerning the received power, bandwidth and RMS delay spread at all locations within the room for both single element and multispot receivers, under varying receiver FOV. At this stage of the thesis it should now be clear how the channel is affected, and more importantly, how variable it can be, by the both the environment and the the way the system within it is deployed including factors such as receiver design.

Chapter 3

Optimisation of the Channel

3.1 Introduction

This chapter presents a GA method for optical wireless channel control. Through the use of a multi spot diffusion transmitter capable of dynamically altering the intensity of the diffusion spots, it is possible to not only produce a consistent power distribution within a multiple environments, but also to account for user movement. The research emphasis in this chapter is placed upon the development of the GA from the ground up specifically tailored to be effective for this application.

Section 3.2 provides details on the theory of how and why the channel can be controlled. This is followed by section 3.3 that describes the theory of the GA. Section 3.4 then discusses the first set of results from the possible GA permutations, with an analysis in section 3.5 that covers the relationships between receiver FOV and the number of diffusion spots. Results are then provided in section 3.6, which show how the GA copes with a moving person, followed by section 3.8 where the GA is demonstrated to work within a second environment and user movement pattern.

3.2 Channel Scaling Factors

For a diffuse infrared channel employing IM/DD, a source $\mathcal{S}_i$ which emits an instantaneous optical power $X_i(t)$, will produce an instantaneous photocurrent $Y_{ij}(t)$ at receiver $\mathcal{R}_j$ with photodiode responsivity r_j, in the presence of an additive, white Gaussian shot noise $N_j(t)$, and can be modelled as the linear baseband system given by [129]

$$Y_{ij}(t) = r_j X_i(t) * h(t; \mathcal{S}_i, \mathcal{R}_j) + N_j(t) \tag{3.1}$$

Where $h(t; \mathcal{S}_i, \mathcal{R}_j)$ is the impulse response given by (2.6), and is fixed for a given system configuration of $\mathcal{S}_i$ and $\mathcal{R}_j$.

For a multi spot diffuse configuration, if it is assumed that all I sources $\mathcal{S}_i$ emit an identical signal waveform, such that $X_1(t) = X_2(t) = \ldots = X_I(t)$, but whose magnitude is individually scaled by a factor a_i, the instantaneous photocurrent generated at a given receiver $Y_j(t)$ is simply the summation of (3.1) for all sources

$$Y_j(t) = \sum_{i=1}^{I} \left(r_j a_i X_i(t) * h(t; \mathcal{S}_i, \mathcal{R}_j) \right) + N_j(t) \tag{3.2}$$

Furthermore, as only single receiver design is concerned, the photodiode responsivity r_j is constant for each receiver or receiver location, such that there may exist a set of I scaling factors a_i, that can be applied to the I identical signal waveforms $X_i(t)$, that will allow for the J receivers, to attain the same or very similar instantaneous photocurrents

$$Y_1(t) \approx Y_2(t) \approx \ldots \approx Y_J(t) \tag{3.3}$$

Knowing that the IM/DD OW channel is linear, (3.2) can be rewritten as

$$Y_j(t) = \sum_{i=1}^{I} \left(r_j X_i(t) * a_i h(t; \mathcal{S}_i, \mathcal{R}_j) \right) + N_j(t) \tag{3.4}$$

And as the method for determining the impulse response has already been described in chapter 2, and that it can be readily obtained, (3.3) can be solved by solving

$$\sum_{i=1}^{I} a_i h(t; \mathcal{S}_i, \mathcal{R}_1) \approx \sum_{i=1}^{I} a_i h(t; \mathcal{S}_i, \mathcal{R}_2) \approx \ldots \approx \sum_{i=1}^{I} a_i h(t; \mathcal{S}_i, \mathcal{R}_J) \tag{3.5}$$

By inspection of equations (3.2) to (3.5), it can be seen that, in order to solve the problem, some scaling factors will be < 1, and therefore will reduce the total amount of power received, compared to when all sources emit the same power. Ultimately, solving equation (3.3) for one environment will yield a different set of scaling factors than those needed to solve the problem for a different environment. Moreover, whilst all powers in both independent environments will be similar or the same, the relative magnitudes will be different.

An optical wireless system designer needs to achieve a high SNR at the receiver, which is proportional to the square of the received power [130], but also maintain system eye safety under IEC825 regulations [25]. These regulations mean that the maximum source power attainable will be determined by factors such as wavelength, exposure duration, pulse characteristics, distance from the eye and image size [131], which are all variable in terms of what the system designer is trying to achieve. In fact, as shown in section 2.3 determining the impulse response requires the use of a 1 W source by definition, and hence is almost certainly outside being classified as 'eye safe'. Therefore, in any event, the impulse response of the system needs to be scaled using the source power to make it 'eye safe'. The technique presented here will follow the same lines, such that once the scaling factors are determined for a given environment, they can be normalised and subsequently applied to the I sources of the same power magnitude, where the magnitude is set to be at the maximum acceptable exposure limit. The equality result of (3.3) is then independent of receiver power magnitude. In a second environment, where again the same set of steps is carried out to find the set of normalised scaling factors to solve (3.3), and it is found that the magnitude is different, adjustments can be made, for example, to the pulse characteristics in order to vary the magnitude of the power at the receiver such that both environments now have the same power distribution. This allows the use of the same receiver hardware, but where the system performance is different in the each environment. In many respects this concept draws many parallels to the IEEE 802.11a WiFi physical layer specification, that incorporates multi-rate transmission of up to 54Mbit/s, depending on channel characteristics [132, 133], and recent

work [40, 42, 134, 135, 136] in the IR domain has shown promising avenues for rate-adaptive transmission.

Considering the problem of solving (3.5) more closely: if an environment of dimensions with $X_e = 5\,\text{m}, Y_e = 5\,\text{m}, Z_e = 3\,\text{m}$ is assumed, similar to configuration A in [87], for a three reflection impulse response ($k = 3$), the longest time of flight for the radiation to travel is when it undergoes a path reflecting off the opposite corners of the room, where the time $t = (4(5^2 + 5^2 + 3^2)^{0.5})/c \approx 102.4\,\text{ns}$, and,using a sampling time of 0.1 ns would therefore yield a 1024 sample impulse response train, for every combination of I sources and J receivers, which will prove to be unwieldy, for two reasons.

Firstly, for all system designs and purposes, there will be an infinite number of environments, source and transmitter system configurations that can be modelled, and even if a solution could be formed for some of these environments, the computation time would be too large to allow the concept to be readily applicable except for system designers with state of the art computational facilities. Secondly, if no ideal solution could be found, it might be possible to produce several partial scaling factor solutions that each manage to equate some elements of (3.5) but not others. Therefore how does the system designer decide which of the solutions is optimal?

It is possible however, to simplify the task, replacing the need to evaluate each element of the impulse response train, with the need to find only the scaling factor solution for the time integral, or the DC value of the frequency response given by (2.15), $H(0;\mathcal{S}_i,\mathcal{R}_j) = \int_{-\infty}^{\infty} h(t;\mathcal{S}_i,\mathcal{R}_j)dt$, such that the simplified task is to find a solution to

$$\sum_{i=1}^{I} a_i H(0;\mathcal{S}_i,\mathcal{R}_1) \approx \sum_{i=1}^{I} a_i H(0;\mathcal{S}_i,\mathcal{R}_2) \approx \ldots \approx \sum_{i=1}^{I} a_i H(0;\mathcal{S}_i,\mathcal{R}_J) \tag{3.6}$$

Whilst the solution of (3.6) may appear to be simpler than solving (3.5), the DC response only quantifies the amount of power received, not when the power was received. Therefore, as the technique for solving (3.6) is presented, the solution will be fed back into the original system

model to quantify how both system bandwidth and RMS delay spread have been affected. The worst case bandwidth and RMS delay spread are defined to be the smallest and largest values found at any receiver or location within the room, respectively.

3.3 The Genetic Algorithm

The GA is a stochastic global search method that mimics the metaphor of natural biological evolution [137]. It operates on a population of potential solutions represented as chromosomes by evaluating and selecting individuals according to their relative fitness in the problem domain. This Darwinian survival-of-the-fittest approach exerts an evolutionary pressure upon the fittest individuals of a generation to reproduce with each other, forming a new, hopefully better population of solutions than the population from which they were created [138]. However, GAs should not be considered off-the-peg, ready to use algorithms, but rather a general framework that needs to be tailored to the specific problem [139]. Described below the methodology and justifications for the choices made in adapting the representation, fitness function, selection, recombination and mutation routines found in a so-called canonical GA.

3.3.1 Representation

The genotype represents all the information stored in the chromosome and allows for an explicit description of an individual at the level of the genes. The aim is to find a set of scaling factors that can be used to solve (3.5), such that, by allowing $a_i \forall i \in \{1, \ldots, I\}$ to take on a value in the set $\{0, 0.01, \ldots, 1\}$, the genotypic search space can be defined as $\Phi_g = \{0, 0.01, \ldots, 1\}^I$, which will provide $|\Phi_g| = 101^I$ possible solutions to the problem [140]. The methodology behind defining the set $\{0, 0.01, \ldots, 1\}$, is one of simplicity for normalised comparison. A ratio of 1 indicated maximum power, or 100% power. Defining a population $\Psi(t)$ at time t, of μ chromosomes $\mathbf{a}_\nu = (a_1, \ldots, a_I) \in \Phi_g, \forall \nu \in \{1, \ldots, \mu\}$ provides the basic representation of a possible solution

in a form that can be operated on by the GA. The initial population of chromosomes is formed by a uniform pseudo random number generator capable of only generating numbers in the set $\{0, 0.01, \ldots, 1\}$, such that, the larger the population, the better the chance of an initialisation with a uniform distribution of possible solution values. However, this would also require a larger memory overhead on the hardware implementation, and so it is important to find the smallest population size that will not adversely affect the GAs performance when some ratios are not initialised, and subsequently cannot be evaluated as a possible solution. Therefore, using some *typical* text book values [141, 142], the population sizes to be tested in this work will be $\mu = \{50, 100, 200\}$.

Another area of genetic representation that will be investigated is a phenomenon known as chromosome epistasis, which refers to a problem-dependent condition in the genotype structure where genes are highly interdependent, such that a good solution may only be found when the value of the genes occur in a particular pattern [143]. To illustrate this with the problem, consider for example a system with $I = 16$, such that the chromosome will contain 16 scaling factors, as in figure 3.1(a), which translate to the sources on the ceiling in two ways, depending upon how the genotype structure, $\mathcal{G}$, is defined. Firstly if a wrap-around structure, ($\mathcal{G} = \text{WA}$) is implemented, the scaling factors, when translated to their respective sources, as in figure 3.1(b), can be seen to be at the end of the rows a_4 and a_5, a_8 and a_9 etc. and are physically far apart in application, but adjacent in the chromosome. On the other hand, with a concertina ($\mathcal{G} = \text{CON}$) structure, the translation, as in figure 3.1(c), now shows this problem is alleviated, but other scaling factors, such as a_1 and a_8, are now positioned physically close, while further apart in the chromosome, compared to a_1 and a_5 when $\mathcal{G} = \text{WA}$. This condition will be tested by application of identical GAs for each genotype structure.

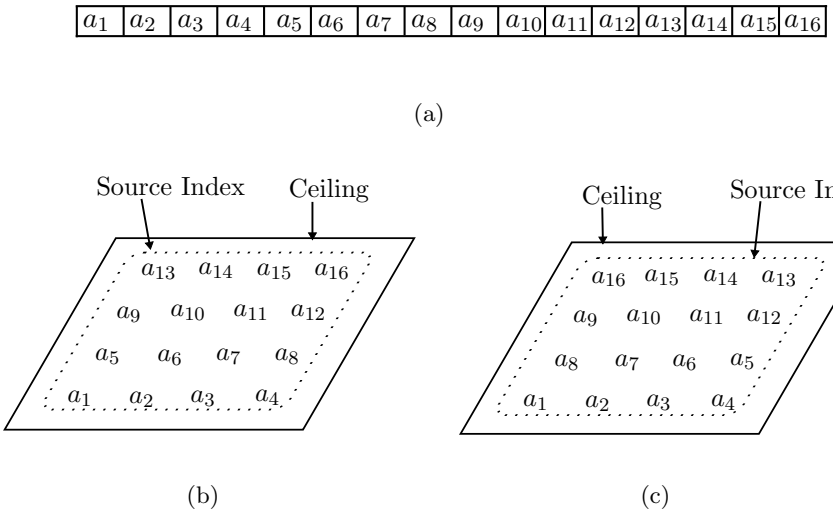

Figure 3.1: Diagrammatic representation of chromosome epistasis. (a) Chromosome structure. (b) Wrap around (WA) genotype structure. (c) Concertina (CON) genotype structure.

3.3.2 The Fitness Function

Whereas the genotype describes an individual on the level of the genes, the phenotype describes its outward appearance, and it is this phenotypic appearance that determines an individual's success in life. The GA's genetic operators, such as recombination and mutation, work on the level of the genes, but offspring of parents do not inherit the phenotypic properties, only the genotypic properties which still require evaluation at the level of the phenotype [140]. This evaluation is commonly known as the fitness, or objective function, F, which, for the results presented here, is given by

$$F(\mathbf{a}_\nu) = 100 - \left(100\left(\frac{\max H(0;\mathbf{a}_\nu) - \min H(0;\mathbf{a}_\nu)}{\max H(0;\mathbf{a}_\nu)}\right)\right) \tag{3.7}$$

Where $\max H(0;\mathbf{a}_\nu)$ and $\min H(0;\mathbf{a}_\nu)$ are the maximum and minimum DC responses at any receiver in the environment after application of the scaling factors $\mathbf{a}_\nu$ to the source powers, respectively. It can be seen that the function is measuring the percentage change or deviation from the peak power in the room, for an individual $\mathbf{a}_\nu$, whose source scaling factors will produce a perfectly uniform power distribution within the room and will have a fitness of 100%.

Furthermore, the global maximum optimal solution $\hat{\mathbf{a}}_\nu$ can be defined as

$$\hat{\mathbf{a}}_\nu = \max_{\mathbf{a}_\nu \in \Phi_g} F(\mathbf{a}_\nu) \tag{3.8}$$

Although there is no specific need to apply a normalised fitness function, it has been done so for the reasons given in section 3.2, relating to the need to produce a set of normalised ratios that can be applied independently of the absolute power magnitudes, which are then scaled for the purposes of eye safety.

One important point to make at this point is to the reasoning as to why only received power deviation is optimised. It could be possible, for example, to optimise bandwidth or RMS delay spread, or it could also be possible to use a multi objective fitness function that attempts to optimise both power and bandwidth. However in the initial stages of the research, when the feasibility of the GA was being determined for this application and test simulations were being conducted, no such fitness function based on bandwidth was found to be successful. This is not to say that there is not one, or that optimisation of the bandwidth cannot be achieved, just that for all the algorithms tested nothing of significance was found.

3.3.3 Selection

The primary objective of the selection operator is to emphasize the fitter solutions, such that their genotypic information is passed onto the next generation [144], and can be used to control the explorative and exploitative nature of the algorithm [145]. Three selection routines are proposed in this work, namely, Roulette, and stochastic uniform sampling (SUS), which are both proportional selection schemes [146], and tournament selection, which is a rank-based scheme [147].

The roulette and SUS selection schemes assign a probability of selection proportional to an individual's relative fitness within the population, such that an individual's probability of selection,

p_ν^{prop}, is given by

$$p_\nu^{\text{prop}} = \frac{F(\mathbf{a}_\nu)}{\sum_{\nu=1}^{\mu} F(\mathbf{a}_\nu)} \tag{3.9}$$

Referring to figure 3.2 (a) which illustrates an example of a simple hypothetical population of six chromosomes, $\{\mathbf{a}_1, \ldots, \mathbf{a}_6\}$, and their respective probability of selections, $\{15, 18, 5, 16, 21, 25\}\%$, these probabilities are then contiguously mapped onto a wheel, such that $\sum_{\nu=1}^{\mu} p_\nu^{\text{prop}} = 1$. A uniform random number is then generated in the interval $[0, 1]$, and the individuals whose cumulative probability within the population that spans the number is chosen. The process is repeated μ times, until a new population has been selected. The roulette wheel is unbiased, but suffers from a possible infinite spread, in that statistically any member of the population with $p_\nu^{\text{prop}} > 0$ can be chosen μ times for the next generation [148]. SUS overcomes this by generating μ uniformly spaced numbers in the range $[0, 1]$, as in figure 3.2(b) and applying a single randomly generated offset value, that moves the position of the numbers such that each individual is still selected, based upon its cumulative probability position relative to others in the population. It thus maintains zero bias, but now it is not possible for a given individual to be chosen beyond its expected number [146].

Tournament selection is carried out by first ranking all members in the population $\Psi(t) = \{\mathbf{a}_1, \ldots, \mathbf{a}_\mu\}$ by their absolute fitness in the population $F(\mathbf{a}_\nu)$, where $\mathbf{a}_1$ is the fittest, and $\mathbf{a}_\mu$ is the least. Then, by randomly selecting q members, the best for the next generation is chosen. The probability of a member $\mathbf{a}_\nu$ being selected is given by [145]

$$p_\nu^{\text{torn}} = \frac{1}{\mu^q} \left((\mu - \nu + 1)^q - (\mu - \nu)^q \right) \tag{3.10}$$

By increasing the size of the tournament q, the selective pressure can be increased, giving fitter members of the population a higher probability of selection and being allowed to reproduce into the next generation. Tournament selection would be easier to implement in hardware [149], as there is no need to carry out proportional fitness assignments as in (3.9). Depending upon the size of the tournament, the algorithm will be very exploitative, losing diversity and possibly

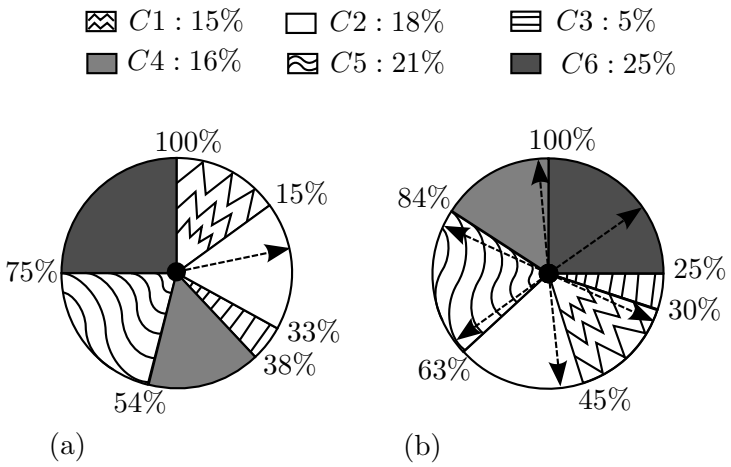

Figure 3.2: A comparison of roulette and stochastic uniform sampling methods. (a) Roulette Selection. (b) Stochastic uniform sampling.

finding a non optimal solution [150]. The loss of diversity is given by [151]

$$D_T(t,\mu) = \frac{1}{\mu}\sum_{k=1}^{\mu}\left(1 - \frac{k^q - (k-1)^q}{\mu_q}\right)^{\mu} \tag{3.11}$$

For example, with reference to figure 3.3, with the chosen population sizes of this work, it can be expected that, as tournament selection is going to be implemented with $q = 2$ and $q = 3$, approximately 40% and 50% of the genetic material will be lost, respectively, through the selection process alone [151].

3.3.4 Reproduction

Crossover imitates the principles of natural reproduction, and is applied with a probability of ρ_c to randomly selected individuals chosen by the selection routine. Its purpose is to form new individuals for the next generation which have some parts of the genotypic information as the parents [148]. For this work a single point $m = 1$ and a double point $m = 2$ crossover are investigated. In a single point crossover, a random crossover point in the range $\{1, \ldots, I-1\}$ is chosen,

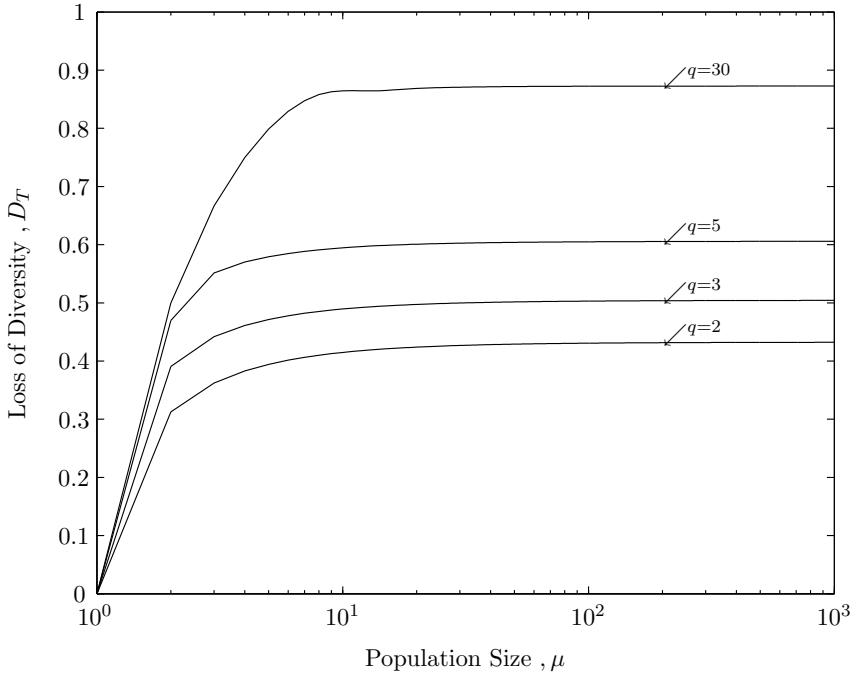

Figure 3.3: Loss of diversity in tournament selection for varying population and tournament sizes.

and two new individuals are formed by swapping the substrings about that point. For a double point crossover, a similar method is applied, but, by generating two unique random numbers in the range $\{1, \ldots, I-1\}$, and sorting into ascending order, followed by exchanging substrings between successive cross over points. For this work, $\rho_c = 0.7$ is maintained throughout.

3.3.5 Mutation

Mutation was originally developed as a background operator [139], able to introduce new genetic material into the search routine, such that the probability of evaluating a string in Φ will never be zero [148]. Thus it would still be possible to recover good genetic information that may have been lost through selection [140]. Unlike the crossover operator, mutation is seen as a local search method, because it can only modify elements of an individual, perturbing its genetic

information in a much smaller way than crossover, which allows the combining of genotypic information from different parents. As different selection routines are going to be evaluated, the mutation operator will be applied to each gene in each individual with varying probabilities $\rho_m = \{0, 0.05, 0.1, 0.2\}$, such that when a random number is generated that is less than the chosen probability, that gene is replaced with a new randomly-generated value, in the set $\{0, 0.01, \ldots, 1\}$. As with the choices of population size, these values have been chosen as they are *typical* values used in many publications [152, 143]. An attempt will be made to find the highest possible value aiding in the search, but not too high that, what is known as mutation interference is encountered, defined as when the mutation rate is so high that solutions are so frequently or drastically mutated that the algorithm never manages to explore any of the region of the search space thoroughly as good solutions are rapidly destroyed, rather than being formed by mutation [143].

3.3.6 Termination and Repeatability

In general, a GA is run over many generations until the the algorithm converges or the result has satisfied some defined solution criteria. However, as the minimum power deviation of the room is unknown, some simple simulations were carried out to find that 5000 generations was an appropriate number, as this was a reasonable compromise between computational effort, and it allows the algorithm a chance to find any better solutions should it be able. As will be shown in the following section, all GAs (that would converge) converged within this time frame.

Due to the stochastic nature of the GA, for each simulation the results were inevitably slightly different, meaning that, to allow presentation of results that are both representative of the GAs performance and repeatable, each simulation was completed 30 times, such that each performance value presented within the results section is the average, with an associated standard deviation if applicable, after 30 retrials. The choice for 30 retrials was determined by repeating

the simulation $10, 20, 30$ and 50 times, but it was seen that the average and standard deviation did not change after 30 retrials, such that it was the lowest number of retrials required to produce consistent results with the lowest possible computational effort.

3.4 Evaluating the Genetic Algorithm

To begin the testing of all the permutations of algorithms described in section 3.3, what will be known as room 1, was established, with a width $X_e = 5\,\text{m}$, depth, $Y_e = 5\,\text{m}$ and height, $X_e = 3\,\text{m}$. For future reference all room configurations can be seen in detail in appendix C. The reflectivity of the floor, $\rho = 0.3$, whilst the reflectivity of the walls and ceiling $\rho = 0.8$. Starting with the middle number of diffusion spots tested so far in section 2.6.3, 16 diffusion spots were uniformly distributed over the ceiling, orientated vertically downwards and assumed to have a pure Lambertian, $n = 1$, intensity distribution pattern. 1024 receivers were uniformly distributed at a height, $z = 1\,\text{m}$, all vertically orientated with a $\text{FOV}_{\mathcal{R}_j} = 45^\circ$ and an area $A_{\mathcal{R}_j} = 1\,\text{cm}^2$. In total, 192 algorithmic permutations were tested, with the full results presented in appendix B, whilst a more concise table or results detailing only the most important algorithms required for the analysis, is shown in table 3.1.

Before the optimisation of the room, as can be seen from figure 3.4(a), the power varies throughout the room between $22.5\,\mu\text{W}$ and $41.3\,\mu\text{W}$, or a $18.8\,\mu\text{W}$, (45%) deviation. The bandwidth as in figure 3.4(c), varies between $14.6\,\text{MHz}$ and $134\,\text{MHz}$, whilst the RMS delay spread, as in figure 3.4(e), varies between $0.619\,\text{ns}$ and $1.45\,\text{ns}$.

After the optimisation of the room described, using algorithm 6 of table 3.1, the power distribution now ranges between $17.4\,\mu\text{W}$ and $25.0\,\mu\text{W}$, or a deviation of $7.60\,\mu\text{W}$, (30%). This is an improvement or gain of (15%) compared to a system without the scheme. The resulting optimisation has changed the bandwidth distribution as shown in figure 3.4(d), and now varies

Algorithm	Selection Method	Generations	N	ρ_c	ρ_m	m	$\mathcal{G}$	R	Best (St.D)	Mean (St.D)
1	Roulette	5000	50	0.7	0.1	2	CON	30	36(1.8)	42(2.3)
2	Roulette	5000	100	0.7	0.1	2	WA	30	34(1.0)	41(1.9)
3	Roulette	5000	200	0.7	0.05	2	WA	30	32(0.9)	36(1.3)
4	SUS	5000	50	0.7	0.05	2	CON	30	31(0.8)	36(1.4)
5	SUS	5000	100	0.7	0.05	1	CON	30	31(0.5)	35(0.8)
6	SUS	5000	200	0.7	0.05	2	CON	30	30(0.3)	34(0.6)
7	Tournament (2)	5000	50	0.7	0.2	2	CON	30	33(1.3)	35(1.8)
8	Tournament (2)	5000	100	0.7	0.2	2	WA	30	32(1.0)	34(1.2)
9	Tournament (2)	5000	200	0.7	0.2	2	CON	30	31(1.0)	33(0.9)
10	Tournament (3)	5000	50	0.7	0.2	2	CON	30	33(1.2)	35(1.4)
11	Tournament (3)	5000	100	0.7	0.1	2	CON	30	32(1.1)	33(1.1)
12	Tournament (3)	5000	200	0.7	0.2	2	CON	30	32(0.8)	33(0.8)

Table 3.1: The 12 algorithms for analysis.

between 14.6 MHz and 110 MHz. Therefore the worst case bandwidth around the room has not been changed, whilst the top end has only been reduced by 24 MHz. The resulting RMS delay spread, as shown in figure 3.4(f) now varies between 0.527 ns and 1.43 ns, which is actually shown as an improvement, although fairly negligible at, ≈ 0.1 ns at the lower range, but without penalty at the top end.

.

In terms of how each selection routine performed relative to each other, figure 3.5 shows the convergence curves of the best individual within the population for algorithms $2, 6$ and 11 of table 3.1 at each generation. The curves shown are actually typical for a given selection scheme used, with only the point of convergence changing by varying the parameters such as mutation rate, number of crossover points, and genotype structure.

SUS selection routines performed the most predictably and with the best overall results. The slow and gradual convergence to a solution was always achievable, even at higher mutation rates

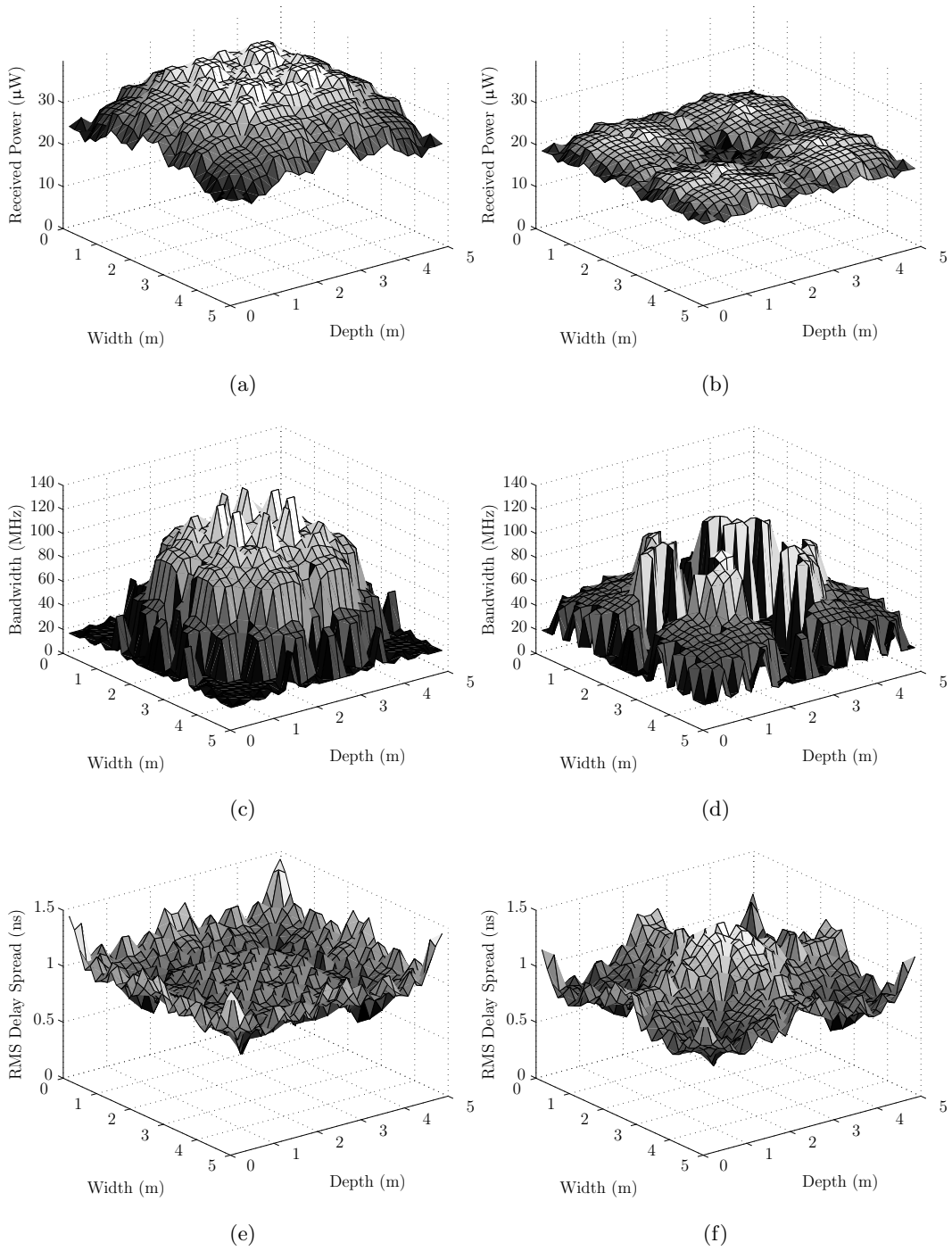

Figure 3.4: Algorithm 6 optimisation of room 1. Power: (a) non optimised, (b) optimised. Bandwidth: (c) non optimised, (d) optimised. RMS delay spread: (e) non optimised, (f) optimised.

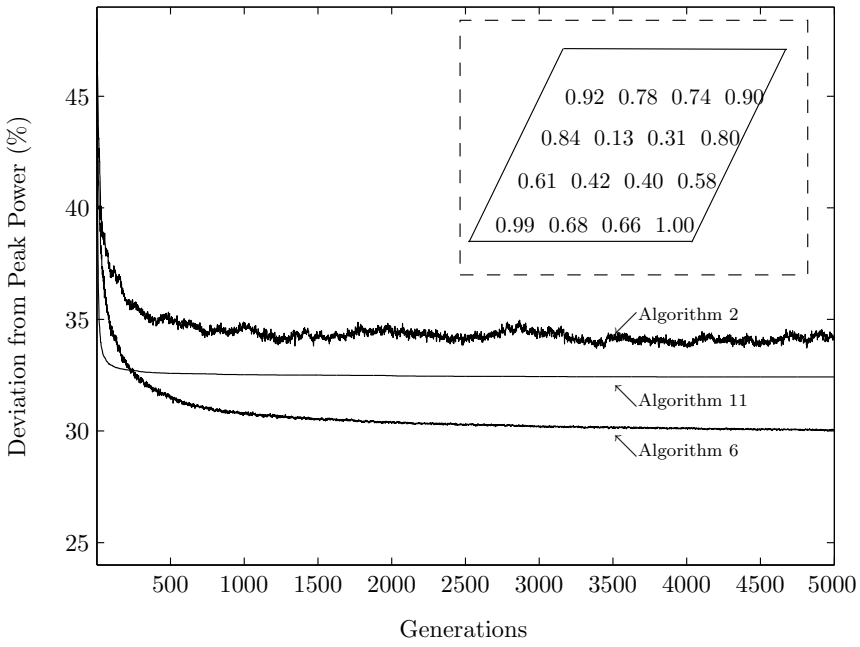

Figure 3.5: Convergence curves for algorithms $2, 6$ and 11. Insert depicts the 16 normalised ratios for the respective spot posistions provided by the last generation of algorithm 6.

($\rho_m = 0.1$), although best performances were always found when $\rho_m = 0.05$, independent of genotype structure, number of cross over points, and population size. They also performed better with the concertina genotypic structure ($\mathcal{G} = \text{CON}$), achieving around $1 - 2\%$ improvement over a routine with identical parameters and a wrap around structure ($\mathcal{G} = \text{WA}$). The use of a double point cross over ($m = 2$) produced only what appeared to be an improvement in the standard deviation, that is, its repeatability of the algorithm, but seemed to have little effect on the ability to converge to better solutions. SUS selection also performed better with the highest population size ($\mu = 200$), such that, for any permutation of parameters at this population size, the worst performer was only just worse than the best, with $\mu = 100$.

Tournament Selection, with either 2 or 3 tournament candidates, tended to quickly but sub-optimally converge. As can be seen from figure 3.5, beyond 500 generations, the selection routine will not allow for new solutions to be considered, and even when using a high mutation

rate ($\rho_m = 0.2$) in order to overcome the predicted loss of diversity encountered due to the *greedy* nature of the selection scheme, it is not fully capable of performing a thorough solution search. Tournament selection showed very little dependence upon the number of crossover points used, but generally produced better results using the concertina genotype structure ($\mathcal{G} = \text{CON}$). The performance was also very similar when $\mu = 100$ and $\mu = 200$ for a given set of parameters, implying that, for these population sizes, the initialisation must have produced enough genetic values for the algorithm to work with, before the selection scheme ruthlessly removed up to 50% of the genetic information.

The GAs using Roulette selection were by far the worst performing of all tested. They showed almost no consistency or pattern towards either how well they would perform, or to why a performance level was achieved. Variation of an individual parameter resulted in contradictory behaviours for any other relations of the fixed parameters. As algorithm 2 shows in figure 3.5, the convergence curve, if convergence occurred, tended to drift around as the selection routine seemed to be losing good genetic information from one generation to the next.

The insert to figure 3.5 details the normalised ratios found in the final generation of algorithm 6 in their respective positions upon the ceiling. These ratios can used to form the distributions shown in figures 3.4(b), 3.4(d) and 3.4(f) respectively. An interesting result of these ratios and their positions is the apparent symmetry of the ratios, around the center of the ceiling. Whereas the work described in this thesis, relies on fixed spot position and varying intensities, other work has been published [153, 50], that varies sport position at fixed intensities. The elegance of applying the GA does not rule out reproducing, albeit not perfectly due spacing of our uniform spot distribution, any of these established spot patterns such as uniform, diamond of line-strip [109].

3.5 GA Performance with Varying Receiver FOV

Continuing with room 1, the number of sources is now varied within the set $\{9, 16, 25\}$ and the receivers FOV in the set $\{10°, 15°, 25°, \ldots, 85°\}$ such that more optimisation relationships can be drawn. As the GA optimisation technique will add some complexity to the transmitter driver electronics, the number of diffusion spots was limited to 25, to maintain a system that is still cost effective. Algorithm 6, still considered to be the best global optimiser, has been used for the results.

As shown in figures 3.6(a), 3.7(a) 3.8(a), for receivers with a $\text{FOV}_{\mathcal{R}_j} < 35°$, virtually no optimisation can be achieved. This is down to the fact that at these small FOVs, the receiver does not detect much power from the multiple reflections from the surfaces of the environment, only the direct LOS links. The FOV is too small to see the walls or the room, so any power that is received from reflections has to be a reflection off the ceiling, which will have undergone more that one reflection already thus having a low magnitude. For example, figures 3.9(a) and 3.9(b), which show the before and after optimisation of a receiver with a $\text{FOV}_{\mathcal{R}_j} = 15°$ under 16 spots, whereby before optimisation the power varies between 0.762 µW and 9.02 µW, a deviation of 8.26 µW or (92%). After the optimisation the power ranges between 0.750 µW and 8.79 µW, a deviation of 8.04 µW, (91%), an optimisation gain of only (1%).

In contrast to this is a receiver with a slightly higher $\text{FOV}_{\mathcal{R}_j} = 35°$ under 25 spots, as shown in figure 3.10(a), which has a power ranging between 14.7 µW and 43.9 µW, a deviation of 29.2 µW, (66%). After optimisation using algorithm 6, as shown in figure 3.10(b), the power now ranges between 10.4 µW and 18.2 µW, a deviation of 7.8 µW, (42%), such that there is an optimisation gain of (24%). This is the configuration that provides the highest achievable optimisation gain.

Using a receiver with a $\text{FOV}_{\mathcal{R}_j} = 55°$ under 25 spots provides the configuration, as in figure 3.11(a), and the power ranges from between 45.1 µW and 80.8 µW, which is a deviation of

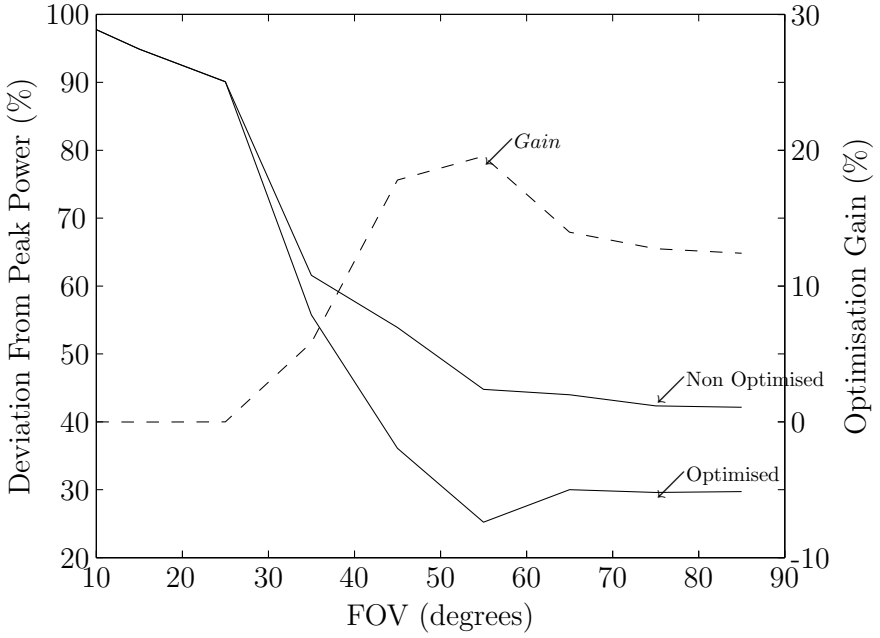

(a)

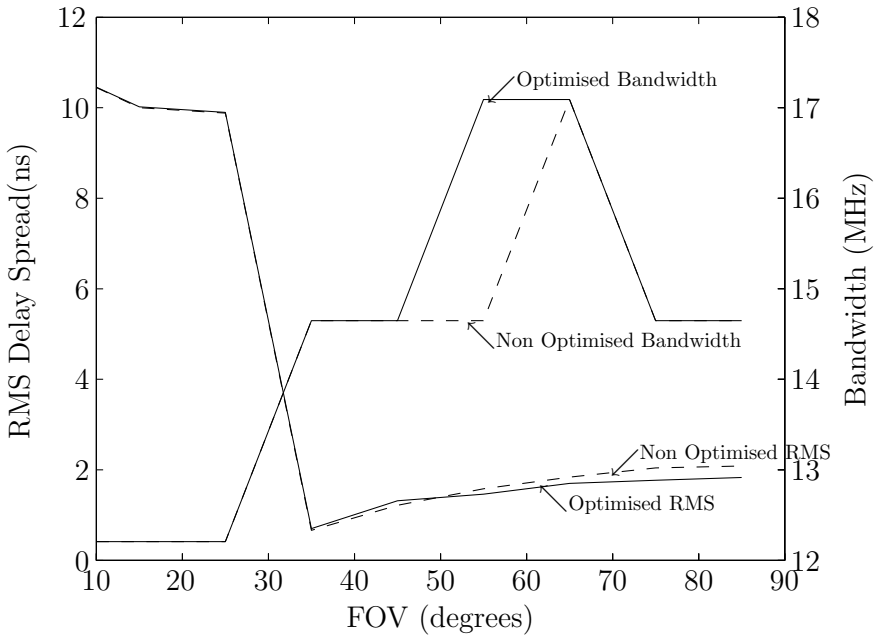

(b)

Figure 3.6: GA performance for 9 spots and varying receiver FOV. (a) Power. (b) Bandwidth and RMS delay spread.

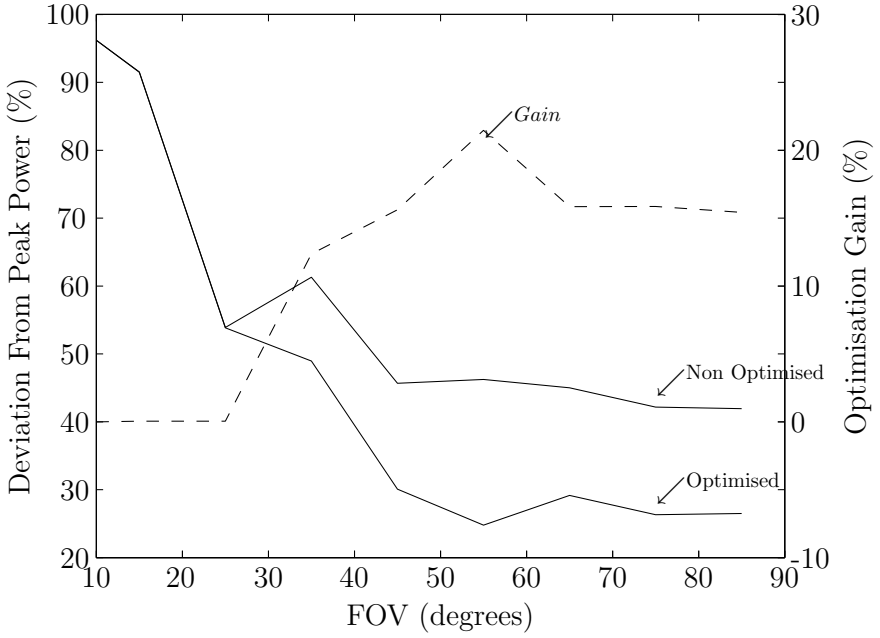

(a)

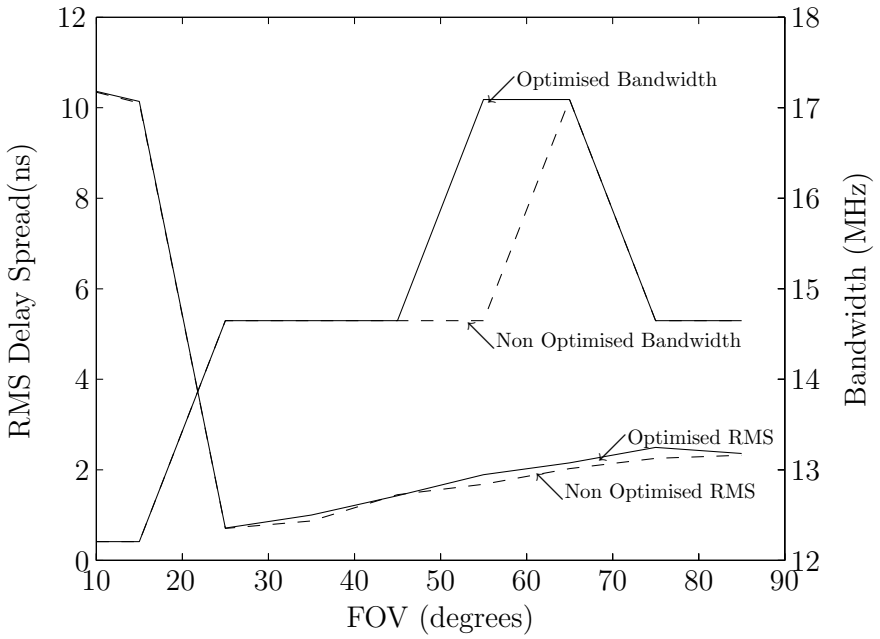

(b)

Figure 3.7: GA performance for 16 spots and varying receiver FOV. (a) Power. (b) Bandwidth and RMS delay spread.

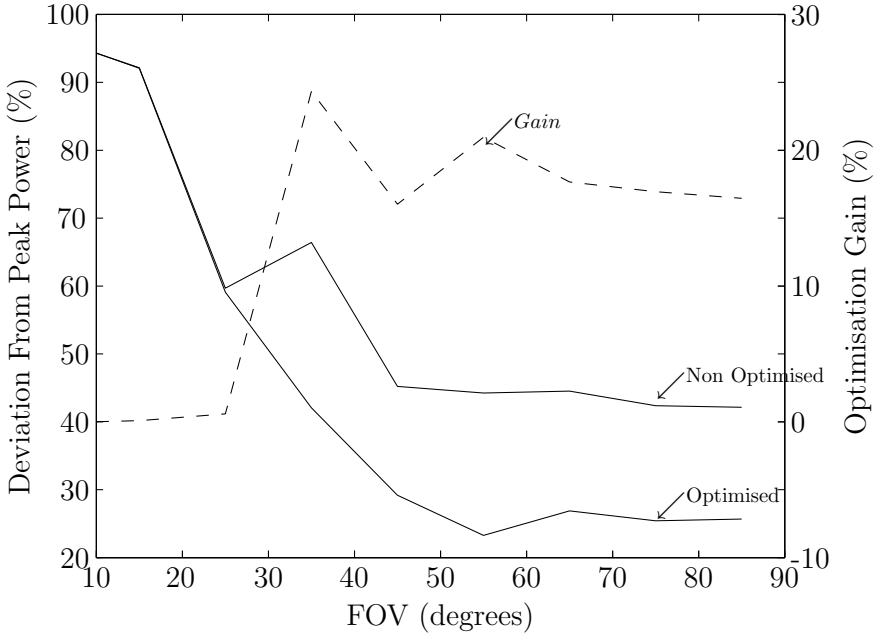

(a)

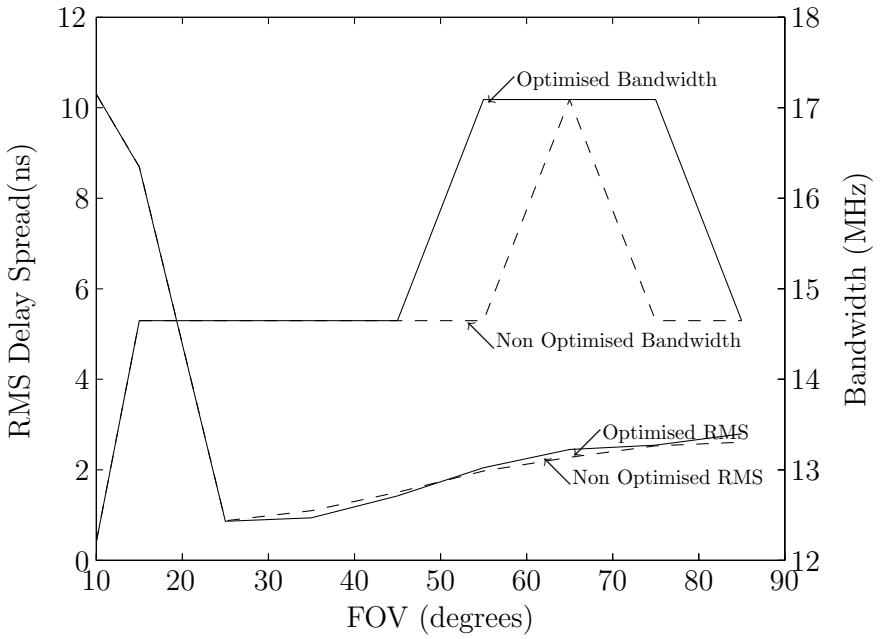

(b)

Figure 3.8: GA performance for 25 spots and varying receiver FOV. (a) Power. (b) Bandwidth and RMS delay spread.

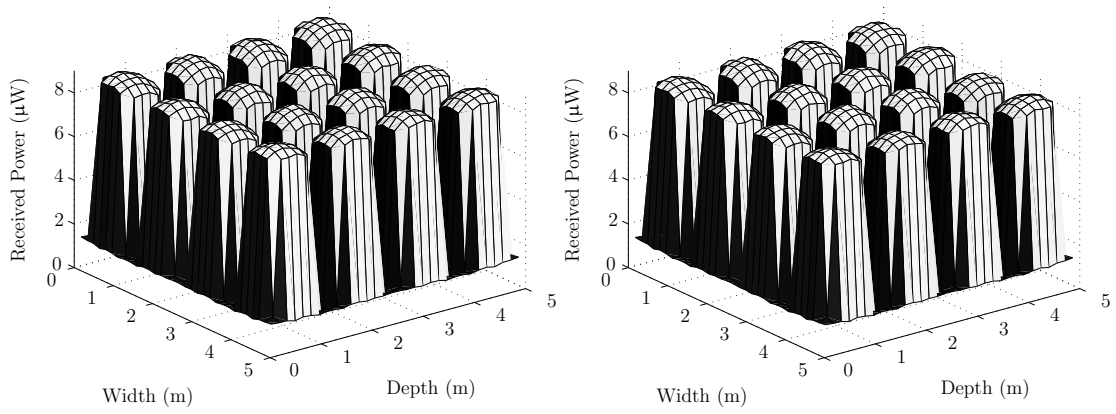

(a) (b)

Figure 3.9: Illustrative examples of GA performance for $I = 16$, $\text{FOV}_{\mathcal{R}_j} = 15°$. (a) Non optimised power. (b) Optimised power.

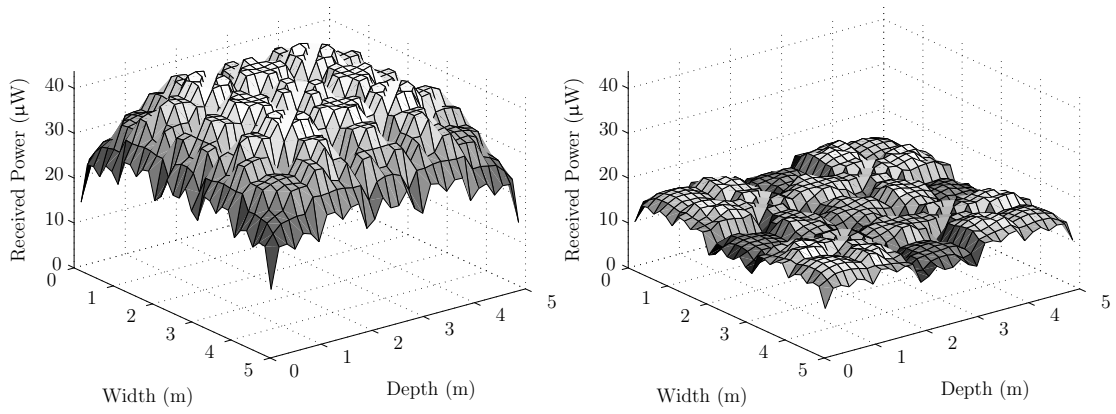

(a) (b)

Figure 3.10: Illustrative examples of GA performance for $I = 25$, $\text{FOV}_{\mathcal{R}_j} = 35°$. (a) Non optimised power. (b) Optimised power.

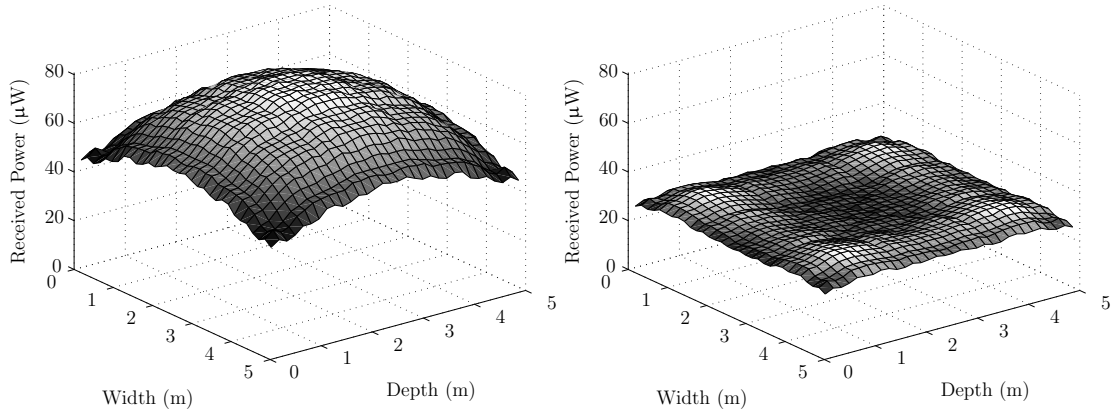

(a) (b)

Figure 3.11: Illustrative examples of GA performance for $I = 25$, $\text{FOV}_{\mathcal{R}_j} = 55°$. (a) Non optimised power. (b) Optimised power.

35.7 μW, (44%). After the optimisation, as in figure 3.11(b), the power ranges from between 25.9 μW and 33.8 μW, a deviation of 7.90 μW, (23%). This is the configuration that provides the lowest achievable deviation from peak power after optimisation, although, as can be seen from figures 3.7(a) and 3.8(a) for 16 and 25 spots and a $\text{FOV}_{\mathcal{R}_j} > 75°$, it is possible to get close to the lowest deviation from peak power.

As in previous results, using the GA to reduce the power deviation around the room has negligible effects on worst case bandwidth and RMS delay spread, as shown in figures 3.6(b), 3.7(b) and 3.8(b) for $9, 16$ and 25 spots respectively under varying $\text{FOV}_{\mathcal{R}_j}$. It can be seen that the optimised bandwidth and RMS delay spread remain within 2.4 MHz and 0.27 ns respectively from the non optimised case.

3.6 Including the Moving Person

To begin the investigation into including a moving person within the room, 9 positions were set up within the environment as shown in figure 3.12. Using the intersection algorithm of section

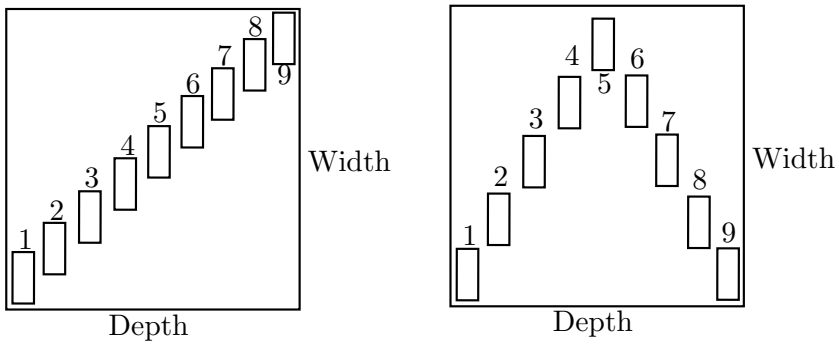

Figure 3.12: Movement Positions of the Person. (a) Movement pattern 1. (b) Movement pattern 2.

2.4, an solid block, representing a person, of depth (chest to back) 0.4 m, depth (shoulder to shoulder) 0.7 m and height 1.8 m was placed sequentially at each of the positions. Tabulated positional coordinates can be seen in appendix C, along with the room data. Each step was carried out discretely, as it has been shown in section 2.3 that the user does not move fast enough to force the effects of multipath fading. Referring to figure 3.13(a), for the scenario of a $\text{FOV}_{\mathcal{R}_j} = 45°$ in room 1 with movement pattern 1, as in figure 3.12 (a), when empty, the non optimised power distribution has a deviation of 45%, which, upon instigation of user movement, is perturbed by up to 29% with a range of 28% as the deviation varies between 46% and 74%. Using the optimisation with algorithm 6, the deviation is reduced 16% to 29% when empty, and the perturbation is reduced 2% to 27% as the range is reduced 5% to 23% as it varies between 33% and 56%.

Considering the case of the $\text{FOV}_{\mathcal{R}_j} = 55°$ receiver in room 1, with movement pattern 1 as shown in figure 3.13(b). When empty, the power deviation is 44%, which is perturbed through user movement by up to 32%, with a range of 32% between 44% and 76%. Using algorithm 6, when empty, the deviation is reduced 21% to 23% and the maximum perturbation is increased 2% to 34%, as the range is reduced 7% to 25% as it varies between 32% and 57%.

The results shows some consistency with earlier findings, such as the $\text{FOV}_{\mathcal{R}_j} = 55°$ achieved a higher gain, and lower deviation than $\text{FOV}_{\mathcal{R}_j} = 45°$, but one thing seemed not quite right. When looking at the results, the use of the fixed receiver location and the use of the moving person, meant that occasionally, as in the position 9 for example, the receiver was literally on the edge of the person, within 1 cm. Referring to figure 3.14, it appears that these positions affect the metric of power deviation, which is fed back to the GA, which alters the ratios, and, as such, is not performing quite as well as it should be.

3.7 Adding the Exclusion Zone

Now knowing that the fixed layout grid positions of the receivers causes the improper results to be fed back to the GA, it is necessary to add an exclusion zone around the object, as, in theory, a handheld device would probably not be located that close. Taking a reasonable assumption that, if the average breath of a male hand is 9 cm [154], an exclusion zone of 10 cm would be set up, as this is the closest distance a receiver could be located when held against the body. The results of section 3.6 were re-simulated to incorporate the addition of the exclusion zone. It is beneficial to refer to figures 3.15 and 3.16, which show the respective time shifted power distributions of room 1 with movement pattern 1 for the case of the $\text{FOV}_{\mathcal{R}_j} = 55°$ under 25 diffusion spots, before and after optimisation with algorithm 6.

Referring to figure 3.17(a), which shows the deviation from peak power for room 1 with, $\text{FOV}_{\mathcal{R}_j} = 45°$ receivers under movement pattern 1, when empty the power deviation is 45%, which, upon user movement, is perturbed up to 15% within a range of 14%, between 46% and 60%. After optimisation, the power deviation of the empty room is reduced 16% to 29%, and the maximum perturbation is reduced 5% to 10%, as the range is reduced 4% to 10% when it varies between 29% and 39%.

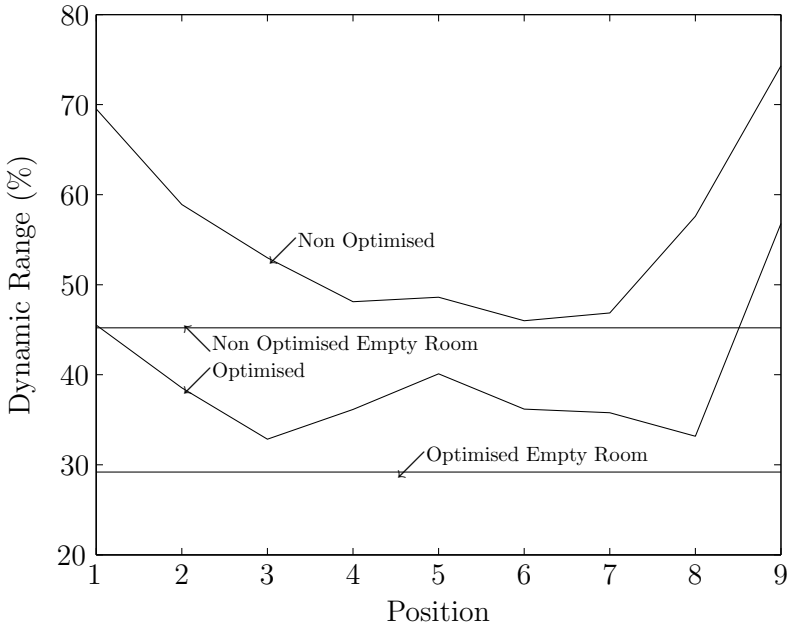

(a)

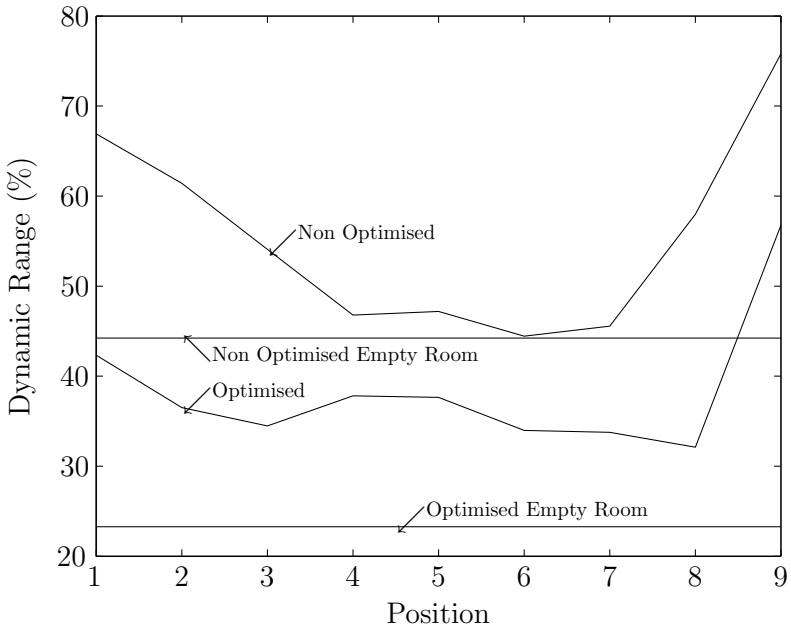

(b)

Figure 3.13: Power distribution in two dynamic scenarios. (a) Environment 1 with $\text{FOV}_{\mathcal{R}_j} = 45°$. (b) Environment 1 with $\text{FOV}_{\mathcal{R}_j} = 55°$.

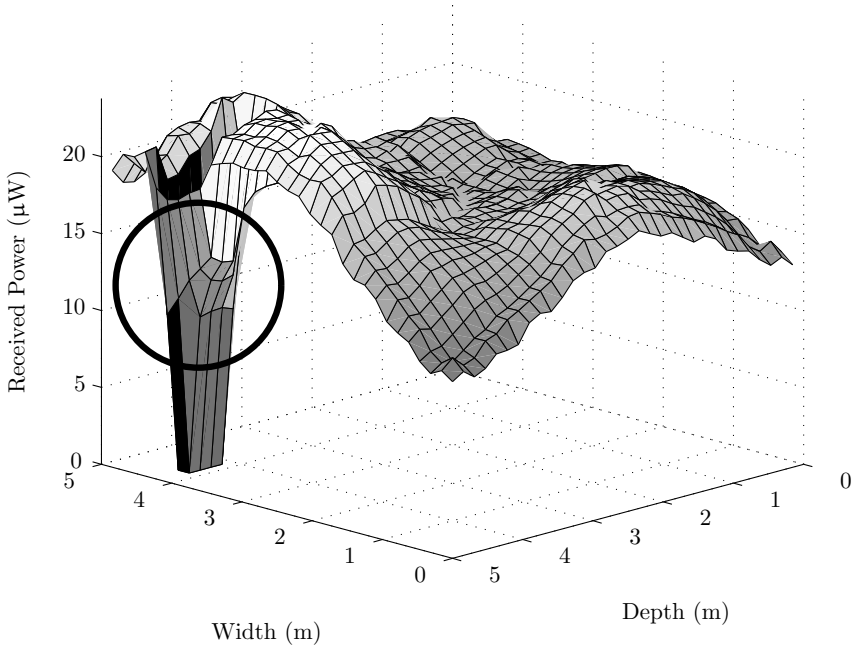

Figure 3.14: Receiver to object proximity power distribution disturbance.

Referring to figure 3.18(a), which shows the deviation from peak power for room 1 with, $\text{FOV}_{\mathcal{R}_j} = 55°$ receivers under movement pattern 1, when empty the power deviation is 44%, which, upon user movement, is perturbed up to 17% within a range of 18%, between 43% and 61%. After optimisation the power deviation of the empty room is reduced 21% to 23%, and maximum perturbation is reduced 4% to 13%, as the range is reduced 8% to 10% when it varies between 26% and 36%.

The optimisation of the power deviation has an effect upon the bandwidth and the RMS delay spread, as in figures 3.17(b) and 3.18(b) which show the non optimised bandwidth (NOB), non optimised RMS delay spread (NOrms), optimised bandwidth (OB), and optimised RMS delay spread (Orms) when the room is empty (/E), and with movement (/M) for the $\text{FOV}_{\mathcal{R}_j} = 45°$ and $\text{FOV}_{\mathcal{R}_j} = 55°$ rooms respectively. For the case of $\text{FOV}_{\mathcal{R}_j} = 45°$, the worst case bandwidth before and after optimisation are within 3 MHz, whilst the RMS delay spread is less than 0.2 ns

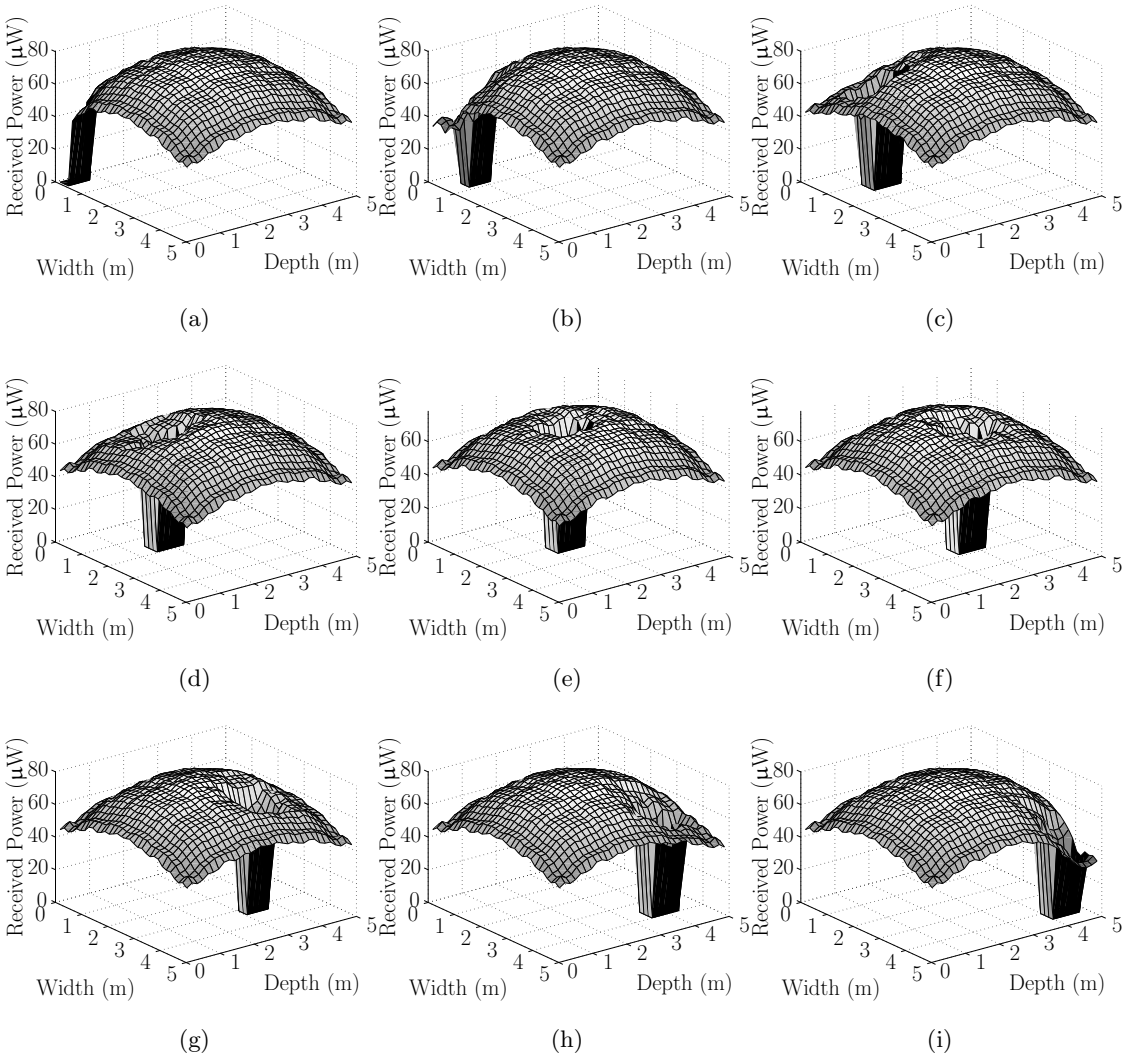

Figure 3.15: Non optimised power distribution for the 9 movement positions, in environment 1, movement pattern 1, $\text{FOV}_{\mathcal{R}_j} = 55°$ under 25 diffusion spots.(a) to (i) refer to positions 1 to 9.

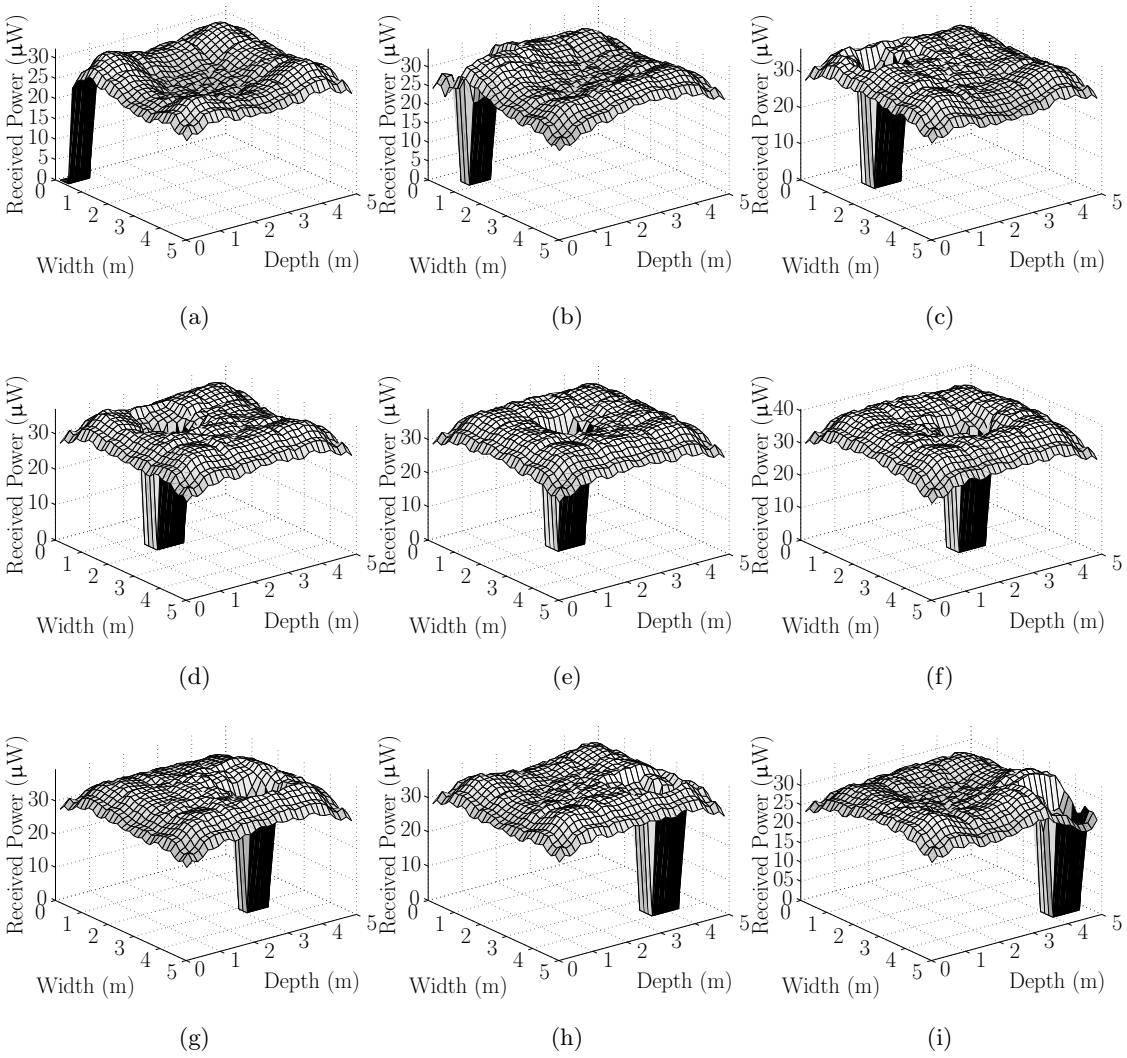

Figure 3.16: Optimised power distribution for the 9 movement positions, in environment 1, movement pattern 1, $\text{FOV}_{\mathcal{R}_j} = 55°$ under 25 diffusion spots. (a) to (i) refer to positions 1 to 9.

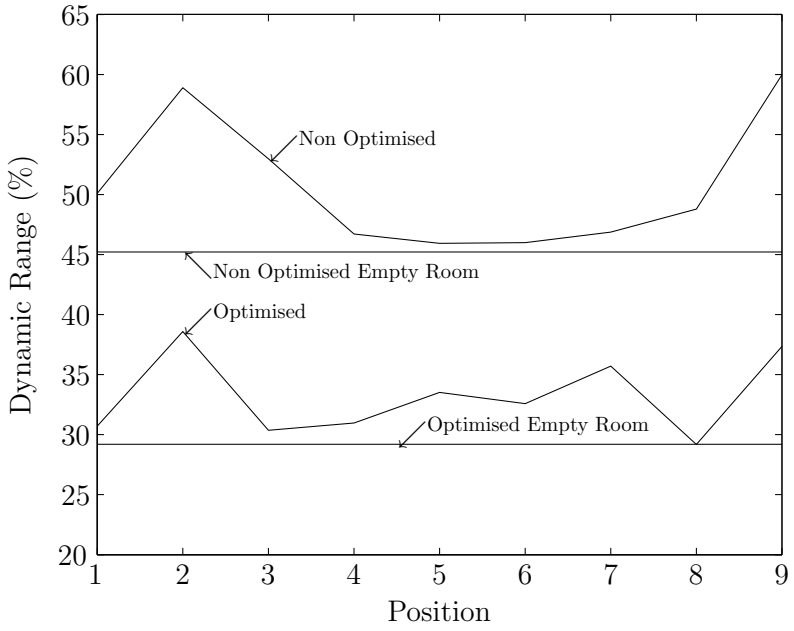

(a)

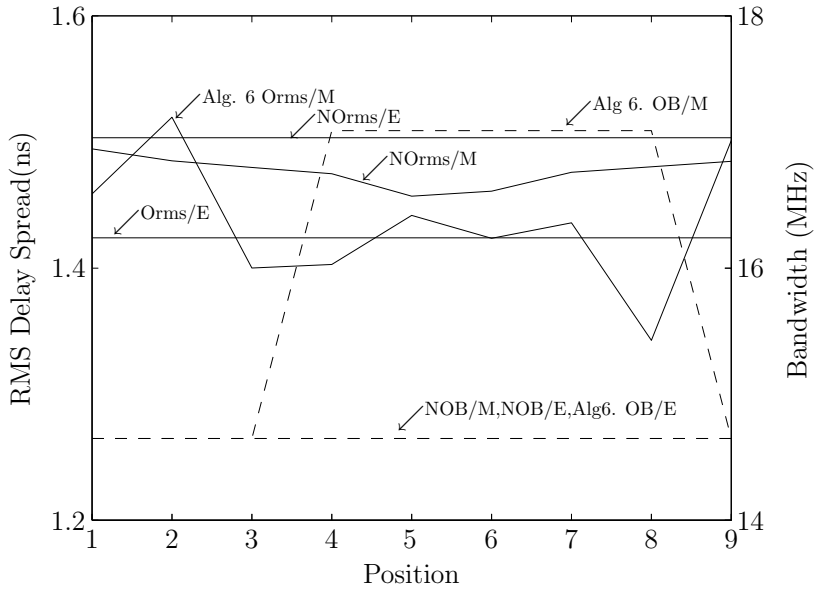

(b)

Figure 3.17: Dynamic environment 1, movement pattern 1, $\text{FOV}_{\mathcal{R}_j} = 45°$, $I = 25$. (a) Power. (b) Bandwidth and RMS delay spread.

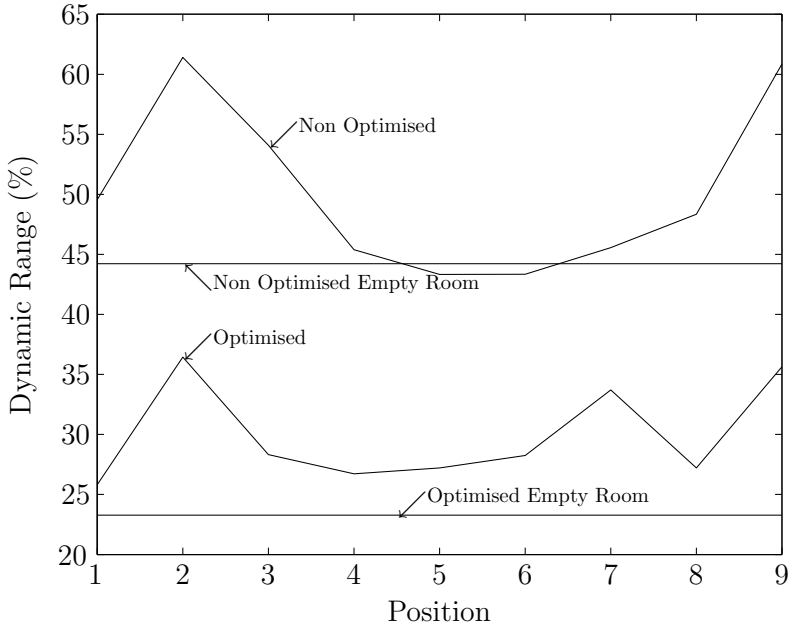

(a)

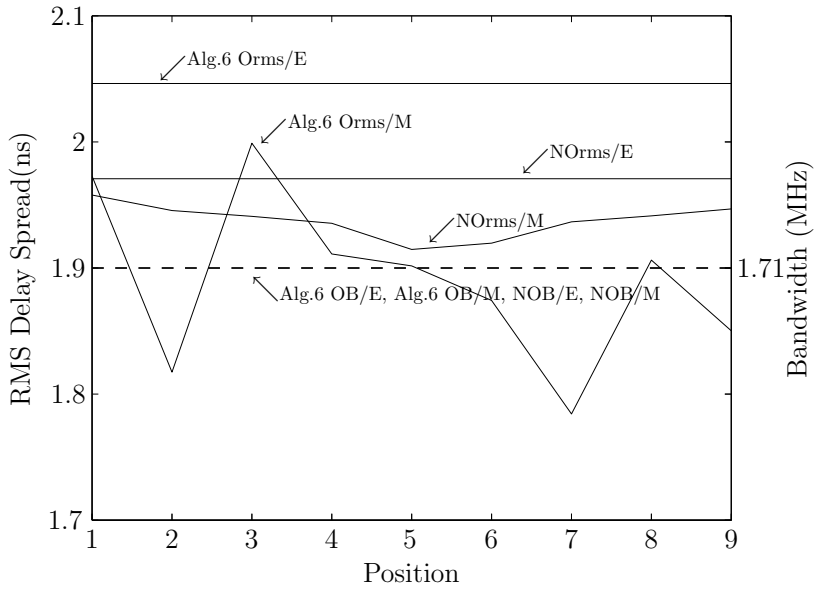

(b)

Figure 3.18: Dynamic environment 1, movement pattern 1, $\text{FOV}_{\mathcal{R}_j} = 55°$, $I = 25$. (a) Power. (b) Bandwidth and RMS delay spread.

over all movement positions. For the case of the $\text{FOV}_{\mathcal{R}_j} = 55°$, the worst case bandwidth is the same both before and after optimisation, whilst the RMS delay spread is within 0.3 ns.

3.8 A Second Room and a Second GA

Now that the GA has been shown to work, and is capable of adapting the power distribution to the scenarios presented, it would also be suitable at this stage to test a second environment with a person moving in a different movement pattern, as in figure 3.12 (b). The use of the receiver with a $\text{FOV}_{\mathcal{R}_j} = 55°$ is maintained, but room 2 is defined to be the same as environment 1, but where the reflectivity of the ceiling is reduced to $\rho = 0.75$, the north wall reduced to $\rho = 0.7$ and the east wall reflectivity reduced to $\rho = 0.6$. Furthermore, whereas algorithm 6 is considered to be the best global search algorithm, algorithm 11 in table 3.1 is also tested as it is based upon a tournament 3 selection scheme. This selection scheme should be more practical to implement within hardware as is does not require the computation of proportional fitness assignments and uses a lower population.Furthermore as has been shown in table 3.1 it is still able to find solutions to within a few percent of what is considered to be the global optimum solution.

Referring to figure 3.18(a), which shows the deviation from peak power for room 1 with, $\text{FOV}_{\mathcal{R}_j} = 55°$ receivers under movement pattern 1, when empty the power deviation is 44%, which, upon user movement, is perturbed up to 17% within a range of 18% between 43% and 61%. After optimisation the power deviation of the empty room is reduced 21% to 23%, and maximum perturbation is reduced 4% to 13%, as the range is reduced 8% to 10% when it varies between 26% and 36%.

Referring to figure 3.19(a), applying algorithm 11 to our established environment of room 1, movement pattern 1 with $\text{FOV}_{\mathcal{R}_j} = 45°$ receivers, a comparison can be made between this algorithm and algorithm 6. As before, when empty, the power deviation is 45%, which upon

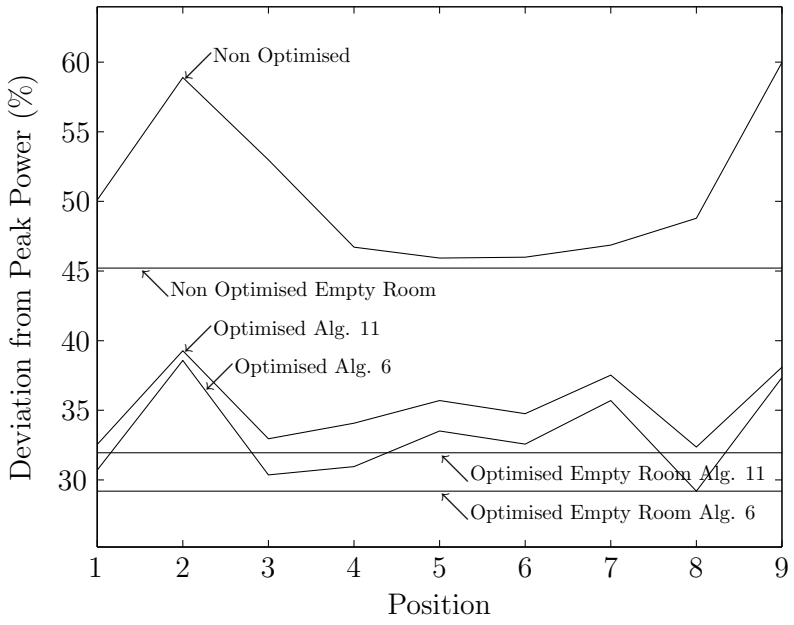

(a)

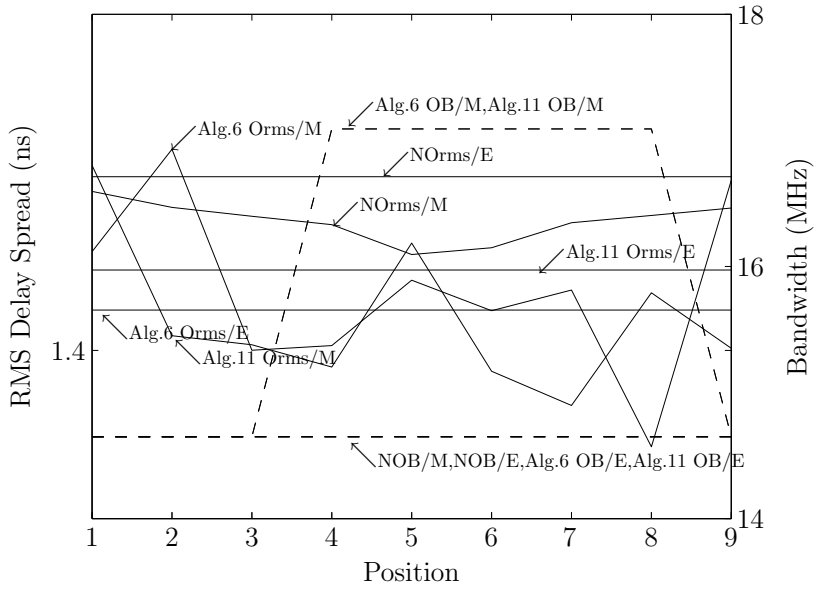

(b)

Figure 3.19: Comparison of algorithms 6 and 11 for room 1, MP 1, $\text{FOV}_{\mathcal{R}_j} = 45°$. (a) Power.(b) Bandwidth and RMS.

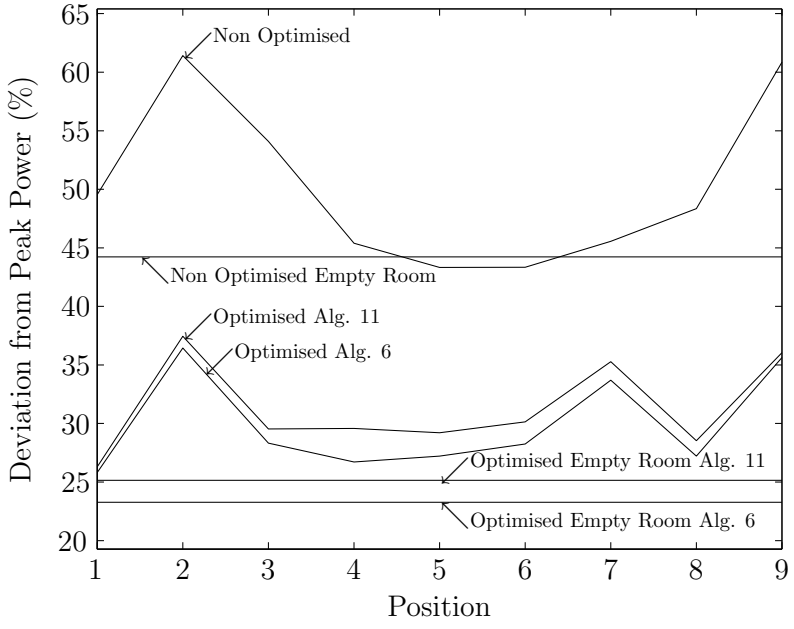

(a)

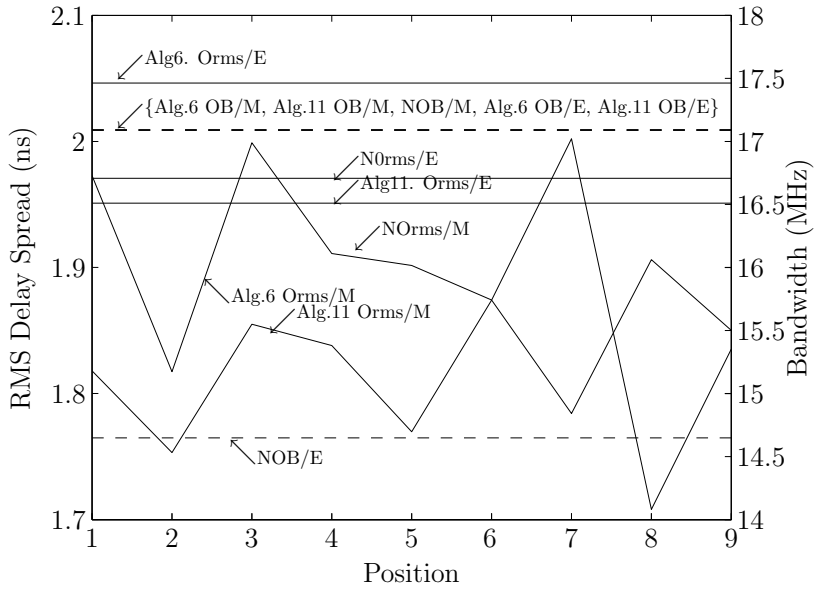

(b)

Figure 3.20: Comparison of algorithms 6 and 11 for room 1, MP 1, $\text{FOV}_{\mathcal{R}_j} = 55°$. (a) Power.(b) Bandwidth and RMS.

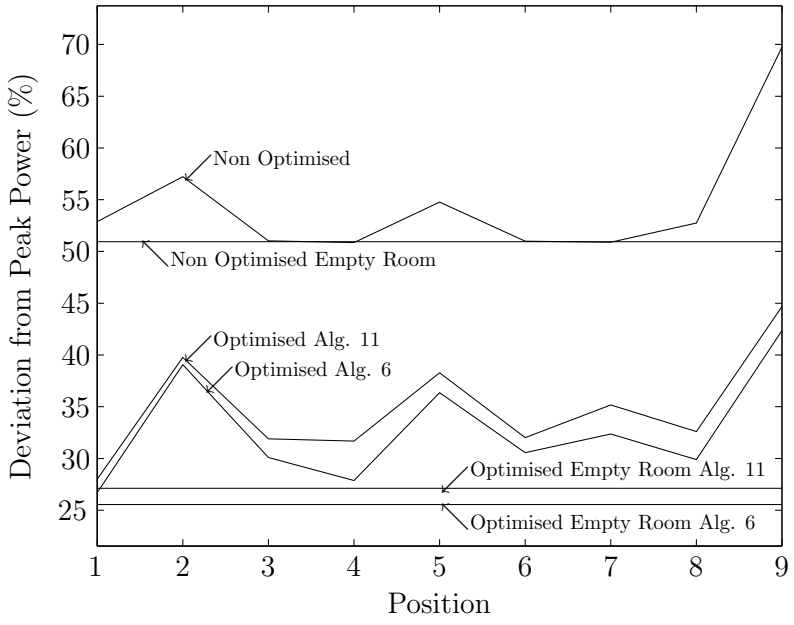

(a)

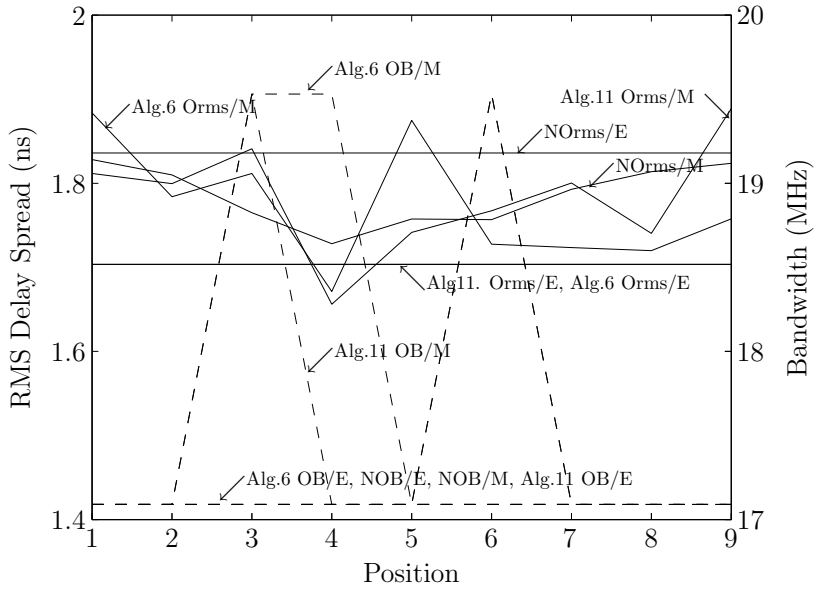

(b)

Figure 3.21: Comparison of algorithms 6 and 11 for room 2, MP 2, $\text{FOV}_{\mathcal{R}_j} = 55°$. (a) Power.(b) Bandwidth and RMS.

user movement is perturbed up to 15% within a range of 14% between 46% and 60%. After optimisation, the power deviation of the empty room is reduced 13% to 32%, and maximum perturbation is reduced 8% to 7%, as the range is reduced 8% to 7% when it varies between 32% and 39%. Algorithm 11, in this case has managed to reduce perturbation and the range of variation greater than algorithm 6 but is not as effective with the empty room.

Referring to figure 3.20(a), which shows the deviation from peak power for a room with, $\text{FOV}_{\mathcal{R}_j} = 55°$ receivers under movement pattern 1, when empty the power deviation is 44%, which, upon user movement, is perturbed up to 17% within a range of 18% between 43% and 61%. After optimisation using algorithm 11 the power deviation of the empty room is reduced 19% to 25%, and maximum perturbation is reduced 5% to 12%, as the range is reduced 7% to 11% when it varies between 26% and 37%. In this scenario, algorithm 11 is is approximately equal in its ability to reduce perturbation and range of variation compared to algorithm 6.

Referring to figure 3.21(a) in the case of the second room which is undergoing movement pattern 2, when empty the power deviation is 51%, which upon user movement is perturbed up to 19% within the range of 19% between 51% and 70%. After optimisation with algorithm 6 the power deviation of the empty room is reduced 25% to 26%, and the maximum perturbation is reduced 3% to 16%, as the range is reduced 4% to 15%, as it varies between 27% and 42%.After optimisation with algorithm 11 the power deviation of the empty room is reduced 24% to 27%, and the maximum perturbation is reduced 1% to 18%, as the range is reduced 2% to 17%, as it varies between 27% and 45%. In this scenario algorithm 6 is more effective by a few % in all measures of optimisation, which is showing good consistency of results and abilities.

Whilst the aim was to try and optimise the power distribution, the worst case bandwidth and RMS delay spread can be seen in figures 3.19(b) 3.20(b) 3.21(b), whereby for all the scenarios the bandwidth and RMS delay spread of the non optimised and optimised scenarios remain

within less than 2.5 MHz and less than 0.3 ns of each other, showing there is virtually no penalty to using the GA.

3.9 Conclusion

This chapter has provided the theoretical background of how a GA can be used to optimise the impulse response of the channel. The structure of the GA, including representation, fitness function, selection and mutation rates were examined against the original goal of creating a received power distribution with as little deviation as possible. After the analysis, two algorithms, one based upon SUS selection, and one based on tournament 3 selection, were seem to be strong candidates. Based upon the results from the two chosen algorithms, the receivers FOV was adjusted to find a complementary performance optimum between algorithm performance and a single receiver design. The algorithms were then tested in new scenarios, introducing two moving persons, with further successful demonstrations of the GA concept.

Chapter 4

Further Results and Relationships

4.1 Introduction

Chapter 3 established that the GA is an effective technique of reducing the received power deviation within an environment for which an OW system is deployed. There are two remaining tasks, or challenges, that need to be completed to provide a good enough justification of the algorithms effectiveness and user friendliness. Firstly, the the performance of the algorithm must be extended to larger environments, changes in the environments reflectivity characteristics and changes in user movement. Secondly, although the scenarios so far, have assumed the receiver is vertically aligned, it is inevitable that the user will also cause a change in the direction the receiver is pointing [155, 156, 157]. At this stage of the work, the movement algorithm will be modified to allow the receiver to randomly align, within some justifiable parameters, and the GA will be subjected to this channel alteration. To begin the chapter, the room will be expanded, followed by a small investigation into how receiver alignment affects the respective channel performance characteristics and the GA optimisation performance. This optimisation performance analysis will be coupled with another receiver FOV analysis to further clarify the validity of previous results. Finally the results are extended to encompass multiple users in multiple environments.

4.2 Expanding the Environment

A new large environment, environment 3, is generated with width $X_e = 6\,\text{m}$, depth $Y_e = 6\,\text{m}$ and height $Z_e = 3\,\text{m}$. The ceiling and walls have a reflectivity $\rho = 0.8$, whilst the floor has a reflectivity $\rho = 0.3$. Another environment, environment 4 was also established with the same dimensions as environment 3, but where the reflectivity of the ceiling, north wall and east wall have been reduced to 0.75, 0.7 and 0.6 respectively. These reflectivity values are commonly assumed to be representative of indoor materials, [158, 87, 85]. Within both environments, on the ceiling, 25 uniformly-distributed diffusion spots are formed, and, as before 1024 receivers are uniformly distributed, oriented vertically upwards at a height of 1 m. Each receiver has a $\text{FOV}_{\mathcal{R}_j} = 55°$, and active collection area of $A_{\mathcal{R}} = 1\,\text{cm}^2$.

Room 3, as can be seen in figure 4.1(a), shows the non optimised power deviation which varies from a 59.4 µW to 31.4 µW a deviation of 28.0 µW, or 47%. The bandwidth, figure 4.1(c) varies between 14.6 MHz to 61 MHz, whilst the RMS delay spread varies, 4.1(e), varies between 0.937 ns to 1.82 ns. Upon optimisation of the empty room environment using algorithm 6, the power, figure 4.1(b) now ranges from 22.2 µW to 30.3 µW, a deviation of 8.1 µW or 26%, resulting in an optimisation gain of 21%. The bandwidth, figure 4.1(d) varies between 14.6 MHz and 48.8 MHz, thus the worst case has achieved no penalty whilst the top end has lost 12.2 MHz. The RMS delay spread, figure 4.1(f), varies between 0.68 ns and 2.16 ns, which is an improvement in the worst case scenario of ≈ 0.3 ns.

Adding movement to environment 3 with movement pattern 1, as shown in figure 4.2(a), the non optimised empty room power deviation is 47%, which, upon user movement, is perturbed by up to 13%, with a range of 15% between 45% and 60%. After optimisation with algorithm 6, the empty room deviation is reduced by 21% to 26%, with the maximum perturbation being

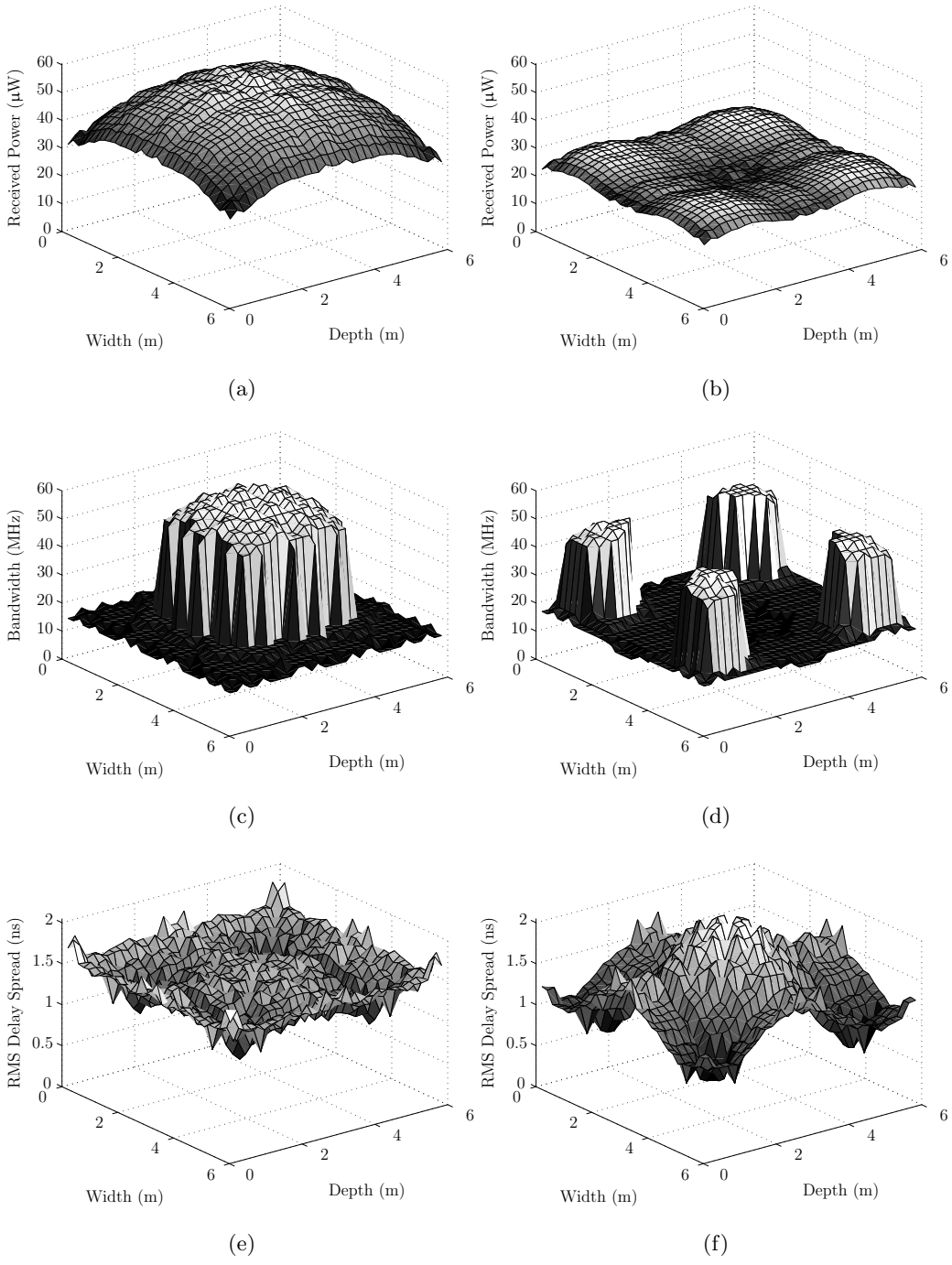

Figure 4.1: Algorithm 6 optimisation of environment 3. Power: (a) non optimised, (b) optimised power. Bandwidth: (c) non optimised, (d) optimised. RMS delay spread: (e) non optimised, (f) optimised.

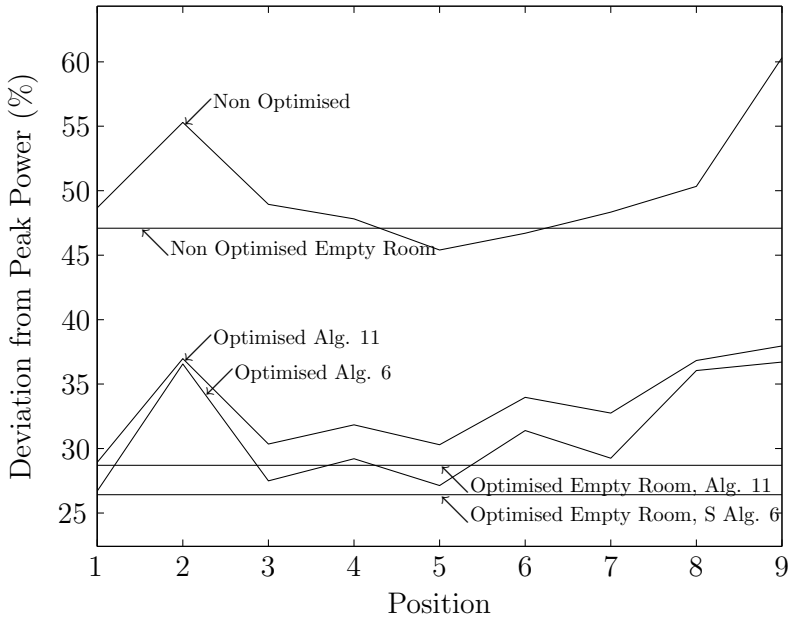

(a)

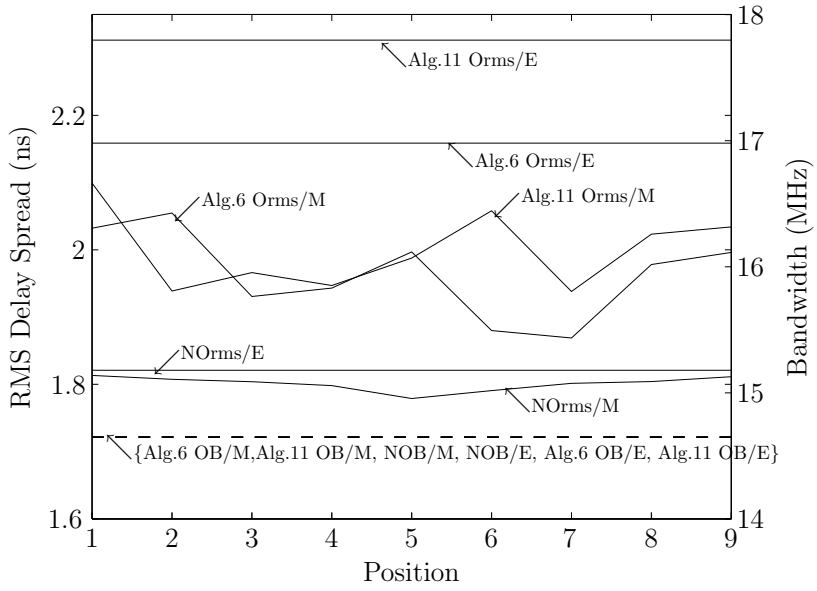

(b)

Figure 4.2: Optimisation of environment 3 with algorithms 6 and 11 respectively. (a) Deviation from peak power. (b) Bandwidth and RMS delay spread.

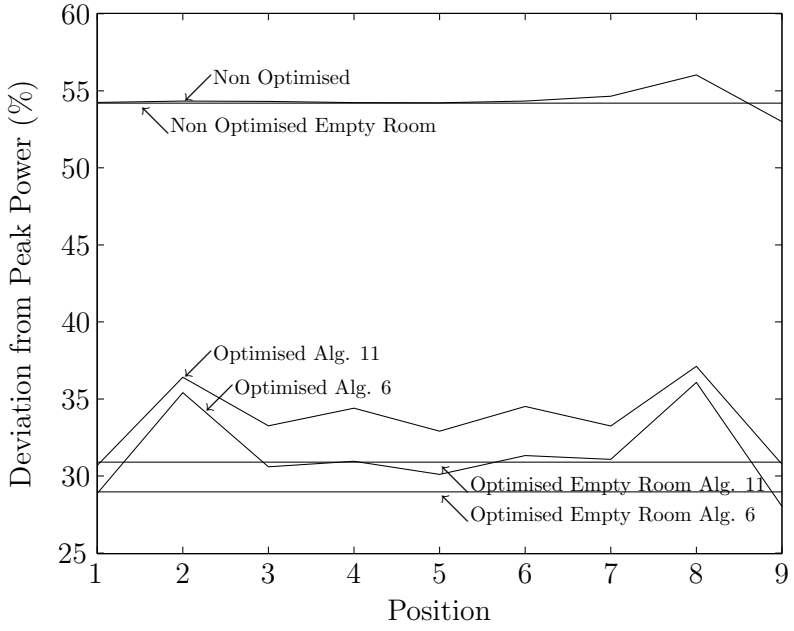

(a)

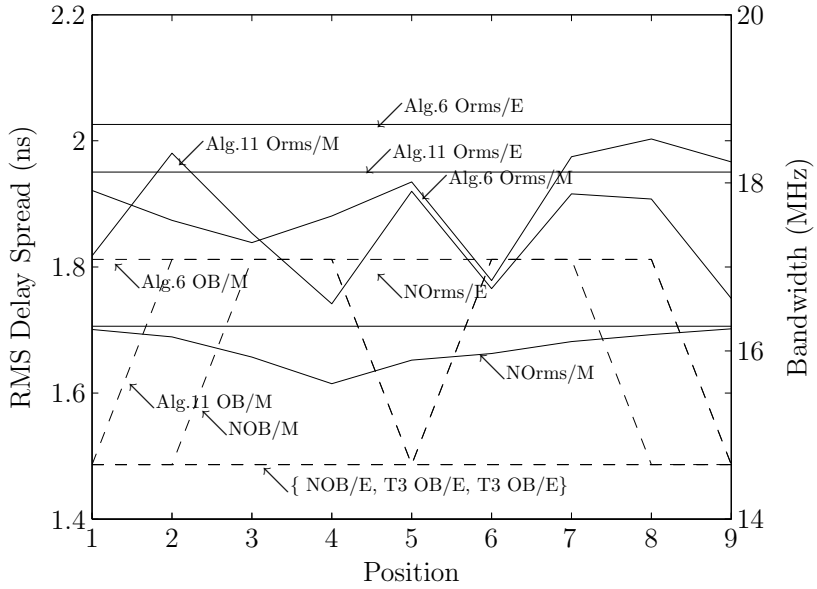

(b)

Figure 4.3: Optimisation of environment 4 with algorithms 6 and 11 respectively. (a) Deviation from peak power. (b) Bandwidth and RMS delay spread.

reduced 2% to 11%, as the range is reduced 5% to 10% as it varies between 27% and 37%. Using algorithm 11, the the empty room deviation is reduced by 18% to 29%, with the maximum perturbation being reduced 4% to 9%, as the range is reduced 6% to 9%, as it varies between 29% and 38%.

Adding movement to environment 4 with movement pattern 2, as shown in figure 4.3(a), the non optimised empty room power deviation is 54%, which, upon user movement, is perturbed by upto 2%, with a range of 2% between 54% and 56%. After optimisation with algorithm 6, the empty room deviation is reduced by 25% to 29%, with the maximum perturbation being increased 5% to 7%, as the range is increased 6% to 8% as it varies between 28% and 36%. Using algorithm 11, the the empty room deviation is reduced by 23% to 31%, with the maximum perturbation being increased 4% to 6%, as the range is increased 4% to 6% as it varies between 31% and 37%.

An interesting observation should be noted regarding figure 4.3(a). The non optimised power deviation when empty and with user movement is almost identical except at positions $7, 8$ and 9. It could be considered an anomaly that the user does not perturb the power distribution, and, if this analysis only focused on this room, the use of the GA, may seem unnecessary. However, the fact that this specific room configuration was stumbled upon, can also serve as a good example to highlight the need for the GA optimisation in the first place. Without the GA optimisation, the system employed has shown a high level of variability, within the two environments, but with the GA, the received power distribution is now very consistent.

Therefore even in scenarios where the user induced received power perturbation is very small, and even though the GA has essentially increased this perturbation for environment 4, the overall reduction can still be considered beneficial, and most importantly from a receiver design point of view, the power distribution is consistent. It is not possible to define the exact number of

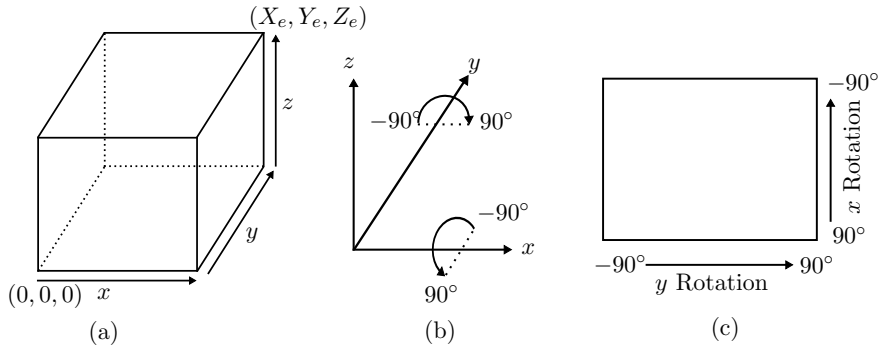

Figure 4.4: Receiver orientation coordinate system. (a) Room orientation. (b) Axis rotation. (c) Plot rotation representation.

possible room configurations that may exhibit this immunity to user movement, but the author considers them to be less in number than the number of rooms that are not, and so to have a small number of over engineered systems employing a GA where it is not needed, is better than a large number of systems not using them. It is of course noteworthy to remember that these environments are not only dynamic in terms of short term effects like user movement, but can be dynamic over longer periods of time, should for example the carpet be removed and a wooden floor be installed.

From figure 4.2(b) the worst case bandwidth is unaffected, whilst the RMS delay spread, for the optimised and non optimised case are within 0.5 ns of each other. For room 4 with movement pattern 2, the bandwidth of the optimised and non optimised cases are within 2.4 MHz of each other, whilst the RMS delay spread is within 0.4 ns of each other.

4.3 Varying Receiver Orientation

As with the object intersection algorithm of section 2.4, the programming conventions used throughout this work are based on techniques adapted from computer graphics applications.

In order to introduce to the simulation software the ability to investigate receiver alignment, another algorithm, founded upon 3D transformations was applied [159]. The simulations room coordinate system can be seen in figure 4.4 (a), with vectors x, y and z shown in the respective normal directions. By convention, all computer graphics orientation is carried out under the assumption that a positive rotation is counter clockwise about the axis normal as it is viewed [160], as shown in figure 4.4 (b). Figure 4.4 shows the coordinate system of the way in which many of the results are plotted. It can be seen that a y rotation is plotted in what would normally be used for x positional vectors, and similarly x rotation replaces the y positional vectors.

The rotation process is carried out discretely, consecutively for each axis in turn, but is independent of the order. As the receiver is already assumed to have a unit length direction vector, for example a vertically orientated receiver has direction vector $[x, y, z] = [0, 0, 1]$, the resultant rotated direction vector is also a unit length and is still compatible with the theory of section 2.3. To rotate an angle θ about the x axis.

$$y' = y\cos\theta - z\cos\theta \tag{4.1}$$

$$z' = y\sin\theta + z\cos\theta \tag{4.2}$$

$$x' = x \tag{4.3}$$

Where the x', y', z' equals the new vector coordinates. To rotate about the y axis

$$z' = z\cos\theta - x\sin\theta \tag{4.4}$$

$$x' = z\cos\theta + x\cos\theta \tag{4.5}$$

$$y' = y \tag{4.6}$$

And to rotate about the z axis

$$x' = x\cos\theta - y\sin\theta \tag{4.7}$$

$$y' = x\cos\theta + y\cos\theta \tag{4.8}$$

$$z' = z \tag{4.9}$$

In this work, z axis rotation is not performed. To visualise why, consider the hypohthectical situation of the dial of a wristwatch being the photodiode area. The x and y axis rotation govern who in the room could see the time, whilst the z rotation only serves to confuse the onlooker as to whether time is 12 and 6 o'clock. Thus z axis rotation does not affect the ability to convert incident infrared radiation into a current and can be ignored.

To illustrate the effects of x and y axis rotation on the received power and channel bandwidth and RMS delay spread, consider a single receiver with a $\text{FOV}_{\mathcal{R}_j} = 55^\circ$ and active collection area $A_{\mathcal{R}_j} = 1\,\text{cm}^2$ placed at a height of $x = 1\,\text{m}$ in the center of a new environment, environment 5, that has the same dimension as environment 3, but where the reflectivity of the walls is $\rho = 0.75$. It was then rotated $\pm 90^\circ$ around the x and y axis.

Referring to figure 4.5(a) which details the change in power distribution as the angle of the receiver is changed, the power peaks at 58.3 µW, reducing to 19.5 µW at the maximum tilt. This is a change of 38.8 µW, or a deviation of $\approx 67\%$ of the peak value. The bandwidth as shown, in figure 4.5(b), varies between 61.0 MHz and 12.2 MHz. The RMS delay spread, shown in figure 4.5(c), varies between 3.69 ns and 1.09 ns. The results show the system is very sensitive to angular orientation, whereby, the most preferential results are always obtained when the receiver is pointed vertically upwards towards the ceiling.

As there is a clear change in receiver power, with change in receiver alignment, it was decided to investigate how the channel and furthermore the GA can accommodate this real world problem. It has to be assumed that users of OW systems are aware that some level of transmitter-receiver alignment must exist to take advantage of the larger bandwidth availability compared to a RF system where freedom of user movement is invariably higher. It is therefore assumed that in general, a user, knowing the diffusion spots are on the ceiling, will at least attempt to orientate their hand held device towards it.

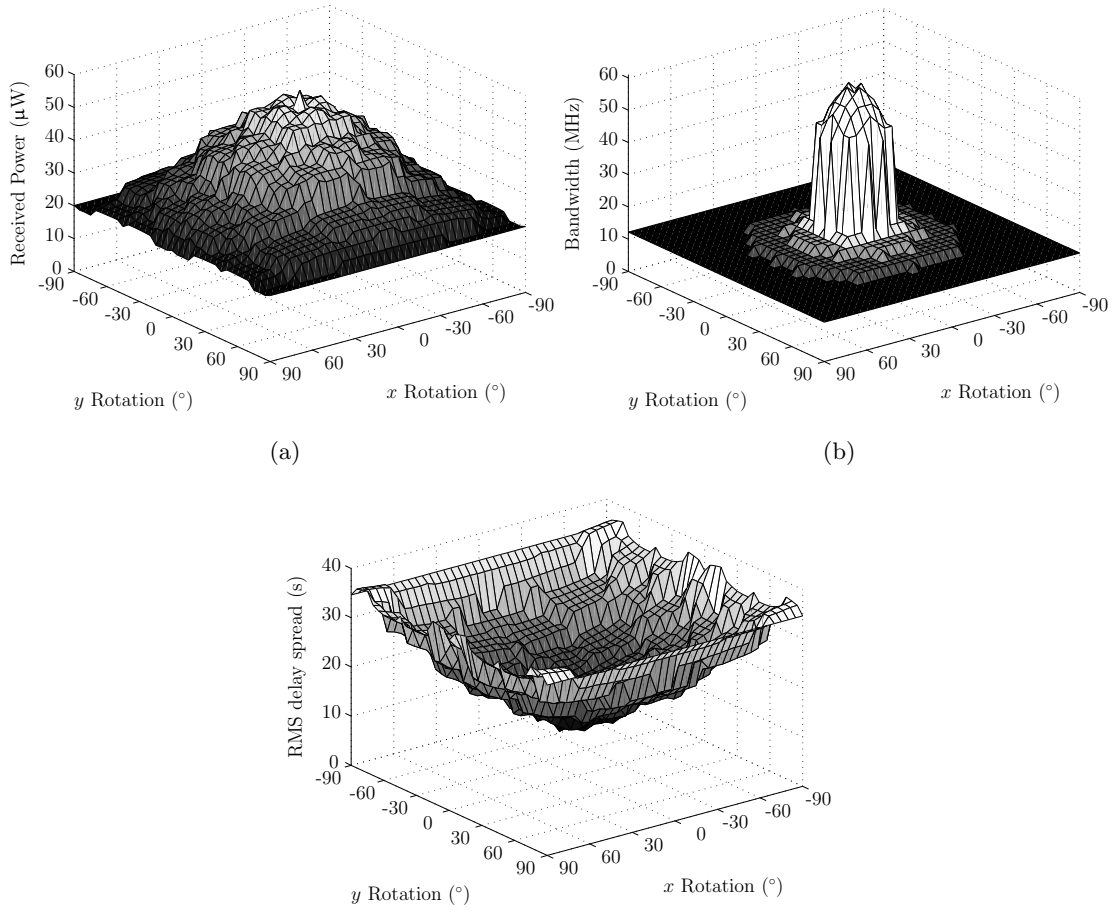

Figure 4.5: The x and y rotation affecting channel characteristics. (a) Received Power. (b) Channel Bandwidth. (c) Channel RMS delay spread.

Whilst figure 4.5 illustrated the results for $\pm 90°$ rotation, it gave little regard to what may be considered typical user behaviour. Five random variable normal distributions were formed with a mean $\bar{z} = 0$, (no rotation) and a standard deviation of $\sigma = \{7.8, 11.7, 19.5, 27, 35\}$ providing a respective 0.8 probability of rotation around an axis within $\pm\{10, 15, 25, 35, 45\}°$, and a 0.99 probability of being within $\pm\{20, 30, 50, 70, 90\}°$ from the unrotated case. Each axis of rotation in x and y was treated independently, but distributions were not mixed. Such that, for example, there was a 0.64 chance of both axes resulting in a rotation of $\pm 25°$, but scenarios that allowed

for the x axis to rotate with a probability of 0.8 within $\pm 15^\circ$ and the y axis to rotate with a probability of 0.8 within $\pm 45^\circ$ were not investigated.

Within environment 5, at a height of $z = 1\,\text{m}$, 1024 receivers with a $\text{FOV}_{\mathcal{R}_j} = 55^\circ$, were evenly distributed. Each receiver was allowed to randomly have an alignment as governed by the normal distribution described above with standard deviation $\sigma = 35$, which therefore allowed a maximum tilt of $\pm 90^\circ$ from the normal. The received power distribution, as seen in fugure 4.6(a), shows around the room, a variation ranging from between 10.4 µW and 56.9 µW, a huge deviation of 46.5 µW, or 82% of the peak value. The bandwidth, as in figure 4.6(c), varies between 12.2 MHz and 63.5 MHz, whilst the RMS delay spread, shown in figure 4.6(e), varies between 0.716 ns and 7.13 ns.

However, it is not just the numbers that should be highlighted, but emphasis should also be placed on the shape of the distribution. The large, almost instantaneous rise and falls from one position to the next highlight the channel susceptibility to receiver alignment. The typical centralised increase in bandwidth found in environments such as those in figures 2.10, 2.11 and 2.12, or 4.1 are gone, and replaced, sporadically, with peaks and valleys easily associated with a high bandwidth, only when the receiver is vertically, or close to vertically orientated.

Upon application of algorithm 6 to the transmitter powers, figure 4.6(b) shows that the optimisation has little effect. It appears the extreme conditions cannot be dealt with by the algorithm, such that alignment variation may be too random, with no pattern for the GA to evolve towards. The power varies between 6.39 µW and 29.1 µW, a deviation of 22.7 µW, or 78% of peak value, so only a 4% optimisation gain was achieved. The resultant optimised bandwidth and RMS delay spread in figures 4.6(d) and 4.6(f) vary between 12.2 MHz and 53.7 MHz, and 0.576 ns and 7.45 ns respectively.

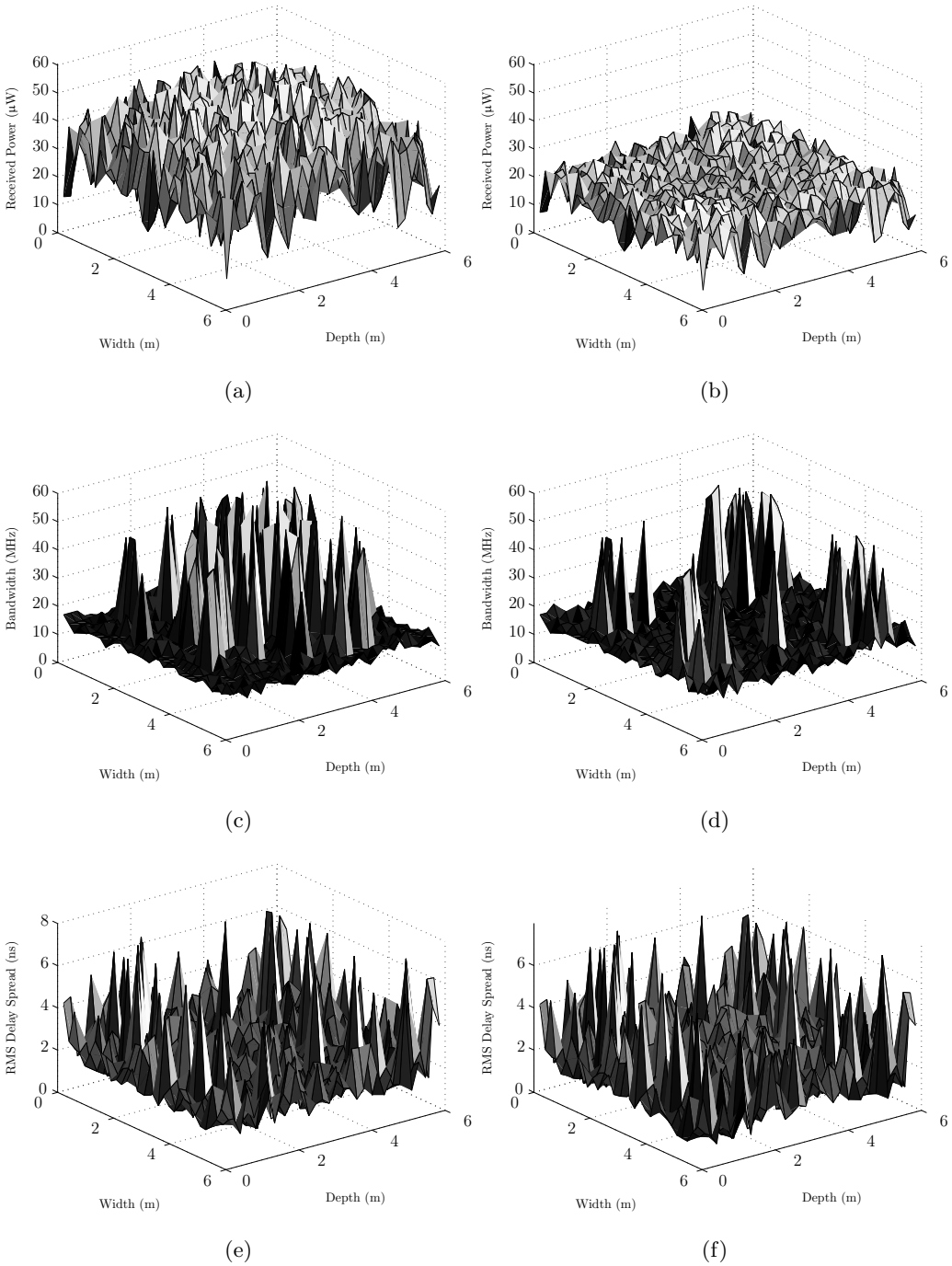

Figure 4.6: The effect on the channel due to randomly aligned receivers. Power: (a) non optimised, (b) optimised. Bandwidth: (c) Non optimised, (d) optimised. RMS delay spread: (e) Non optimised, (f) optimised.

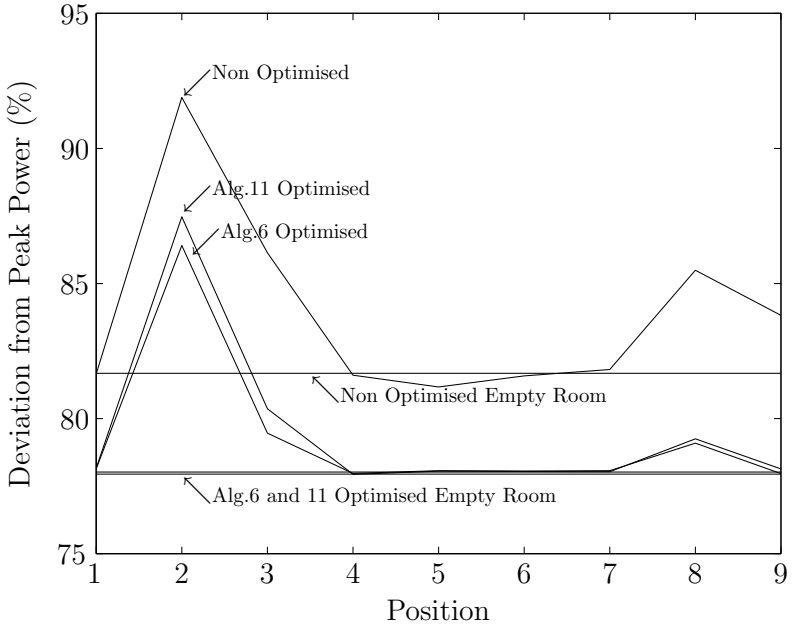

(a)

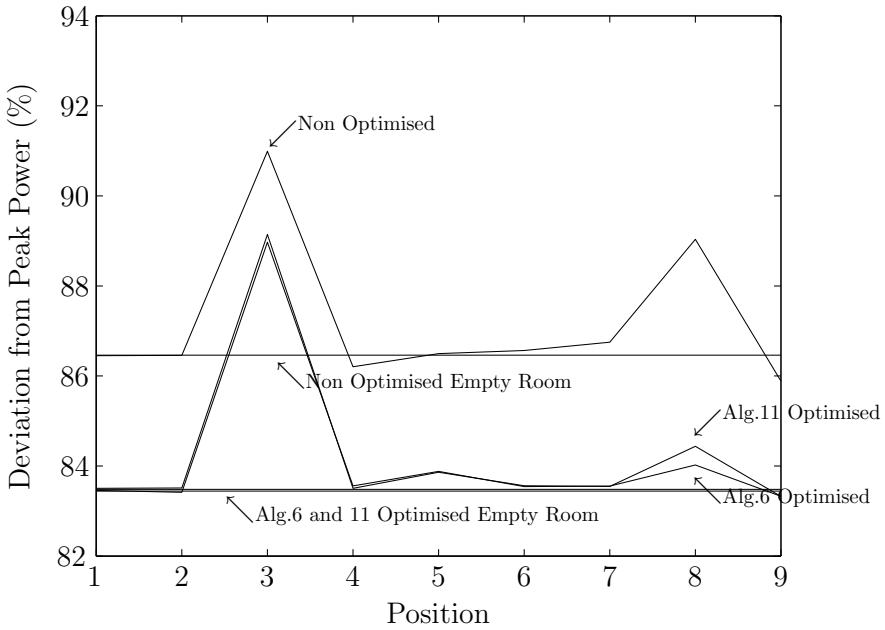

(b)

Figure 4.7: The effect of random alignment on two dynamic environments. (a) Environment 5, movement pattern 1. (b) Environment 5, movement pattern 2.

Upon user movement, with movement pattern 1, to environment 5, as shown in figure 4.7(a), the non optimised empty room power deviation is 82%, which upon user movement is perturbed by upto 10%, within a range of 11% between 81% and 92%. After optimisation with algorithm 6, the empty room deviation is reduced by 4% to 78%, with the maximum perturbation being reduced 2% to 8%, as the range is reduced 3% to 8% as it varies between 78% and 86%. Using algorithm 11, the empty room deviation is reduced by 4% to 78%, with the maximum perturbation being reduced 1% to 9%, as the range is reduced 2% to 9% as it varies between 78% and 87%.

Although the optimisation does not appear to be very effective, environment 6 was set up, with the same dimensions as environment 5, but with the reflectivity of the ceiling, south and east walls increased to $\rho = 0.8$, the north wall reduced to a reflectivity of $\rho = 0.5$ and the east wall having a reduced reflectivity of $\rho = 0.6$. A user following movement pattern 2, was then simulated, whereby, the non optimised empty room power deviation is 86%, which upon user movement is perturbed by up to 5%, with a range of 5% between 86% and 91%. After optimisation with algorithm 6, the empty room deviation is reduced by 3% to 83%, with the maximum perturbation being increased 1% to 6%, as the range is increased 1% to 6% as it varies between 83% and 89%. Application of algorithm 11, means that the empty room deviation is reduced by 3% to 83%, with the maximum perturbation being increased 1% to 6%, as the range is increased 1% to 6% as it varies between 83% and 89%.

4.4 Changing the level of Alignment

As the results seem to be tied to the effect of the level of angular dependence it is important to determine if there is a relationship between the performance of the optimisation and the different levels of alignment. Five normal distributions have so far been defined each one will be tested with algorithm 6 and 11, in turn, on an empty environment 5. As is normal, 1024 receivers were uniformly distributed over the environment at a height of $z = 1\,\mathrm{m}$, but instead of using a fixed

$\text{FOV}_{\mathcal{R}_j}$, it was varied for each case within the set $\text{FOV}_{\mathcal{R}_j} = \{35, 45, 55, 65\}^\circ$.

Figures 4.8(a) and 4.8(b) show the GA's optimisation gain dependency, on both $\text{FOV}_{\mathcal{R}_j}$ and angular distribution, for algorithm 6 and 11, respectively. The x axes of figures 4.8, 4.9 and 4.10 use the 80% angle measure, defined as the normal distribution which forms a 0.8 rotational probability of a single axis being rotated with a $\pm\{10, 15, 25, 35, 45\}^\circ$ of the unrotated position. The 80% = 0 angle defines all the receivers to be vertically orientated. Figure 4.9 shows the associated worst case bandwidth and RMS delay spread for the empty room before any optimisation. Figure 4.10(a) and 4.10(b) show the corresponding worst case bandwidth and RMS delay spread after the optimisation of the environment, using algorithm 6 and 11 respectively.

Figures 4.10(a) and 4.10(b) show a clear correlation between lower bandwidth and larger RMS delay spread as the user's 80% angle increases. As these graphs show only the worst case performance metrics, this observation is most likely due to the fact that as users 80% angle increases, so does the maximum angle of rotation found in the remaining 20% of the distributions statistically allowable range. Therefore there is also likely to be at least one receiver that skews the results. Whilst it may seem strange to include this, a system designer is concerned with this worst case. Designing a system for the best cases only is not realistic when considering the unpredictability of the user, as users expect a high quality of service, not just the supposed maximum performance.

Furthermore from figures 4.8(a) and 4.8(b), it can also be seen that the GA provides very little optimisation gain using a receiver with a $\text{FOV}_{\mathcal{R}_j} = 35^\circ$ when the user is statistically likely to align the receiver beyond $\pm 10^\circ$ from the vertical in either, or both, axes. For this reason, and with complementary reasons already discussed in section 3.5, a receiver with a $\text{FOV}_{\mathcal{R}_j} = 35^\circ$, will again, no longer be considered a viable option.

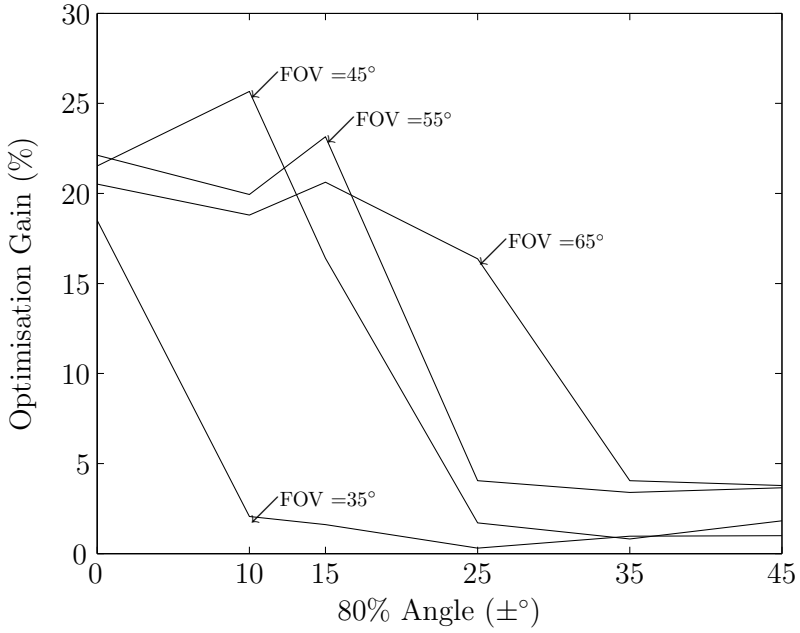

(a)

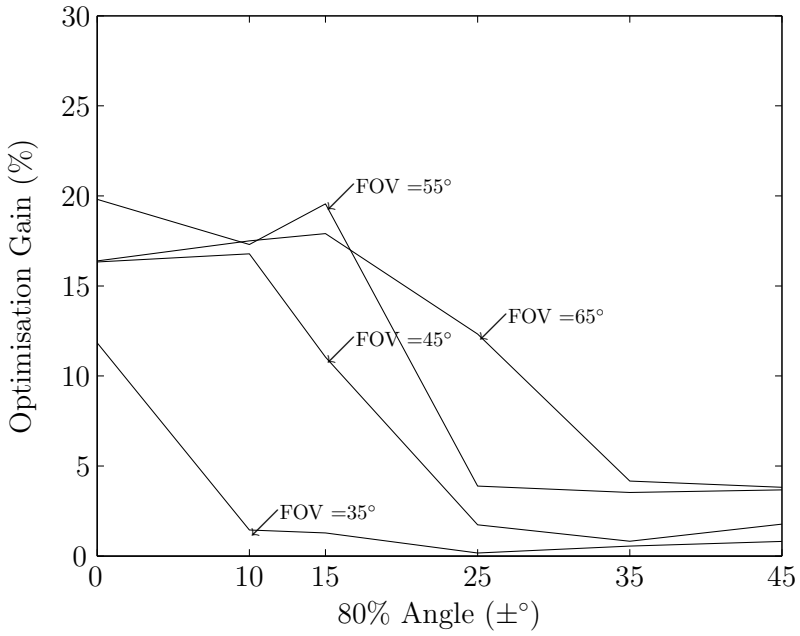

(b)

Figure 4.8: Optimisation gain dependency on receiver FOV and orientation. (a) Optimisation gain of algorithm 6. (b) Optimisation gain of algorithm 11.

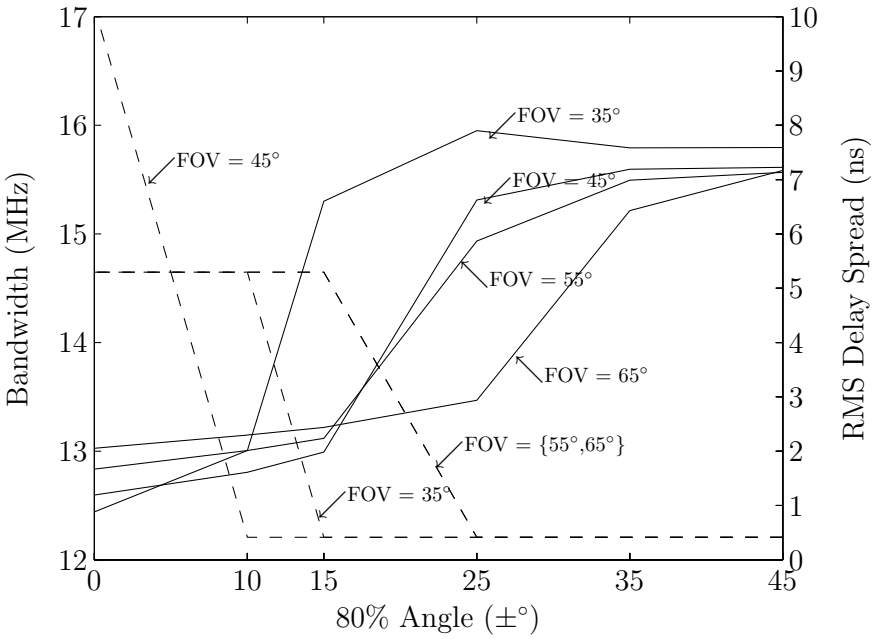

Figure 4.9: Non optimised bandwidth and RMS delay spread for varying receiver FOV and orientation.

Conversely, a receiver with a $\text{FOV}_{\mathcal{R}_j} = 65°$, allows the the GA to provide at least 16% gain up to an 80% angle of ±25°. A bandwidth penalty however, is incurred above an 80% angle of ±15°, and the RMS delay spread is highest of all scenarios tested for lower 80% angles where the user should statistically spend most of their time. Using algorithm 11, a receiver with a $\text{FOV}_{\mathcal{R}_j} = 65°$ allows the GA to provide at least 13% gain up to an 80% angle of ±25°, but a bandwidth penalty is incurred around the 80% angle of ±10°, with again, a highest RMS delay spread at the lower 80% angles using this FOV.

Considering a receiver with $\text{FOV}_{\mathcal{R}_j} = 45°$ and using algorithm 6, an optimisation gain can be achieved of between 21% and 25%, up to an 80% angle of ±10°, with negligible penalties with regards to the bandwidth and RMS delay spread. With algorithm 11, however, a gain of around 16% can be achieved, up to an 80% angle of ±10° but the bandwidth penalty is incurred instantly.

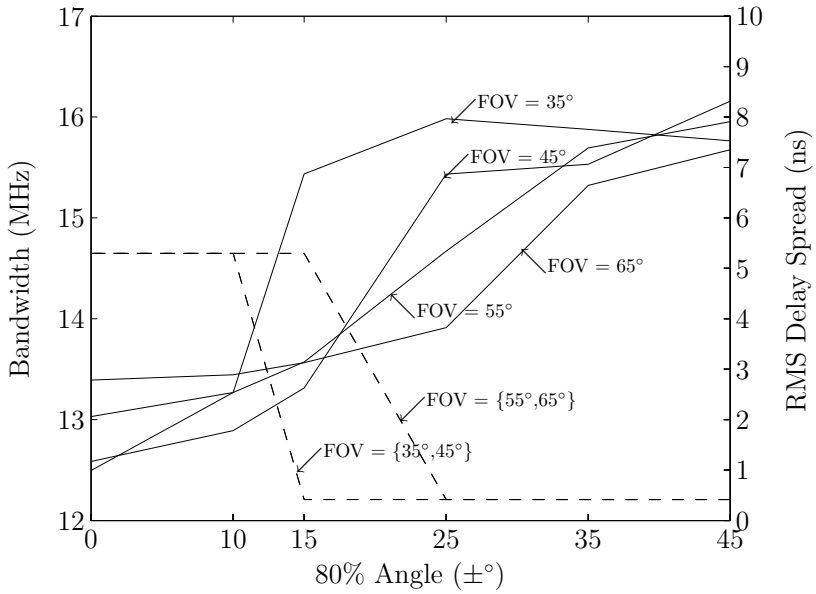

(a)

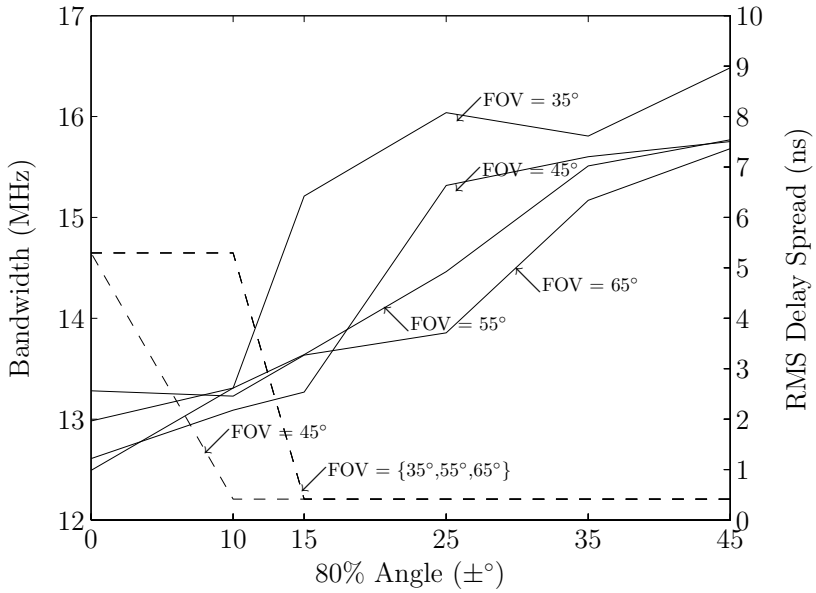

(b)

Figure 4.10: Optimisation dependency on receiver FOV and orientation. (a) Optimised bandwidth and RMS delay spread using algorithm 6. (b) Optimised bandwidth and RMS delay spread using algorithm 11.

There is an argument for using either a $\text{FOV}_{\mathcal{R}_j} = 45°$ or 65°, but care must be taken to balance the trade off in GA optimisation gain, the user's 80% rotation angle, and the bandwidth and RMS delay spread penalties. For the remainder of this work a receiver with a $\text{FOV}_{\mathcal{R}_j} = 55°$ will be assumed, as, when using algorithm 6, it provides an optimisation gain of between 20% and 23% for a user 80% angle of ±15°. This 80% is in line with the bandwidth penalty drop off point, and furthermore, incurs a negligible RMS delay spread penalty. When using algorithm 11 with a $\text{FOV}_{\mathcal{R}_j} = 55°$, an optimisation gain of at least 20% can be achieved up to a 80% angle of ±15°, the highest achievable for any FOV and 80% angle configuration employing algorithm 11. It also had a negligible RMS delay spread penalty, but this will be traded off with bandwidth penalty that is incurred at an 80% angle of ±10°.

Examining environment 5 with 1024 receivers having a $\text{FOV}_{\mathcal{R}_j} = 55°$, that have the ability to be randomly rotated based upon the normal distribution with a standard deviation with $\sigma = 11.7$ (the 80% is ±15°), the received power distribution can be seen in figure 4.11(a). The received power is shown to have a range between 19.9 µW and 56.7 µW, a deviation of 36.8 µW, or 65% of the peak value. The bandwidth, as in figure 4.11(c) varies between 14.6 MHz and 65.9 MHz, whilst the RMS delay spread varies between 0.73 ns and 2.17 ns. It is still interesting to note the peaks and valleys of the received power distribution patterns compared to those in figure 4.6, as the irregularities still exist, but are not as extreme.

Upon optimisation with algorithm 6, the received power distribution, as in figure 4.11(b), is reduced to vary between 10.7 µW and 18.8 µW, a deviation of 8.1 µW, or 43% from peak value. This is an optimisation gain of 22%, consistent with figure 4.8(a). The bandwidth, shown in figure 4.11(d) varies between 14.6 MHz and 53.7 MHz, whilst the RMS delay spread, shown in figure 4.11(f) varies between 0.503 ns and 2.73 ns.

When adding a user moving in pattern 1, to environment 5, as can be seen in figure 4.12(a),

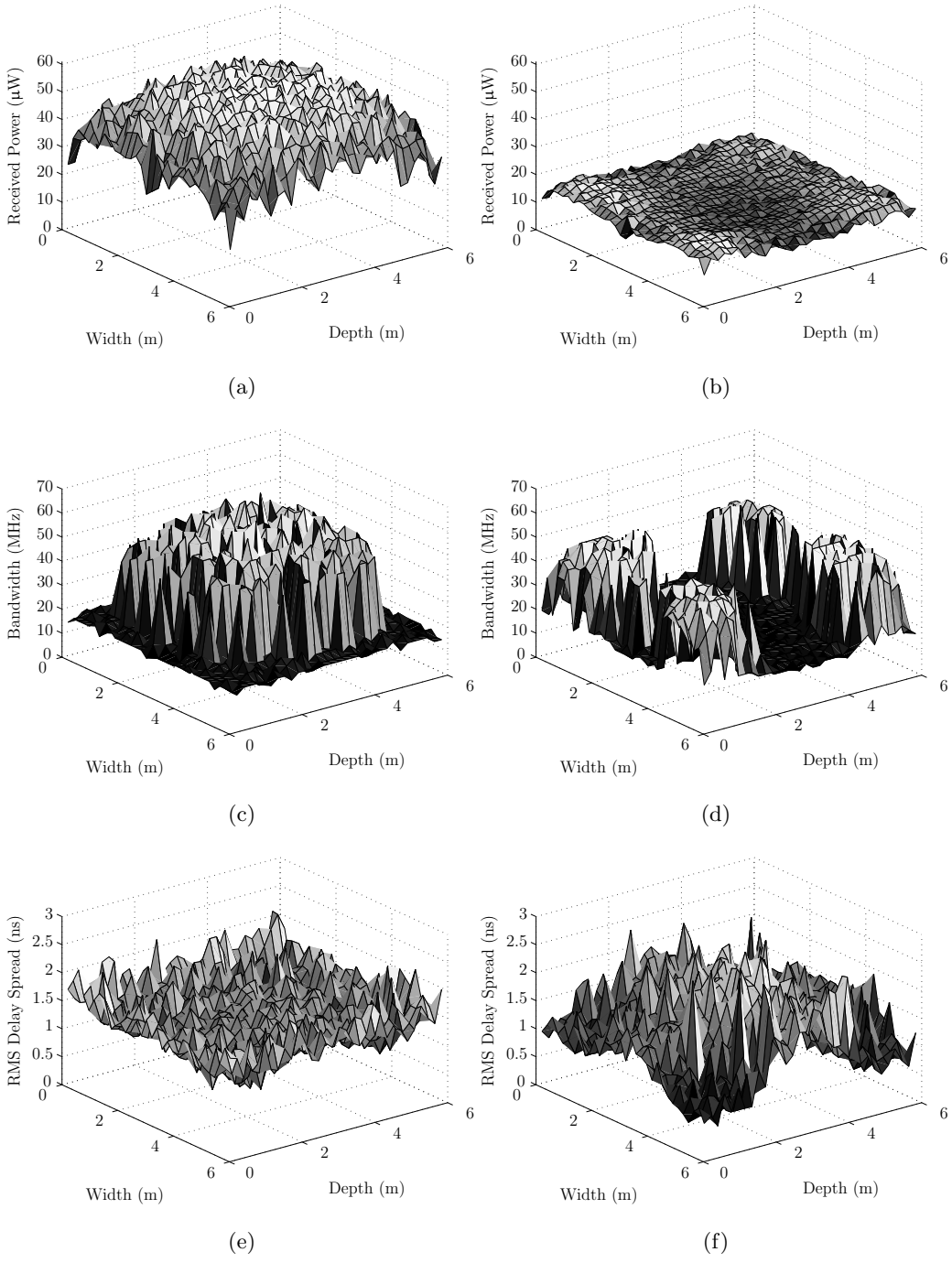

Figure 4.11: Optimisation random receiver alignment using algorithm 6. Power: (a)non optimised, (b) optimised. Bandwidth: (c) non optimised, (d) optimised. RMS delay spread: (e) non optimised, (f) optimised.

the non optimised empty room power deviation is 65%, which upon user movement is perturbed by up to 6%, with a range of 7% between 59% and 66%. After optimisation with algorithm 6, the empty room deviation is reduced by 23% to 42%, with the maximum perturbation being reduced 1% to 5%, as the range is reduced 1% to 6% as it varies between 41% and 47%. Using algorithm 11, the empty room deviation is reduced by 19% to 46%, with the maximum perturbation being reduced 4% to 2%, as the range is reduced 3% to 4% as it varies between 45% and 49%.

Adding movement to environment 6, with movement pattern 2, as shown in figure 4.13(a), the non optimised empty room power deviation is 73%, which upon user movement is perturbed by up to 10%, with a range of 10% between 63% and 73%. After optimisation with algorithm 6, the empty room deviation is reduced by 27% to 46%, with the maximum perturbation being reduced 6% to 4%, as the range is reduced 4% to 6% as it varies between 44% and 50%. Using algorithm 11, the empty room deviation is reduced by 22% to 51%, with the maximum perturbation being reduced 6% to 4%, as the range is reduced 5% to 5% as it varies between 47% and 52%.

The bandwidth and RMS delay spread for environments 5 and 6, are shown in figures 4.12(b) and 4.13(b) respectively. For room 5 the bandwidth does not vary much between the optimised and non optimised case, changing by only 2.4 MHz, whilst RMS delay spread varies between 1.25 ns. For environment 6 the bandwidth variation is also only 2.4 MHz, whilst the RMS delay spread is 0.30 ns. These results agree with those in chapter 3, in that the optimisation has little effect on the bandwidth and RMS delay spread, neither much gain or penalty.

4.5 Multi User Movement with Random Alignment

Now that the GA with varying receiver alignment has been demonstrated the final proof of concept, is just to extend the algorithm to scenarios involving multiple users moving within the environment. The same environment 5 and 6 is maintained, with the first user undergoing the

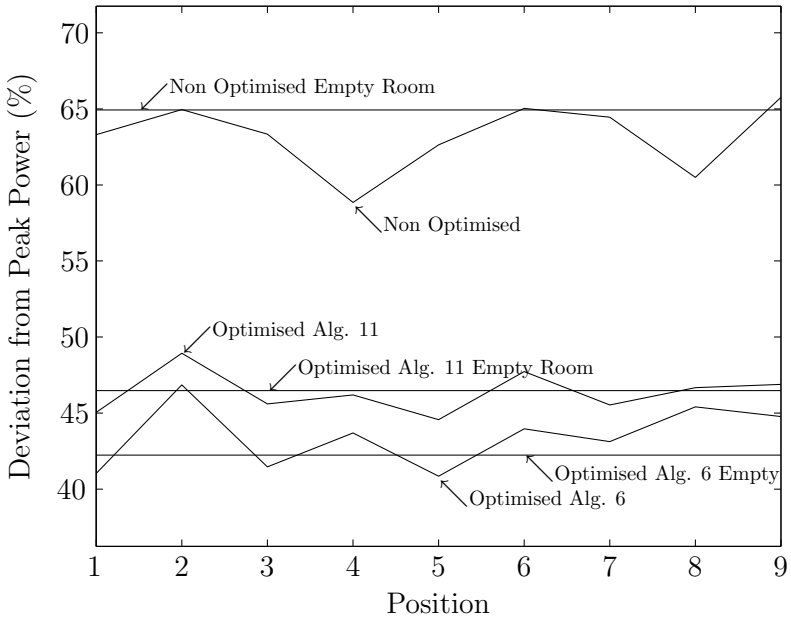

(a)

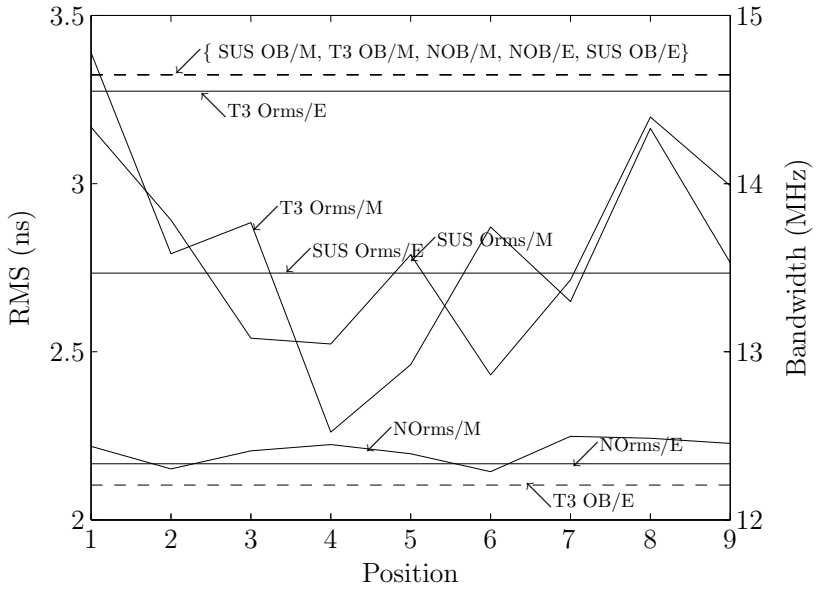

(b)

Figure 4.12: Environment 5 movement pattern 1 optimisation. (a) Received power. (c) Bandwidth and RMS delay spread.

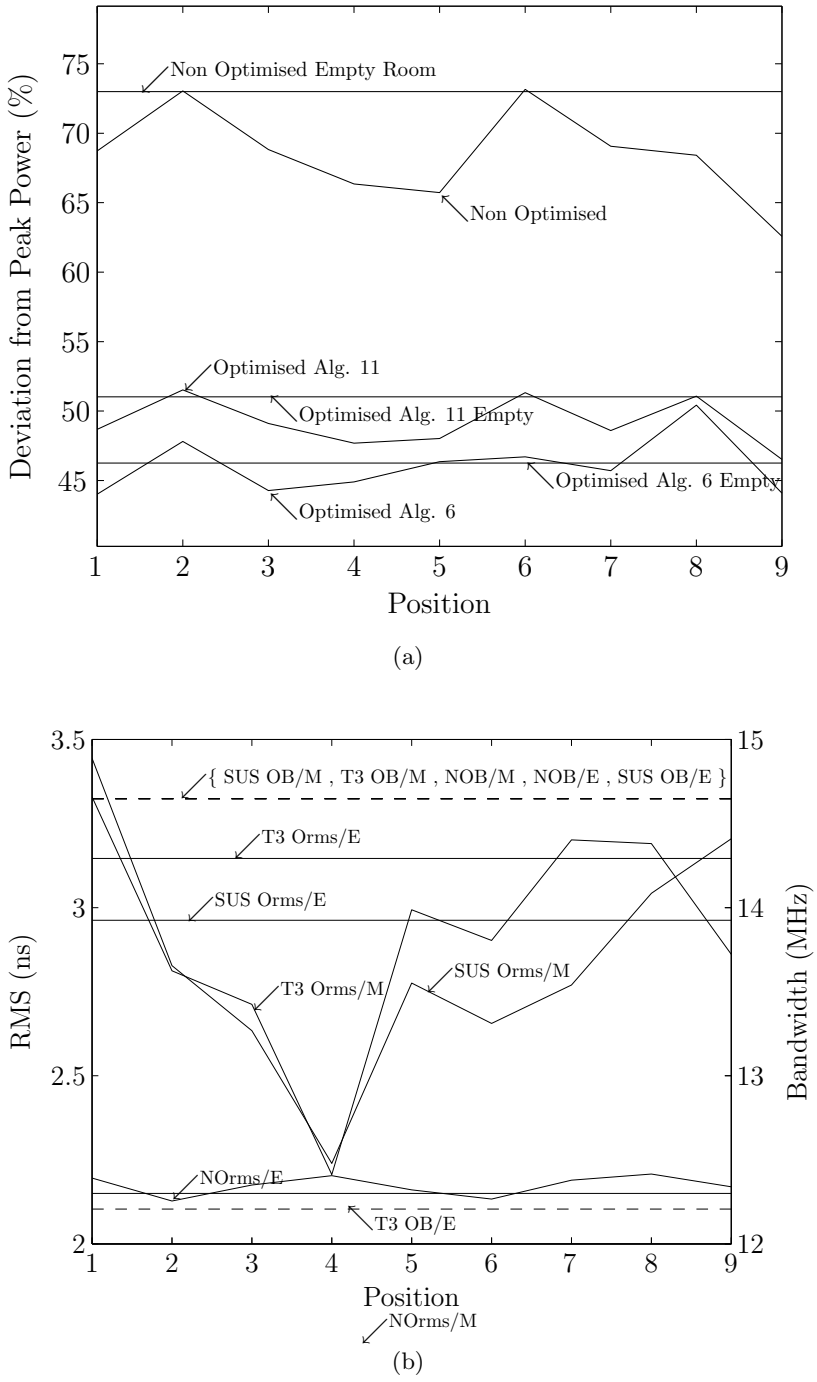

Figure 4.13: Environment 6 movement pattern 2 optimisation. (a) Received power. (c) Bandwidth and RMS delay spread.

same movement pattern 1 and 2 respectively. The second user, of the same reflectivity properties as user one, but with a reduced height of 1.6 m, undergoes 9 movement positions as detailed in figures 4.14 (c) and (d) respectively for environment 5 and 6. Each user moves sequentially through the steps, and it should be noted that the two users do not, and cannot occupy the same space, at the same time. As before the positional coordinates of the second person can be seen in appendix C. It should be noted that the choice of the second users height, 1.6 m is simply to provide another variability of the channel, in that not all users will be identically sized. The height could be set to any value realistic for the scenario.

Furthermore as the GA has been shown to be capable of optimising receivers with random alignment, in this scenario all, 1024 receivers with a $\text{FOV}_{\mathcal{R}_j} = 55°$, are allowed to vary with the normal distribution set with $\sigma = 11.7$, equating to an 80% angle of $\pm 15°$ and a maximum angle of $\pm 30°$. This scenario will be the most complex dynamic scenario illustrated within this work and it more advanced than the work in [27], where only one receiver was allowed to have variable alignment, or the work in [161], which only considered one moving user.

Figure 4.15 shows the non optimised power distribution for two users undergoing movement pattern 1 and 3, (figure 4.14 (a) and (c)), in environment 5, whilst figure 4.16 shows the optimised power distribution after application of algorithm 6. Similar to the results presented in section 4.4, the inclusion of the random alignment, makes the received power very unpredictable. Another reason why the use of the GA for indoor OW systems is beneficial.

Adding movement to environment 5 with the two users undergoing movement pattern 1 and 3, as shown in figure 4.17(a), the non optimised empty room power deviation is 65%, which upon user movement is perturbed by up to 6%, with a range of 9% between 62% and 71%. After optimisation with algorithm 6, the empty room deviation is reduced by 23% to 42%, with the maximum perturbation being increased 2% to 8%, and the range is reduced 3% to 6% as it

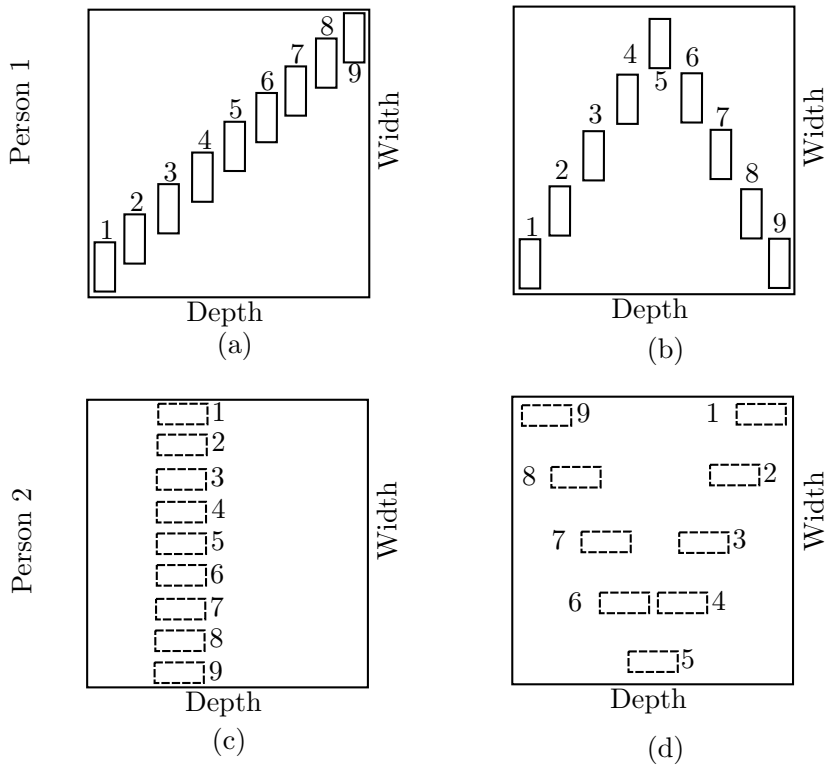

Figure 4.14: Movement positions of 2 users. (a) Person 1, movement pattern 1. (b) Person 1, movement pattern 2. (c) Person 2, movement pattern 3. (d) Person 2, movement pattern 4.

varies between 44% and 50%. Using algorithm 11, the empty room deviation is reduced by 18% to 47%, with the maximum perturbation being reduced 2% to 4%, as the range is reduced 5% to 4% as it varies between 47% and 51%.

Adding movement to environment 6 with movement patterns 2 and 4, as shown in figure 4.18(a), the non optimised empty room power deviation is 73%, which upon user movement is perturbed by up to 8%, with a range of 9% between 65% and 74%. After optimisation with algorithm 6, the empty room deviation is reduced by 27% to 46%, with the maximum perturbation being reduced 3% to 5%, as the range is maintained at 9% as it varies between 42% and 51%. Using algo-

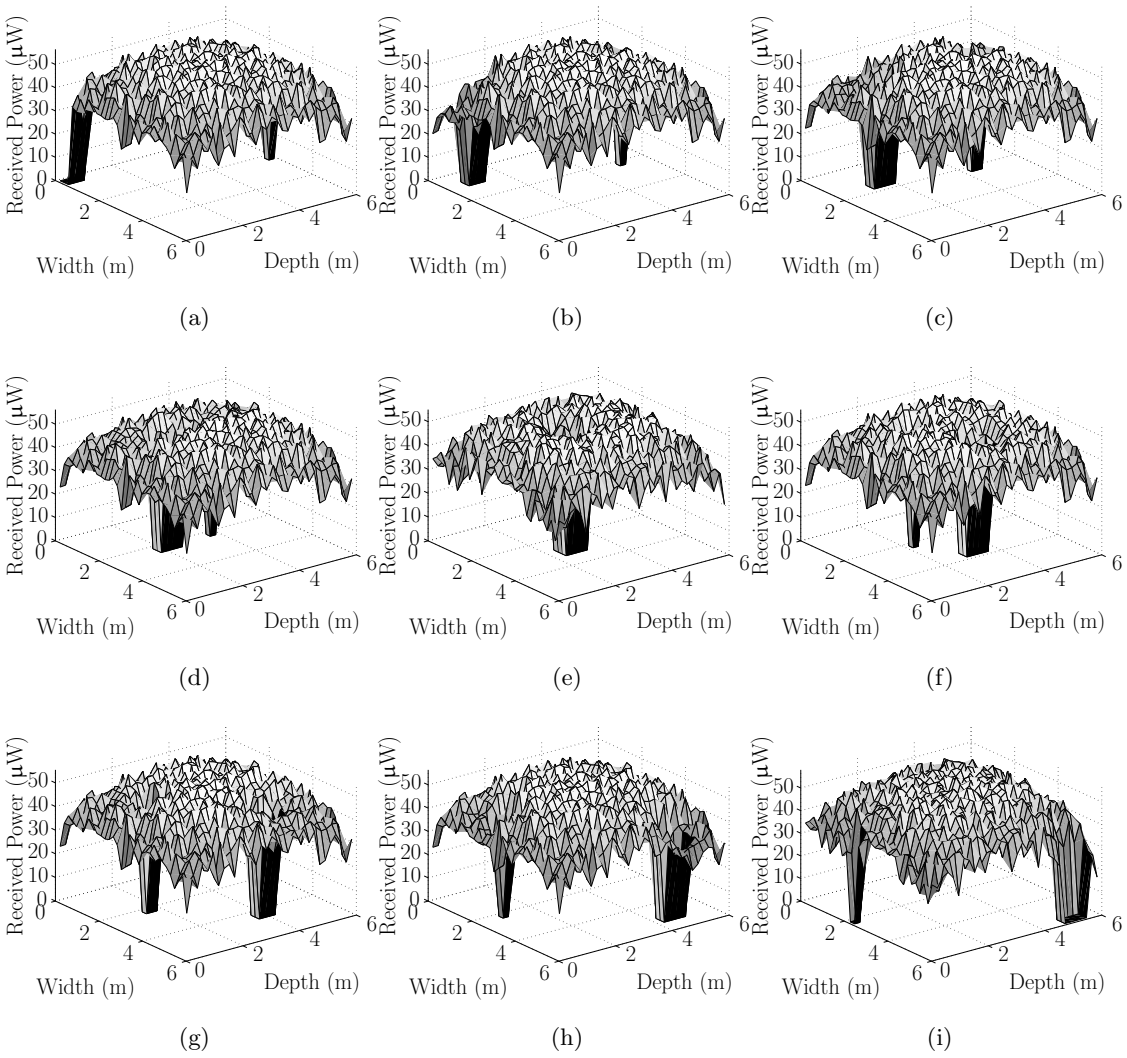

Figure 4.15: Non optimised power distribution for two moving persons. Environment 5, movement pattern 1 and 3, $\text{FOV}_{\mathcal{R}_j} = 55°$ under 25 diffusion spots. (a) to (i) refer to positions 1 to 9 respectively.

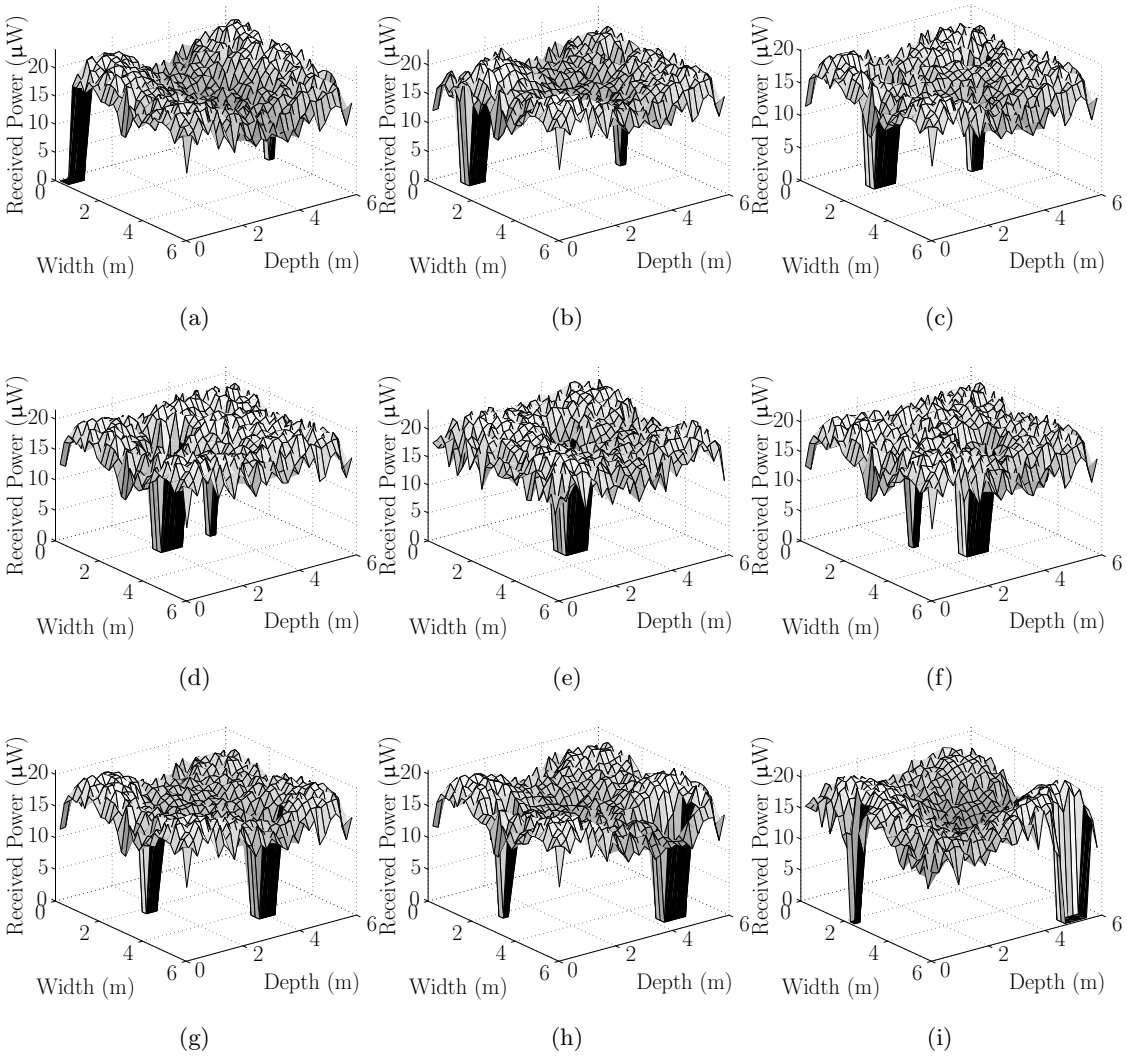

Figure 4.16: Optimised power distribution for two moving persons. Environment 5, movement pattern 1 and 3, $\text{FOV}_{\mathcal{R}_j} = 55°$ under 25 diffusion spots. (a) to (i) refer to positions 1 to 9 respectively.

rithm 11, the empty room deviation is reduced by 22% to 51%, with the maximum perturbation being reduced 1% to 7%, as the range is also maintained at 9% as it varies between 44% and 53%.

Figures 4.17(b) and 4.18(b) show the respective bandwidth and RMS delay spreads for the scenarios presented, whereby as can be seen, the use of the GA has not caused significant detriment to the performance characteristics compared to if they were not used.

One question still remains with the system about how the feedback path could be implemented. For the work carried out in thesis, the feedback is implemented in MATLAB in such a way that the deviation from peak power is simply passed back to the transmitter for it to make a decision. In reality there are several possible practical realisations. One method, probably the simpler of the two, is for the receiver to pass back a "too high"or "too low"command. This is possible as the receiver knows the limits of its operation and can be predefined with the levels of powers it knows the transmitter can produce. The second method would require the transmitter to be able to determine the received power and transmit back the value. At the transmitter, the value can be stored which over time, will be optimised as the receiver moves around the environment.

4.6 Conclusion

This chapter has provided probably the most realistic user and environmental scenario tests that could be tested. In each test the GA performed well, optimising change in received power deviation. The inclusion of random alignment also brought about the verification of the choice in receiver FOV, and once again shows consistency in the results as the scenarios are modified. The constraints on the GA's ability have been established, it is now known to what extent the users have freedom in receiver alignment. It is now known the GA can still optimise environments with two users. As in chapter 3, the GA has shown little capability to optimise the bandwidth or RMS delay spread, and although this was not the original intention, the GA application is still

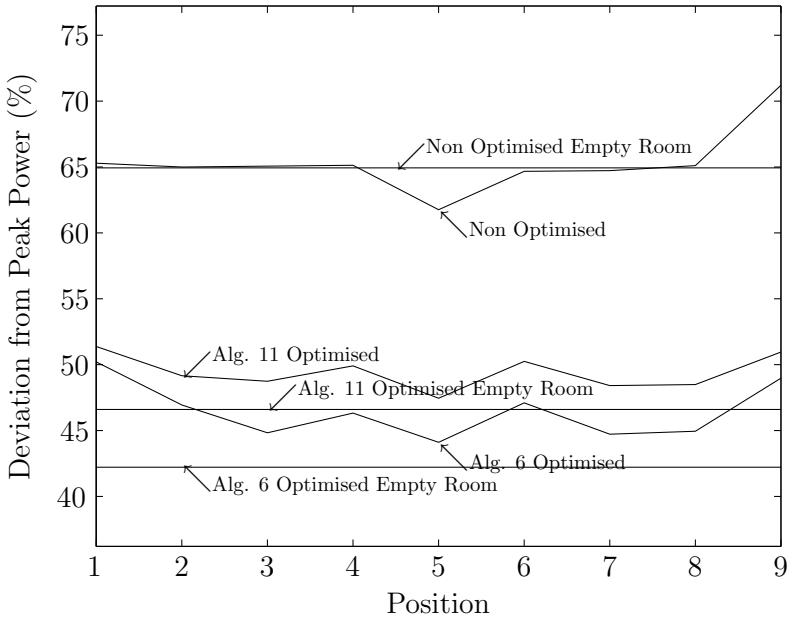

(a)

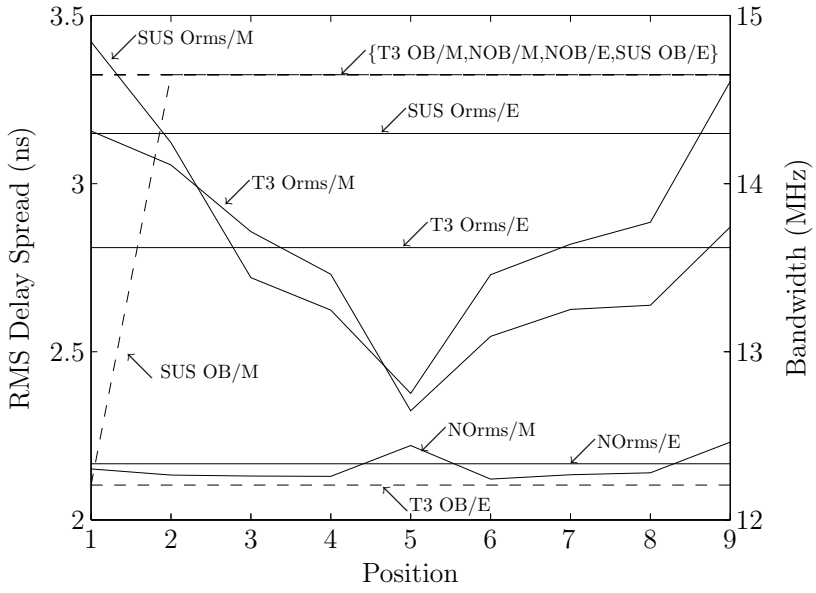

(b)

Figure 4.17: Environment 5 movement pattern 1 and 3 optimisation. (a) Power deviation. (b) Bandwidth and RMS delay spread.

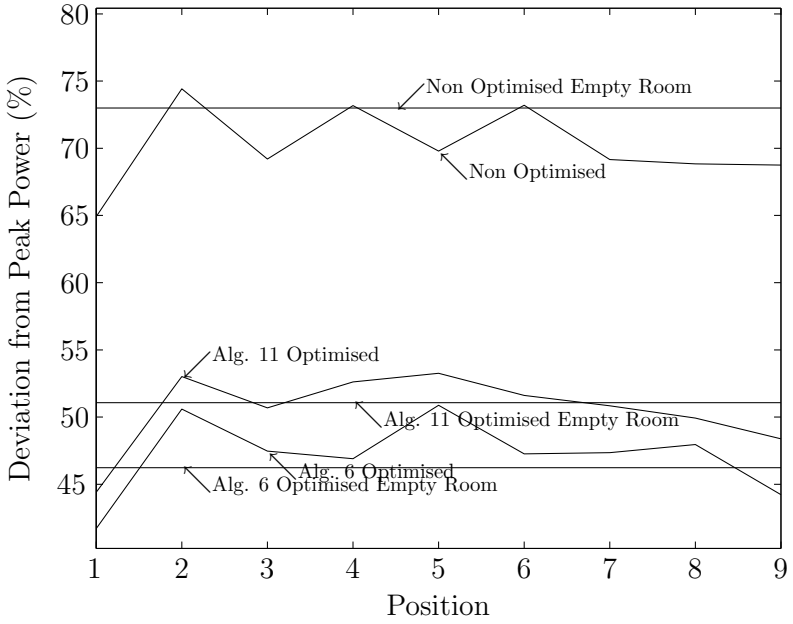

(a)

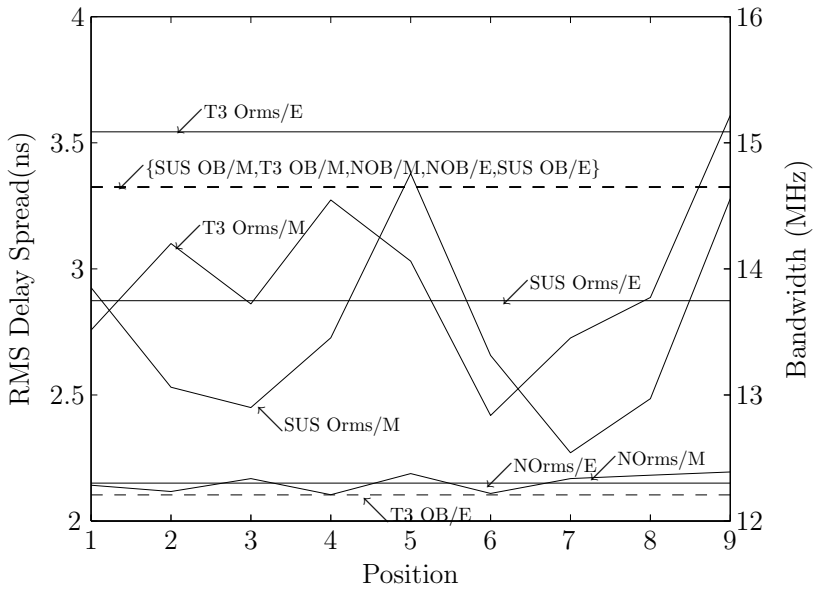

(b)

Figure 4.18: Environment 6 movement pattern 2 and 4 optimisation. (a) Power deviation. (b) Bandwidth and RMS delay spread.

showing a benefit, in terms of power optimisation, that would be applicable to mass produced non-bespoke systems.

Chapter 5

Optimisation of Channel Noise

5.1 Introduction

Now that the GA has been shown to work on optimising the channel without noise, it is time to put the noise into the channel. In previous chapter the receiver has been modelled simply as the photodiode receiving area, thus in this chapter, to accomadate noise, a more detailed receiver model needs to be established. The aim of this chapter is to investigate the ability for the GA to optimise the distribution of the SNR or the BER. This chapter is considered to be a similar, but different, application for the GA than the one it previously was designed for. The aims before were to optimise the received power deviation. In this chapter, although the GA is in control of the transmitted power, it might not be necessary to reduce the deviation from peak power. Here the noise may not be uniform and so, the GA should not try and reduce received power, but rather to match the transmitted power to the noise power, in effect reducing the SNR.

5.2 The Noise Model

In general, the term noise, is used very loosely to cover a broad range of possible real world manifestations that interfere with the desired system performance. For indoor OW communica-

tions, however, and from a channel perspective, noise is considered to be a combination of two major factors, shot noise and interference noise [162, 163, 164]. Furthermore, noise can itself be considered to be a type of signal that is fully dependent upon the channel characteristics between the noise source and the receiver. In the same way as the signal, the quantity of noise arriving at the receiver is dependent upon the room configuration and reflectivity properties, receiver properties such as photodiode area, FOV, position and orientation, not to mention the original distribution of the noise signal from the noise source. In this section a mathematical representation of the noise model will be proposed for inclusion into the SNR and BER calculations and further optimisation by the GA.

The steady, or very slow time varying, background irradiance produced by natural and artificial light sources is usually characterised by the DC current it induces in the receiver photodiode since the shot noise power density, N_0, is directly proportional to that current, I_b, or alternatively the incident background noise power, P_b, and is given by [165]

$$N_0 = qI_b = qRP_b \tag{5.1}$$

Where R is the photodiode responsivity, and $q = 1.6 \times 10^{-19}$ is the electronic charge. For this work, it will be most common to refer to the power, as opposed to current as the simulation software developed so far in chapter 2 is designed for received power, regardless of whether it is signal or noise, and follows the same rules already established in section 2.2 to 2.2.

The missing topic in the theory of chapter 2 is a lack of incorporation of a realistic noise source model. When dealing with the channel characteristics, regarding the signal, it could be assumed that the signal sources radiation emission wavelength was known, and in the case of infrared communications, fairly narrow band operating at the typical center wavelengths, 780 nm, 870 nm or 970 nm [162]. This implies that for a given source power, the power was contained within a known range of radiation wavelengths and could be assumed to be well matched with photodiode responsivity at those wavelengths. Furthermore, it is also more common to find such infrared

devices characterised by their radiometric properties [166].

Illumination light sources, on the other hand, are normally characterised by their photometric (how they interact with the human eye) properties [167] or electrical characteristics. A Typical 60 watt incandescent bulb does not emit that quantity of power into a wavelength of interest for communication purposes. All illumination light sources, including the sun, emit radiation to varying degree within a silicon photodiode responsivity range. Commonly employed daylight filters with a cut off wavelength < 780 nm remove some of the background radiation but above that wavelength, the light sources still induce a background photocurrent [162].

The most common way for authors to deal with this missing model, is to default to practical measurements. To name but a few published works, in [168], 21 off the shelf light sources were tested in 15 different configurations, whilst in [169], 7 sources were tested in 4 configurations, and finally in [170], 4 different sources were tested in various combinations of the same environment. Each set of measurements was carried out in a different environments using different receivers with different properties. Although the results give very good approximations or expectations to the level of how much received background noise power is present, the results are not truly comparable.

The results presented hereafter will be formed by a two stage process. Firstly, the physical specifications of the source will be accounted for, that is the directivity in the form of a generalised Lambertian order, the position of the source, and the direction it is orientated in. This is the same three parameters used for the signal source model and is therefore fully compatible with the software developed so far. Each source will be given an optical power of 1 W, and the received power simulated. Once the received noise power has been determined, and knowing the channel is linear, this power will be increased, or decreased, until it is similar to what has been previously published using measured results. One advantage of treating the noise sources this

way, not only because it fits the simulation software, is that it allows the specifics of the receiver to be removed from the analysis. This will reduce the complexity in proving the concept of the GA optimisation of SNR or BER, using a general framework, not specific to any factors not involved with the channel.

The other noise component, interference, is a little better known as it can be mathematically represented. Work my Moreira *et al.* [168, 165] has provided, through measurement, an accurate, but general model for interference from 3 types of light bulb, incandescent lamps, fluorescent lamps with conventional ballasts and fluorescent lamps with electronic ballasts. Each model is is based upon the measurements from a wide ranging collection of lamps from many manufacture's. The resultant formulation is a Fourier series that can be used to represent to a good approximation the level of interference a given type of lamp will produce, and each one of these will be dealt with in turn to build the interference model.

5.2.1 Incandescent Lamps

Incandescent, or Tungsten filament lamps are currently very common in offices and in the household. They will become less common under the new European parliament and council directive 2005/32/EC [171], where they will be phased out in coming years, due to energy usage concerns, but they are still very prominent and worth investigating for now. For incandescent lamps the interference signal can be given as [165]

$$i_{\text{incand}}(t) = \frac{I_B}{F_1 A_1} \sum_{i=1}^{10} a_i \cos\left(2\pi 100 i t + \phi_i\right) \tag{5.2}$$

Where the magnitude factors, a_i, and the phase factors, ϕ_i, of the 100 Hz harmonics are given in table 5.1. The optical attenuation factor, F_1, and A_1, the factor that relates the interference with the background current, I_B, take on the values of 1.5 and 8.7 respectively. Figure 5.1(a) shows the time varying waveform of the interference, whilst the associated coefficients of table

5.1 are shown in figure 5.1(b).

i	1	2	3	4	5	6	7	8	9	10
a_i	1.0	1.72×10^{-2}	1.50×10^{-2}	5.51×10^{-3}	2.85×10^{-3}	4.37×10^{-4}	8.17×10^{-4}	1.28×10^{-3}	8.30×10^{-4}	6.00×10^{-4}
ϕ_i(rad)	0.0	1.30	−1.28	−2.98	1.07	−1.08	1.34	−1.37	2.09	−1.80

Table 5.1: Average parameter values for incandescent light interference [168].

5.2.2 Fluorescent Lamps Driven by Conventional Ballasts

Fluorescent lamps driven by conventional ballasts are very common in office's and have interference up to around 2 kHz. The interfering signal can be described by

$$i_{\text{fluor}}(t) = \frac{I_B}{F_2 A_2} \sum_{i=1}^{20} [b_i \cos(2\pi(100i - 50)t + \varphi_i) + c_i \cos(2\pi 100it + \zeta_i)] \tag{5.3}$$

Where the phase values, φ_i and ζ_i can be seen in table 5.2. F_2, the optical filter attenuation factor, and the factor A_2, which relates the interference amplitude with the induced background current, I_B, have values of 4.7, and 1.2 respectively. b_i and c_i are the magnitude coefficients of the odd and even Fourier harmonics and are given by the expressions

$$\log_{10}(b_i) = \left(\frac{-13.1 \ln(100i - 50) + 27.1}{20}\right) \tag{5.4}$$

$$\log_{10}(c_i) = \left(\frac{-20.8 \ln(100i) + 92.4}{20}\right) \tag{5.5}$$

The time varying waveform of equation 5.3 and the the values of b_i and c_i are plotted in figures 5.2(a) and 5.2(b), respectively.

i	1	2	3	4	5	6	7	8	9	10	11	12	13	14	15	16	17	18	19	20
φ_i(rad)	4.65	2.86	5.43	3.90	2.00	5.98	2.38	4.35	5.87	0.70	1.26	1.29	1.28	1.63	6.06	5.49	4.45	3.24	2.07	0.87
ζ_i(rad)	0.00	0.08	6.00	5.31	2.27	5.70	2.07	3.44	5.01	6.01	6.00	6.17	5.69	5.37	4.00	3.69	1.86	1.38	5.91	4.88

Table 5.2: Typical values for the fluorescent lamp phase parameters [168].

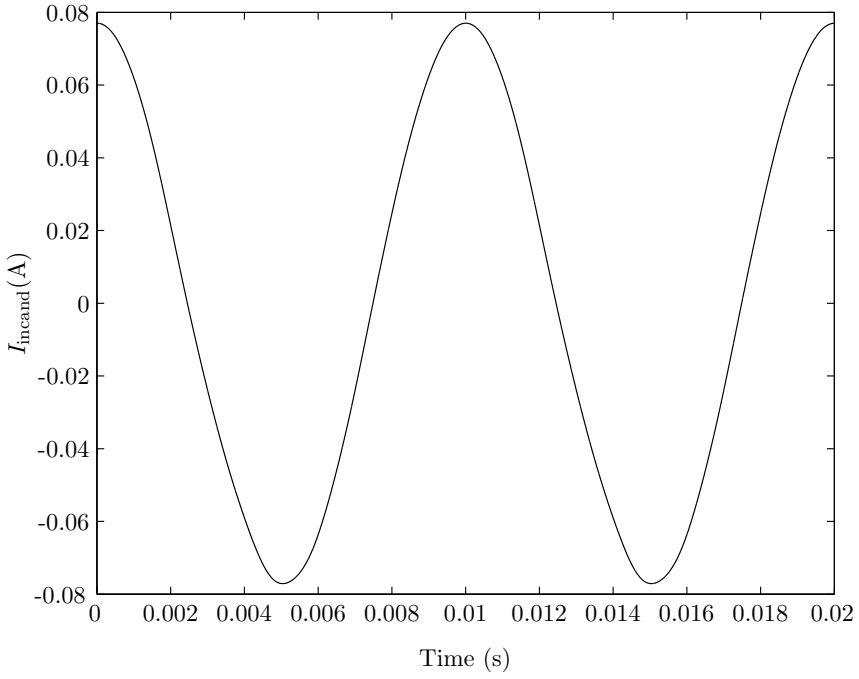

(a)

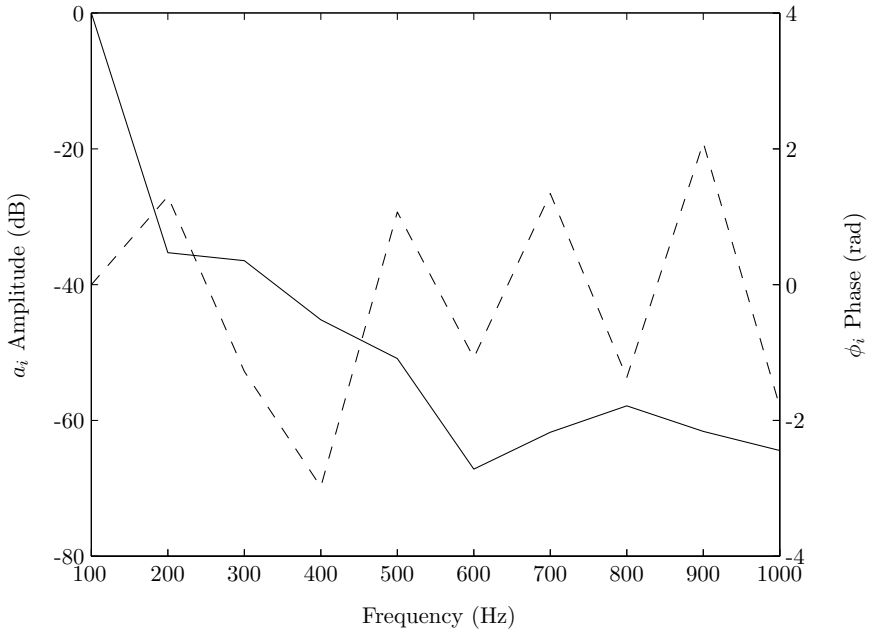

(b)

Figure 5.1: Incandescent noise model parameters [168]. (a) Time waveform of the incandescent interference. (b) Magnitude (-) and phase (- -) of the incandescent lamp Fourier coefficients.

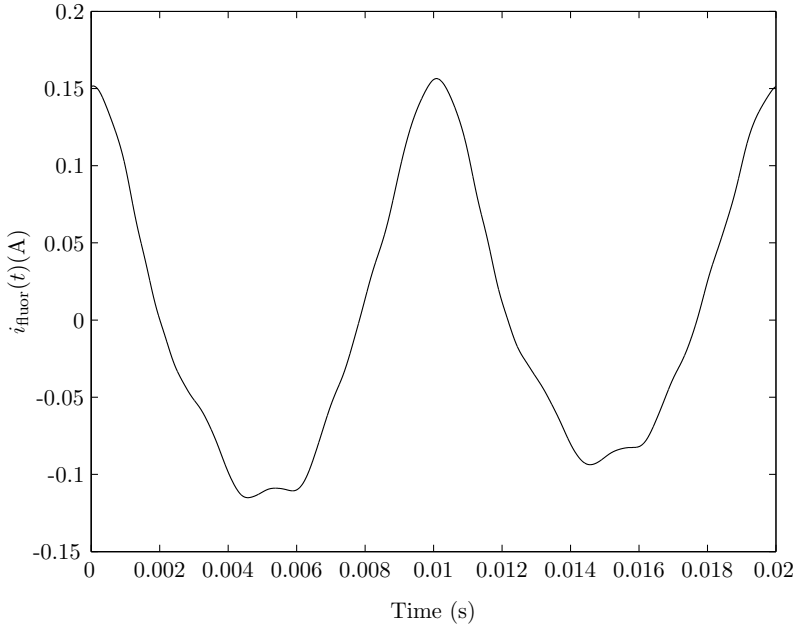

(a)

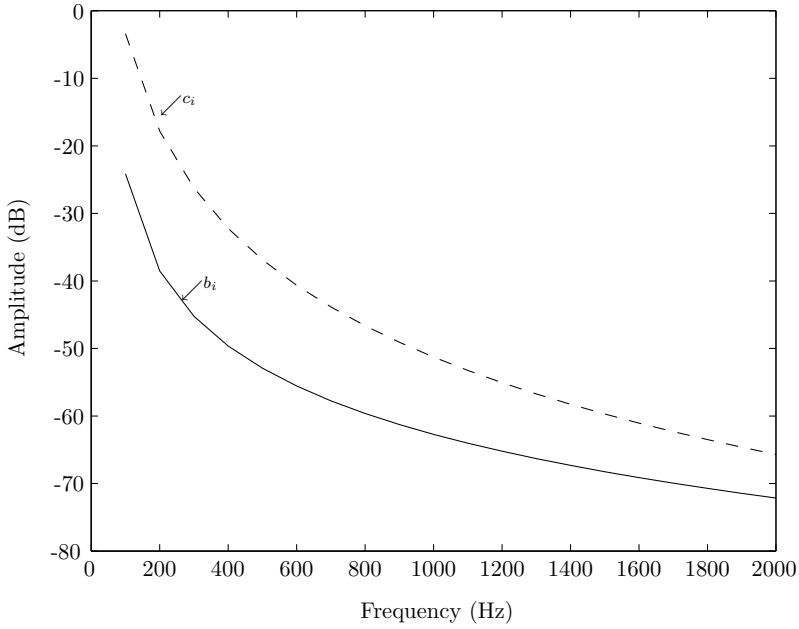

(b)

Figure 5.2: Fluorescent lamp noise model parameters [168]. (a) Time waveform of the Fluorescent lamps. (b) Fluorescent lamps b_i and c_i coefficients.

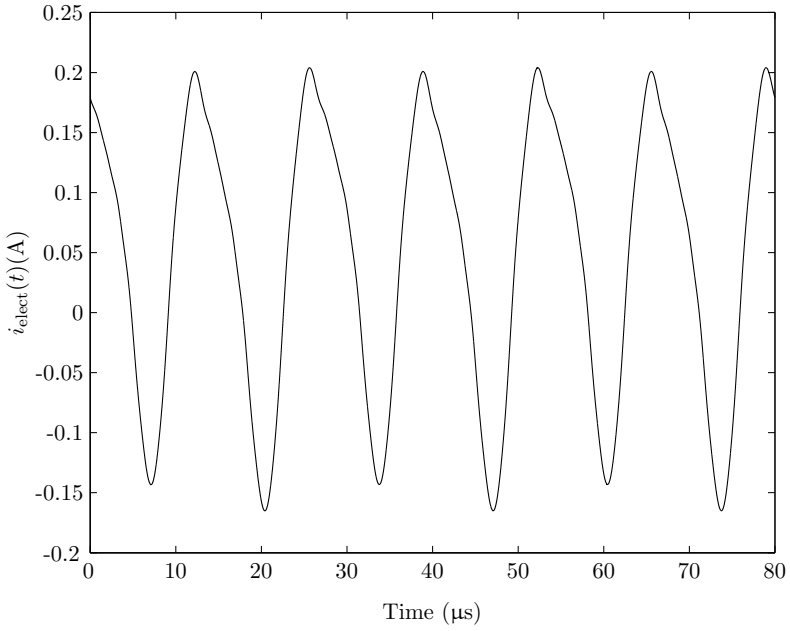

(a)

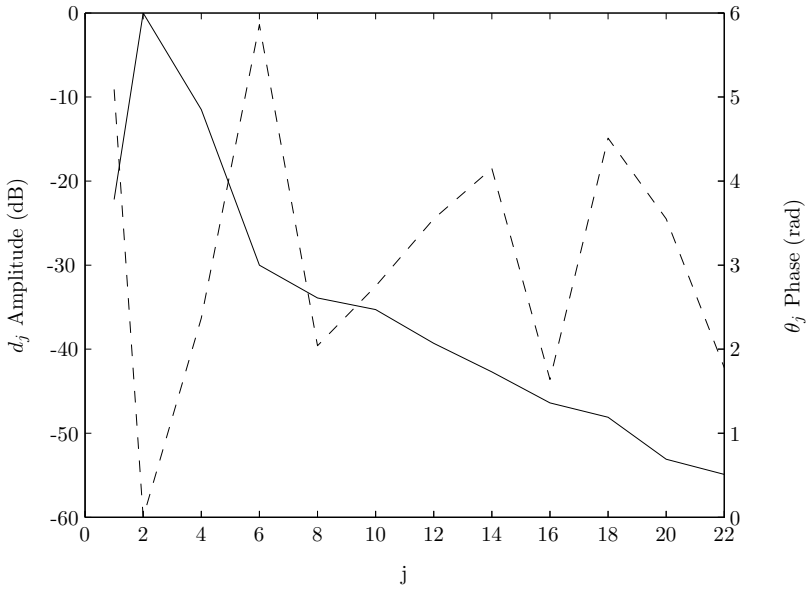

(b)

Figure 5.3: Electronic ballast lamp noise model parameters [168]. (a) Time waveform of the electronic ballast lamps. (b) Magnitude (-) and phase (- -) of the electronic ballast lamp Fourier coefficients.

5.2.3 Fluorescent Lamps driven by Electronic Ballasts

Fluorescent lamps driven by electronic ballasts, or sometimes known as high frequency fluorescent lamps, are a more recent development. The technology is commonly found in energy saving lights and will become more dominant in years to come [171]. They present the worst case of noise interference for indoor optical wireless communication systems for two reasons. Firstly they have a settling time after the initial switch on when the output radiation spectrum changes drastically. It has been shown in [162] that upon initial switch on, the output spectrum is dominated by emission of infrared radiation, which after approximately 6 min shifts into the visible spectrum. This is commonly observed with the energy saving bulbs, in that they appear dim to begin with, where the human eye is not sensitive to infrared. In this work it is assumed that any bulbs are in their settled state, but it would be interesting in the future to look at how the initial switch on, of such bulbs, affects the system performance. This might be most interesting in the residential scenarios where people move from room to room, turning lights on a off as they do.

The second reason they provide the highest level of interference, is that the harmonics of the interference extend into several MHz. The interference signal can be modelled as the sum of two components, a low frequency, $i_{\text{low}}(t)$ component, and high frequency, $i_{\text{high}}(t)$, component.

$$i_{\text{elec}}(t) = i_{\text{low}}(t) + i_{\text{high}}(t) \tag{5.6}$$

Where, similar to equation 5.3, but noting different coefficients

$$\begin{aligned} i_{\text{low}}(t) = \frac{I_B}{F_3 A_3} \sum_{i=1}^{20} [b_i \cos(2\pi(100i - 50)t + \varphi_i) \\ + c_i \cos(2\pi 100it + \zeta_i)] \end{aligned} \tag{5.7}$$

$$i_{\text{high}} = \frac{I_B}{F_3 A_4} \sum_{j=1}^{22} d_j \cos(2\pi f_{\text{high}} jt + \theta_j) \tag{5.8}$$

In equation 5.7, the values of φ_i and ζ_i can be found from table 5.2, whilst the values of b_i and c_i can be found from equations 5.4 and 5.5 respectively. The coefficients d_j, and θ_j are

shown in table 5.3, whilst A_3, and A_4, the attenuation coefficients that link the interference magnitude to the induced background current I_B, are set to 5.9 and 2.1 respectively. F_3, the optical attenuation filtering coefficient is set to 3, and finally, f_{high}, is set to 37.5 kHz [165]. The resultant time varying waveform of equation 5.6 can be seen in figure 5.3(a), with a graphical representation of the values of table 5.3 shown in figure 5.3(b).

j	1	2	4	6	8	10	12	14	16	18	20	22
d_j(dB)	−22.20	0.00	−11.50	−30.00	−33.90	−35.30	−39.30	−42.70	−46.40	−48.10	−53.10	−54.90
θ_j(rad)	5.09	0.00	2.37	5.86	2.04	2.75	3.55	4.15	1.64	4.51	3.55	1.78

Table 5.3: Typical values for high frequency lamp interference [168].

5.3 SNR and BER Model

Now the the noise model has been presented, the system model used in the determination of the SNR and BER will be provided. This model is predominantly based on the culmination of work carried out by K. K. Wong *et al.* [172]. The work provided a good representation of the true SNR and BER of a indoor OW system, although, as will be explained, it has some simplifications and assumptions that require some careful interpretation to be confident of the results the model provides. In order to compare, or verify, the results produced within this work, to begin with the same environmental scenario, as the one used in theirs, must be formed.

A room, with the same dimensions as Barry's configuration A in [87], was formed, with a width and depth, $X_e = Y_e = 5\,\text{m}$, and height $Z_e = 3\,\text{m}$. The room was empty, and the reflectivity of each surface, including the floor, which unlike Barry, was set to $\rho = 0.8$. Centrally upon the ceiling, a single transmitter with a Lambertian emission profile of $n = 1$ was placed, orientated towards the floor. Finally at the location, $x = y = 1\,\text{m}$, on the floor, ($z = 0\,\text{m}$), a receiver with a $\text{FOV}_{\mathcal{R}} = 90°$ and an active area of $1\,\text{cm}^2$, with photodiode responsivity $R = 1$, was positioned,

vertically orientated towards the ceiling.

5.3.1 Impulse Response Calculation

Using the simulation program already presented in this work, the impulse response between source and receiver for the configuration just described was determined and can be seen in figure 5.4(a). The LOS link, $h^0(t)$, has a received power of 1.57 µW whilst the total received power, $H(0)$, equals 3.35 µW. As presented earlier in section 2.3, the simulation program developed here uses a time bin of $\Delta t = 0.1$ ns, however, K. K. Wong *et al.* assume time bins of a different length. In their work they set the time bins to a width τ, related to the Nyquist bandwidth, B, as $\tau = (2B)^{-1}$. He also assumes that if the arrival of the LOS path is taken to be the time origin, then the first impulse will have a weight equal to the total power received in the first time bin with zero delay. The second impulse will have weight equal to the total power in the second bin with a τ second delay and so on. For OOK, where T_B is the bit duration

$$T_B = \frac{1}{2B} = \tau_{\text{OOK}} \tag{5.9}$$

The equivalent channel can be modelled as

$$h(t) = \sum_{l=0}^{L-1} \beta_k \delta(t - \tau_l) \tag{5.10}$$

Where β_l and $\tau_l = lT_B$, are the relative optical power and the time delay, or the l^{th}, resolved multipath. The total number of paths is L. In discrete form, this can be reduced to

$$h_k = \sum_{l=0}^{L-1} \beta_k \delta(k - \tau_l) \tag{5.11}$$

Where now, $h(t)$ is normalised such that $\beta_0 = 1$. $\delta(n)$ is the Kronecker delta function defined as

$$\delta(n) = \begin{cases} 1 & n = 0 \\ 0 & n \neq 0 \end{cases} \tag{5.12}$$

For a $2\,\mathrm{Mbit\,s^{-1}}$ system, $T_B = 500\,\mathrm{ns}$ is much larger than the impulse response train of figure 5.4(a) and so reduces to the normalised form of figure 5.4(b). Alternatively for an $80\,\mathrm{Mbit\,s^{-1}}$ system, $T_B = 12.5\,\mathrm{ns}$ and so reduces to the normalised impulse response train as in figure 5.4(c). For the work presented in this thesis, instead of modifying our code, which is known to work, with the new time bin system, the impulse response will be worked out as before, then rebuilt to follow the time bins required for the SNR and BER equations.

5.3.2 System Block Diagram

Referring to figure 5.5 (a), for OOK modulation, a rectangular pulse of duration T_B and constant power $2P_{av}$ is transmitted for a symbol 1, and no power transmitted for a symbol 0. P_{av} is the average transmitted optical power. The input bits, b_k, at a rate R_b are assumed to be independent and identically distributed (IID), and uniform in the set $b_k \in \{1, 0\}$. The bits are passed through a transmit filter with a rectangular impulse response of unit amplitude and duration, $1/R_b$. In the frequency domain, this would be a sinc function with bandwidth R_b. The rectangular pulse is then scaled by $2RP_{av}$, where R is the photodiode responsivity. This pulse is then transmitted through the channel, where is susceptible to the channel effects such as attenuation and multipath dispersion as it is reflected of the surfaces and objects in the room. Shot noise, $n(t)$, which is modelled as zero mean additive white Gaussian noise with a double-sided power spectral density (PSD) of $N_0/2$, and the interference noise, $m(t)$, is added to the received signal before detection. The receiver filter is matched to the transmit filter, such that the electrical passband is R_b. The output from the filter is then sampled at a rate R_b, and passed to the slicer with a threshold set at $RP_{av}T_b$.

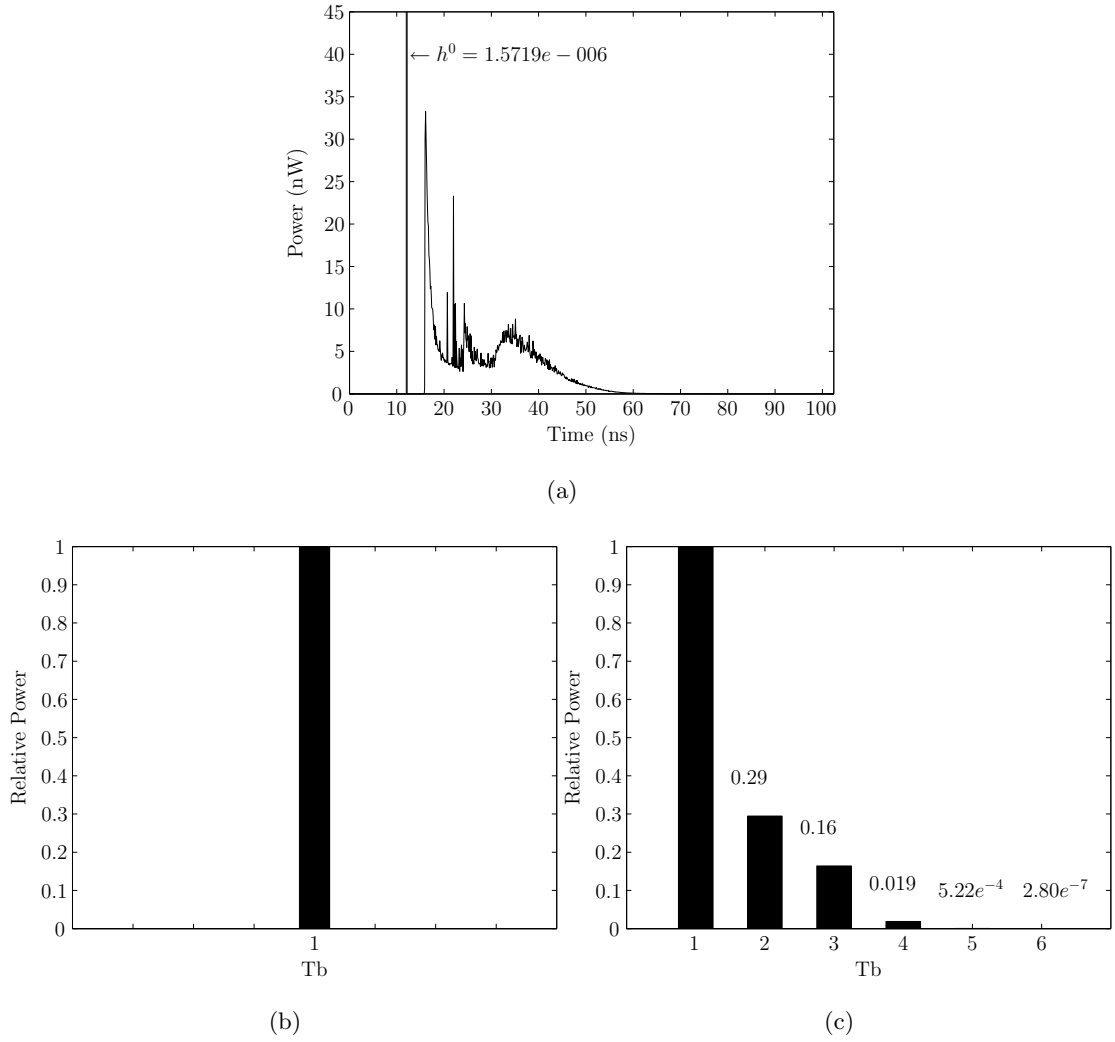

Figure 5.4: BER calculation modified impulse responses. (a) Original impulse response, bin width of 0.1 ns. (b) Normalised impulse response for a 2 Mbit s^{-1}, bin width of 500 ns. (c) Normalised impulse response for a 80 Mbit s^{-1} system, bin width of 12.5 ns.

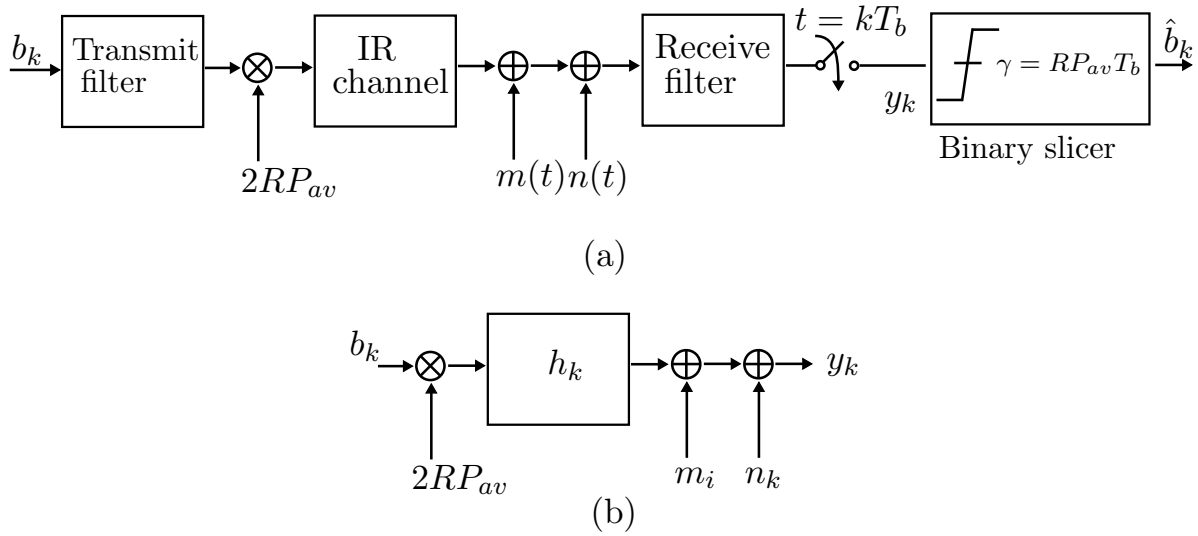

Figure 5.5: OOK system block diagram. (a) Continuous time OOK system. (b) Discrete time OOK system.

In discrete time, this can be modelled by figure 5.5(b), and the output, y_k is given by

$$\begin{aligned} y_k &= 2RP_{av}T_b b_k * h_k + n_k + m_i \\ &= 2RP_{av}T_b \sum_{j=0}^{X-1} b_k \beta_j + n_k + m_i \\ &= 2RP_{av}T_b b_k \beta_0 + 2RP_{av}T_b \sum_{1=0}^{X-1} b_{k-j}\beta_j + n_k + m_i \end{aligned} \tag{5.13}$$

X is the length of the discrete time equivalent impulse channel response. The first term in equation 5.13, is the component due to the desired signal, the second term is the component received from ISI effects, the third term is the ambient shot noise and the fourth term is the noise from interference sources.

5.3.3 Including Interference Noise

Section 5.2 detailed the general noise model for use here. At this stage of the work, a slight variation on the noise model presented so far will be used. The noise current, $m(t)$ is given by

$$\begin{aligned} m(t) =& RP_m \\ &+ \frac{RP_m}{A_2} \sum_{i=1}^{20} \left[b_i \cos\left(2\pi(100i - 50)t + \varphi_i\right) + c_i \cos\left(2\pi 100it + \zeta_i\right) \right] \\ &+ \frac{RP_m}{A_4} \sum_{j=1}^{22} d_j \cos\left(2\pi f_{\text{high}} jt + \theta_j\right) \end{aligned} \tag{5.14}$$

Where all the symbols take on the same meaning and values as presented in section 5.2. The first, second and third terms in equation 5.14 represent the mean interference, the interference due to fluorescent lights with conventional ballasts and from electronic ballasts, respectively. There is some uncertainty as to why, incandescent lamps were omitted from their analysis. The only logical reason is that due to the low harmonics they generate, and the use of, a relatively faster bit rate, the interference did not affect the system that much . m_i as presented in equation 5.13 is given by

$$m_i = \int_t^{t+T_b} m(\tau) d\tau = v_i T_b \tag{5.15}$$

Where v_i is constant over the duration T_b. It should be noted at this stage that there is a slight, but justified, simplification in the position of $m(t)$, or m_k in discrete time, within the system block diagram of figures 5.5 (a) and (b), but this will be highlighted in section 5.3.3.

5.3.4 SNR and BER Equations

The system BER performance is evaluated in terms of the ratio $\text{SNR}_o = P_{av}/P_n$, where P_{av} is the average optical power of the input signal and $P_n = \sqrt{N_0/2T_b}/R$ is the average optical power with a noise equivalent signal of bandwidth $1/T_b$. Substituting yields

$$\text{SNR}_o = RP_{av}\sqrt{\frac{2T_b}{N_0}} = \sqrt{\text{SNR}} \tag{5.16}$$

Where SNR is the electrical SNR at the correlator output. The BER is then given by

$$\mathrm{BER} = Q\left(\sqrt{\mathrm{SNR}}\right) = Q\left(\mathrm{SNR}_o\right) \tag{5.17}$$

Where Q is the Marcum function

$$Q(x) = \frac{1}{\sqrt{2\pi}} \int_x^\infty e^{\frac{t^2}{2}} dt \tag{5.18}$$

To include the effects of multipath, or ISI, into the BER equations, let the present bit of the system be denoted by $b_0 \in \{1, 0\}$, and still assuming that a 1 and a 0 bit are IID, by averaging over all possible combinations of bit sequences $\mathbf{b}$ of length $X-1$, the BER is given by [172]

$$\begin{aligned} \mathrm{BER} = & \frac{1}{2^X} \sum_{\mathbf{b}} \left\{ Q\left[RP_{av} \sqrt{\frac{2T_b}{N_0}} \left(2\beta_0 - 1 + 2 \sum_{j=1}^{X-1} b_{k-j}\beta_j \right) \right] \right. \\ & \left. + Q\left[RP_{av} \sqrt{\frac{2T_b}{N_0}} \left(1 - 2 \sum_{j=1}^{X-1} b_{k-j}\beta_j \right) \right] \right\} \end{aligned} \tag{5.19}$$

At this point, a very interesting observation was made when attempts to implement equation 5.19 within the previously developed simulation package were carried out. The validation of the equation within the simulation is an important stage in checking the implementation, however, the results generated were always several dB's less than what was previously published in [172]. After investigation the problem seemed to be with the impulse response reshaping described in section 5.3.1. For a low bit rate system, such as transmission at $2, 10, 20\mathrm{Mbit\,s^{-1}}$, where the bit duration is longer than the impulse response train, and subsequently $\beta_0 = 1$ and $\beta_j = 0 \forall j > 1$, the BER results, as shown by the solid line in figure 5.6(a), agreed with published results. For a higher bit rate system, such as $80\,\mathrm{Mbit\,s^{-1}}$, the value of $\beta_j \forall j > 0$ will be dependent upon the original impulse response calculations, which are, as shown in section 2.5, dependent upon the ΔA, the segmentation level of the third order component.

The top trace in figure 5.6(b), using the lower resolution of $\Delta A = 1$, shows the received power from the third component, i.e just the power undergoing 3 reflections, of the impulse response, and it sums to be 597 nW. The lower plot of figure 5.6(b), shows the same third component of

the impulse response, but using a resolution of $\Delta A = 2$, and this response sums to 492 nW. Not only is received power higher when using a lower resolution but the shape is different. When this response is then recomposed into the new discrete time response, essentially a higher proportion of power is in the tail of the total impulse response, thus skewing the results to the effect that equation 5.19 interprets a higher level of ISI than is actually present. From figure 5.6(a), by increasing the resolution to higher levels of $\Delta A = \{1, 2, 3, 4, 5\}$ requires a SNR of $\{19.7, 16.3, 15.8, 15.6, 15.5\}$dB to achieve a BER of 10^{-6}, respectively. From this analysis it would appear K. K. Wong *et al.* used a resolution of $\Delta A < 1$.

It is important to reiterate that with the analysis carried out, the segmentation of the first and second components did not affect the results. In this work a value of $\Delta A = 2$, will still be maintained as it ascertains what is believed to be the best compromise between accuracy of results and computational effort both now and as was previously shown in section 2.5. One justifiable reason why K. K. Wong *et al.* used a resolution of $\Delta A < 1$, is that the work was carried out in 1990, when the computational effort would have been even longer, possibly ≈ 24 h for one source and receiver combination.

5.3.5 Including Interference

The interference is periodic, with period T_i, and so the BER can can be found by averaging the average of all combinations of previous bit sequences $\mathbf{b}$, of length $X - 1$, and is given by

$$\begin{aligned}\text{BER} = &\frac{1}{T_i}\int_{t_0}^{t_0+T_i}\frac{1}{2^X}\sum_{\mathbf{b}}\left\{Q\left[RP_{av}\sqrt{\frac{2T_b}{N_0}}\left(2\beta_0 - 1 + 2\sum_{j=1}^{X-1} b_{k-j}\beta_j + \frac{v_i}{RP_{av}}\right)\right]\right. \\ &\left. +Q\left[RP_{av}\sqrt{\frac{2T_b}{N_0}}\left(1 - 2\sum_{j=1}^{X-1} b_{k-j}\beta_j - \frac{v_i}{RP_{av}}\right)\right]\right\} dt\end{aligned} \tag{5.20}$$

Equation 5.20 is computationally intensive to solve. There is an approach however, that allows

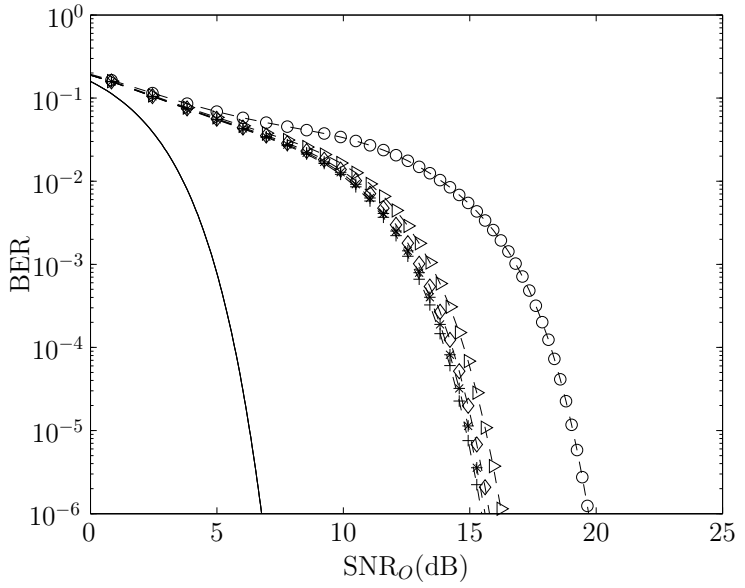

(a)

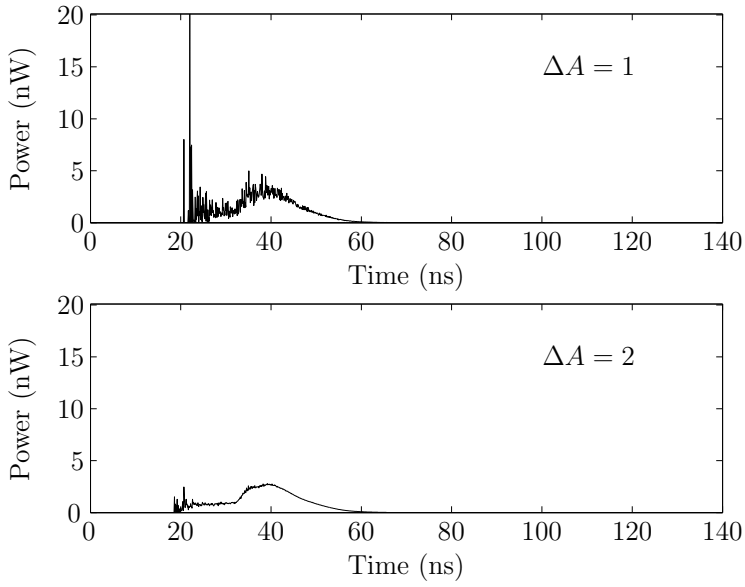

(b)

Figure 5.6: BER Vs. SNR for varying ΔA. (a) $2, 10, 20\text{Mbit}\,\text{s}^{-1}$, ΔA = independent,(—). $80\,\text{Mbit}\,\text{s}^{-1}$, $\Delta A = 1, (-\circ-)$, $\Delta A = 2, (-\triangleright-)$, $\Delta A = 3, (-\diamond-)$, $\Delta A = 4, (-*-)$, $\Delta A = 5, (-+-)$. (b) Third Order Component Powers for $\Delta A = 1$ (top), $\Delta A = 2$ (bottom).

the computation of the BER with interference in an acceptable manor. The analysis by K. K. Wong *et al.* was conducted by substituting the ratio $K = P_m/P_{av}$ into equation 5.14, such that, upon application of equation 5.15, v_i is given by

$$\begin{aligned} v_i =& \frac{1}{T_b}\int_t^{t+T_b} \{KRP_{av} \\ &+ \frac{KRP_{av}}{A_2}\sum_{i=1}^{20}\left[b_i\cos\left(2\pi(100i-50)t+\varphi_i\right)+c_i\cos\left(2\pi 100it+\zeta_i\right)\right] \\ &+ \frac{KRP_{av}}{A_4}\sum_{j=1}^{22} d_j\cos\left(2\pi f_{\text{high}}jt+\theta_j\right)\Bigg\} \end{aligned} \tag{5.21}$$

A higher value of K indicated a higher level of interference in proportion to the received noise power, but as equation 5.21 is proportional to RP_{av} and subsequently divided by RP_{av} in equation 5.20, v_i is essentially independent of the received power, and becomes a constant coefficient. Therefore instead of continually determining v_i, an interference scaling factor, N_i can be substituted resulting in the BER given by

$$\begin{aligned} \text{BER} =& \frac{1}{2^X}\sum_{\mathbf{b}}\Bigg\{Q\left[RP_{av}\sqrt{\frac{2T_b}{N_0}}\left(2\beta_0-1+2\sum_{j=1}^{X-1}b_{k-j}\beta_j+N_i\right)\right] \\ &+Q\left[RP_{av}\sqrt{\frac{2T_b}{N_0}}\left(1-2\sum_{j=1}^{X-1}b_{k-j}\beta_j-N_i\right)\right]\Bigg\} \end{aligned} \tag{5.22}$$

The substitution of N_i for v_i may seem incorrect upon first inspection. Intuitively, the magnitude of the interference noise is proportional to the optical power the source emits. However, the use of the matched receive filter in the block diagram of figure 5.5 (a), implies that the DC level of the noise interference is completely removed. If all sources emit the same optical power, thus the same magnitude of interference, all that needs to be determined is a suitable value of N_i that imposes the correct power penalty. To work out this level, the work by K. K. Wong *et al.* , was repeated as published (using the same spacial resolution factors), and values of N_i have been chosen that agree with both the published and experimental results presented.

Referring to figure 5.7, for the system running at $2, 10$ and $20\text{Mbit}\,\text{s}^{-1}$ without interference, there is, as before, no multipath penalty, requiring a SNR of 7.0 dB to achieve a BER of 10^{-6}.

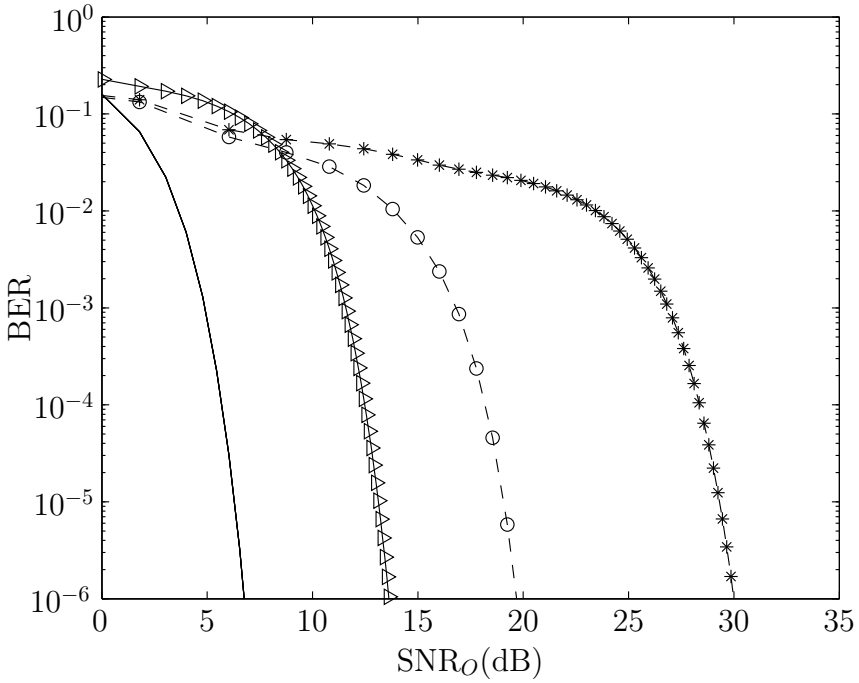

Figure 5.7: BER Vs. SNR with interference. (—) $2, 10, 20\mathrm{Mbit\,s^{-1}}$, no interference. $(-\circ-)80\mathrm{Mbit\,s^{-1}}$, no interference. $(-\triangleright-)2, 10, 20\mathrm{Mbit\,s^{-1}}$, interference, $N_i = 0.8$. $(-*-)80\mathrm{Mbit\,s^{-1}}$, interference, $N_i = 0.04$.

At $80\,\mathrm{Mbit\,s^{-1}}$ a penalty of 12.7 dB is required to achieve the same BER. Including interference at a level $N_i = 0.8$, to the $2, 10$ and $20\mathrm{Mbit\,s^{-1}}$ signals the SNR required for a BER of 10^{-6} increases to 13.7 dB, a penalty of 6.7 dB. For the $80\mathrm{Mbit\,s^{-1}}$, and with a interference level of $N_i = 0.04$, the same BER requires an SNR of 30.0 dB, a 10.3 dB penalty. These two interference factors agree with the numbers set out in [172].

It can be seen from figure 5.7 that no BER floor was encountered. This is because the no SNR is not limited. Due to the use of filters that limit the noise to the bandwidth of the signal, it is possible to keep increasing the signal power, thus increasing SNR, thus improving BER.

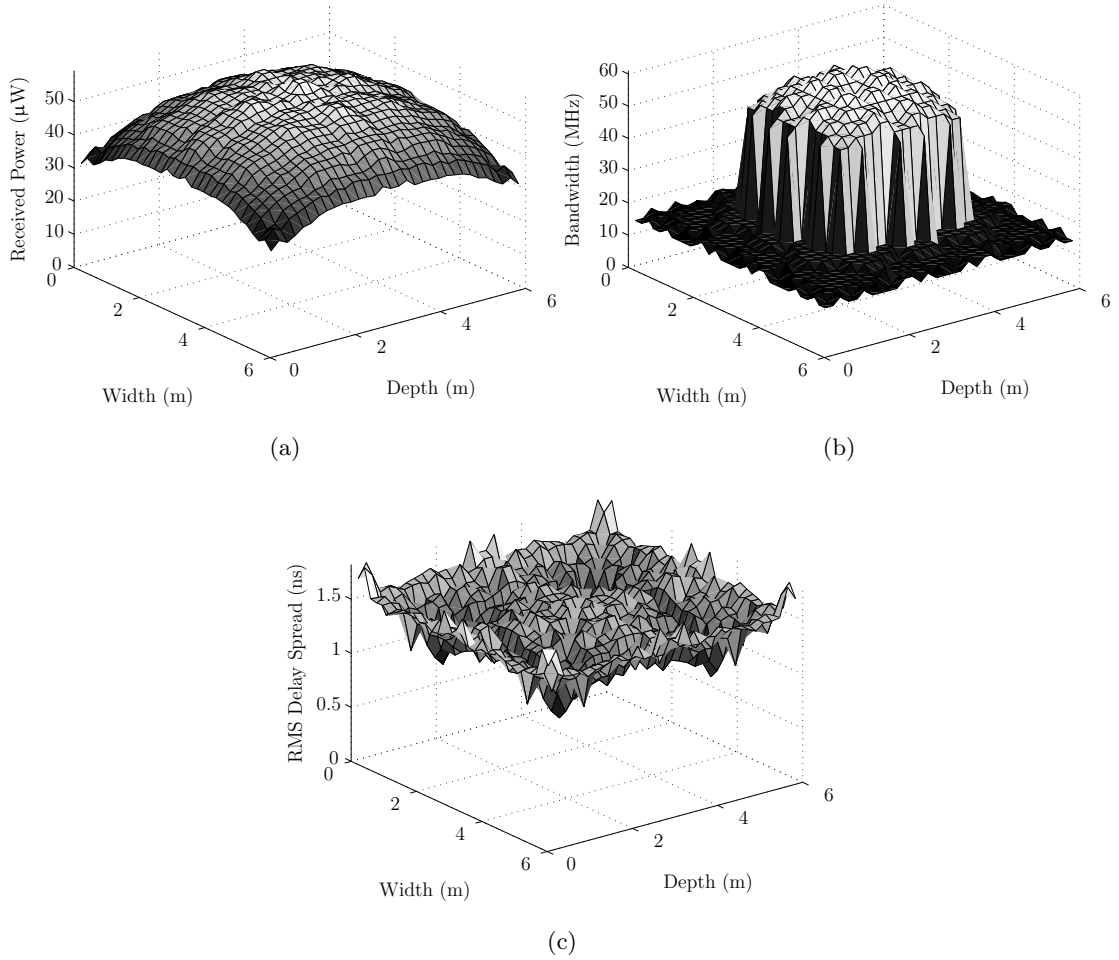

Figure 5.8: Non optimised signal environment 3. (a) Non optimised power. (b) Non optimised bandwidth. (c) Non optimised RMS delay spread.

5.4 The Signal and Noise Environment

To begin the investigation into the optimisation of the SNR or BER using the GA, environment 3, was set up firstly as the signal domain. The received, power, bandwidth and RMS delay spread can be seen in figure 5.8, where the the power ranges from 31.4 μW to 59.3 μW, a difference of 27.7 μW or, 47% deviation of peak power. The bandwidth varies between 14.6 MHz and 61.0 MHz whilst the RMS delay spread varies between 0.93 ns and 1.82 ns.

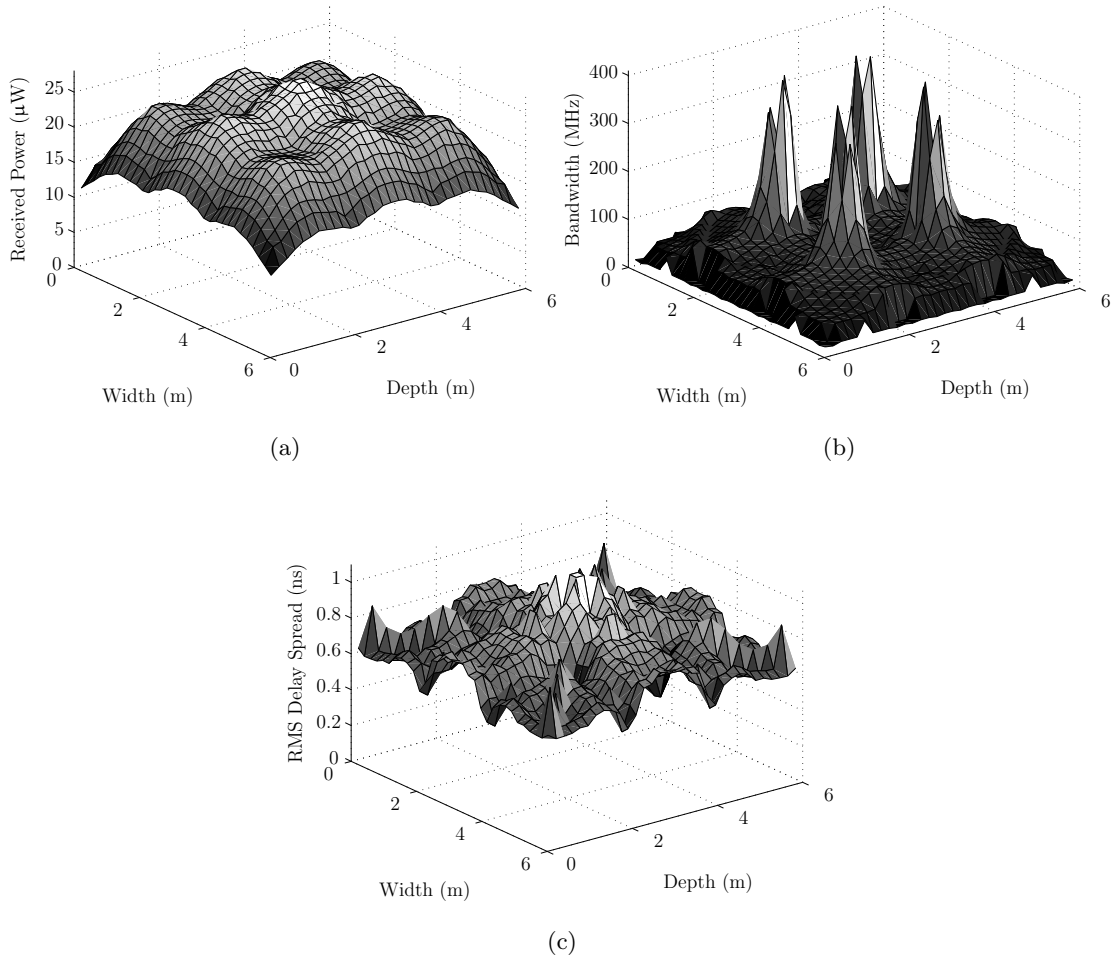

Figure 5.9: Noise environment 3. (a) Noise power. (b) Noise bandwidth. (c) Noise RMS delay spread.

In the same environment 3, upon the ceiling, 9 "GE Lighting R80 "lamps were evenly distributed. Each of these lamps has an electrical power of 65 W and a wide Lambertian order of $n = 2.64$ [170]. Although the electrical power is 65 W, for a comparison, optical power was set to 1 W, but as mentioned in section 5.2will be scaled later to fit realistic measured results. This noise signal was then simulated at all the receiver locations within the room. The results can be seen in figure 5.9. It is interesting to treat the noise as a signal in this way, as it can be seen that the noise power ranges from 11.4 μW to 28.0 μW, a difference of 16.6 μW or 60% of peak value. The noise bandwidth varies from 14.6 MHz to peaks higher than the resolution limits of the program.

The RMS delay spread varies between 0.44 ns and 1.10 ns.

5.5 Initial SNR and BER Distributions Estimates

Due to certain unknowns about the receiver design, including the optical filters used, the noise was manually increased to an optical power of 5 W, where the equivalent received noise power can be seen in figure 5.10(a). Here the received noise power varies between 56.8 μW and 140 μW. This value is comparable to the level of noise received under practical measurement found in [169]. The power of the signal sources was then set to 1 mW, resulting in a received signal power ranging between 31.4 nW and 59.3 nW.

The results of the SNR calculations based upon equation 5.16, can be seen in figures 5.10(c) and 5.10(d) for systems running at 2 Mbit s^{-1} and 80 Mbit s^{-1}, respectively. Under these conditions, at 2 Mbit s^{-1}, the SNR varies around the room between 10.0 dB and 11.1 dB, whilst for the 80 Mbit s^{-1} system there is a constant 8.0 dB reduction in SNR, as it varies between 2.0 dB and 3.1 dB.

In terms of the BER values, for this scenario, not considering multipath dispersion, figures 5.11(a) and 5.11(b), show two considerably extreme results when the system is running at 2 Mbit s^{-1} and 80 Mbit s^{-1}, respectively. At 2 Mbit s^{-1}, the BER is virtually zero, ranging from between 10^{-40} to 10^{-24}. At 80 Mbit s^{-1}, the BER is so close to 1, that the use of a log plot is not justified, having values ranging from between to 0.018 to 0.055. Including the multipath penalty, the BER of the 80 Mbit s^{-1} system is shown in figure 5.11(c), where the BER ranges from between 0.031 and 0.086. Finally figure 5.11(d) shows the increase in BER due to multipath. It can be seen that the change from one location to the next is not uniform like in the case of SNR as the multipath is dependent upon the impulse response which is different at different locations. The BER for the 2 Mbit s^{-1} system including multipath is identical to without as the bit rate is low enough for each bit to fit within the time of the impulse train so there are no penalties.

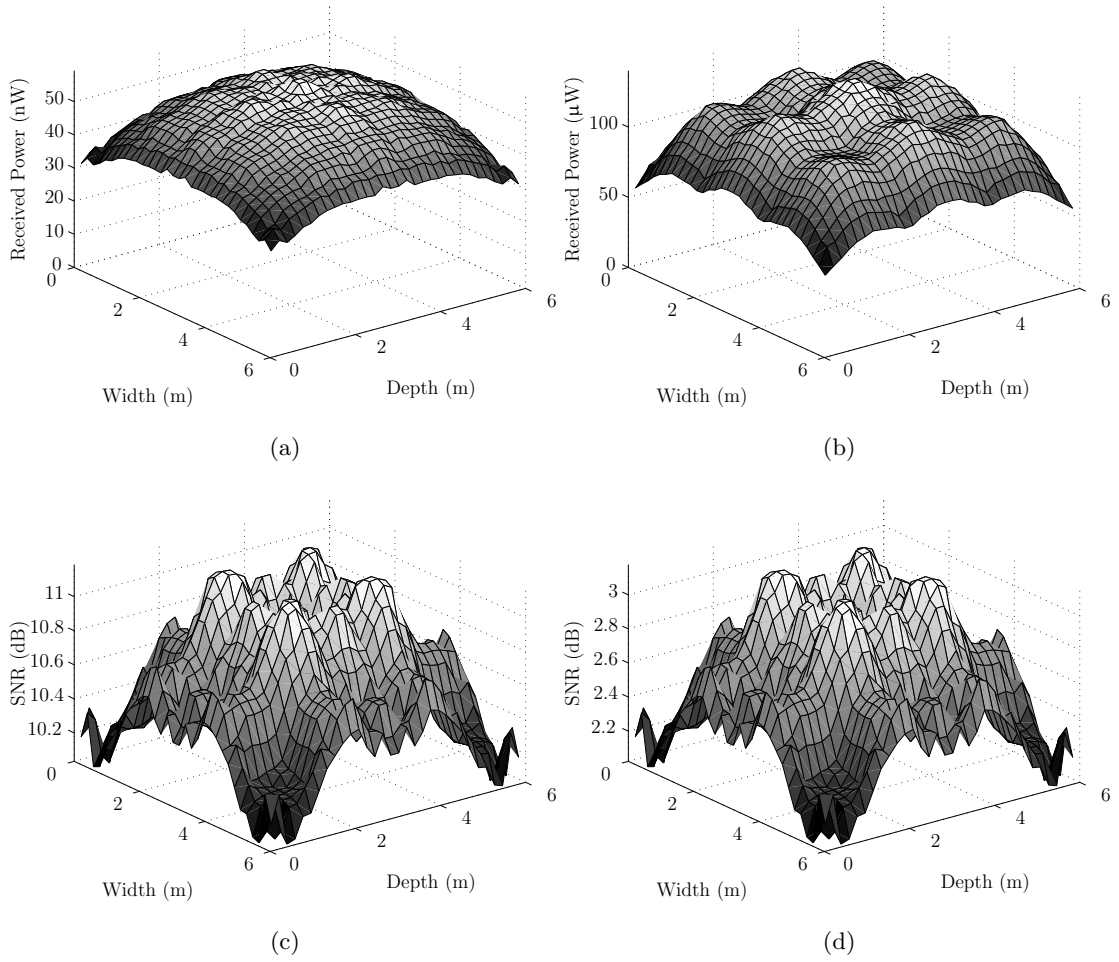

Figure 5.10: Initial SNR estimates. (a) Received signal from 1 mW sources. (b) Received noise power from 5 W sources. (c) 2 Mbit s^{-1} SNR. (d) 80 Mbit s^{-1} SNR.

Due to the magnitudes of the SNR and BER distributions around the room being so different to each other, it may be hard to not only form a general optimisation of the signal source power ratios, but also to explain the results or make useful comparisons. In order to form the general framework, or for a better comparison, the signal source powers of the 2 Mbit s^{-1} system were adjusted to 500 µW, and for the 80 Mbit s^{-1} system, the signal source powers were set to 3 mW, thus, by maintaining the noise source power to be 5 W, the SNR of both bit rate systems are very similar.

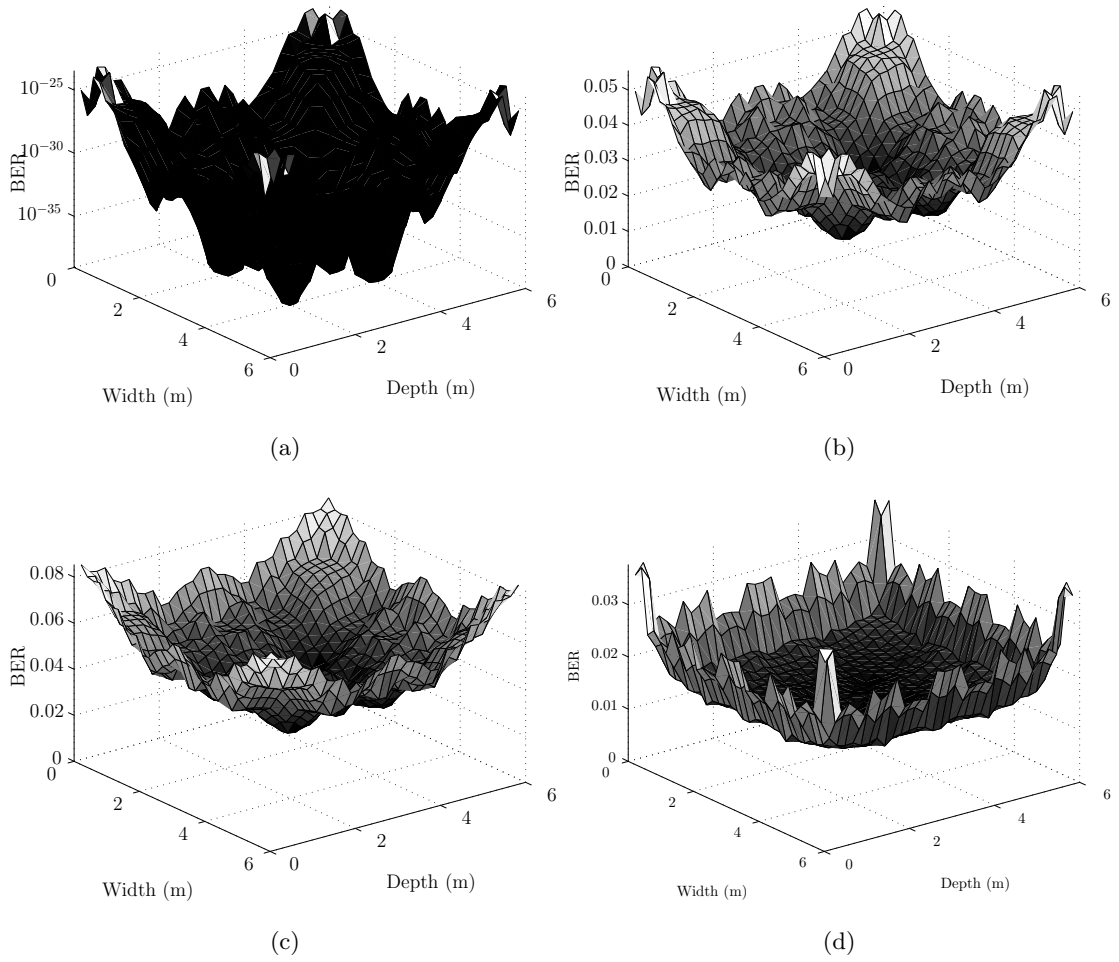

Figure 5.11: Initial BER estimates. (a) $2\,\mathrm{Mbit\,s^{-1}}$ BER, no multipath. (b) $80\,\mathrm{Mbit\,s^{-1}}$ BER, no multipath. (c) $80\,\mathrm{Mbit\,s^{-1}}$ BER with multipath. (d) Bit rate induced power BER penalty.

Figure 5.12(a) plots the received noise power, where it can be seen the power varies between $56.8\,\mu\mathrm{W}$ and $140\,\mu\mathrm{W}$. Figure 5.12(b) and 5.12(c) show the new adjusted received signal powers for the $2\,\mathrm{Mbit\,s^{-1}}$ and $80\,\mathrm{Mbit\,s^{-1}}$ systems which vary between $15.7\,\mathrm{nW}$ and $30.0\,\mathrm{nW}$, and between $94.2\,\mathrm{nW}$ and $178\,\mathrm{nW}$, respectively. Figures 5.12(d) and 5.12(e) show the now, very nearly identical SNR distribution varying between $7.0\,\mathrm{dB}$ and $8.2\,\mathrm{dB}$. Figures 5.13(b) shows the BER for the $2\,\mathrm{Mbit\,s^{-1}}$ system including multipath, whilst figure 5.13(b) shows the BER for the $80\,\mathrm{Mbit\,s^{-1}}$ system. Figure 5.13(c) shows the penalty imposed purely by multipath, upon the

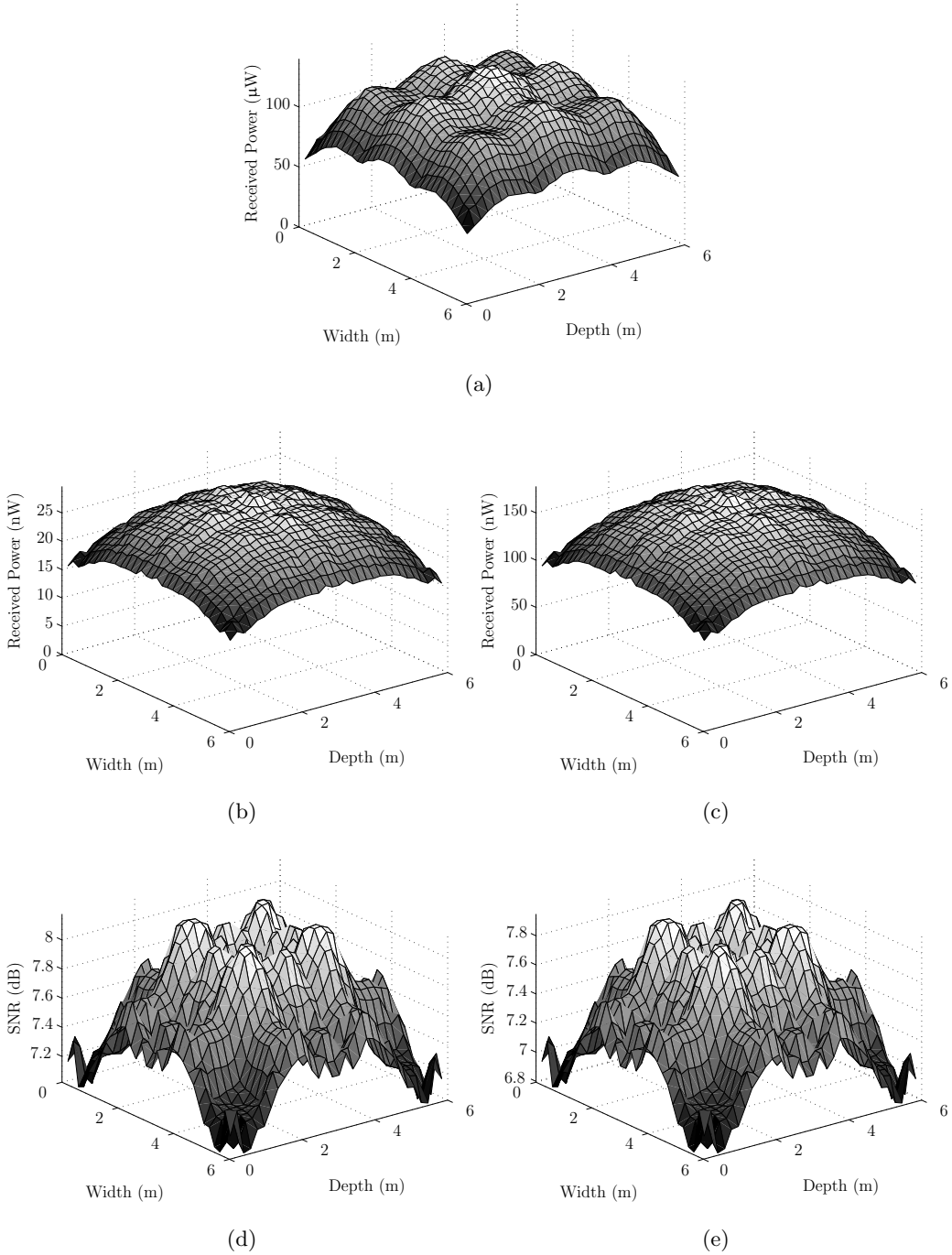

Figure 5.12: Signal source power modification for SNR comparison. (a) Received noise power. (b) Received signal power, $2\,\mathrm{Mbit\,s^{-1}}$. (c) Received signal power, $80\,\mathrm{Mbit\,s^{-1}}$. (d) SNR at $2\,\mathrm{Mbit\,s^{-1}}$. (e) SNR at $80\,\mathrm{Mbit\,s^{-1}}$.

$80\,\mathrm{Mbit\,s^{-1}}$ system which by inspection is very similar to the actual BER with multipath, ranging between 10^{-6} and 0.005, due to the non multipath penalty being so small, ranging between 10^{-11} and 10^{-7}.

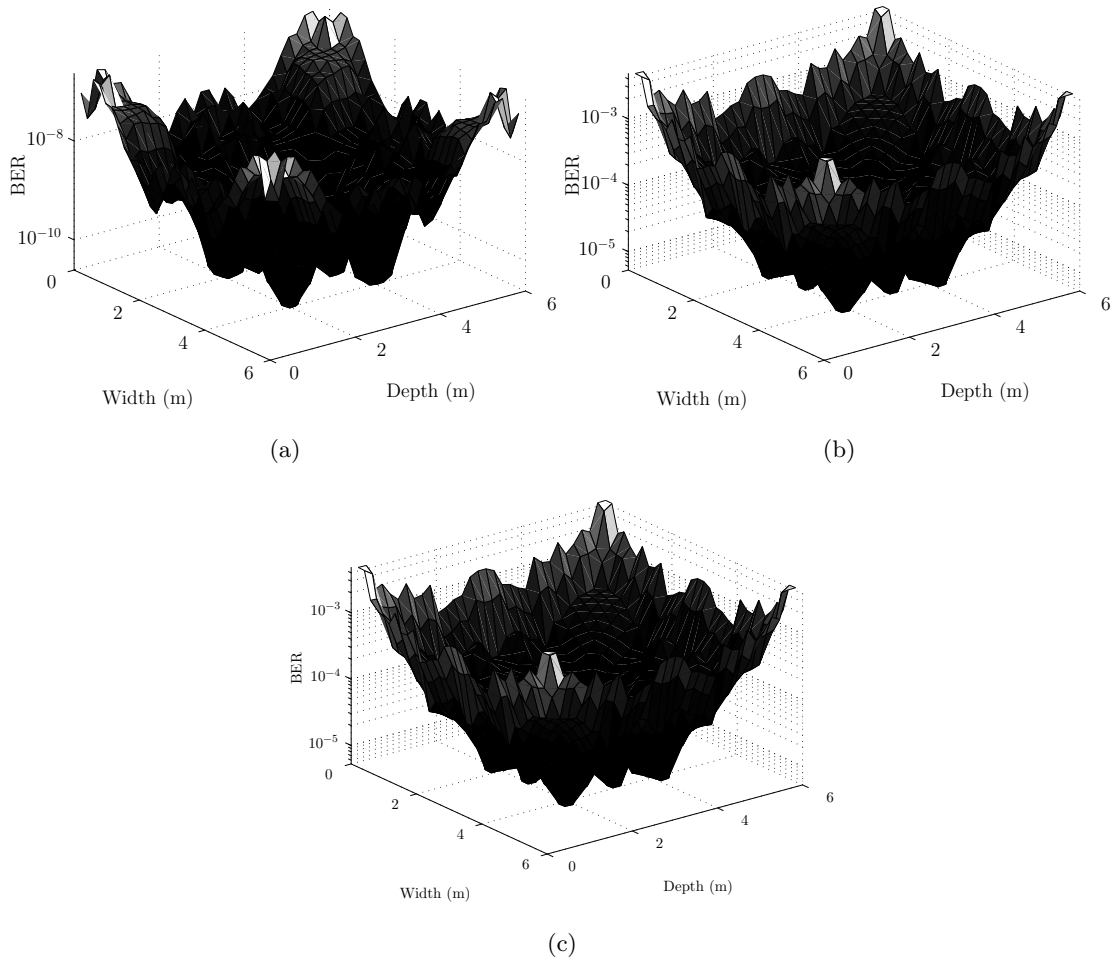

Figure 5.13: Signal source power modification for BER comparison. (a) BER with multipath at $2\,\mathrm{Mbit\,s^{-1}}$. (b) BER with multipath at $80\,\mathrm{Mbit\,s^{-1}}$. (c) Reduction in BER due to multipath,$80\,\mathrm{Mbit\,s^{-1}}$.

5.6 Starting the SNR Optimisation

The aim of this chapter was to try and reduce the deviation in BER around the room. A uniform BER may aid in producing a uniform QoS, or at provide more predictable system performance. It has been shown in chapters 3 and 4 that there has been very little control of the received bandwidth. The worst case did not fluctuate much, but nor were any remarkable improvements seen either. This implies, that there will be very little control over the BER penalty imposed by the bandwidth limitations. It is wished to reduce the dynamic range of the BER, and due to this lack of bandwidth control, the first stage is to reduce the range of the SNR, at least then, one factor in equation 5.19 is accounted for. It can also be seen from figure 5.6(a) that a small reduction in the SNR can produce a larger reduction in the BER. Due to the satisfactory performance of the GAs already developed, they will carried forward to this application, but to account for SNR reduction, the only change required to the structure of algorithm 6 and algorithm 11, is a change in fitness function, which for this situation will be

$$F(\mathbf{a}_\nu) = 100 - \left(100\left(\frac{\max\left(\mathrm{SNR}\right) - \min\left(\mathrm{SNR}\right)}{\max\left(\mathrm{SNR}\right)}\right)\right) \tag{5.23}$$

Where the SNR for each position in the environment will be given by equation 5.16. Furthermore, the fitness function will use the real, not logarithmic values of the SNR.

For the first round of optimisations, algorithm 6, was applied to the source powers of the $2\,\mathrm{Mbit\,s^{-1}}$ system only, but the same resultant ratios were applied afterwards to the $80\,\mathrm{Mbit\,s^{-1}}$ system. The non optimised powers of figures 5.12(b) and 5.12(c), produced the optimised powers shown in figures 5.14(b) and 5.14(c), for the $2\,\mathrm{Mbit\,s^{-1}}$ and $80\,\mathrm{Mbit\,s^{-1}}$ systems respectively. For the $2\,\mathrm{Mbit\,s^{-1}}$ system the received power now ranges between 11.4 nW and 18.3 nW, a variation of 6.9 nW or 37% of peak power. For the $80\,\mathrm{Mbit\,s^{-1}}$ system the power ranges between 68.7 nW and 109 nW, a deviation of 40.3 nW, or 37% of peak power. Note how the application of the GA to one system, actually meant, due to the channel being linear, and thus the actual source power being independent, the deviation, in percentage terms is the same. This

also results in approximately the same SNR distribution for both systems, as in figures 5.14(d) and 5.14(e), where it ranges between 5.67 dB and 6.25 dB, or $\approx 9\%$. This is, in real numbers a variation between 3.69 and 4.22, a range of 0.53 or 11% of peak value. Figure 5.15(a), shows the optimised BER of between 10^5 and 10^{-4} for the $2\,\mathrm{Mbit\,s^{-1}}$ system, whilst for the $80\,\mathrm{Mbit\,s^{-1}}$ system the BER, including multipath, ranges between 10^{-4} and 0.01, as shown in figure 5.15(b). Figure 5.15(c) shows the penalty due to multipath distortion, which, due to the channel being bandwidth limited, means the BER also ranges between 10^{-4} and 0.01.

Comparing the optimised and non optimised distributions, for the $2\,\mathrm{Mbit\,s^{-1}}$ system the change in received power deviation has reduced from 47% to 37%, whilst the deviation of the $80\,\mathrm{Mbit\,s^{-1}}$ system has also, as expected, reduced from 47% deviation to 37%. This reduction in received power has led to a reduction in the SNR, in real terms, from 23% to 11%, to produce, in decibel terms, a variation reduction from $\approx 14\%$ to $\approx 9\%$. Unfortunately the BER cannot be quantified as a reduction in percentage terms. The range is to high to make it sensible to quantify it this way. Also due to the change in magnitude of the SNR, the BER has been affected by that measure alone, as well as the change due to the optimisation of the uniformity.

What is required at this stage is some factor that is already normalised to see how the optimisation affects the BER. From equation 5.19, the term responsible for multipath

$$\sum_{j=1}^{X-1} b_{k-j}\beta_j \tag{5.24}$$

is already normalised. It is also known that whilst the optimised bandwidth is not affected much, it is affected, which is due to a change in the impulse response. From equation 3.5, for a given receiver, say $\mathcal{R}_1$, and where $\hat{a}_i$ is the set of non optimised ratios and a_i is the set of optimised ratios

$$\sum_{i=1}^{I} \hat{a}_i h(t;\mathcal{S}_i,\mathcal{R}_1) \neq \sum_{i=1}^{I} a_i h(t;\mathcal{S}_i,\mathcal{R}_1) \text{ for } \hat{a}_i \neq a_i \tag{5.25}$$

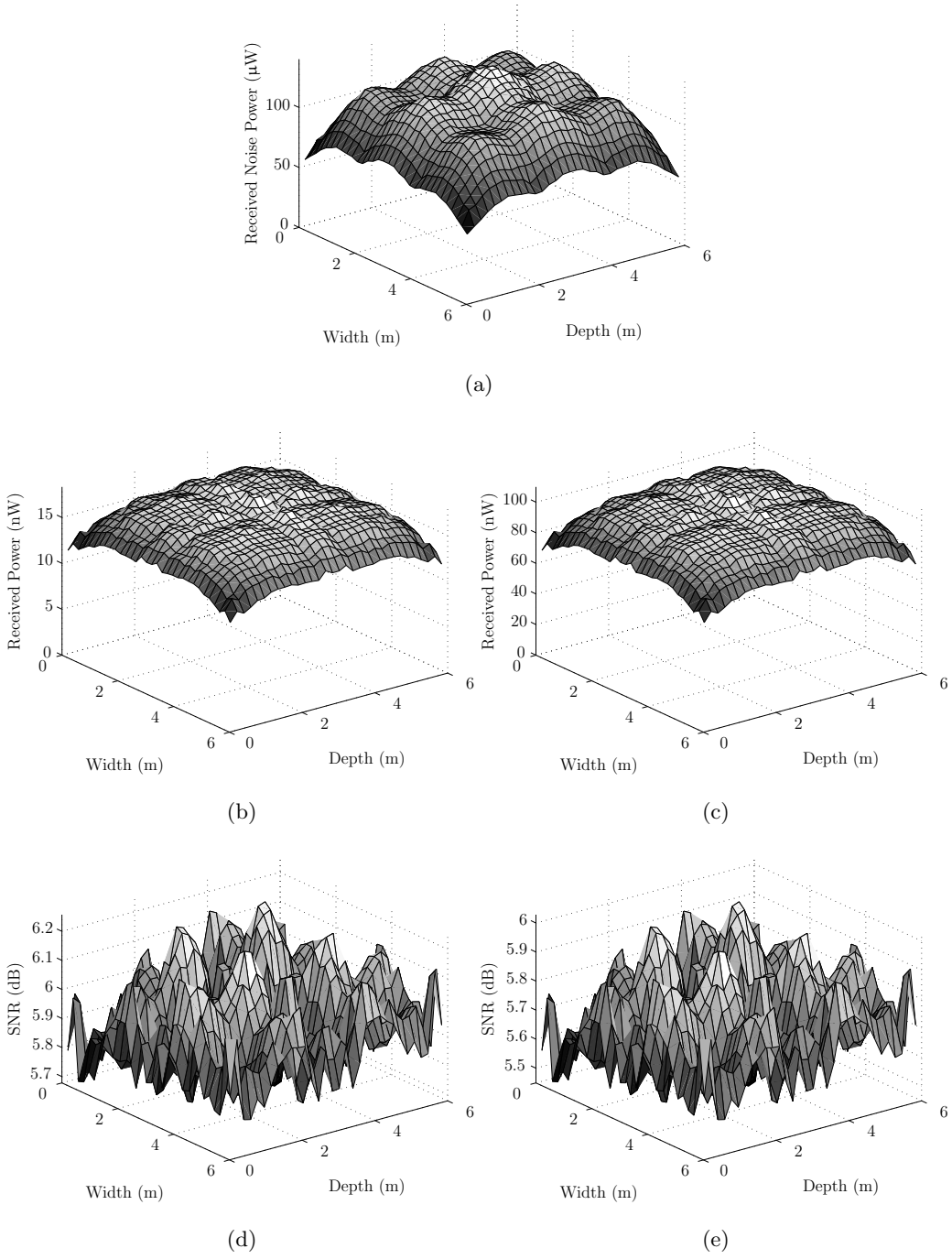

Figure 5.14: Optimised noisy empty environment 3. (a) Noise power. (b) $2\,\mathrm{Mbit\,s^{-1}}$ system received power. (c) $80\,\mathrm{Mbit\,s^{-1}}$ system received power. (d) $2\,\mathrm{Mbit\,s^{-1}}$ SNR. (e) $80\,\mathrm{Mbit\,s^{-1}}$ SNR.

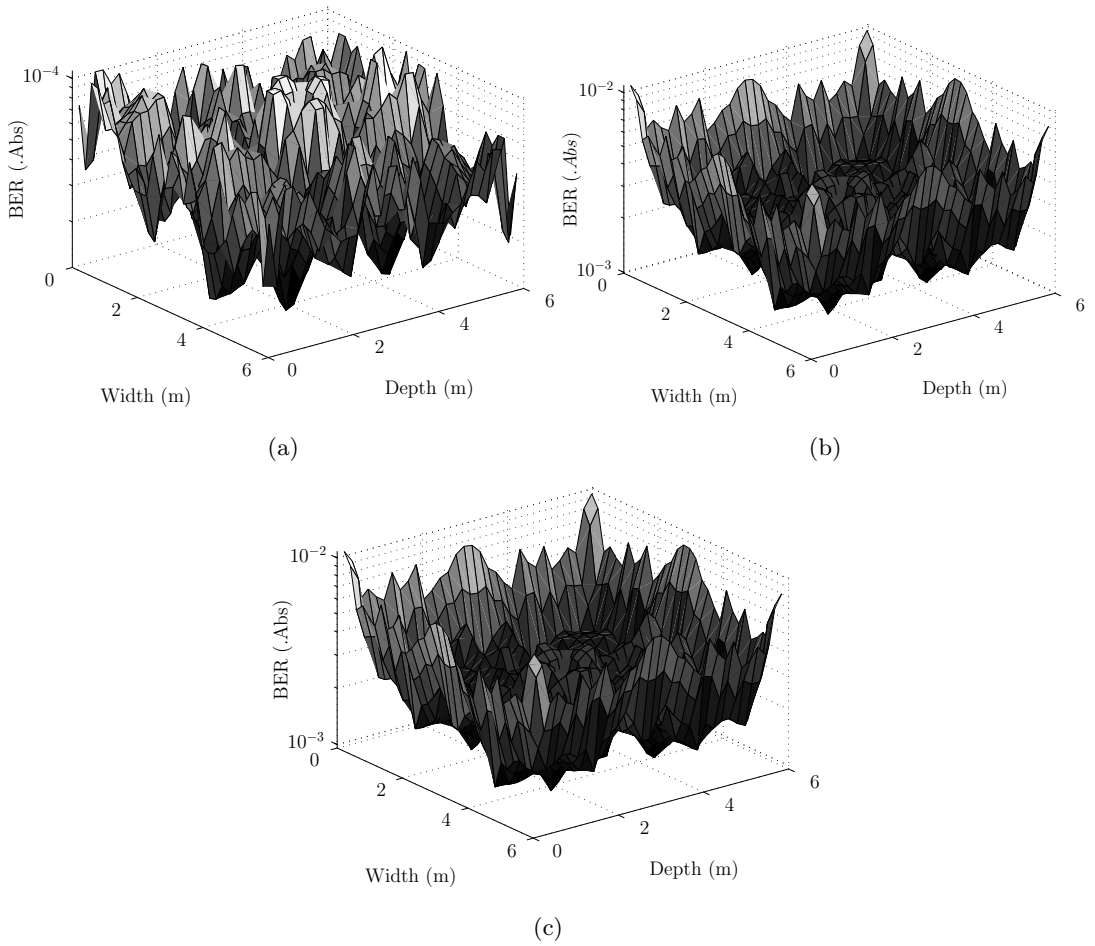

Figure 5.15: Optimised noisy empty environment 3 BER values. (a) $2\,\mathrm{Mbit\,s^{-1}}$ BER with multipath. (b) $80\,\mathrm{Mbit\,s^{-1}}$ system BER with multipath. (c) BER penalty due to multipath.

Which implies that therefore

$$\sum_{j=1}^{X-1} b_{k-j}\beta_j \neq \sum_{j=1}^{X-1} b_{k-j}\beta_j \text{for } \hat{a}_i \neq a_i \tag{5.26}$$

To give an example of how the ratios change this function, a constant SNR $= 6$ (Abs.), was assumed. The ratios from the previous optimisation attempt, in figure 5.14, were then used to modify the impulse response. As the scheme is normalised, this is mathematically correct to do. Figure 5.16(a) and 5.16(b) show the result of equation 5.24 at each location within the room, for the non optimised and optimised scenarios respectively. Figure 5.16(c) shows the difference in

the values, defined to be the non optimised minus the optimised, such that the positive numbers imply equation 5.24 is lower for the optimised response. The associated BER for the non optimised and optimised cases, are shown in figures 5.16(d) and 5.16(e). Finally the ratio of the non optimised over the optimised version is shown in figure 5.16(f), where the higher the number, the higher the ratio reduction in BER at that location. For example at the receiver location of the highest ratio, $x = 5.9\,\mathrm{m}, y = 5.53\,\mathrm{m}, z = 1\,\mathrm{m}$, the non optimised BER is 3.84×10^{-4}, whilst the optimised BER is 9.90×10^{-5}, resulting in a 3.9 factor of improvement at this location. It can be seen that there are locations within the room, where the ratio is < 1, resulting in an increase in BER due to the optimisation. Over the space of the room, there are 515 locations where the ratio is > 1, an improvement or reduction in BER, and there are 505 locations where the ratio is < 1, a decrease in BER. These results show good consistency with, for example, figure 4.1, where the optimisation was shown to cause a bandwidth reduction in the interior of the room, and an improvement towards the corners and walls.

In terms of how the algorithm reaches it solution, figure 5.17 shows the convergence curves for both algorithm 6 and algorithm 11. Algorithm 6, conververges slowly, but in a predictable manner towards its final convergence point of a SNR deviation of 12%. Algorithm 11 reduces very quickly from the original 23% SNR deviation to 12.6%. As is consistently seen when comparing algorithms 6 and 11, algorithm 6 outperforms it, but only slowly. The traits that algorithm 11 has to quickly but sub optimally converge still holds in this application.

Looking at how the GA performs under movement, a user was simulated undergoing movement pattern 1 within the environment and is shown in figure 5.18. The user induces a perturbation to the SNR, and during the movement, for the non optimised case, the SNR deviation from peak power can range between 24% and 57%. Using the GA, this is reduced to vary between 13% and 51%. For these results, when under movement the use of either algorithm 6 or algorithm 11 does not make much difference. The degree to which they can optimise is almost identical

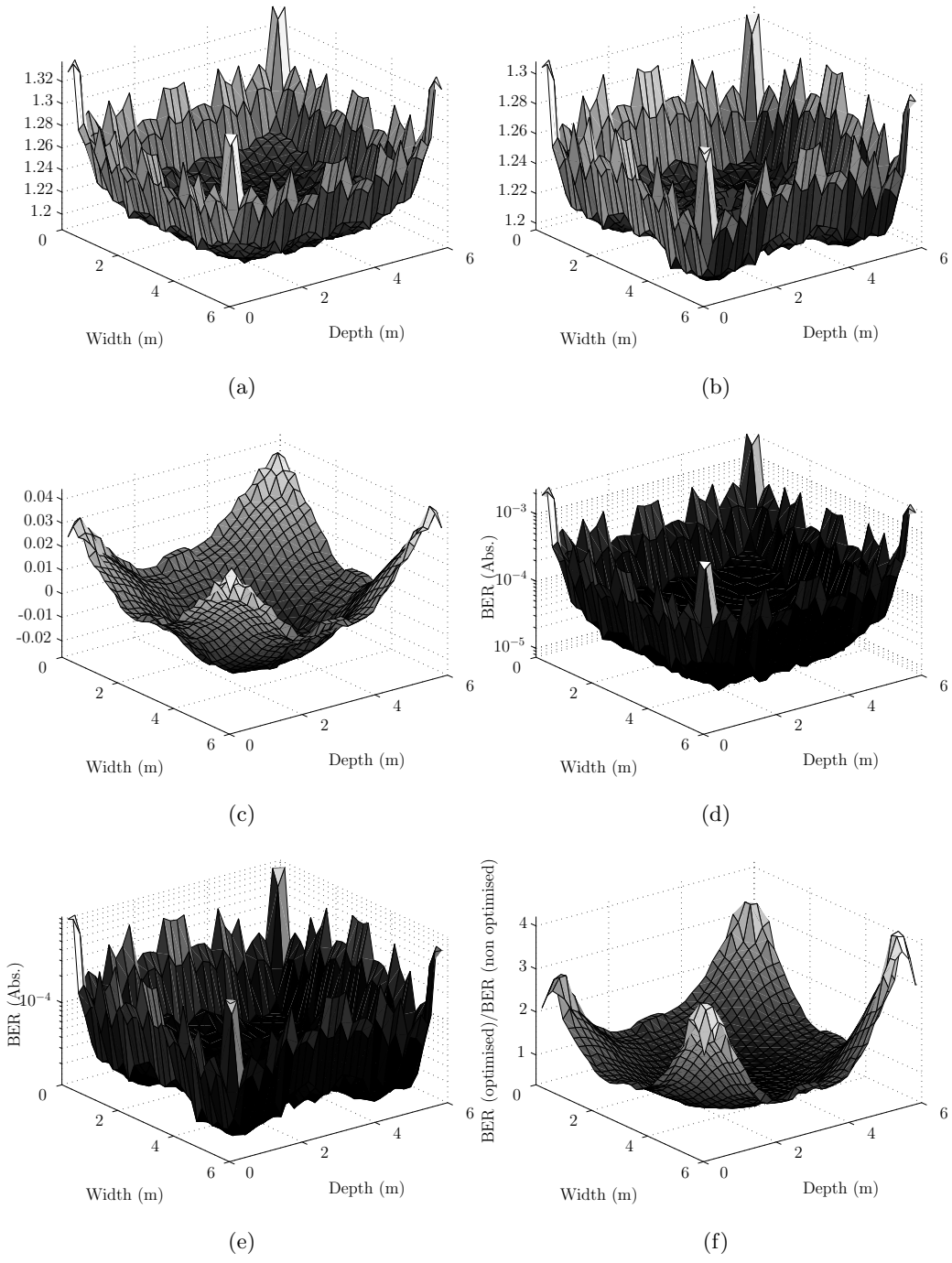

Figure 5.16: Comparison of the beta factor under optimisation. (a) Non optimised beta factor. (b) Optimised beta factor. (c) Non optimised beta minus optimised beta. (d) Non optimised BER. (e) Optimised BER. (f) Non optimised beta / optimised beta.

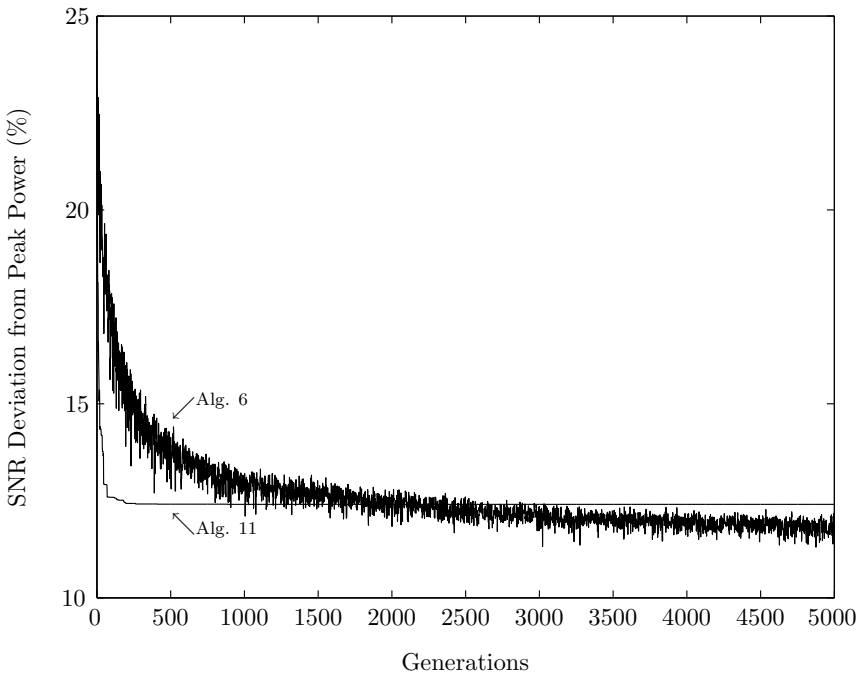

Figure 5.17: Comparison of Algorithm 6 and 11 for SNR optimisation.

except in position 9.

5.7 A Second Room and a Second Movement Pattern

As it is important to show the change in noise distribution, or to show how not only the room can change the distribution, but the type of sources also, in the same environment 3 with the same transmitter configuration, six fluorescent lights were this time placed on the ceiling. A good approximation to the spatial model for fluorescent strip lights, similar to the ones found in offices, is to approximate them with an array of Lambertian sources evenly spaced at 10 cm gaps across the effective length of the tube [173]. In this scenario, 6 tubes, each of length 60 cm, were placed across the ceiling, such that in total 36 Lambertian sources were used for the simulation. The intensity characteristics of the strip lamps are, in general, varying, due mainly to the type of reflector housing the lamps are situated within. Some are made to be very directive, whilst

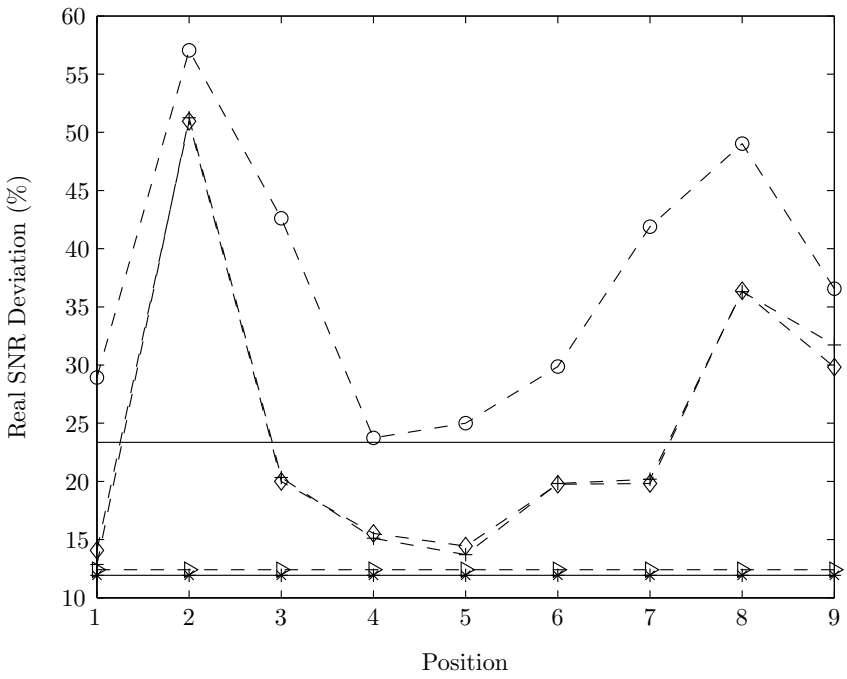

Figure 5.18: SNR optimisation of dynamic environment 3, movement pattern 1. (—) Non optimised empty room. $(-\triangleright-)$ optimised empty room Alg 11. $(-*-)$ optimised empty room Alg 6. $(-\circ-)$ non optimised dynamic environment. $(-\diamond-)$ optimised dynamic environment Alg 6. $(-+-)$ optimised dynamic environment Alg 11.

others are made to illuminate a room evenly, as in this case, each source will have a Lambertian profile of $n = 1$ [174].

Figures 5.19 and 5.20 provide the key results for this scenario. Each of the 6 Lambertian sources used to approximate one fluorescent tube has an optical noise power of 4 W [173, 114], and the received noise power can be seen in figure 5.19(a), varying between 122 µW and 534 µW. For the 2 Mbit s^{-1} system, the sources were given a power of 1 mW, and for the 80 Mbit s^{-1}, the sources were given a power of 6 mW, so the power can be seen ranging between 31 nW and 59 nW, and between 180 nW and 356 nW in figures, 5.19(b) and 5.19(c) respectively.

The SNR distributions in figures 5.19(d) and 5.19(e) have some interesting properties. Although it possibly could not be seen from the received noise power, where the lamps were upon the ceiling, these two figures together clearly show the points above which the lamps reside. There are two peaks of high SNR, where due to the FOV of the receiver, the radiation from one side of lamps is not incident upon the receiver, but in the middle of the room, where both sets of lamps decrease the SNR considerably. The choice in source powers means the SNR distributions are very similar allowing for better comparison. Also note that for this system, to transmit at the increased rate of $80\,\mathrm{Mbit\,s^{-1}}$ required each source to transmit an extra 5 mW of power.

The BER results for the $2\,\mathrm{Mbit\,s^{-1}}$ and $80\,\mathrm{Mbit\,s^{-1}}$ systems are shown in figures 5.20(a) and 5.20(b), respectively. These BER results are still without interference, where for the $2\,\mathrm{Mbit\,s^{-1}}$, the BER varies between 10^{-16} and 10^{-10}. For the $80\,\mathrm{Mbit\,s^{-1}}$ system, this is reduced to the range of 10^{-7} and 10^{-3}.

Adding interference at a rate $N_i = 0.1$, the BER for the $2\,\mathrm{Mbit\,s^{-1}}$ and $80\,\mathrm{Mbit\,s^{-1}}$ systems can be seen in figures 5.21(a) and 5.21(b) ranging between 10^{-14} and 10^{-8}, and between 10^{-6} and 0.0055. Even this small level of interference has caused a considerable effect upon the BER rates.

Algorithm 6 was then applied to the scenario to test further the optimisation performance of the GA. The results can be seen in figures 5.22 and 5.23. Figure 5.22(a) reaffirms the received noise power varying between 122 µW and 534 µW. Figures 5.22(b) and 5.22(c) show the received signal power for the $2\,\mathrm{Mbit\,s^{-1}}$ and $80\,\mathrm{Mbit\,s^{-1}}$ systems, varying between 19 nW and 43 nW, and between 115 nW and 261 nW. Comparing the optimised and non optimised distributions, for the $2\,\mathrm{Mbit\,s^{-1}}$ system the change in received power deviation has reduced from a 77% to 55%, whilst the deviation of the $80\,\mathrm{Mbit\,s^{-1}}$ system has also, as expected, reduced from 77% deviation to 55%. This reduction in received power has led to a reduction in the SNR, in real terms, from 26% to 17%, to produce, in decibel terms, a variation reduction from $\approx 15\%$ to $\approx 12\%$. The

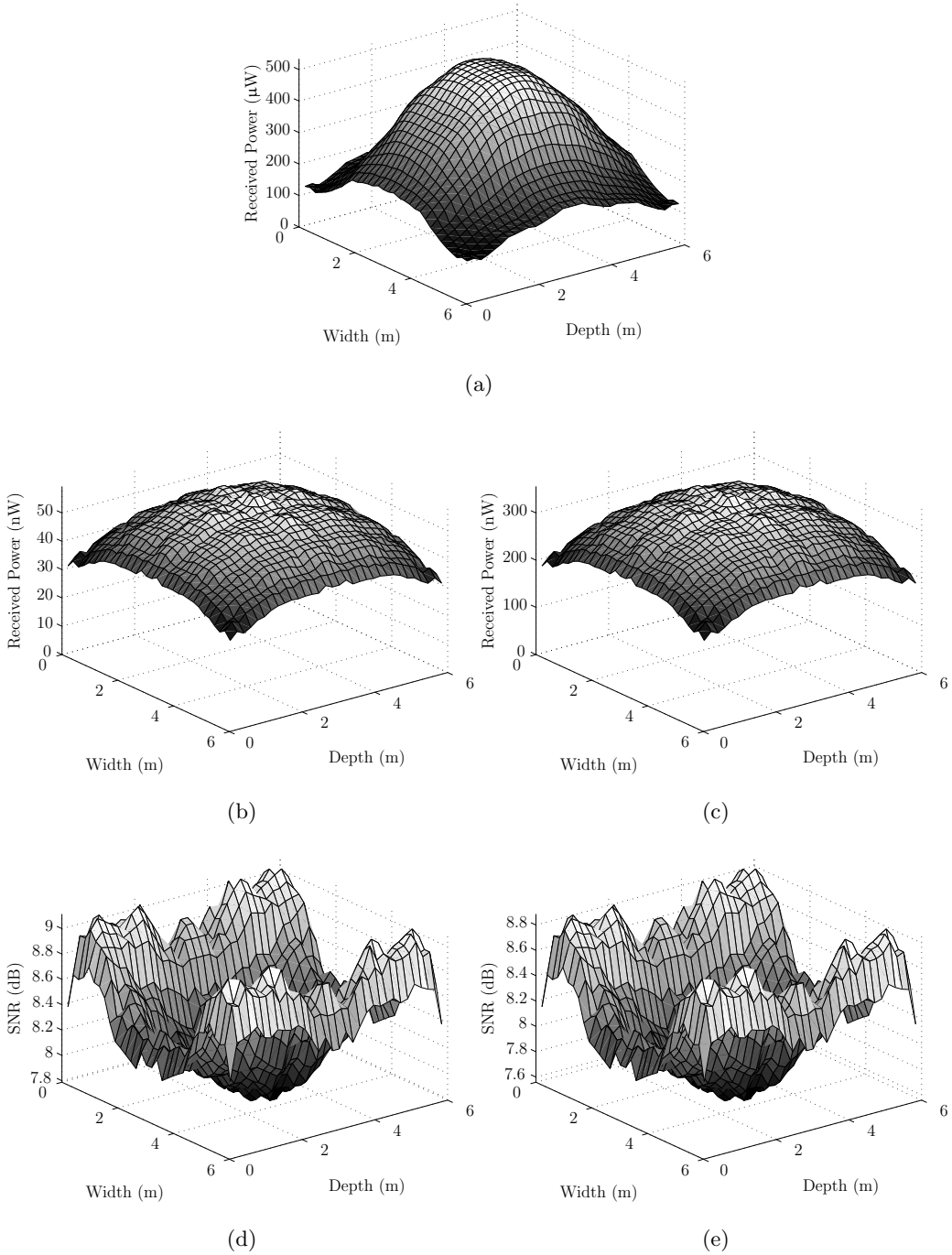

Figure 5.19: Signal source power modification for SNR comparison. (a) Received noise power. (b) Received signal power, $2\,\mathrm{Mbit\,s^{-1}}$. (c) Received signal power, $80\,\mathrm{Mbit\,s^{-1}}$. (d) SNR at $2\,\mathrm{Mbit\,s^{-1}}$. (e) SNR at $80\,\mathrm{Mbit\,s^{-1}}$.

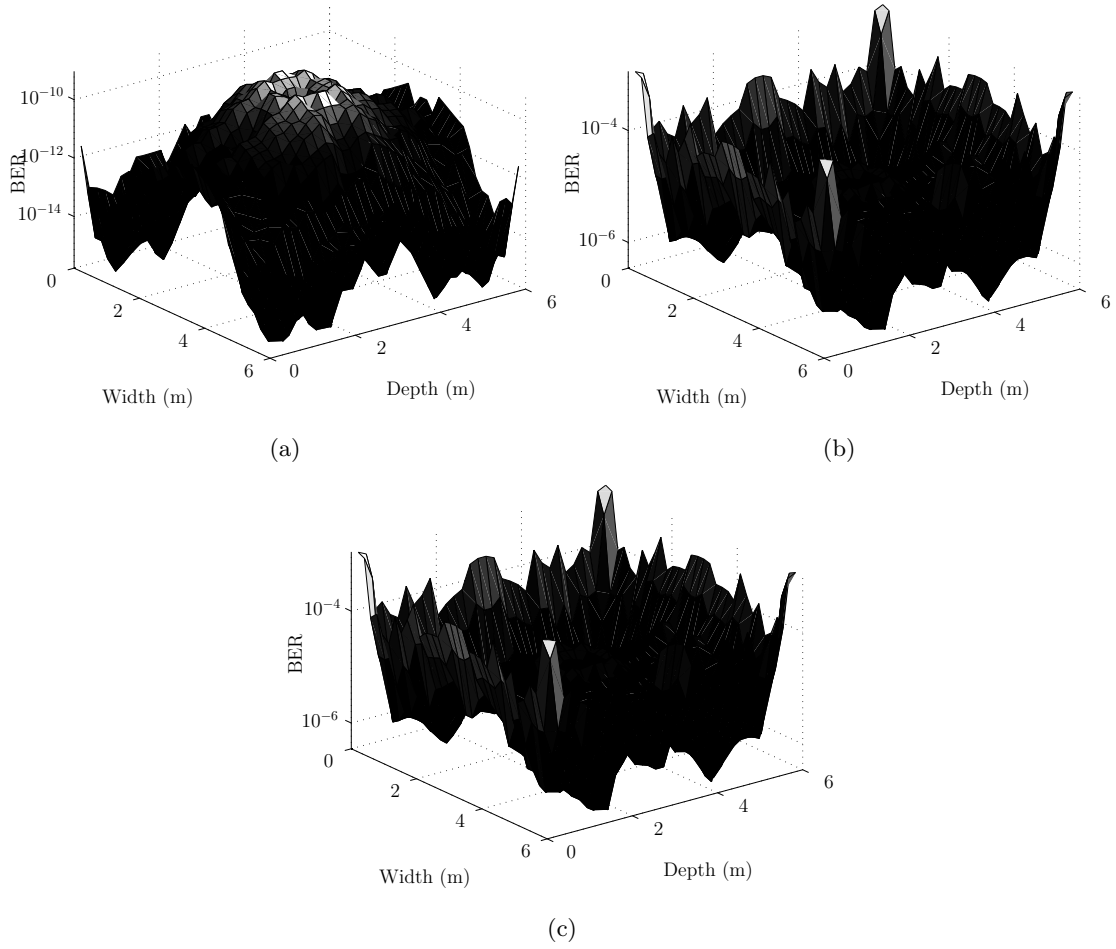

Figure 5.20: Signal source power modification for BER comparison. (a) BER with multipath at $2\,\mathrm{Mbit\,s^{-1}}$. (b) BER with multipath at $80\,\mathrm{Mbit\,s^{-1}}$. (c) Reduction in BER due to multipath, $80\,\mathrm{Mbit\,s^{-1}}$.

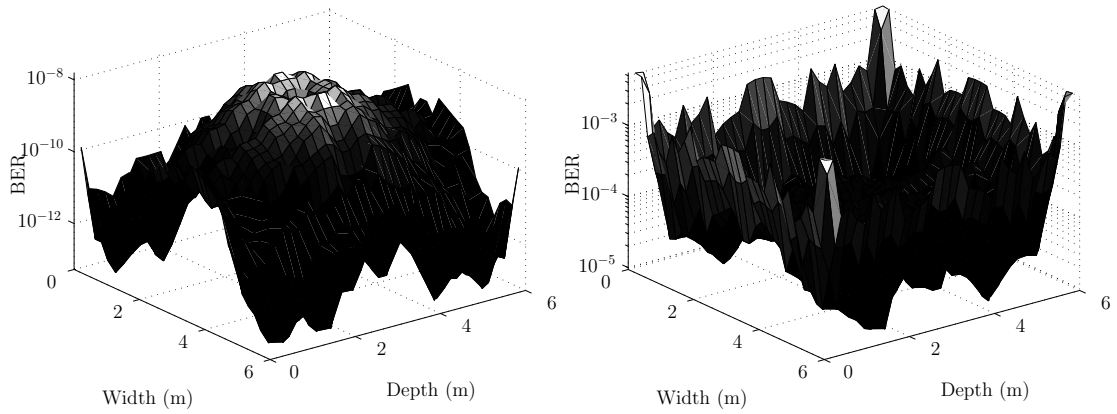

(a) (b)

Figure 5.21: BER with interference for the two systems. (a) BER with multipath and interference at $2\,\mathrm{Mbit\,s^{-1}}$. (b) BER with multipath and interference at $80\,\mathrm{Mbit\,s^{-1}}$.

BER for the $2\,\mathrm{Mbit\,s^{-1}}$ varied between 10^{-7} to 10^{-5}. Whilst for the $80\,\mathrm{Mbit\,s^{-1}}$ the BER varies between 10^{-4} to 0.02.

The optimised BER values including interference can be seen in figures 5.24(a) and 5.24(b) for the $2\,\mathrm{Mbit\,s^{-1}}$ and $80\,\mathrm{Mbit\,s^{-1}}$ systems respectively. With the inclusion of the interference the $2\,\mathrm{Mbit\,s^{-1}}$ varies between 10^{-5} and 10^{-7}, whilst for the $80\,\mathrm{Mbit\,s^{-1}}$ the BER with interference varies between 10^{-4} to 0.034.

Looking into how this second environment deals with movement, in the empty case, the room has a real power SNR variance of 26% which upon optimisation has reduced to 17% for either of the algorithms. Under user movement the power is perturbed anywhere between 26% and 58%, which is reduced to between 16% and 38%. In this scenario, the advantage between employing either algorithm 6 or algorithm 11 is negligible, but the optimisation is showing a consistent result of following of the users movement.

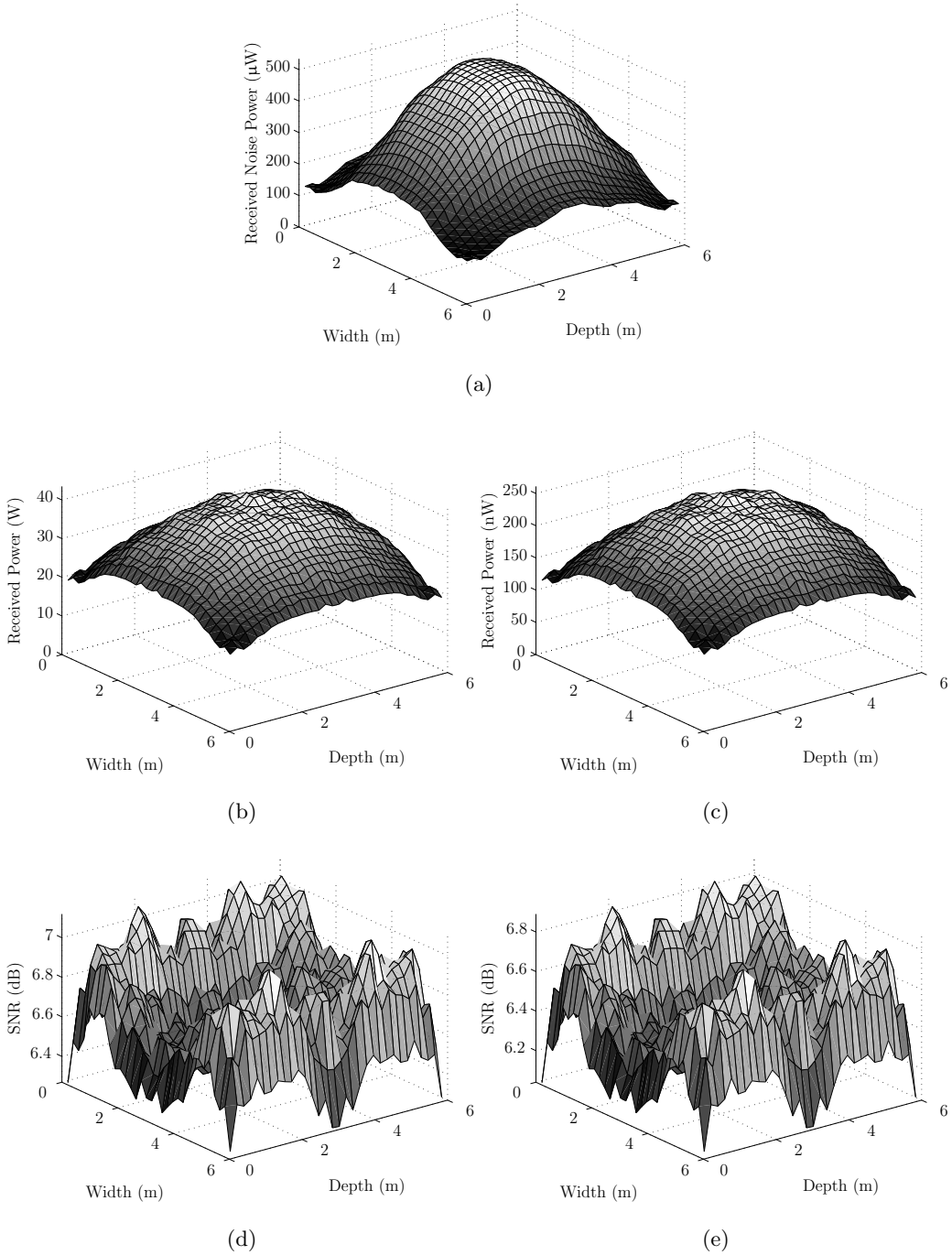

Figure 5.22: Power and SNR optimised noisy empty environment 3. (a) Noise power. (b) $2\,\mathrm{Mbit\,s^{-1}}$ system received power. (c) $80\,\mathrm{Mbit\,s^{-1}}$ system received power. (d) $2\,\mathrm{Mbit\,s^{-1}}$ SNR. (e) $80\,\mathrm{Mbit\,s^{-1}}$ SNR.

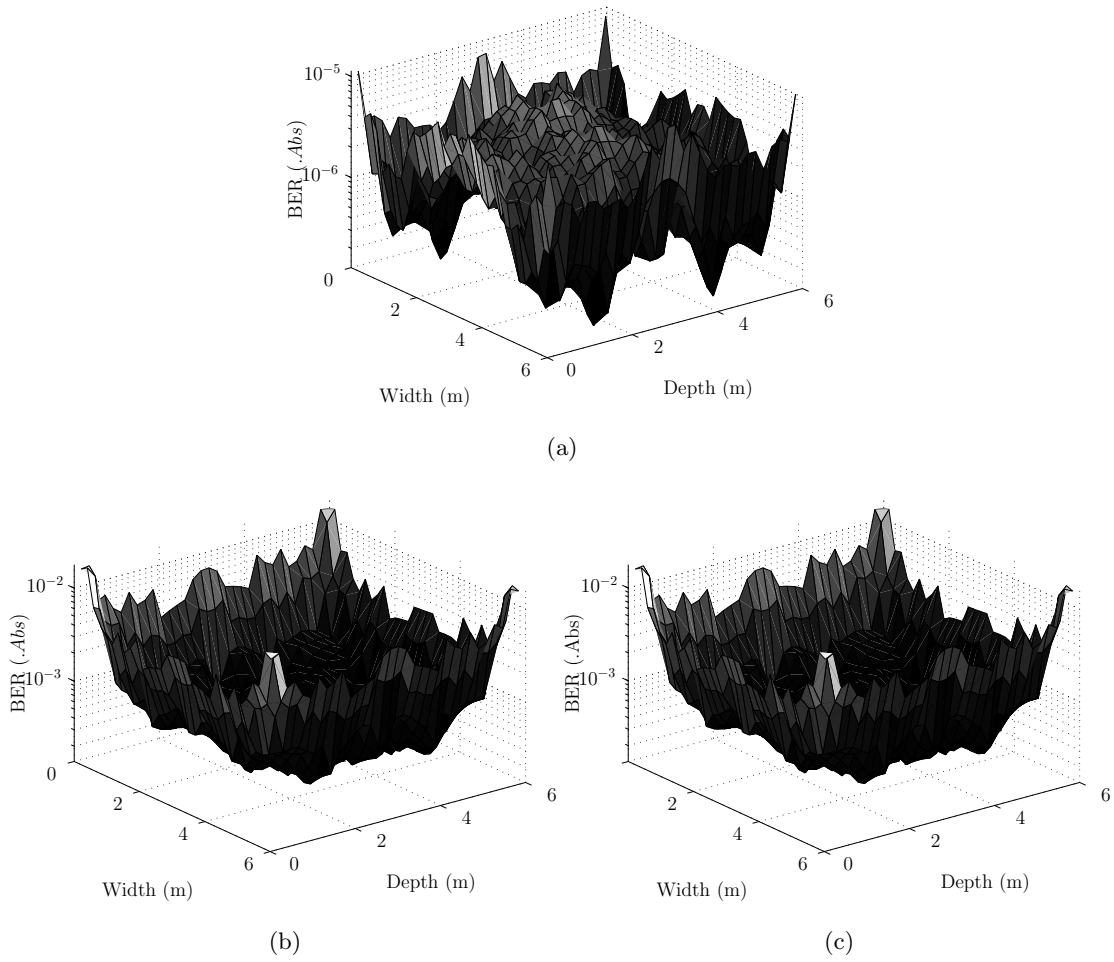

Figure 5.23: BER optimised noisy empty environment 3. (a) $2\,\mathrm{Mbit\,s^{-1}}$ BER with multipath. (b) $80\,\mathrm{Mbit\,s^{-1}}$ system BER with multipath. (c) BER penalty due to multipath.

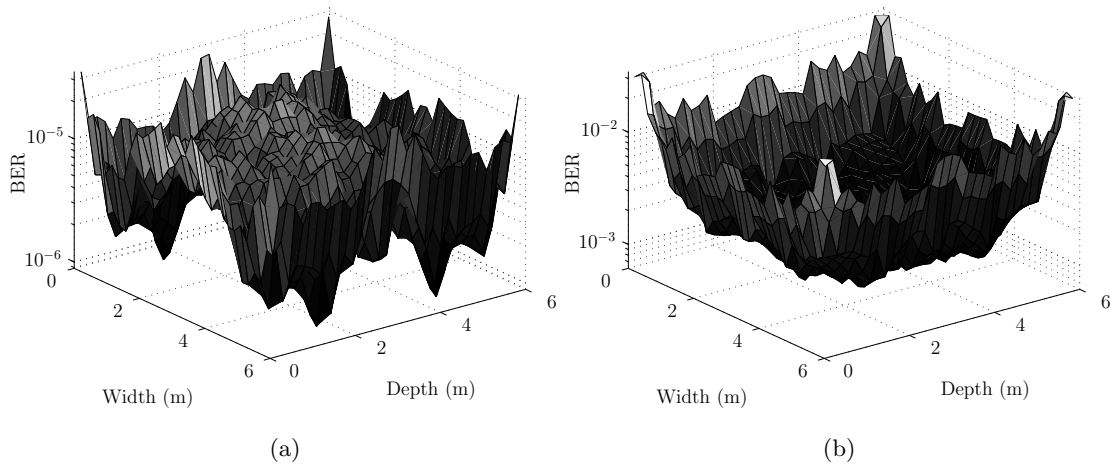

Figure 5.24: BER with interference for the two systems. (a) BER with multipath and interference at $2\,\mathrm{Mbit\,s^{-1}}$. (b) BER with multipath and interference at $80\,\mathrm{Mbit\,s^{-1}}$.

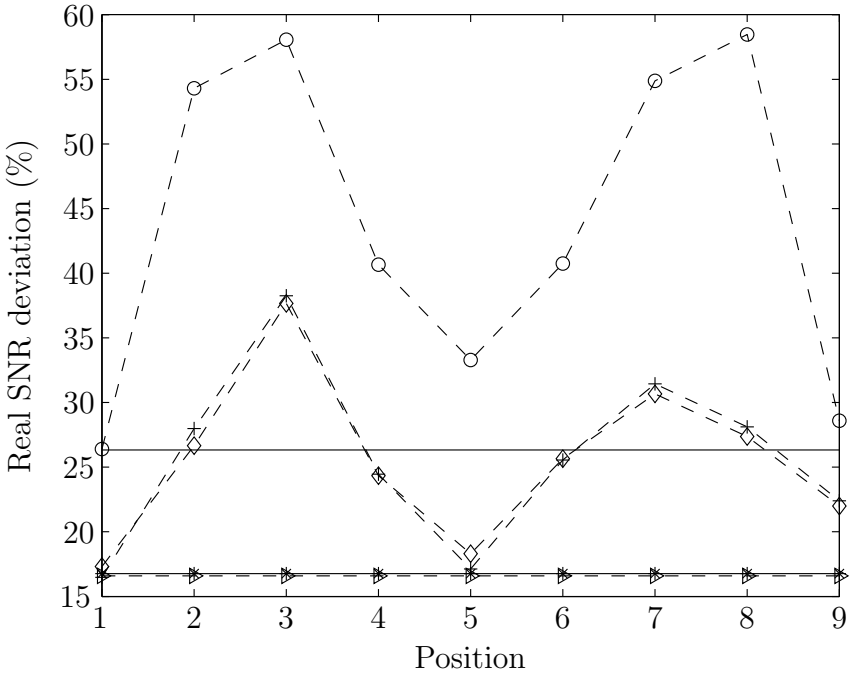

Figure 5.25: SNR optimisation of dynamic environment 3, movement pattern 1. (—) Non optimised empty room. $(-\triangleright-)$ optimised empty room Alg. 11. $(-*-)$ optimised empty room Alg. 6. $(-\circ-)$ non optimised dynamic environment. $(-\diamond-)$ optimised dynamic environment Alg. 6. $(-+-)$ optimised dynamic environment Alg. 11.

5.8 Conclusion

In conclusion, this chapter has presented a detailed noise model for the interference and background noise. The GA was slightly modified to take into account a new optimisation aim of reducing the range of the SNR found throughout the environment. It proved some success in two environments with mobile users. Optimising the BER does not appear possible using this structure of GA for two reasons. Firstly, as the simulations are designed to be realistic using essentially measured results, forming direct comparison between optimisation performance and system performance is very difficult, and as such hard for a fitness function to use, and secondly, some of the factors in the BER cannot be controlled by the GA. The GA has no control over the level of interference induced by the artificial lighting, and as was shown, has little control on the length of the impulse response. This chapter has provided a good illustrative example of why the GA is just a framework, it cannot be readily applied to all applications without the time consuming process of starting from new each time. However the GA approach does still seem applicable. The BER equations are highly non linear, composed of many factors derived from complex mathematical relationships, and as such a global stochastic search optimiser is appropriate. It remains to be seen, however, what the appropriate structure of GA is required for successful optimisation.

Chapter 6

Conclusions

Over the preceding chapters it has been shown that the application of genetic algorithms to a few of the problems of indoor optical wireless communications may prove to be one of a possible number of advantageous techniques. In chapter 2, a purpose built simulator was developed for the determination of the impulse response at any location within the room, from any multispot transmitter arrangement. This allowed factors such as received power, bandwidth and RMS delay spread to be easily found, and very importantly, for relationships to be formed based upon aspects like receiver FOV. The program was optimised to allow a high speed of computation, yet also provide some flexibility in the subroutines for aspects such as moving objects. It was verified against known, published results. The main results of chapter 2 were showing how the receiver FOV affects the total received power and the deviation from peak power around the room. It did highlight the benefits of using angular diversity receivers, but also shows some of the possible drawbacks in the complexity they require, for sometimes only a small benefit, such as depending upon the number of spots, whether in fact a high received power can be obtained at all positions in the room.

Chapter 3 provides a detailed and careful analysis of the GA performance, building several relationships between the population size, selection scheme, mutation rate and genotype struc-

ture. In total 192 algorithms were evaluated on a single test environment, resulting in several possible algorithms that were deemed to have acceptable performance. These algorithms were then reduced to 2 after factoring in their repeatability and computational effort. One algorithm, algorithm 6, was based upon a stochastic uniform sampling routine, having a slow, but gradual convergence to an optimal solution. The other, algorithm 11, was based upon a tournament 3 sampling method with a lower population size. Algorithm 11 tended to converge very quickly to a sub optimal solution, but would suit deployment scenarios where the controller has for example a micro controller that was slower or has lower memory capabilities. At all stages of the algorithm's development this performance to complexity trade-off was maintained. For the initial stages, using 16 diffusion spots and a receiver FOV of 45°, algorithm 6 provided a reduction in received power deviation of around 15% with negligible impact on bandwidth and RMS delay spread.

Furthermore in chapter 3, the relationships between receiver FOV, number of diffusion spots and algorithm performance were investigated. Here it was seen that the algorithm proved most effective for receivers with a FOV of 55°. It was also seen here that the GA may not be entirely compatible with diversity receivers as they, by definition, have a much lower FOV. Upon deciding which FOV to use, the scenarios were extended to include the two user movement patterns in two different environments. The first signs of algorithm limitations were seen when receivers were very close to objects, it did not allow the algorithm to converge correctly. The scenarios were then extended to include user movement, in two different environments, with two movement patterns. The GA managed to reduce power deviation by up to 26%, and forming, while the user perturbed the channel, a consistent power distribution to within 12%. Furthermore the application of algorithms 6 and 11 showed good performance consistency with the case of the empty room, where algorithm 6 always produced results a few % better at all locations than algorithm 11. The optimisation of the received power deviation was again carried out with little detriment to the bandwidth and RMS delay spread.

Chapter 4 extends the results of the GA to further environments with good success. Two larger environments, with different reflectivity characteristics were tested, within which the GA was shown capable of reducing the received power deviation by up to 26% when empty, and maintaining to within 7% of this optimised case, the power distribution when the user perturbs the channel. This chapter also introduces the complexity of the channel when taking into account the typical user alignment variability. Analysis is conducted here, with both varying the FOV of the receiver, the number of spots and the degree to which a user can adjust the receivers orientation. It was shown here, that like the previous decision to employ a receiver with a FOV of 55°, this FOV provided the best trade-off in optimisation performance and user flexibility with statistical models. A gain of up to 27% can be achieved for empty rooms, whilst a gain of up to 26% can be achieved when users are moving. Furthermore, user movement has been shown to perturb the channel by up to 10%, which can be reduced to as little as 2.5% using the GA.

The chapter then moved onto showing how the received power deviation for 2 mobile users, with variable alignment, and in two separate environments can still be optimised by the GA. It has been shown for this scenario the GA can reduce the received power deviation by up to 27%, when empty and to within 6% of this optimised case when the user perturbs the channel. The optimisation, managed to find good solutions to the problem with little effect to the worst case bandwidth or RMS delay spread.

In chapter 5 a slightly different application of the GA was tested. Instead of trying to optimise the receiver power deviation, it was decided to try and optimise the received SNR and/or BER. Two environments were tested for this application, both with user movement, under the constraints already established. Both algorithms acted as already known, with algorithm 6 converging to a good solution steadily, whilst algorithm 11 converged very quickly but in this

application the difference in final solution was negligible, such that it was not sub-optimal, as therefore it would be more appropriate to use algorithm 11 in a final solution. The algorithms managed to reduce the received SNR by 12% and keeps the user movement perturbation of the channel to within 10% of the optimised case. Both algorithms tracked movement well.

Chapter 5 did show a limitation of the algorithm in the present structure. Optimisation of the system BER was not directly solvable by the GA. The BER to some extent is controlled by the SNR, but factors such as interference and multipath dispersion are outside the control of the GA. By using the GA to control the intensity of the diffusion spots, the multipath penalty may never be solved, it would require a completely new approach.

Overall the original aims of this work have been fulfilled. It has been shown that it is possible based upon a single receiver design with a FOV of 55° that a GA can be used to optimise the receiver power distribution in multiple environments, with user movement and user alignment freedom. As mentioned in chaper 1 , it is not the only solution, nor is it, potentially the only GA that could be used in any final application, but the principle has been proved. If a standards body, such as the IrDA, were to enforce a given FOV for a receiver such as this one, then coupling this receiver with a multispot diffusion transmitter with GA capabilities could provide a non bespoke solution for indoor optical wireless system. It is not the fastest system within the research community, but it is shown to be relatively flexible. The method is not tied to any specific environment or user characteristics. It may find good applications in the consumer, industrial of office domain where the environment will change considerably from one scenario to the next. The GA has also managed to fulfil its requirements with little penalty to the worst case bandwidth and RMS delay spread.

This is not to say the GA does not have drawbacks. It does add complexity to the transmitter, and it does not have much control over the bandwidth and as such the multipath penalty it

induces for the BER with faster systems. For these applications other approaches may be more valid, but they could be expensive to implement. This is the tradeoff that any system designer will have to overcome.

Inherently, the GA is software based. It is important therefore to bear in mind that software based approaches like this, can of course coexist, or be easily integrated into other software based solutions. For example, if a system is already employing spread spectrum techniques, or handover protocols, and the transmitter micro controller has memory available, the GA can be used along side it. In a cellular system, anything that makes the receiver cheaper or simpler to design is beneficial, regardless of a small addition to the complexity of the transmitter.

Other possibilities include using this system in combination with diversity receivers. Typically the diversity receivers have many receiving elements. Normally the receiver will be able to decide which element should be responsible for reception based upon which element has the best signal characteristics. However, it could be possible, in extreme conditions for the diversity receiver to default to a diffuse mode, where all elements are useful and the GA is then left to make the channel as suitable as possible. It is furthermore also possible, for software based control systems, to have many modes of operation. There could be several GAs implemented, each one for a different purpose, one for reducing the received power deviation, one for reducing SNR deviation and so forth. Dependent upon the scenario, the modes could be switched.

It is believed that the approaches and work found within this thesis will be beneficial to the community. Each result presented here has been verified as well as can be, and the author believes everything here to be true and correct. It was mentioned in the introduction that the principles of the work presented here are not the only solutions to the problems within indoor optical wireless communications, but this method should be considered of some reasonable merit as a solution for systems that need to operate in dynamic and variable environments where cost

and user flexibility is paramount.

During the time spent on this work, most of the investigations were carried out successfully with little problems. A lot of time was spent optimising the impulse response simulation program for computational efficiency in understanding how MATLAB computes the equations it is given. The program had to be rewritten several times to overcome memory limitations and individual lines of code were adjusted to take advantage of newer and faster functions developed by the MATLAB company over the 3 years. There are still some areas that would be interesting to investigate in the future. The main one would be to look at why optimisation of the bandwidth could not be achieved. It is unclear if this a GA problem or a physical problem, for example there are limits to what can be achieved when radiation is reflected off the walls of the environment. Should optimisation of bandwidth be achieved, another advancement would be to determine if a multi objective GA could be found, optimising both bandwidth and power distribution, and how much benefit one optimisation would be compared to the other.

Another point of investigation is the practical implementation of the GA. Currently it is understood that the use of a tournament 3 selection routine is beneficial over SUS in terms of computation time as there is no need to compute proportional fitness assignments are sorting, but how would this work on a micro controller at the transmitter? It would take a substantial amount of time to determine the GAs operations count and a compatible micro-controller suitable for the task. It would also need to be established if either of the selection routines was fast enough. Knowing how the micro controller behaves is also the next step in determining the operational method of feedback, that is to say how the tr

Appendix A

Computational Effort and Error Tables.

In this Appendix, the full tables of results are shown that are used to form figure 2.4. Tables A.1, A.3 and A.5 provide the first, second, and third order computation times required to determine their respective impulse responses, for different numbers of receivers, J, within the test environment at varying levels of segmentation ΔA. Tables, A.2, A.4 and A.6 show the respective first, second and third order impulse response percentage error results for varying number of receivers and level of segmentation, ΔA.

	Number of Receivers J											
Resolution ΔA	1	4	25	64	121	196	289	400	529	676	841	1024
300	14	37	192	480	925	1466	2154	2982	3950	5021	6264	7644
280	13	33	171	433	795	1308	1886	2620	3434	4383	5464	6664
260	11	28	146	365	685	1107	1631	2258	2981	3810	4733	5764
240	9	24	124	310	583	948	1387	1945	2533	3268	4067	4921
220	8	22	114	278	502	786	1200	1723	2121	2715	3373	4104
200	6	16	86	216	406	655	972	1347	1779	2274	2826	3414
180	5	13	70	175	329	533	783	1083	1431	1830	2273	2772
160	4	11	55	138	260	419	617	856	1132	1442	1797	2182
140	3	8	42	106	199	321	473	653	863	1101	1371	1668
120	2	6	31	78	146	236	347	480	635	811	1008	1235
100	2	5	23	57	108	169	257	338	447	568	730	850
90	≤ 1	3	17	44	82	132	194	270	366	484	581	695
80	≤ 1	3	14	35	65	105	155	218	288	361	449	548
70	≤ 1	2	11	27	50	81	118	164	217	279	345	420
60	≤ 1	2	8	19	37	59	87	120	158	203	251	307
50	≤ 1	≤ 1	5	14	25	41	60	83	110	140	175	213
40	≤ 1	≤ 1	4	9	16	27	39	54	71	91	125	140
30	≤ 1	≤ 1	2	4	8	14	19	26	34	44	55	67
20	≤ 1	≤ 1	≤ 1	2	4	6	8	11	14	19	23	28
10	≤ 1	≤ 1	≤ 1	≤ 1	≤ 1	1	2	3	3	4	5	7
9	≤ 1	≤ 1	≤ 1	≤ 1	≤ 1	≤ 1	2	2	3	4	5	6
8	≤ 1	≤ 1	≤ 1	≤ 1	≤ 1	≤ 1	≤ 1	2	2	3	4	4
7	≤ 1	≤ 1	≤ 1	≤ 1	≤ 1	≤ 1	≤ 1	≤ 1	2	2	3	3
6	≤ 1	≤ 1	≤ 1	≤ 1	≤ 1	≤ 1	≤ 1	≤ 1	≤ 1	2	2	3
5	≤ 1	≤ 1	≤ 1	≤ 1	≤ 1	≤ 1	≤ 1	≤ 1	≤ 1	≤ 1	2	2
4	≤ 1	≤ 1	≤ 1	≤ 1	≤ 1	≤ 1	≤ 1	≤ 1	≤ 1	≤ 1	≤ 1	≤ 1
3	≤ 1	≤ 1	≤ 1	≤ 1	≤ 1	≤ 1	≤ 1	≤ 1	≤ 1	≤ 1	≤ 1	≤ 1
2	≤ 1	≤ 1	≤ 1	≤ 1	≤ 1	≤ 1	≤ 1	≤ 1	≤ 1	≤ 1	≤ 1	≤ 1
1	≤ 1	≤ 1	≤ 1	≤ 1	≤ 1	≤ 1	≤ 1	≤ 1	≤ 1	≤ 1	≤ 1	≤ 1

Table A.1: First order impulse response computation times (seconds).

	Number of Receivers J											
Resolution ΔA	1	4	25	64	121	196	289	400	529	676	841	1024
300	0	0	0	0	0	0	0	0	0	0	0	0
280	< 0.1	< 0.1	< 0.1	< 0.1	< 0.1	< 0.1	< 0.1	< 0.1	< 0.1	< 0.1	< 0.1	< 0.1
260	< 0.1	< 0.1	< 0.1	< 0.1	< 0.1	< 0.1	< 0.1	< 0.1	< 0.1	< 0.1	< 0.1	< 0.1
240	< 0.1	< 0.1	< 0.1	< 0.1	< 0.1	< 0.1	< 0.1	< 0.1	< 0.1	< 0.1	< 0.1	< 0.1
220	< 0.1	< 0.1	< 0.1	< 0.1	< 0.1	< 0.1	< 0.1	< 0.1	< 0.1	< 0.1	< 0.1	< 0.1
200	< 0.1	< 0.1	< 0.1	< 0.1	< 0.1	< 0.1	< 0.1	< 0.1	< 0.1	< 0.1	< 0.1	< 0.1
180	< 0.1	< 0.1	< 0.1	< 0.1	< 0.1	< 0.1	< 0.1	< 0.1	< 0.1	< 0.1	< 0.1	< 0.1
160	< 0.1	< 0.1	< 0.1	< 0.1	< 0.1	< 0.1	< 0.1	< 0.1	< 0.1	< 0.1	< 0.1	< 0.1
140	< 0.1	< 0.1	< 0.1	< 0.1	< 0.1	< 0.1	< 0.1	< 0.1	< 0.1	< 0.1	< 0.1	< 0.1
120	< 0.1	< 0.1	< 0.1	< 0.1	< 0.1	< 0.1	< 0.1	< 0.1	< 0.1	< 0.1	< 0.1	< 0.1
100	< 0.1	< 0.1	< 0.1	< 0.1	< 0.1	< 0.1	< 0.1	< 0.1	< 0.1	< 0.1	< 0.1	< 0.1
90	< 0.1	< 0.1	< 0.1	< 0.1	< 0.1	< 0.1	< 0.1	< 0.1	< 0.1	< 0.1	< 0.1	< 0.1
80	< 0.1	< 0.1	< 0.1	< 0.1	< 0.1	< 0.1	< 0.1	< 0.1	< 0.1	< 0.1	< 0.1	< 0.1
70	< 0.1	< 0.1	< 0.1	< 0.1	< 0.1	< 0.1	< 0.1	< 0.1	< 0.1	< 0.1	0.1	< 0.1
60	< 0.1	< 0.1	< 0.1	< 0.1	< 0.1	< 0.1	< 0.1	< 0.1	< 0.1	0.1	< 0.1	< 0.1
50	< 0.1	< 0.1	< 0.1	< 0.1	< 0.1	< 0.1	< 0.1	0.1	< 0.1	< 0.1	< 0.1	< 0.1
40	< 0.1	< 0.1	< 0.1	< 0.1	< 0.1	< 0.1	0.2	< 0.1	< 0.1	0.1	0.1	< 0.1
30	0.1	< 0.1	< 0.1	< 0.1	0.2	< 0.1	< 0.1	0.1	0.1	0.2	0.2	0.2
20	< 0.1	< 0.1	< 0.1	0.3	0.1	0.2	0.3	0.3	0.3	0.4	0.3	0.3
10	0.5	0.4	0.2	0.4	0.6	0.7	0.8	1.0	1.1	1.2	1.3	1.4
9	0.3	0.3	0.3	0.5	0.8	0.7	1.0	1.1	1.2	1.4	1.5	1.6
8	0.2	< 0.1	0.5	0.7	0.8	1.0	1.3	1.3	1.6	1.7	1.8	1.9
7	1.3	< 0.1	0.6	1.0	1.0	1.4	1.6	1.9	2.0	2.1	2.1	2.1
6	0.9	0.6	0.8	1.1	1.4	1.7	2.1	2.3	2.5	2.5	2.3	2.3
5	1.2	1.7	1.2	1.5	2.1	2.6	2.9	3.1	3.0	2.9	2.7	2.5
4	0.2	0.7	1.6	2.4	3.1	3.6	3.7	5.2	3.3	3.1	2.9	2.9
3	2.2	2.0	2.8	4.4	5.2	5.0	4.7	4.1	4.1	4.2	4.5	4.5
2	3.6	3.3	6.2	8.0	7.2	6.4	6.3	5.0	7.0	7.5	8.0	8.4
1	14.1	15.9	28.3	14.9	16.2	18.4	19.9	20.8	21.2	21.4	21.5	21.5

Table A.2: First order percentage error analysis.

	Number of Receivers J											
Resolution ΔA	1	4	25	64	121	196	289	400	529	676	841	1024
10	77	87	160	300	504	777	1146	1475	1927	2440	3015	3672
9	50	56	105	198	327	504	721	981	1285	1628	2016	2445
8	30	35	66	125	214	336	479	624	866	1038	1286	1566
7	17	22	39	76	130	205	283	401	507	643	788	949
6	9	12	22	41	70	109	156	213	279	355	439	536
5	5	5	11	21	38	57	82	111	146	185	230	286
4	2	2	5	10	17	26	38	52	68	86	108	131
3	< 1	< 1	2	4	7	10	15	20	26	33	41	50
2	< 1	< 1	< 1	1	2	3	4	6	8	10	13	15
1	< 1	< 1	< 1	< 1	< 1	< 1	< 1	1	2	2	3	3

Table A.3: Second order impulse response computation times (seconds).

	Number of Receivers J											
Resolution ΔA	1	4	25	64	121	196	289	400	529	676	841	1024
10	0	0	0	0	0	0	0	0	0	0	0	0
9	< 0.1	< 0.1	< 0.1	< 0.1	< 0.1	0.1	0.1	0.1	0.2	0.2	0.2	0.2
8	< 0.1	< 0.1	0.2	0.2	0.2	0.3	0.3	0.4	0.4	0.4	0.4	0.4
7	0.2	< 0.1	0.3	0.3	0.4	0.5	0.6	0.7	0.7	0.7	0.6	0.6
6	0.2	0.1	0.5	0.4	0.7	0.8	0.9	1.0	1.0	0.9	0.9	0.9
5	0.4	0.4	0.7	0.9	1.1	1.4	1.5	1.5	1.4	1.3	1.2	1.2
4	0.4	0.7	1.0	1.5	2.0	2.2	2.2	3.0	1.8	1.8	1.8	1.8
3	0.2	1.6	2.3	3.0	3.5	3.5	3.1	2.8	2.7	2.8	2.9	3.1
2	2.0	3.3	5.3	6.4	6.0	5.1	4.8	4.2	5.3	5.7	6.1	6.4
1	9.3	14.7	21.9	14.6	13.1	13.5	14.4	15.1	15.7	16.0	16.2	16.2

Table A.4: Second order percentage error analysis.

	Number of Receivers J											
Resolution ΔA	1	4	25	64	121	196	289	400	529	676	841	1024
5	649	875	2583	5672	10885	16362	25073	32735	44862	54372	68381	83738
4	195	310	1000	2354	4175	6647	9811	13784	18332	22294	27872	34949
3	45	80	297	696	1301	2082	3077	4228	5595	7071	8891	10782
2	7	13	56	134	250	405	598	823	1087	1390	1726	2089
1	< 1	< 1	4	9	17	28	41	56	75	96	118	144

Table A.5: Second order impulse response computation times (seconds).

	Number of Receivers J											
Resolution ΔA	1	4	25	64	121	196	289	400	529	676	841	1024
5	0	0	0	0	0	0	0	0	0	0	0	0
4	0.8	1.9	1.1	1.4	1.6	1.6	1.6	2.3	1.8	1.8	2.0	2.0
3	1.8	4.2	3.6	4.2	4.4	4.1	3.7	3.4	3.9	4.1	4.2	4.4
2	6.5	8.7	9.2	10.3	9.5	8.3	8.1	7.9	8.9	9.3	9.6	9.8
1	24.4	31.0	37.4	28.3	25.6	25.4	26.0	26.8	27.5	27.9	28.1	28.1

Table A.6: Third order percentage analysis.

Appendix B

Complete List of Genetic Algorithms Tested.

This appendix lists the specification of all the genetic algorithms tested, 192 in total, used to find what were considered to be the 12 best, provided in table 3.1. Each table is separated into sets of 12 of the same selection scheme. Tables B.1 through B.3 provide the designs for GAs based on Roulette selection. Tables B.4 through B.4 provide designs of GAs based on SUS selection, whilst tables B.7 though B.9 and tables B.10 through B.12 proved the designs for GAs based upon a tournament selection with either 2 or 3 contestants respectively.

Selection Method	Generations	N	ρ_c	ρ_m	m	$\mathcal{G}$	R	Best (St.D)	Mean (St.D)
Roulette	5000	50	0.7	0	1	WA	30	45(3.9)	45(3.9)
Roulette	5000	50	0.7	0.01	1	WA	30	38(2.9)	39(3.0)
Roulette	5000	50	0.7	0.05	1	WA	30	36(2.3)	40(2.7)
Roulette	5000	50	0.7	0.1	1	WA	30	37(1.8)	43(2.0)
Roulette	5000	50	0.7	0	2	WA	30	43(3.8)	43(3.8)
Roulette	5000	50	0.7	0.01	2	WA	30	38(2.6)	38(2.5)
Roulette	5000	50	0.7	0.05	2	WA	30	36(2.0)	40(2.0)
Roulette	5000	50	0.7	0.1	2	WA	30	37(1.6)	43(2.2)
Roulette	5000	50	0.7	0	1	CON	30	43(3.6)	43(3.6)
Roulette	5000	50	0.7	0.01	1	CON	30	38(2.3)	39(2.4)
Roulette	5000	50	0.7	0.05	1	CON	30	37(2.6)	41(2.7)
Roulette	5000	50	0.7	0.1	1	CON	30	37(1.5)	43(1.9)
Roulette	5000	50	0.7	0	2	CON	30	43(2.7)	43(2.7)
Roulette	5000	50	0.7	0.01	2	CON	30	38(2.3)	39(2.3)
Roulette	5000	50	0.7	0.05	2	CON	30	36(2.0)	40(2.5)
Roulette	5000	50	0.7	0.1	2	CON	30	36(1.8)	42(2.3)

Table B.1: GAs based on Roulette selection and a population of 50.

Selection Method	Generations	N	ρ_c	ρ_m	m	$\mathcal{G}$	R	Best (St.D)	Mean (St.D)
Roulette	5000	100	0.7	0	1	WA	30	39(2.9)	39(2.9)
Roulette	5000	100	0.7	0.01	1	WA	30	36(2.1)	37(2.2)
Roulette	5000	100	0.7	0.05	1	WA	30	34(1.5)	38(1.9)
Roulette	5000	100	0.7	0.1	1	WA	30	34(1.4)	41(1.7)
Roulette	5000	100	0.7	0	2	WA	30	39(2.5)	39(2.5)
Roulette	5000	100	0.7	0.01	2	WA	30	35(1.7)	36(1.6)
Roulette	5000	100	0.7	0.05	2	WA	30	34(1.3)	38(1.6)
Roulette	5000	100	0.7	0.1	2	WA	30	34(1.0)	41(1.9)
Roulette	5000	100	0.7	0	1	CON	30	39(2.5)	39(2.5)
Roulette	5000	100	0.7	0.01	1	CON	30	35(1.7)	36(1.8)
Roulette	5000	100	0.7	0.05	1	CON	30	34(1.3)	38(1.6)
Roulette	5000	100	0.7	0.1	1	CON	30	35(1.3)	42(1.4)
Roulette	5000	100	0.7	0	2	CON	30	39(2.3)	39(2.3)
Roulette	5000	100	0.7	0.01	2	CON	30	35(1.4)	36(1.6)
Roulette	5000	100	0.7	0.05	2	CON	30	34(1.3)	38(1.6)
Roulette	5000	100	0.7	0.1	2	CON	30	35(1.2)	41(1.5)

Table B.2: GAs based on Roulette selection and a population of 100

Selection Method	Generations	N	ρ_c	ρ_m	m	$\mathcal{G}$	R	Best (St.D)	Mean (St.D)
Roulette	5000	200	0.7	0	1	WA	30	36(1.6)	36(1.6)
Roulette	5000	200	0.7	0.01	1	WA	30	34(1.3)	35(1.3)
Roulette	5000	200	0.7	0.05	1	WA	30	33(1.0)	37(1.3)
Roulette	5000	200	0.7	0.1	1	WA	30	33(0.9)	40(1.2)
Roulette	5000	200	0.7	0	2	WA	30	36(1.8)	36(1.8)
Roulette	5000	200	0.7	0.01	2	WA	30	34(1.1)	34(1.2)
Roulette	5000	200	0.7	0.05	2	WA	30	32(0.9)	36(1.3)
Roulette	5000	200	0.7	0.1	2	WA	30	33(1.1)	40(1.4)
Roulette	5000	200	0.7	0	1	CON	30	36(1.9)	36(1.9)
Roulette	5000	200	0.7	0.01	1	CON	30	34(1.2)	35(1.3)
Roulette	5000	200	0.7	0.05	1	CON	30	33(0.8)	37(1.4)
Roulette	5000	200	0.7	0.1	1	CON	30	33(0.9)	40(1.1)
Roulette	5000	200	0.7	0	2	CON	30	35(1.7)	35(1.7)
Roulette	5000	200	0.7	0.01	2	CON	30	34(1.2)	34(1.1)
Roulette	5000	200	0.7	0.05	2	CON	30	32(1.0)	36(1.3)
Roulette	5000	200	0.7	0.1	2	CON	30	33(0.8)	40(1.2)

Table B.3: GAs based on Roulette selection and a population of 200

Selection Method	Generations	N	ρ_c	ρ_m	m	$\mathcal{G}$	R	Best (St.D)	Mean (St.D)
SUS	5000	50	0.7	0	1	WA	30	34(1.1)	34(1.1)
SUS	5000	50	0.7	0.01	1	WA	30	33(1.1)	34(1.1)
SUS	5000	50	0.7	0.05	1	WA	30	32(0.7)	36(1.1)
SUS	5000	50	0.7	0.1	1	WA	30	32(0.8)	39(1.3)
SUS	5000	50	0.7	0	2	WA	30	33(1.1)	33(1.1)
SUS	5000	50	0.7	0.01	2	WA	30	33(0.9)	33(1.1)
SUS	5000	50	0.7	0.05	2	WA	30	31(0.8)	35(1.1)
SUS	5000	50	0.7	0.1	2	WA	30	33(0.7)	39(1.3)
SUS	5000	50	0.7	0	1	CON	30	34(1.5)	34(1.5)
SUS	5000	50	0.7	0.01	1	CON	30	33(1.0)	33(1.2)
SUS	5000	50	0.7	0.05	1	CON	30	32(0.7)	36(1.1)
SUS	5000	50	0.7	0.1	1	CON	30	33(0.9)	39(1.4)
SUS	5000	50	0.7	0	2	CON	30	33(1.2)	33(1.2)
SUS	5000	50	0.7	0.01	2	CON	30	32(1.1)	33(1.1)
SUS	5000	50	0.7	0.05	2	CON	30	31(0.8)	36(1.4)
SUS	5000	50	0.7	0.1	2	CON	30	32(0.8)	39(1.3)

Table B.4: GAs based on SUS selection and a population of 50.

Selection Method	Generations	N	ρ_c	ρ_m	m	$\mathcal{G}$	R	Best (St.D)	Mean (St.D)
SUS	5000	100	0.7	0	1	WA	30	32(1.1)	32(1.0)
SUS	5000	100	0.7	0.01	1	WA	30	32(1.0)	32(1.1)
SUS	5000	100	0.7	0.05	1	WA	30	31(0.4)	35(0.8)
SUS	5000	100	0.7	0.1	1	WA	30	32(0.7)	39(1.0)
SUS	5000	100	0.7	0	2	WA	30	32(0.8)	32(0.8)
SUS	5000	100	0.7	0.01	2	WA	30	31(0.7)	32(0.7)
SUS	5000	100	0.7	0.05	2	WA	30	31(0.4)	34(0.8)
SUS	5000	100	0.7	0.1	2	WA	30	32(0.6)	39(0.9)
SUS	5000	100	0.7	0	1	CON	30	33(1.0)	33(1.0)
SUS	5000	100	0.7	0.01	1	CON	30	32(0.8)	33(0.8)
SUS	5000	100	0.7	0.05	1	CON	30	31(0.5)	35(0.8)
SUS	5000	100	0.7	0.1	1	CON	30	32(0.8)	39(1.2)
SUS	5000	100	0.7	0	2	CON	30	32(0.7)	32(0.7)
SUS	5000	100	0.7	0.01	2	CON	30	31(0.7)	32(0.7)
SUS	5000	100	0.7	0.05	2	CON	30	31(0.4)	35(0.7)
SUS	5000	100	0.7	0.1	2	CON	30	32(0.5)	39(0.7)

Table B.5: GAs based on SUS selection and a population of 100.

Selection Method	Generations	N	ρ_c	ρ_m	m	$\mathcal{G}$	R	Best (St.D)	Mean (St.D)
SUS	5000	200	0.7	0	1	WA	30	31(0.6)	31(0.6)
SUS	5000	200	0.7	0.01	1	WA	30	31(0.5)	32(0.5)
SUS	5000	200	0.7	0.05	1	WA	30	30(0.3)	34(0.6)
SUS	5000	200	0.7	0.1	1	WA	30	31(0.4)	39(0.7)
SUS	5000	200	0.7	0	2	WA	30	31(0.5)	31(0.5)
SUS	5000	200	0.7	0.01	2	WA	30	31(0.7)	31(0.7)
SUS	5000	200	0.7	0.05	2	WA	30	30(0.3)	34(0.5)
SUS	5000	200	0.7	0.1	2	WA	30	31(0.4)	39(0.7)
SUS	5000	200	0.7	0	1	CON	30	31(0.6)	31(0.6)
SUS	5000	200	0.7	0.01	1	CON	30	31(0.6)	32(0.6)
SUS	5000	200	0.7	0.05	1	CON	30	30(0.5)	34(0.5)
SUS	5000	200	0.7	0.1	1	CON	30	31(0.5)	39(0.8)
SUS	5000	200	0.7	0	2	CON	30	31(0.6)	31(0.6)
SUS	5000	200	0.7	0.01	2	CON	30	30(0.4)	31(0.5)
SUS	5000	200	0.7	0.05	2	CON	30	30(0.3)	34(0.6)
SUS	5000	200	0.7	0.1	2	CON	30	31(0.5)	39(0.5)

Table B.6: GAs based on SUS selection and a population of 200.

Selection Method	Generations	N	ρ_c	ρ_m	m	$\mathcal{G}$	R	Best (St.D)	Mean (St.D)
Tournament (2)	5000	50	0.7	0	1	WA	30	40(2.6)	40(2.6)
Tournament (2)	5000	50	0.7	0.05	1	WA	30	34(2.0)	35(1.9)
Tournament (2)	5000	50	0.7	0.1	1	WA	30	34(2.0)	35(2.0)
Tournament (2)	5000	50	0.7	0.2	1	WA	30	34(1.2)	36(1.1)
Tournament (2)	5000	50	0.7	0	2	WA	30	38(2.7)	38(2.7)
Tournament (2)	5000	50	0.7	0.05	2	WA	30	34(1.9)	35(1.9)
Tournament (2)	5000	50	0.7	0.1	2	WA	30	34(1.5)	35(1.7)
Tournament (2)	5000	50	0.7	0.2	2	WA	30	33(1.0)	35(1.4)
Tournament (2)	5000	50	0.7	0	1	CON	30	40(3.1)	40(3.1)
Tournament (2)	5000	50	0.7	0.05	1	CON	30	34(1.2)	34(1.2)
Tournament (2)	5000	50	0.7	0.1	1	CON	30	34(1.9)	35(1.8)
Tournament (2)	5000	50	0.7	0.2	1	CON	30	33(1.5)	35(1.4)
Tournament (2)	5000	50	0.7	0	2	CON	30	39(2.2)	39(2.2)
Tournament (2)	5000	50	0.7	0.05	2	CON	30	34(1.4)	34(1.4)
Tournament (2)	5000	50	0.7	0.1	2	CON	30	33(1.3)	34(1.3)
Tournament (2)	5000	50	0.7	0.2	2	CON	30	33(1.3)	35(1.8)

Table B.7: GAs based on tournament 2 selection and a population of 50.

Selection Method	Generations	N	ρ_c	ρ_m	m	$\mathcal{G}$	R	Best (St.D)	Mean (St.D)
Tournament (2)	5000	100	0.7	0	1	WA	30	37(1.5)	37(1.5)
Tournament (2)	5000	100	0.7	0.05	1	WA	30	33(1.4)	34(1.5)
Tournament (2)	5000	100	0.7	0.1	1	WA	30	33(1.0)	34(1.1)
Tournament (2)	5000	100	0.7	0.2	1	WA	30	33(1.3)	35(1.2)
Tournament (2)	5000	100	0.7	0	2	WA	30	35(1.8)	35(1.8)
Tournament (2)	5000	100	0.7	0.05	2	WA	30	33(0.9)	33(0.9)
Tournament (2)	5000	100	0.7	0.1	2	WA	30	33(1.5)	34(1.6)
Tournament (2)	5000	100	0.7	0.2	2	WA	30	32(1.0)	34(1.2)
Tournament (2)	5000	100	0.7	0	1	CON	30	37(2.0)	37(2.0)
Tournament (2)	5000	100	0.7	0.05	1	CON	30	33(2.0)	34(2.0)
Tournament (2)	5000	100	0.7	0.1	1	CON	30	33(1.0)	34(1.1)
Tournament (2)	5000	100	0.7	0.2	1	CON	30	33(1.4)	35(1.3)
Tournament (2)	5000	100	0.7	0	2	CON	30	35(1.7)	35(1.7)
Tournament (2)	5000	100	0.7	0.05	2	CON	30	33(1.3)	34(1.4)
Tournament (2)	5000	100	0.7	0.1	2	CON	30	33(1.4)	34(1.5)
Tournament (2)	5000	100	0.7	0.2	2	CON	30	33(1.2)	35(1.3)

Table B.8: GAs based on tournament 2 selection and a population of 100.

Selection Method	Generations	N	ρ_c	ρ_m	m	$\mathcal{G}$	R	Best (St.D)	Mean (St.D)
Tournament (2)	5000	200	0.7	0	1	WA	30	34(1.3)	34(1.3)
Tournament (2)	5000	200	0.7	0.05	1	WA	30	32(1.0)	33(1.0)
Tournament (2)	5000	200	0.7	0.1	1	WA	30	32(0.8)	33(0.8)
Tournament (2)	5000	200	0.7	0.2	1	WA	30	32(1.0)	34(1.0)
Tournament (2)	5000	200	0.7	0	2	WA	30	33(0.9)	33(0.9)
Tournament (2)	5000	200	0.7	0.05	2	WA	30	32(1.0)	32(1.0)
Tournament (2)	5000	200	0.7	0.1	2	WA	30	32(0.9)	32(1.0)
Tournament (2)	5000	200	0.7	0.2	2	WA	30	32(0.9)	34(0.8)
Tournament (2)	5000	200	0.7	0	1	CON	30	35(1.5)	35(1.5)
Tournament (2)	5000	200	0.7	0.05	1	CON	30	32(1.2)	33(1.2)
Tournament (2)	5000	200	0.7	0.1	1	CON	30	32(1.2)	33(1.2)
Tournament (2)	5000	200	0.7	0.2	1	CON	30	32(0.8)	34(0.8)
Tournament (2)	5000	200	0.7	0	2	CON	30	33(1.1)	33(1.1)
Tournament (2)	5000	200	0.7	0.05	2	CON	30	32(1.1)	32(1.1)
Tournament (2)	5000	200	0.7	0.1	2	CON	30	32(0.9)	33(0.8)
Tournament (2)	5000	200	0.7	0.2	2	CON	30	31(1.0)	33(0.9)

Table B.9: GAs based on tournament 2 selection and a population of 200.

Selection Method	Generations	N	ρ_c	ρ_m	m	$\mathcal{G}$	R	Best (St.D)	Mean (St.D)
Tournament (3)	5000	50	0.7	0	1	WA	30	41(2.1)	41(2.1)
Tournament (3)	5000	50	0.7	0.05	1	WA	30	34(1.8)	35(1.8)
Tournament (3)	5000	50	0.7	0.1	1	WA	30	34(1.9)	35(2.0)
Tournament (3)	5000	50	0.7	0.2	1	WA	30	34(1.6)	35(1.7)
Tournament (3)	5000	50	0.7	0	2	WA	30	37(2.2)	37(2.2)
Tournament (3)	5000	50	0.7	0.05	2	WA	30	34(1.8)	34(1.9)
Tournament (3)	5000	50	0.7	0.1	2	WA	30	34(1.5)	35(1.5)
Tournament (3)	5000	50	0.7	0.2	2	WA	30	34(1.4)	36(1.4)
Tournament (3)	5000	50	0.7	0	1	CON	30	41(3.0)	41(3.0)
Tournament (3)	5000	50	0.7	0.05	1	CON	30	34(1.6)	35(1.7)
Tournament (3)	5000	50	0.7	0.1	1	CON	30	34(1.8)	35(1.7)
Tournament (3)	5000	50	0.7	0.2	1	CON	30	34(1.4)	36(1.3)
Tournament (3)	5000	50	0.7	0	2	CON	30	39(2.8)	39(2.8)
Tournament (3)	5000	50	0.7	0.05	2	CON	30	34(1.7)	34(1.8)
Tournament (3)	5000	50	0.7	0.1	2	CON	30	34(1.4)	35(1.4)
Tournament (3)	5000	50	0.7	0.2	2	CON	30	33(1.2)	35(1.4)

Table B.10: GAs based on tournament 3 selection and a population of 50.

Selection Method	Generations	N	ρ_c	ρ_m	m	$\mathcal{G}$	R	Best (St.D)	Mean (St.D)
Tournament (3)	5000	100	0.7	0	1	WA	30	37(1.8)	37(1.8)
Tournament (3)	5000	100	0.7	0.05	1	WA	30	33(1.1)	33(1.2)
Tournament (3)	5000	100	0.7	0.1	1	WA	30	33(1.4)	34(1.5)
Tournament (3)	5000	100	0.7	0.2	1	WA	30	33(1.4)	35(1.3)
Tournament (3)	5000	100	0.7	0	2	WA	30	35(1.5)	35(1.5)
Tournament (3)	5000	100	0.7	0.05	2	WA	30	33(1.1)	33(1.2)
Tournament (3)	5000	100	0.7	0.1	2	WA	30	33(1.2)	34(1.2)
Tournament (3)	5000	100	0.7	0.2	2	WA	30	33(0.9)	35(1.1)
Tournament (3)	5000	100	0.7	0	1	CON	30	38(1.8)	38(1.8)
Tournament (3)	5000	100	0.7	0.05	1	CON	30	33(1.2)	34(1.2)
Tournament (3)	5000	100	0.7	0.1	1	CON	30	33(1.3)	34(1.3)
Tournament (3)	5000	100	0.7	0.2	1	CON	30	33(1.1)	34(1.2)
Tournament (3)	5000	100	0.7	0	2	CON	30	37(1.9)	37(1.9)
Tournament (3)	5000	100	0.7	0.05	2	CON	30	33(1.0)	33(1.0)
Tournament (3)	5000	100	0.7	0.1	2	CON	30	32(1.1)	33(1.1)
Tournament (3)	5000	100	0.7	0.2	2	CON	30	32(1.2)	34(1.3)

Table B.11: GAs based on tournament 3 selection and a population of 100.

Selection Method	Generations	N	ρ_c	ρ_m	m	$\mathcal{G}$	R	Best (St.D)	Mean (St.D)
Tournament (3)	5000	200	0.7	0	1	WA	30	35(1.2)	35(1.2)
Tournament (3)	5000	200	0.7	0.05	1	WA	30	33(1.1)	33(1.1)
Tournament (3)	5000	200	0.7	0.1	1	WA	30	33(0.9)	33(0.9)
Tournament (3)	5000	200	0.7	0.2	1	WA	30	32(1.1)	34(1.1)
Tournament (3)	5000	200	0.7	0	2	WA	30	33(1.1)	33(1.1)
Tournament (3)	5000	200	0.7	0.05	2	WA	30	32(1.0)	32(0.9)
Tournament (3)	5000	200	0.7	0.1	2	WA	30	32(0.9)	33(0.9)
Tournament (3)	5000	200	0.7	0.2	2	WA	30	32(0.9)	33(1.0)
Tournament (3)	5000	200	0.7	0	1	CON	30	35(1.5)	35(1.5)
Tournament (3)	5000	200	0.7	0.05	1	CON	30	32(1.2)	33(1.2)
Tournament (3)	5000	200	0.7	0.1	1	CON	30	32(1.1)	33(1.0)
Tournament (3)	5000	200	0.7	0.2	1	CON	30	32(1.0)	34(0.9)
Tournament (3)	5000	200	0.7	0	2	CON	30	34(1.0)	34(1.0)
Tournament (3)	5000	200	0.7	0.05	2	CON	30	32(1.0)	32(1.0)
Tournament (3)	5000	200	0.7	0.1	2	CON	30	32(0.8)	33(0.9)
Tournament (3)	5000	200	0.7	0.2	2	CON	30	32(0.8)	33(0.8)

Table B.12: GAs based on tournament 3 selection and a population of 200.

Appendix C

Environment and Movement Data.

In this appendix, in tabulated format, the properties for the each environment are provided in C.1 as a consistent reference for reproduction of any results. Table C.2 provides the coordinates of the positions of each movement position used respective to the environment they were simulated within.

Parameter	Value					
	Room 1	Room 2	Room 3	Room 4	Room 5	Room 6
Room Dimensions $(w \times d \times h)$(m)	$5 \times 5 \times 3$	$5 \times 5 \times 3$	$6 \times 6 \times 3$	$6 \times 6 \times 3$	$6 \times 6 \times 3$	$6 \times 6 \times 3$
$\rho_{\text{ceiling}}, \rho_{\text{north}}, \rho_{\text{south}}, \rho_{\text{east}}, \rho_{\text{west}}, \rho_{\text{floor}}$	$\{0.8, 0.8, 0.8, 0.8, 0.8, 0.3\}$	$\{0.75, 0.7, 0.8, 0.6, 0.8, 0.3\}$	$\{0.8, 0.8, 0.8, 0.8, 0.8, 0.3\}$	$\{0.75, 0.7, 0.8, 0.6, 0.8, 0.3\}$	$\{0.75, 0.75, 0.75, 0.75, 0.75, 0.3\}$	$\{0.8, 0.5, 0.8, 0.6, 0.8, 0.3\}$
ρ_{Object}, (if applicable)	0.3					
n	1					
$\{\Delta A_1, \Delta A_2, \Delta A_3\}$	$\{20, 6, 2\}$					
$\Delta_t$ns	0.1					

Table C.1: The properties of each environment used with the work.

Pos.	Movement Pattern 1												Movement Pattern 2												Movement Pattern 3						Movement Pattern 4					
	Room 1						Room 3 and Room 5						Room 2						Room 4 and Room 6						Room 5						Room 6					
	X_0	Y_0	Z_0	X_h	Y_h	Z_h	X_0	Y_0	Z_0	X_h	Y_h	Z_h	X_0	Y_0	Z_0	X_h	Y_h	Z_h	X_0	Y_0	Z_0	X_h	Y_h	Z_h	X_0	Y_0	Z_0	X_h	Y_h	Z_h	X_0	Y_0	Z_0	X_h	Y_h	Z_h
1	0	0	0	0.4	0.7	1.8	0	0	0	0.4	0.7	1.8	0	0	0	0.4	0.7	1.8	0	0	0	0.4	0.7	1.8	2.0	5.6	0	2.7	6.0	1.6	5.3	0	0	6.0	0.4	1.6
2	0.5	0.5	0	0.9	1.2	1.8	0.7	0.6	0	1.1	1.3	1.8	0.5	1.1	0	0.9	1.8	1.8	0.7	1.3	0	1.1	2.0	1.8	2.0	4.9	0	2.7	5.3	1.6	4.6	1.4	0	5.3	1.8	1.6
3	1.0	1.0	0	1.4	1.7	1.8	1.4	1.2	0	1.8	1.9	1.8	1.0	2.2	0	1.4	2.9	1.8	1.4	2.6	0	1.8	3.3	1.8	2.0	4.2	0	2.7	4.6	1.6	4.0	2.8	0	4.7	3.2	1.6
4	1.5	1.5	0	1.9	2.2	1.8	2.1	1.8	0	2.5	2.5	1.8	1.5	3.2	0	1.9	3.9	1.8	2.1	3.9	0	2.5	4.6	1.8	2.0	3.5	0	2.7	3.9	1.6	3.3	4.2	0	4.0	4.6	1.6
5	2.0	2.0	0	2.4	2.7	1.8	2.8	2.4	0	3.2	3.1	1.8	2.0	4.3	0	2.4	5.0	1.8	2.8	5.2	0	3.2	5.9	1.8	2.0	2.8	0	2.7	3.2	1.6	2.6	5.6	0	3.3	6.0	1.6
6	2.5	2.5	0	2.9	3.2	1.8	3.5	3.0	0	3.9	3.7	1.8	2.5	3.2	0	2.9	3.9	1.8	3.5	3.9	0	3.9	4.6	1.8	2.0	2.1	0	2.7	2.5	1.6	2.0	4.2	0	2.7	4.6	1.6
7	3.0	3.0	0	3.4	3.7	1.8	4.2	3.6	0	4.6	4.3	1.8	3.0	2.2	0	3.4	2.9	1.8	4.2	2.6	0	4.6	3.3	1.8	2.0	1.4	0	2.7	1.8	1.6	1.3	2.8	0	2.0	3.2	1.6
8	3.5	3.5	0	3.9	4.2	1.8	4.9	4.2	0	5.3	4.9	1.8	3.5	1.1	0	3.9	1.8	1.8	4.9	1.3	0	5.3	2.0	1.8	2.0	0.7	0	2.7	1.1	1.6	0.7	1.4	0	1.4	1.8	1.6
9	4.0	4.0	0	4.4	4.7	1.8	5.6	4.8	0	6.0	5.5	1.8	4.0	0	0	4.4	0.7	1.8	5.6	0	0	6.0	0.7	1.8	2.0	0	0	2.7	0.4	1.6	0.0	0	0	0.7	0.4	1.6

Table C.2: The coordinates of each movement position.

Bibliography

[1] J. M. Kahn and J. R. Barry, "Wireless infrared communications," *Proceedings of the IEEE*, vol. 85, no. 2, pp. 265–298, 1997.

[2] F. R. Gfeller, H. R. Müller, and P. Vettiger, "Infrared communications for in-house applications," in *IEEE COMPCON'78*, pp. 132–138, 5-8 Sept. 1979.

[3] F. R. Gfeller and U. Bapst, "Wireless in-house data communication via diffuse infrared radiation," *Proc. IEEE*, vol. 67, no. 11, pp. 1474–1486, 1979.

[4] T. Minami, Y. Kenjiro, and T. Touge, "Optical wireless modem for office communications," *AFIPS Conference Proceedings*, vol. 52, pp. 721–728, 1983.

[5] N. Baran, "Wireless networking," *BYTE*, no. April, pp. 291–294, 1992.

[6] O. Takahashi and T. Touge, "Optical wireless network for office communication," *JARACT*, vol. 20, pp. 217–228, 1985/1986.

[7] C.-S. Yen and R. D. Crawford, "The use of directed optical beams in wireless comuputer communications," *IEEE GLOBECOM*, pp. 1181–1184, 1985.

[8] M. D. Kotzin and A. P. van den Heuvel, "A duplex infra-red system for in-building communications," vol. 36, pp. 179–185, 1986.

[9] T. S. Chu and M. Gans, "High speed infrared local wireless communication," *Communications Magazine, IEEE*, vol. 25, no. 8, pp. 4–10, 1987.

[10] T. Fuji and Y. Kikkawa, "Optical space transmission module," *National Technical Report*, vol. 34, no. 1, pp. 101–106, 1988.

[11] R. L. Poulin, D. R. Pauluzzi, and M. R. Walker, "A multi-channel infrared telephony demonstration system for public access applications," pp. 286–291, 1992.

[12] G. W. Marsh and J. M. Kahn, "50-mb/s diffuse infrared free-space link using on-off keying with decision-feedback equalization," *Photonics Technology Letters, IEEE*, vol. 6, no. 10, pp. 1268–1270, 1994.

[13] M. J. McCullagh and D. R. Wisely, "155 mbit/s optical wireless link using a bootstrapped silicon apd receiver," *Electronics Letters*, vol. 30, pp. 430–432, 03/03/ 1994.

[14] D. C. O'Brien, M. Katz, P. Wang, K. Kalliojarvi, S. Arnon, M. Matsumoto, R. J. Green, and S. Jivkova, "Short range optical wireless communications," *Wireless World Research Forum*, 2005.

[15] C. D. Knutson and J. M. Brown, *IrDA Principles and Protocols: The IrDA Library, Vol. 1.* MCL Press, 2004.

[16] S. Roy, J. R. Foerster, V. S. Somayazulu, and D. G. Leeper, "Ultrawideband radio design: the promise of high-speed, short-range wireless connectivity," *Proceedings of the IEEE*, vol. 92, no. 2, pp. 295–311, 2004.

[17] D. Geer, "Users make a beeline for zigbee sensor technology," *Computer*, vol. 38, no. 12, pp. 16–19, 2005.

[18] M. J. Lee, J. Zheng, Y.-B. Ko, and D. M. Shrestha, "Emerging standards for wireless mesh technology," *Wireless Communications, IEEE*, vol. 13, no. 2, pp. 56–63, 2006.

[19] K. V. S. S. S. S. Sairam, N. Gunasekaran, and S. R. Redd, "Bluetooth in wireless communication," *Communications Magazine, IEEE*, vol. 40, no. 6, pp. 90–96, 2002.

[20] J. G. Proakis, *Wiley encyclopedia of telecommunications.* Hoboken, N.J: Wiley, 2003.

[21] J. B. Carruthers and J. M. Kahn, "Multiple-subcarrier modulation for nondirected wireless infrared communication," *Selected Areas in Communications, IEEE Journal on*, vol. 14, no. 3, pp. 538–546, 1996.

[22] D. C. M. Lee, J. M. Kahn, and M. D. Audeh, "Trellis-coded pulse-position modulation for indoor wireless infrared communications," *IEEE Trans. Commun.*, vol. 45, no. 9, pp. 1080–1087, 1997.

[23] Z. Ghassemlooy and A. R. Hayes, "Digital pulse interval modulation for ir communication systems - a review," *International Journal of Communication Systems*, vol. 13, no. 7-8, pp. 519–536, 2000.

[24] K. Park, "Convolutional coded pulse-position modulation on wireless infrared link," *IEE Proceedings - Optoelectronics*, vol. 148, pp. 199–203, 08/00/ 2001.

[25] "BS EN 60825-1:2007: Safety of laser products. equipment classification, requirements and user's guide," 2007.

[26] V. Jungnickel, V. Pohl, S. Nonnig, and C. von Helmolt, "A physical model of the wireless infrared communication channel," *Selected Areas in Communications, IEEE Journal on*, vol. 20, no. 3, pp. 631–640, 2002.

[27] P. Barker and A. C. Boucouvalas, "Effect of random alignment sway on the performance of irda handheld devices," *IEE Seminar Digests*, vol. 1999, pp. 9–9, 01/00/ 1999.

[28] M. R. Pakravan and M. Kavehrad, "Design considerations for broadband indoor infrared wireless communication systems," *International Journal of Wireless Information Networks*, vol. 2, pp. 223–238, 10/29 1995.

[29] F. R. Gfeller and W. Hirt, "A robust wireless infrared system with channel reciprocity," *Communications Magazine, IEEE*, vol. 36, no. 1, pp. 100–106, 1998.

[30] W. Hirt, M. Hassner, and N. Heise, "Irda-vfir (16 mb/s): modulation code and system design," *Personal Communications, IEEE [see also IEEE Wireless Communications]*, vol. 8, no. 1, pp. 58–71, 2001.

[31] M. D. Audeh, J. M. Kahn, and J. R. Barry, "Performance of pulse-position modulation on measured non-directed indoor infrared channels," *Communications, IEEE Transactions on*, vol. 44, no. 6, pp. 654–659, 1996.

[32] T. Lueftner, C. Kroepl, M. Huemer, J. Hausner, R. Hagelauer, and R. Weigel, "Edge-position modulation for high-speed wireless infrared communications," *IEE Proceedings - Optoelectronics*, vol. 150, pp. 427–437, 10/00/ 2003.

[33] C. Singh, J. John, Y. N. Singh, and K. K. Tripathi, "A review of optical wireless systems," *IETE Technical Review*, vol. 19, no. 1 Jan-Feb, pp. 3–17, 2002.

[34] T. Lueftner, C. Kropl, R. Hagelauer, M. Huemer, R. Weigel, and J. Hausner, "Wireless infrared communications with edge position modulation for mobile devices," *Wireless Communications, IEEE [see also IEEE Personal Communications]*, vol. 10, no. 2, pp. 15–21, 2003.

[35] J. R. Barry, *Wireless infrared communications*, vol. SECS 280. Kluwer Academic, 1994.

[36] K. K. Wong and T. O'Farrell, "Spread spectrum techniques for indoor wireless ir communications," *Wireless Communications, IEEE [see also IEEE Personal Communications]*, vol. 10, no. 2, pp. 54–63, 2003.

[37] D.-S. Shiu and J. M. Kahn, "Differential pulse-position modulation for power-efficient optical communication," *Communications, IEEE Transactions on*, vol. 47, no. 8, pp. 1201–1210, 1999.

[38] S. Teramoto and T. Ohtsuki, "Multiple-subcarrier optical communication system with peak reduction carriers," *Trans. of IEICE*, vol. E87-B, no. 11, pp. 3385–3388, 2004.

[39] H. Park and J. R. Barry, "Trellis-coded multiple-pulse-position modulation for wireless infrared communications," *Communications, IEEE Transactions on*, vol. 52, no. 4, pp. 643–651, 2004.

[40] A. Garcia-Zambrana and A. Puerta-Notario, "Novel approach for increasing the peak-to-average optical power ratio in rate-adaptive optical wireless communication systems," *IEE Proc., Optoelectron.*, vol. 150, no. 5, pp. 439–444, 2003.

[41] IrDA, "Advanced infrared physical layer specification (airphy)-version 1.0," Sept 1998.

[42] J. Grubor, V. Jungnickel, and K. D. Langer, "Rate-adaptive multiple sub-carrier-based transmission for broadband infrared wireless communication," pp. 10–20, 2006.

[43] D. J. T. Heatley, D. R. Wisely, I. Neild, and P. Cochrane, "Optical wireless: the story so far," *Communications Magazine, IEEE*, vol. 36, no. 12, pp. 72–74, 79–82, 1998.

[44] R. Ramirez-Iniguez and R. J. Green, "Optical antenna design for indoor optical wireless communication systems," *Int. J. Commun. Syst.*, vol. 18, no. 3, pp. 229–245, 2005.

[45] R. J. Green and R. Ramirez-Iniguez, "Optical concentrator, patent no. gb0308128.8 - wo 2004/090601 a1," 21/10/04 2004.

[46] A. M. Street, P. N. Stavrinou, D. C. O'Brien, and D. J. Edwards, "Indoor optical wireless systems a review," *Optical and Quantum Electronics*, vol. 29, no. 3, pp. 349–378, 1997.

[47] S. Jivkova and M. Kavehrad, "Receiver designs and channel characterization for multi-spot high-bit-rate wireless infrared communications," *Communications, IEEE Transactions on*, vol. 49, no. 12, pp. 2145–2153, 2001.

[48] A. G. Al-Ghamdi and J. M. H. Elmirghani, "Spot diffusing technique and angle diversity performance for high speed indoor diffuse infra-red wireless transmission," *IEE Proceedings - Optoelectronics*, vol. 151, no. 1, pp. 46–52, 2004.

[49] M. Kavehrad and S. Jivkova, "Indoor broadband optical wireless communications: optical subsystems designs and their impact on channel characteristics," *Wireless Communications, IEEE [see also IEEE Personal Communications]*, vol. 10, no. 2, pp. 30–35, 2003.

[50] G. Yun, G. Yun, and M. Kavehrad, "Spot-diffusing and fly-eye receivers for indoor infrared wireless communications; spot-diffusing and fly-eye receivers for indoor infrared wireless communications," in *Wireless Communications, 1992. Conference Proceedings., 1992 IEEE International Conference on Selected Topics in* (M. Kavehrad, ed.), pp. 262–265, 1992.

[51] S. H. Khoo, E. B. Zyambo, G. E. Faulkner, D. C. O'Brien, D. J. Edwards, M. Ghisoni, and J. Bengtsson, "Eyesafe optical link using a holographic diffuser," *IEE Seminar Digests*, vol. 1999, pp. 3–3, 01/00/ 1999.

[52] D. C. O'Brien, G. E. Faulkner, K. Jim, E. B. Zyambo, D. J. Edwards, M. Whitehead, P. Stavrinou, G. Parry, J. Bellon, M. J. Sibley, V. A. Lalithambika, V. M. Joyner, R. J. Samsudin, D. M. Holburn, and R. J. Mears, "High-speed integrated transceivers for optical wireless," *IEEE Commun. Mag.*, vol. 41, no. 3, pp. 58–62, 2003.

[53] J. P. Savicki and S. P. Morgan, "Hemispherical concentrators and spectral filters for planar sensors in diffuse radiation fields," *Applied Optics*, vol. 33, no. 34, pp. 8057–8061, 1994.

[54] M. E. Marhic, M. D. Kotzin, and A. P. van den Heuvel, "Reflectors and immersion lenses for detectors of diffuse radiation," *J.Opt.Soc.Am.*, vol. 72, no. 3, pp. 352–355, 1982.

[55] J. R. Barry and J. M. Kahn, "Link design for nondirected wireless infrared communications," *Applied Optics*, vol. 34, no. 19, pp. 3764–3776, 1995.

[56] K. Ho and J. M. Kahn, "Compound parabolic concetrators for narrowband wireless infrared receivers," *Optical Engineering*, vol. 34, no. 5, pp. 1385–1395, 1995.

[57] L. M. Wasiczko, I. I. Smolyaninov, and C. C. Davis, "Analysis of compound parabolic concentrators and aperture averaging to mitigate fading on free-space optical links," vol. 5160, (San Diego, CA, USA), pp. 133–142, SPIE, 01/27 2004.

[58] J. M. Kahn, J. R. Barry, M. D. Audeh, J. B. Carruthers, W. J. Krause, and G. W. Marsh, "Non-directed infrared links for high-capacity wireless lans," *Personal Communications, IEEE [see also IEEE Wireless Communications]*, vol. 1, no. 2, p. 12, 1994.

[59] J. M. Kahn, R. You, P. Djahani, A. G. Weisbin, B. K. Teik, and A. Tang, "Imaging diversity receivers for high-speed infrared wireless communication," *Communications Magazine, IEEE*, vol. 36, no. 12, pp. 88–94, 1998.

[60] J. B. Carruthers and J. M. Kahn, "Angle diversity for nondirected wireless infrared communication," *Communications, IEEE Transactions on*, vol. 48, no. 6, pp. 960–969, 2000.

[61] V. Jungnickel, A. Forck, T. Haustein, U. Kruger, V. Pohl, and C. von Helmolt, "Electronic tracking for wireless infrared communications," *Wireless Communications, IEEE Transactions on*, vol. 2, no. 5, pp. 989–999, 2003.

[62] D. C. O'Brien, G. E. Faulkner, E. B. Zyambo, K. Jim, D. J. Edwards, P. Stavrinou, G. Parry, J. Bellon, M. J. Sibley, V. A. Lalithambika, V. M. Joyner, R. J. Samsudin, D. M. Holburn, and R. J. Mears, "Integrated transceivers for optical wireless communications," *IEEE J. Sel. Topics. Quantum Electron.*, vol. 11, no. 1, pp. 173–183, 2005.

[63] D. O'Brien, G. Faulkner, K. Jim, D. Edwards, E. Zyambo, P. Stavrinou, G. Parry, J. Bellon, M. Sibley, R. Samsudin, D. Holburn, V. Lalithambika, V. Joyner, and R. Mears, "Experimental characterization of integrated optical wireless components," *Photonics Technology Letters, IEEE*, vol. 18, no. 8, pp. 977–979, 2006.

[64] M. Castillo-Vazquez and A. Puerta-Notario, "Single-channel imaging receiver for optical wireless communications," *Communications Letters, IEEE*, vol. 9, no. 10, pp. 897–899, 2005.

[65] P. C. Fetterolf and G. Anandalingam, "Optimizing interconnections of local area networks: An approach using simulated annealing.," *ORSA Journal on Computing;*, vol. 3, no. 4, pp. 275–287, 1991.

[66] B. Yener and T. E. Boult, "A study of upper and lower bounds for minimum congestion routing in lightwave networks," in *INFOCOM '94. Networking for Global Communications., 13th Proceedings IEEE*, pp. 138–147 vol.1, 1994.

[67] J. A. Bannister, L. Fratta, and M. Gerla, "Topological design of the wavelength-division optical network," in *INFOCOM '90. Ninth Annual Joint Conference of the IEEE Computer and Communication Societies. 'The Multiple Facets of Integration'. Proceedings., IEEE*, pp. 1005–1013 vol.3, 1990.

[68] A. Desai and S. Milner, "Autonomous reconfiguration in free-space optical sensor networks," *Selected Areas in Communications, IEEE Journal on*, vol. 23, no. 8, pp. 1556–1563, 2005.

[69] N. Telzhensky and Y. Leviatan, "Novel method of uwb antenna optimization for specified input signal forms by means of genetic algorithm," *Antennas and Propagation, IEEE Transactions on*, vol. 54, no. 8, pp. 2216–2225, 2006.

[70] K. Chen, X. Yun, Z. He, and C. Han, "Synthesis of sparse planar arrays using modified real genetic algorithm," *Antennas and Propagation, IEEE Transactions on*, vol. 55, no. 4, pp. 1067–1073, 2007.

[71] R. J. Allard, D. H. Werner, and P. L. Werner, "Radiation pattern synthesis for arrays of conformal antennas mounted on arbitrarily-shaped three-dimensional platforms using genetic algorithms," *Antennas and Propagation, IEEE Transactions on*, vol. 51, no. 5, pp. 1054–1062, 2003.

[72] R. L. Haupt, "An introduction to genetic algorithms for electromagnetics," *Antennas and Propagation Magazine, IEEE*, vol. 37, no. 2, pp. 7–15, 1995.

[73] D. W. K. Wong, G. Chen, and J. Yao, "Optimization of spot pattern in indoor diffuse optical wireless local area networks," *Opt. Express*, vol. 13, no. 8, pp. 3000–3014, 2005.

[74] S. Kirkpatrick, C. D. Gelatt, and M. P. Vecchi, "Optimization by simulated annealing," *Science*, vol. 220, no. 4598, pp. 671–680, 1983.

[75] M. Wen, J. Yao, D. W. K. Wong, and G. C. K. Chen, "Holographic diffuser design using a modified genetic algorithm," *Opt.Eng.*, vol. 44, no. 8, pp. 085801–8, 2005.

[76] R. J. Dickenson and Z. Ghassemlooy, "A feature extraction and pattern recognition receiver employing wavelet analysis and artificial intelligence for signal detection in diffuse optical wireless communications," *IEEE Trans. Wireless Commun.*, vol. 10, no. 2, pp. 64–72, 2003.

[77] J. Hou and D. C. O'Brien, "Adaptive inter-system handover for heterogeneous rf and ir networks," in *Parallel and Distributed Processing Symposium, 2005. Proceedings. 19th IEEE International*, pp. 125a–125a, 2005.

[78] J. Hou and D. C. O'Brien, "Vertical handover-decision-making algorithm using fuzzy logic for the integrated radio-and-ow system," *Wireless Communications, IEEE Transactions on*, vol. 5, no. 1, pp. 176–185, 2006.

[79] J. Bellon, M. J. N. Sibley, D. R. Wisely, and S. D. Greaves, "Hub architecture for infrared wireless networks in office environments," *IEE Proceedings - Optoelectronics*, vol. 146, pp. 78–82, 04/00/ 1999.

[80] F. Parand, G. E. Faulkner, and D. C. O'Brien, "Cellular tracked optical wireless demonstration link," *IEE Proceedings - Optoelectronics*, vol. 150, pp. 490–496, 10/00/ 2003.

[81] J. R. Barry, J. M. Kahn, E. A. Lee, and D. G. Messerschmitt, "High-speed nondirective optical communication for wireless networks," *Network, IEEE*, vol. 5, no. 6, pp. 44–54, 1991.

[82] A. Sivabalan and J. John, "Modeling and simulation of indoor optical wireless channels: a review," in *Modeling and simulation of indoor optical wireless channels: a review*, vol. 3, pp. 1082–1085 Vol.3, 2003.

[83] H. Hashemi, G. Yun, M. Kavehrad, F. Behbahani, and P. A. Galko, "Indoor propagation measurements at infrared frequencies for wireless local area networks applications," *IEEE Trans. Veh. Technol.*, vol. 43, no. 3, pp. 562–576, 1994.

[84] M. R. Pakravan and M. Kavehrad, "Indoor wireless infrared channel characterization by measurements," *IEEE Trans. Veh. Technol.*, vol. 50, no. 4, pp. 1053–1073, 2001.

[85] J. M. Kahn, W. J. Krause, and J. B. Carruthers, "Experimental characterization of non-directed indoor infrared channels," *IEEE Trans. Commun.*, vol. 43, no. 234, pp. 1613–1623, 1995.

[86] C. R. Lomba, R. T. Valadas, and A. M. de Oliveira Duarte, "Efficient simulation of the impulse response of the indoor wireless optical channel," *Int. J. Commun. Syst.*, vol. 13, no. 7-8, pp. 537–549, 2000.

[87] J. R. Barry, J. M. Kahn, W. J. Krause, E. A. Lee, and D. G. Messerschmitt, "Simulation of multipath impulse response for indoor wireless optical channels," *IEEE J. Sel. Areas Commun.*, vol. 11, no. 3, pp. 367–379, 1993.

[88] C. M. Goral, K. E. Torrance, D. P. Greenberg, and B. Battaile, "Modeling the interaction of light between diffuse surfaces," in *SIGGRAPH '84: Proceedings of the 11th annual conference on Computer graphics and interactive techniques*, (New York, NY, USA), pp. 213–222, ACM Press, 1984.

[89] F. J. López-Hernández and M. J. Betancor, "Dustin: algorithm for calculation of impulse response on ir wireless indoor channels," *Electronics Letters*, vol. 33, no. 21, pp. 1804–1806, 1997.

[90] J. B. Carruthers, S. M. Carroll, and P. Kannan, "Propagation modelling for indoor optical wireless communications using fast multi-receiver channel estimation," *IEE Proc., Optoelectron.*, vol. 150, no. 5, pp. 473–481, 2003.

[91] J. B. Carruthers and P. Kannan, "Iterative site-based modelling for wireless infrared channels," *IEEE Trans. Antennas Propag.*, vol. 50, no. 5, pp. 759–765, 2002.

[92] R. Pérez-Jiménez, J. Berges, and M. J. Betancor, "Statistical model for the impulse response on infrared indoor diffuse channels," *Electron. Lett.*, vol. 33, no. 15, pp. 1298–1300, 1997.

[93] F. J. López-Hernández, R. Pérez-Jiménez, and A. Santamaría, "Monte carlo calculation of impulse response on diffuse ir wireless indoor channels," *Electronics Letters*, vol. 34, pp. 1260–1262, 06/11/ 1998.

[94] F. J. López-Hernández, R. Pérez-Jiménez, and A. Santamaría, "Modified monte carlo scheme for high-efficiency simulation of the impulse response on diffuse ir wireless indoor channels," *Electronics Letters*, vol. 34, pp. 1819–1820, 09/17/ 1998.

[95] F. J. López-Hernández, R. Pérez-Jiménez, and A. Santamaría, "Ray-tracing algorithms for fast calculation of the channel impulse response on diffuse ir wireless indoor channels," *Journal of Optical Engineering*, vol. 39, no. 10, pp. 2775–2780, 2000.

[96] O. González, C. Militello, S. Rodríguez, R. Pérez-Jiménez, and A. Ayala, "Error estimation of the impulse response on diffuse wireless infrared indoor channels using a monte carlo ray-tracing algorithm," *IEE Proceedings - Optoelectronics*, vol. 149, pp. 222–227, 10/00/ 2002.

[97] V. Pohl, V. Jungnickel, R. Hentges, and C. V. Helmolt, "Integrating sphere diffuser for wireless infrared communication," *IEE Seminar Digests*, vol. 1999, pp. 4–4, 01/00/ 1999.

[98] V. Pohl, V. Jungnickel, and C. von Helmolt, "Integrating-sphere diffuser for wireless infrared communication," *IEE Proc. Optoelectron.*, vol. 147, no. 4, pp. 281–285, 2000.

[99] P. L. Eardley, D. R. Wisely, D. Wood, and P. McKee, "Holograms for optical wireless lans," *IEE Proc. Optoelectron.*, vol. 143, no. 6, pp. 365–369, 1996.

[100] M. R. Pakravan, E. Simova, and M. Kavehrad, "Holographic diffusers for indoor infrared communication systems," *Int. J. Wireless Information Networks*, vol. 4, pp. 259–274, 1997.

[101] J. Yao, G. C. K. Chen, and T. K. Lim, "Holographic diffuser for diffuse infrared wireless home networking," *Opt. Eng.*, vol. 42, pp. 317–324, 2003.

[102] J. J. G. Fernandes, P. A. Watson, and J. C. Neves, "Wireless lans: physical properties of infra-red systems vs. mmw systems," *IEEE Commun. Mag.*, vol. 32, no. 8, pp. 68–73, 1994.

[103] G. N. Bakalidis, E. Glavas, and P. Tsalides, "Optical power distribution in wireless infrared lans," *IEE Proc. Commun.*, vol. 143, no. 2, pp. 93–97, 1996.

[104] H. Yang and C. Lu, "Infrared wireless LAN using multiple optical sources," *IEE Proc. Optoelectron.*, vol. 147, no. 4, pp. 301–307, 2000.

[105] T. Komine and M. Nakagawa, "Integrated system of white led visible-light communication and power-line communication," *IEEE Trans. Consum. Electron.*, vol. 49, no. 1, pp. 71–79, 2003.

[106] F. J. López-Hernández, E. Poves, R. Pérez-Jiménez, and J. Rabadan, "Low-cost diffuse wireless optical communication system based on white led," in *Consumer Electronics, 2006. ISCE '06. 2006 IEEE Tenth International Symposium on*, pp. 1–4, 2006.

[107] J. Grubor, S. Randel, K. D. Langer, and J. W. Walewski, "Bandwidth-efficient indoor optical wireless communications with white light-emitting diodes," in *Communication Systems, Networks and Digital Signal Processing, 2008. CNSDSP 2008. 6th International Symposium on*, pp. 165–169, 2008.

[108] S. Jivkova, B. A. Hristov, and M. Kavehrad, "Power-efficient multispot-diffuse multiple-input-multiple-output approach to broad-band optical wireless communications," *IEEE Trans. Veh. Technol.*, vol. 53, no. 3, pp. 882–889, 2004.

[109] A. G. Al-Ghamdi and J. M. H. Elmirghani, "Analysis of diffuse optical wireless channels employing spot-diffusing techniques, diversity receivers, and combining schemes," *IEEE Trans. Commun.*, vol. 52, no. 10, pp. 1622–1631, 2004.

[110] E. Massera, I. Rea, I. Nasti, P. Maddalena, and G. D. Francia, "Silicon infrared diffuser for wireless communication," *Applied Optics*, vol. 45, no. 26, pp. 6746–6749, 2006.

[111] H. L. Minh, D. C. O'Brien, G. E. Faulkner, L. Zeng, K. Lee, D. Jung, and Y. Oh, "80 mbit/s visible light communications using pre-equalized white led," in *Optical Communication, 2008. ECOC 2008. 34th European Conference on*, pp. 1–2, 2008.

[112] C. Singh, J. John, Y. N. Singh, and K. K. Tripathi, "Design aspects of high-performance indoor optical wireless transceivers [lan applications]," pp. 14–18, 2005.

[113] C. R. Lomba, R. T. Valadas, and A. M. de Oliveira Duarte, "Experimental characterisation and modelling of the reflection of infrared signals on indoor surfaces," *IEE Proc. Optoelectron.*, vol. 145, pp. 191–197, 1998.

[114] E. Uiga, *Optoelectronics*. Englewood Cliffs, N.J. ; London : Prentice Hall: Prentice-Hall International, 1995.

[115] D. Malacara and B. J. Thompson, *Handbook of optical engineering*, vol. 73. New York: Marcel Dekker, 2001.

[116] C. T. Lomba, R. Valadas, and A. M. de Oliveira Duarte, "Propagation losses and impulse response of the indoor optical channel: A simulation package," *Proceedings of the 1994 International Zurich Seminar on Digital Communications: Mobile Communications: Advanced Systems and Components*, pp. 285–297, 1994.

[117] B. T. Phong, "Illumination for computer generated pictures," *Commun ACM*, vol. 18, no. 6, pp. 311–317, 1975.

[118] S. R. Perez, R. P. Jimenez, F. J. López-Hernández, O. B. G. Hernandez, and A. J. A. Alfonso, "Reflection model for calculation of the impulse response on ir-wireless indoor channels using ray-tracing algorithm," *Microwave. Opt. Technol. Lett.*, vol. 32, no. 4, pp. 296–300, 2002.

[119] M. Karppinen, K. Kataja, J.-T. Makinen, S. Juuso, H. J. Rajaniemi, P. Paakkonen, J. Turunen, J. T. Rantala, and P. Karioja, "Wireless infrared data links: ray-trace simulations of diffuse channels and demonstration of diffractive element for multibeam transmitters," *Opt. Eng.*, vol. 41, pp. 899–910, 2002.

[120] H. Willebrand and B. S. Ghuman, *Free space optics : enabling optical connectivity in today's networks*. SAMS, 2002.

[121] C. T. A. T. Lomba, R. T. Valadas, and A. M. de Oliveira Duarte, "Update of propagation losses and impulse response of the indoor optical channel," Tech. Rep. IEEE P802.11-93/142, IEEE, 1993.

[122] S. S. Haykin and B. V. Veen, *Signals and systems*. New York, NY: Wiley, 2003.

[123] A. V. Oppenheim, A. S. Willsky, and S. H. Nawab, *Signals and Systems*. Prentice Hall, 1996.

[124] S. T. Jovkova and M. Kavehard, "Multispot diffusing configuration for wireless infrared access," *Communications, IEEE Transactions on*, vol. 48, no. 6, pp. 970–978, 2000.

[125] T. L. Kay and J. T. Kajiya, "Ray tracing complex scenes," 1986.

[126] A. S. Glassner, *An introduction to ray tracing*. London: Academic Press, 1989.

[127] A. S. Glassner, "Space subdivision for fast ray tracing," *IEEE Comput. Graph. Appl.*, vol. 4, no. 10, pp. 15–22, 1984.

[128] D. Goldberg, "What every computer scientist should know about floating-point arithmetic," *ACM Comput.Surv.*, vol. 23, no. 1, pp. 5–48, 1991.

[129] J. B. Carruthers and J. M. Kahn, "Modeling of nondirected wireless infrared channels," *IEEE Trans. Commun.*, vol. 45, no. 10, pp. 1260–1268, 1997.

[130] P. Djahani and J. M. Kahn, "Analysis of infrared wireless links employing multibeam transmitters and imaging diversity receivers," *IEEE Trans. Commun.*, vol. 48, no. 12, pp. 2077–2088, 2000.

[131] A. C. Boucouvalas, "Iec 825-1 eye safety classification of some consumer electronic products," *IEE Seminar Digests*, vol. 1996, no. 32, pp. 13/1–13/6, 1996.

[132] I. Haratcherev, J. Taal, K. Langendoen, R. Lagendijk, and H. Sips, "Automatic ieee 802.11 rate control for streaming applications," *Wireless Commun. Mob. Comput.*, vol. 5, no. 4, pp. 421–437, 2005.

[133] M. Lacage, M. H. Manshaei, and T. Turletti, "Ieee 802.11 rate adaptation: a practical approach," in *MSWiM '04: Proceedings of the 7th ACM international symposium on Modeling, analysis and simulation of wireless and mobile systems*, (New York, NY, USA), pp. 126–134, ACM Press, 2004.

[134] J. Grubor, V. Jungnickel, and K. D. Langer, "Capacity analysis in indoor wireless infrared communication using adaptive multiple subcarrier transmission," vol. 2, pp. 171–174 Vol. 2, 2005.

[135] A. Garcia-Zambrana and A. Puerta-Notario, "Rate-adaptive indoor wireless infrared links using ook formats with alternate-position gaussian pulses," *Electronics Letters*, vol. 37, pp. 1409–1411, 11/08/ 2001.

[136] A. Garcia-Zambrana and A. Puerta-Notario, "Rate-adaptive modulation techniques for indoor wireless infrared links at bit rates of wide dynamic range," in *Vehicular Technology Conference, 2001. VTC 2001 Spring. IEEE VTS 53rd*, vol. 4, pp. 2313–2317 vol.4, 2001.

[137] J. H. Holland, *Adaptation in natural and artificial systems : an introductory analysis with applications to biology, control, and artificial intelligence*. MIT Press, 1992.

[138] Y. Rahmat-Samii and E. Michielssen, *Electromagnetic optimization by genetic algorithms*. New York, N.Y. ; Chichester: J. Wiley, c1999.

[139] T. Bäck, U. Hammel, and H. P. Schwefel, "Evolutionary computation: Comments on the history and current state," *IEEE Trans. Evol. Comput.*, vol. 1, no. 1, pp. 3–17, 1997.

[140] F. Rothlauf, *Representations for genetic and evolutionary algorithms*. Physica-Verlag, 2002.

[141] D. E. Goldberg, *Genetic algorithms in search, optimization and machine learning*. Reading, Mass ; Wokingham: Addison-Wesley, 1988.

[142] S. E. Haupt and R. L. Haupt, *Practical genetic algorithms*. Hoboken, N.J. ; [Chichester]: Wiley-Interscience, 2004.

[143] F. O'Karray and C. W. D. Silva, *Soft computing and intelligent systems design : theory, tools, and applications*. Pearson/Addison Wesley, 2004.

[144] T. Bäck, D. B. Fogel, and T. Michalewicz, *Evolutionary computation 1 : basic algorithms and operators*. Bristol: Institute of Physics Publishing, c2000.

[145] T. Bäck, *Evolutionary algorithms in theory and practice : evolution strategies, evolutionary programming, genetic algorithms*. Oxford University Press, 1996.

[146] J. E. Baker, "Reducing bias and inefficiency in the selection algorithm," in *Proceedings of the Second International Conference on Genetic Algorithms and their application*, (Mahwah, NJ, USA), pp. 14–21, Lawrence Erlbaum Associates, Inc, 1987.

[147] T. Blickle and L. Thiele, "A comparison of selection schemes used in genetic algorithms," tech. rep., 1995.

[148] A. M. S. Zalzala and P. J. Fleming, *Genetic algorithms in engineering systems*, vol. 55. London: Institution of Electrical Engineers, 1997.

[149] I. J. Griffiths, Q. H. Mehdi, and N. E. Gough, "Microcontroller based genetic algorithms," *Microprocessors and Microsystems*, vol. 21, pp. 403–413, 1998.

[150] A. Sokolov and D. Whitley, "Unbiased tournament selection," in *GECCO '05: Proceedings of the 2005 conference on Genetic and evolutionary computation*, (New York, NY, USA), pp. 1131–1138, ACM Press, 2005.

[151] R. Poli, "Tournament selection, iterated coupon-collection problem, and backward-chaining evolutionary algorithms," in *Foundations of Genetic Algorithms*, pp. 132–155, 2005.

[152] M. Negnevitsky, *Artificial intelligence : a guide to intelligent systems*. Harlow, England ; New York: Addison-Wesley, 2005.

[153] A. G. Al-Ghamdi and J. M. H. Elmirghani, "Analysis of optical wireless links employing a beam clustering method and diversity receivers;," in *Communications, 2004 IEEE International Conference on* (J. M. H. Elmirghani, ed.), vol. 6, pp. 3341–3347 Vol.6, 2004.

[154] C. W. Nicolay and A. L. Walker, "Grip strength and endurance: Influences of anthropometric variation, hand dominance, and gender," *Int. J. Industrial Ergonomics*, vol. 35, no. 7, pp. 605–618, 2005.

[155] A. C. Boucouvalas, "Symmetry of irda optical links," *IEE Seminar Digests*, vol. 1996, pp. 6–6, 01/00/ 1996.

[156] A. C. Boucouvalas and P. Barker, "Asymmetric throughput in irda links," *IEE Seminar Digests*, vol. 1999, pp. 7–7, 01/00/ 1999.

[157] A. C. Boucouvalas and P. Barker, "Asymmetry in optical wireless links," *IEE Proceedings - Optoelectronics*, vol. 147, pp. 315–321, 08/00/ 2000.

[158] A. G. Al-Ghamdi and J. M. H. Elmirghani, "Line strip spot-diffusing transmitter configuration for optical wireless systems influenced by background noise and multipath dispersion," *Communications, IEEE Transactions on*, vol. 52, no. 1, pp. 37–45, 2004.

[159] F. S. J. Hill, *Computer graphics*. New York : London: Macmillan ; Collier Macmillan, 1990.

[160] M. P. Baker and D. Hearn, *Computer graphics*. Englewood Cliffs, N.J. ; London: Prentice Hall, c1994.

[161] P. L. Royds and J. M. H. Elmirghani, "Optical wireless cellular network motion model," *Electronics Letters*, vol. 39, pp. 928–930, 06/12/ 2003.

[162] A. C. Boucouvalas, "Indoor ambient light noise and its effect on wireless optical links," *IEE Proceedings - Optoelectronics*, vol. 143, no. 6, pp. 334–338, 1996.

[163] R. Narasimhan, M. D. Audeh, and J. M. Kahn, "Effect of electronic-ballast fluorescent lighting on wireless infrared links," *IEE Proceedings - Optoelectronics*, vol. 143, no. 6, pp. 347–354, 1996.

[164] A. J. C. Moreira, R. T. Valadas, and A. M. de Oliveira Duarte, "Performance of infrared transmission systems under ambient light interference," *IEE Proceedings - Optoelectronics*, vol. 143, pp. 339–346, 12/00/ 1996.

[165] A. J. C. Moreira, R. T. Valadas, and A. M. de Oliveira Duarte, "Characterisation and modelling of artificial light interference in optical wireless communication systems," vol. 1, pp. 326–331 vol.1, 1995.

[166] F. E. Nicodemus, "Radiance," *American Journal of Physics*, vol. 31, pp. 368–377, 05/00/ 1963.

[167] J. R. Meyer-Arendt, "Radiometry and photometry: Units and conversion factors," *Applied Optics*, vol. 7, no. 10, pp. 2081–2084, 1968.

[168] A. J. C. Moreira, R. T. Valadas, and A. M. de Oliveira Duarte, "Optical interference produced by artificial light," *Wirel.Netw.*, vol. 3, no. 2, pp. 131–140, 1997.

[169] R. T. Valadas, A. R. Tavares, and A. M. de Oliveira Duarte, "Angle diversity to combat the ambient noise in indoor optical wireless communication systems," *International Journal of Wireless Information Networks*, vol. 4, pp. 275–288, 10/01 1997.

[170] A. G. Al-Ghamdi and J. M. H. Elmirghani, "Optimization of a triangular pfdr antenna in a fully diffuse ow system influenced by background noise and multipath propagation," *Communications, IEEE Transactions on*, vol. 51, no. 12, pp. 2103–2114, 2003.

[171] E. Union, "Directive 2005/32/ec of the european union," *Official Journal of the European Union*, vol. 48,, no. July L191, pp. 29–58, 2005.

[172] K. K. Wong, T. O'Farrell, and M. Kiatweerasakul, "The performance of optical wireless ook, 2-ppm and spread spectrum under the effects of multipath dispersion and artificial light interference," *International Journal of Communication Systems*, vol. 13, no. 7-8, pp. 551–576, 2000.

[173] A. Tavares, R. Valadas, R. L. Aguiar, and A. M. de Oliveira Duarte, "Angle diversity and rate-adaptive transmission for indoor wireless optical communications," *Communications Magazine, IEEE*, vol. 41, no. 3, pp. 64–73, 2003.

[174] C.-H. Tsuei, J.-W. Pen, and W.-S. Sun, "Simulating the illuminance and the efficiency of the led and fluorescent lights used in indoor lighting design," *Optics Express*, vol. 16, pp. 18692–18701, 11/10 2008.